Landscape Response to Oblique Convergence: Insights from Numerical Modeling and from the Marlborough Fault System, New Zealand

Sarah A. Harbert

A dissertation

submitted in partial fulfillment of the

requirements for the degree of

Doctor of Philosophy

University of Washington

2019

Reading Committee:

Alison R. Duvall, Chair

Juliet G. Crider

David R. Montgomery

Program Authorized to Offer Degree:

Earth and Space Sciences

University of Washington

Abstract

Landscape Response to Oblique Convergence: Insights from Numerical Modeling and from the Marlborough Fault System, New Zealand

Sarah A. Harbert

Chair of the Supervisory Committee:
Alison R. Duvall
Earth and Space Sciences

Strike-slip and oblique faults are prominent tectonic features that can dramatically influence the landscape at all scales. In this dissertation, I explore the effects of strike-slip and oblique faults on the landscape, from the scale of orogenies to individual river channels. I focus on the Marlborough Fault System, a multi-strand strike-slip fault system in New Zealand, at the transition between the Hikurangi Subduction Zone and the oblique Alpine fault. In Chapters 2 and 3 I use low-temperature thermochronology to investigate tectonic histories by interpreting timing and relative rates of exhumation across the landscape. Chapter 2 reveals the 10-13 Ma development of the Wairau fault, the resultant formation of a restraining bend at the Alpine-Wairau fault junction, and the onset of exhumation in a broad region caused by this restraining bend. In Chapter 3, using the same method, I identify the earliest manifestation of the Early Kaikōura Orogeny, with exhumation focused on the (present-day) north side of the Awatere fault beginning in the early Eocene. In the western MFS, the modern MFS faults do not exert a strong

control on exhumation. I invert thermochronology data from Chapters 2 and 3, with other published data, for recent exhumation rates across the MFS. Exhumation rates are ~3-3.6 mm/yr adjacent to the Alpine fault, and ~0.9-1.4 mm/yr in the Seaward Kaikōura range. In Chapter 4, I use a landscape evolution model to determine the effects of preexisting topography on the landscape expression of a strike-slip fault. Modeled channels crossing a strike-slip fault were subject to a regular and effective cycle of channel offset by fault slip and shortening by stream capture. Relief of shutter ridges makes stream capture more difficult, especially when the fault slip rate is slow relative to channel and hillslope erosion. Comparison to the MFS shows that real-world complexities – such as lithological variations – can disrupt these expected patterns, allowing long, fault-parallel channel offsets to form. Videos 1-5 show example models from Ch.4: 1 shows the initial condition; 2, a faster-slipping fault; 3, a slower-slipping fault; 4 and 5, a stream channel “evading” capture. Attached dataset contains model input files.

TABLE OF CONTENTS

LIST OF FIGURES

LIST OF TABLES

Chapter 1. INTRODUCTION

Strike-slip faults are prominent tectonic features that have a dramatic influence on the landscape. Some, especially transform plate boundaries, advect rock for hundreds of kilometers and can cause large earthquakes (Schwartz and Coppersmith, 1984; Sylvester, 1988). It is common for strike-slip faults and transform plate margins to include a component of convergence, which can cause rock uplift, exhumation, and mountain building; for example, New Zealand's dextral-reverse Alpine fault is responsible for building the Southern Alps, one of the world's most rapidly uplifting mountain ranges (e.g., Walcott, 1998).

Strike-slip and oblique-slip faults have characteristic effects on the landscape at local and regional scales. At a local scale, the strike-slip landscape is often characterized by offset features, such as stream channels, river terraces, and glacial moraines; sag ponds; and shutter ridges (Keller et al., 1982; Keller, 1986; Sylvester, 1988; Wallace, 1990; Ouchi, 2005;). Offset features have often been used to date fault movement and determine slip rates (e.g., Wallace, 1968; Walker and Jackson, 2002; Mason et al., 2006). Through continued lateral motion over time, strike-slip fault motion can disrupt drainage network topology, causing channel lengthening and stream capture (e.g., Walker and Allen, 2012). While channel and landscape response to vertical tectonic uplift has been extensively studied (e.g., Merritts and Vincent, 1989; Whipple and Tucker, 1999; Snyder et al., 2000; Duvall et al., 2004; Schoenbohm et al., 2004; Wobus et al., 2006; Amos and Burbank, 2007; Hilley and Arrowsmith, 2008), research on the effect of lateral motion on channels and the surrounding landscape has been more limited (e.g., Castelltort et al., 2012; Walker and Allen, 2012; Gray et al., 2017).

In this thesis I investigate some of these local and regional effects of strike-slip and oblique faults on the landscape, through investigations of the tectonic history of an evolving, obliquely

convergent margin, and through more theoretical numerical modeling of landscapes immediately adjacent to strike-slip/oblique faults.

In Chapter 2 I investigate the history of the Alpine fault's prominent restraining bend using low-temperature thermochronology. The results of this study show that the bend, and resultant area of rapid exhumation on its southeast side, formed around 10-13 Ma, when increasingly convergent relative plate motion caused the Wairau fault to form as a primary splay of the Alpine fault. This chapter is currently being reviewed by coauthors and will then be submitted to *Geology*.

In Chapter 3 I use low-temperature thermochronology to reveal the diverse tectonic history of the Marlborough Fault System, a complicated transition zone between the Hikurangi Subduction Zone and dextral-reverse continental collision on the Alpine fault. I demonstrate that the eastern half of the Awatere fault experienced dip-slip motion during the Early Kaikōura Orogeny; that the western MFS has experienced a diverse, piecemeal history of exhumation that has not been strongly controlled by the western Marlborough faults; and that the fastest rates of exhumation over the Pleistocene-present are found in the extreme western MFS, close to the Alpine fault, and along the Clarence River where it cuts through the Seaward Kaikōura mountains. This chapter is being prepared for submission to *Tectonics*.

In Chapter 4 I use a numerical landscape evolution model to simulate the ongoing effects of a strike-slip fault on planform characteristics of the drainage network. Results of this study show that, absent lithological variability or other preexisting complexity, strike-slip landscapes tend to experience a regular and effective cycle of channel lengthening and stream capture, such that channel offsets are generally limited in length to the drainage spacing of the landscape. This chapter was published in *Geophysical Research Letters* in 2018 and appears here as published.

1.1 Field Area Background: The Marlborough Fault System of New Zealand

1.1.1 *The New Zealand Plate Boundary*

The landmass of New Zealand lies at the boundary between the Australian and Pacific plates. Offshore of the North Island and the northernmost South Island, the Pacific plate subducts beneath the Australian plate at the Hikurangi Subduction Zone. The many faults of the Marlborough Fault System connect the southern end of the Hikurangi subduction zone to the dextral-reverse Alpine fault, where oblique continental collision is building the Southern Alps. The Alpine fault runs much of the length of the South Island. South of the Alpine fault, the Australian plate subducts under the Pacific plate at the Puysegur subduction zone (See Fig. 1.1 for the general plate tectonic setting of New Zealand and Fig. 1.2 for a more detailed view).

The obliquity, and changes to that obliquity, of plate motion at this margin have driven its tectonic development and significantly affected the landscape. The modern relative motion at the New Zealand plate boundary varies from ~45 mm/yr off the North Island, to ~37 mm/yr along the central Alpine fault (De Mets et al., 1994, 2010), and convergence at the Hikurangi Subduction Zone becomes more oblique (less orthogonal) from north to south. On the North Island, and where the Hikurangi Subduction Zone extends to the South Island, strain in the Australian Plate is partitioned onto thrust and reverse faults near the trench, including those in the accretionary wedge, and strike-slip faults farther from the trench (Cashman et al., 1992; Barnes et al., 1998). At the Alpine fault, the plate motion vector is about 18° from orthogonal to the strike of the fault. The strike-slip rate on the Alpine fault is 27 +/- 5 mm/yr since at least the Pliocene (Sutherland, 1994; Norris and Cooper, 2001). This rate is about 70-75% of the fault-parallel component of relative plate motion; the rest is partitioned off of the Alpine fault (Norris

and Cooper, 2001; Norris and Toy, 2014). The dip-slip rate varies along strike and is highest, 8-12 mm/yr over the last 50,000 years, in the area of Mt. Cook in the central Southern Alps. Some Alpine-fault-normal displacement is also partitioned off of the main fault, but the amount is difficult to constrain (Norris and Cooper, 2001).

1.1.2 *The Marlborough Fault System*

The Marlborough Fault System is the transition zone between the Hikurangi subduction zone to the north and the dextral-reverse Alpine fault to the south. The relative plate motion across New Zealand is ~48-37 mm/yr of oblique convergence (Beavan et al., 2002; Wallace et al., 2007, 2012). There are four major faults in the MFS: from north to south, they are the Wairau (3-8 mm/yr), Awatere (~5-6 mm/yr), Clarence (~ 5 mm/yr) and Hope/Kekerengu faults (~20 mm/yr) (Benson et al., 2001; Nicol and Van Dissen, 2002; Langridge et al., 2003; Zachariasen et al., 2006; Wallace et al., 2007). The Hope, Clarence and Awatere splay off of the Alpine fault; the Wairau fault is the northern extension of the Alpine fault northeast of its restraining bend. The Hope and Kekerengu faults are linked by the dextral-reverse Jordan Thrust, which strikes more northerly than any other of the MFS faults and uplifts the Inland Kaikōura range (Van Dissen and Yeats, 1991). Models using GPS velocities, earthquake slip vector azimuths, and published fault slip rates to balance the plate motion budget across the Marlborough Fault System conclude that the major Marlborough faults (Wairau, Awatere, Clarence and Hope) are purely strike-slip at present, though there is shortening north of the MFS in the Buller region and also south of the MFS (Wallace et al., 2007, 2012).

South of the MFS there is a complex zone of dextral and reverse faulting – some located just south of the Hope/Jordan/Kekerengu faults, and some farther to the south at the Porters Pass-Amberly fault zone (PPAFZ; Cowan, 1996). Some of these faults were involved in the M_w 7.8

2016 Kaikōura earthquake and the M_w 7.1 2010 Darfield earthquake (e.g., Campbell et al., 2012; Hamling et al., 2017; Stirling et al., 2017). This area may represent the southward migration of the Marlborough Fault System and of the locus of plate boundary slip (Carter and Carter, 1982; Cowan et al., 1996, Litchfield et al., 2014). The numerous ruptures of large and small faults and the up to 8m of surface uplift during the Kaikōura earthquake, and the numerous historical and Holocene earthquakes on or south of the Hope fault, reveal this area as a locus of plate boundary deformation (Howard et al., 2003; Hamling et al., 2017; Stirling et al., 2017).

The landscapes of the eastern and western MFS are quite different. In the east, the Awatere, Clarence, and Jordan faults each bound mountain ranges, despite the interpretation that the Awatere and Clarence faults are purely strike-slip at present. Relief on these mountain ranges increases toward the southeast and the plate boundary, reaching about 2400m in the Inland Kaikōura range and 2600m in the Seaward Kaikōura range. In the western MFS, relief is also fairly high, with peaks greater than 1800m common in the greater Spenser Mountains, on the Pacific plate side of the Alpine-Wairau fault's restraining bend (Suggate, 1979). Here, however, mountain ranges are more discontinuous, and river valleys tend to be aligned more with the regional NNE-SSW strike of the steeply-dipping Torlesse accretionary complex bedrock, and with the many inactive faults in the Torlesse, rather than with the modern MFS faults (Rattenbury et al., 2006; Craw et al., 2013; Roy et al., 2016; Duvall et al., *in review*). Stream captures involving relatively large rivers have occurred in the western and central MFS, in some cases aided by glaciation and by preferential erosion of fault zones (Craw et al., 2008; Duvall et al., *in review)*. For example, the Clarence River's course, thought to be the result of several stream captures, is composed of an upper section that takes a number of sharp bends as it flows

through various, mostly SSW-aligned valleys, then turns NE to flow between the Inland and Seaward Kaikōura mountains (Duvall et al., *in review*).

There are also climatic differences between the eastern and western MFS. The western MFS has been extensively glaciated beginning about 2.5 Ma, although no glaciers remain there today (e.g., Barrell, 2011). In the eastern MFS, only the higher parts of the Inland Kaikōura range, and possibly the Seaward Kaikōura range, were glaciated in the last ~65 ka; no large valley glaciers were present in the eastern MFS (Bacon et al., 2001). Today there is a strong precipitation gradient across the South Island, as precipitation is generally delivered from the west. Mean annual precipitation ranges from less than 0.6 m/yr in the extreme eastern MFS at the Cook Strait coast, to 2.25-2.5 m/yr on the Pacific plate side of the Alpine-Wairau restraining bend, to 4-6 m/yr at the Hope-Alpine fault junction (Chappell, 2016; Macara, 2016a, 2016b).

1.1.3 *Field Area Stratigraphy*

The bedrock in the majority of the Marlborough Fault System is the Torlesse Supergroup, a Permian-early Cretaceous imbricated accretionary complex from the subduction margin of Gondwana (geologic map in Figure 1.3; Howell, 1981; MacKinnon, 1983; Rattenbury et al., 2006). The Torlesse is composed of mostly alternating sandstone and siltstone turbidite and/or fan-delta deposits, with minor conglomerate, basalt, and chert (MacKinnon, 1983; Mortimer, 2004; Rattenbury et al., 2006). The Torlesse is divided into the Permian-Triassic Rakaia Subterrane in the west and the early Cretaceous Pahau Subterrane in the east. The Rakaia and Pahau subterranes are separated by the Esk Head subterrane, a belt of mélange that includes limestones, cherts and pillow basalts derived from the subducting plate, as well as greywacke and mudstone from the Rakaia and Pahau subterranes (Silberling et al., 1988). The Esk Head is one of the only markers of the ~55 km of total offset across the Hope, Clarence, and Awatere

faults, as the Pahau and Rakaia have a great deal of Mesozoic deformation but few continuous marker units (Mortimer, 2014). Units younger than the Torlesse are absent from much of the central and western MFS. The Esk Head mélange is also found in the southern North Island, offset across the Wairau fault by about 140 km (Orr et al., 1991; Rattenbury et al., 2006).

North of the Alpine/Wairau fault are many volcanic and sedimentary terranes that were accreted to the Gondwana margin between, broadly, the Devonian and the Jurassic. These are the Buller, Takaka, Brook Street, Dun Mt.-Maitai, and Caples terranes (Mortimer, 2004). These terranes represent both deposition at the continental margin (Buller, younger Takaka) and accretion of island-arc systems and associated sediments to the margin (older Takaka, Brook Street, Dun Mt-Maitai, Caples) (Münker and Cooper, 1999; Mortimer, 2004; Spandler et al., 2005). Also present north of the Alpine/Wairau fault are plutonic rocks intruded during subduction at this margin; these are the various plutons that make up the Median and Karamea Batholiths (Mortimer, 2004). The ophiolite sequence within the Dun Mt. terrane, and the associated Junction Magnetic Anomaly, are often used as markers of ~480 km of offset across the Alpine fault (e.g., Blake and Landis, 1973; Kamp, 1987; Sutherland, 1999).

In some parts of the field area, the Rakaia subterrane and the Caples terrane have been overprinted by metamorphism to become the Haast Schist, which comprises the Marlborough, Otago and Alpine Schists. The regional metamorphism that generated the correlated Marlborough and Otago schists took place during the Jurassic when the Rakaia subterrane and the Caples terrane, both accretionary complexes off the coast of Gondwana, collided (Little et al., 1999; Rattenbury et al., 2006). In the field area of this study, the Marlborough Schist is found north of the Wairau fault. Metamorphism of the Alpine Schist, found in the western MFS and farther south in a band along the hanging wall of the Alpine fault, occurred during the

Cretaceous and has overprinted the Otago-Marlborough schist (Mortimer and Cooper, 2004; Vry et al., 2004). Both of these schists are mainly biotite zone greenschist facies to prehnite-pumpellyite facies within the field area (Turnbull and Forsyth, 1986). A very narrow band (~2 km wide or less) immediately adjacent to the Alpine fault has a younger metamorphic overprint associated with movement on the fault, as well as up to amphibolite facies rocks (Rose, 1986; Turnbull and Forsyth, 1986).

Cenozoic sedimentary rocks are present in the northwestern and eastern parts of the field area but are absent from the central MFS. Northwest of the Alpine/Wairau fault on the Australian plate are basins, most of which have since been inverted or shortened, created by extension during the Late Cretaceous-Paleogene and the Eocene (Ghisetti and Sibson, 2006). These depocenters include the Moutere Depression, the Murchison Basin, and the Mariua Basin. In the eastern MFS particularly in the southeast, the Pahau subterrane is unconformably overlain by a Cretaceous-Pliocene sequence of marine sedimentary rocks (Rattenbury et al, 2006). Deposition of these units was not spatially uniform and occurred in discontinuous basins, particularly during the early-mid Cretaceous shortly after rifting from Gondwana, and also during the Early and Late Kaikōura Orogenies (e.g., Browne, 1995; Crampton and Laird, 1997; Crampton et al., 1998). In the early Miocene, the coarse fan-delta Great Marlborough Conglomerate was deposited above the mudstone of the Waima Formation. The Great Marlborough conglomerate consists largely of clasts of the Torlesse Greywacke, indicating uplift and erosion of the basement (Browne 1995). The deposition of the Great Marlborough Conglomerate was followed by that of a series of sedimentary units indicating shallowing water followed by subaerial deposition (Lewis et al., 1980; Rait et al., 1991; Browne, 1995; Randall et al., 2011).

1.1.4 *Plate Boundary Evolution*

The continent of Zealandia, most of which is presently below sea level, rifted away from Gondwana around 100-80 Ma (Laird and Bradshaw, 2004; Strogen et al., 2017). As discussed above, this area of continental crust consists of many amalgamated terranes that originated at or were accreted to the Gondwana subduction margin (Mortimer, 2004). This rifting was likely caused by the cessation of subduction there around 100 Ma (Davy, 2014). Subduction ceased around 100 Ma because the Hikurangi Plateau, a part of the ~120 Ma Ontong-Java/Manihiki/Hikurangi Plateau large igneous province, entered the subduction zone but was unable to fully subduct because it was thick, young and buoyant (Davy et al., 2008). The fossil Gondwana subduction margin is still preserved today, with the Hikurangi Plateau partially underplated under the Chatham Rise and central South Island, and extending to the north as an area of thickened Pacific oceanic crust (Davy et al., 2008; Reyners et al., 2011). From that position, the Hikurangi Plateau has been partially subducted in the modern Hikurangi subduction zone, and extends beneath much of the North Island and part of the MFS (Reyners et al., 2011; Reyners et al., 2017).

The modern Hikurangi Subduction Zone, where the Pacific Plate subducts beneath the Australian Plate, initiated north of present-day New Zealand at around 50 Ma, one of many changes in the plate tectonics of the Pacific around this time (e.g., Sutherland et al., 2017). Subduction propagated southward and reached the area of the modern North Island by around 25 Ma (King, 2000; Furlong and Kamp, 2009). By 30 Ma, seafloor spreading in the Emerald Basin began south of modern-day New Zealand (King, 2000; Lebrun et al., 2003). This extension propagated northward and created a series of transtensional basins along the trend of the modern Alpine fault before 25 Ma (King, 2000). Between 30 and 20 Ma, relative plate motion in this

region gradually transitioned from extension to transpression (Furlong and Kamp, 2013). The Alpine fault as a throughgoing, strike-slip feature formed around 25-20 Ma as a result in this change in plate motion, linking up various structures from the previous phase of transtension (Kamp, 1986; Cooper et al., 1987; Batt et al., 2004). It, and some of the preceding structures it took advantage of, may have been localized on a much older fault or other lithospheric boundary (White and Green, 1986; Sutherland et al., 2000).

It is convenient to use the narrower, more distinctive basement terranes as offset markers across the Alpine fault; the Dun Mt. terrane/Junction Magnetic Anomaly are dextrally offset by ~480 km. This distance is generally thought of as the total offset on the Alpine fault since its inception (e.g., Kamp, 1987; Hall et al., 2004). However, this distance accounts for only about 60% of the total Cenozoic relative plate motion (Sutherland, 1999; Lamb et al., 2016). The more widely-accepted model accounts for the rest of the relative plate motion in a broad zone of distributed deformation at least 100 km and possibly up to 300 km wide (Norris et al., 1990; Sutherland, 1999; Little and Mortimer, 2001). This deformation caused much, if not all, of the dramatic oroclinal bending of the basement terranes (Molnar et al., 1975; Kamp, 1987; Sutherland, 1999; Little and Mortimer, 2001; Mortimer, 2014). Off-Alpine-fault deformation likely occurred to a greater degree during the fault's early history, since today ~80% of the relative plate motion at the mid-South Island is accommodated on the Alpine fault. However, another model holds that prior to development of the Alpine fault, the basement terranes were sinistrally offset by 225-300 km, and that slip on and immediately adjacent to the Alpine fault therefore accommodated all ~700 km of relative plate motion since about 25 Ma (Lamb et al., 2016). For the purposes of this thesis I adopt the former model, with ~480 km of dextral offset on the Alpine fault and significant coeval off-fault deformation.

1.1.5 *Early History of the Marlborough Fault System*

The Marlborough Fault System has evolved considerably in the last 25 Ma. Between 25 and 8 Ma, the Hikurangi Subduction Zone rotated clockwise about its southern end (Walcott, 1987; Furlong and Kamp, 2009). In the southern forearc, this rotation was accommodated by clockwise vertical-axis block rotations of about 100°, the boundaries being the eastern Marlborough faults. This history has been well constrained by many paleomagnetic studies, although the number, geometry and arrangement of blocks is less definite (e.g., Lamb, 1988; Lamb and Bibby, 1989; Vickery and Lamb, 1995; Little and Roberts, 1997; Hall et al., 2004; Lamb, 2011; Randall et al., 2011;). Small, equidimensional blocks between the MFS faults, at the extreme northeastern end of the South Island, experienced an additional 30-50 degrees of clockwise rotation, which continued until the present (Hall et al., 2004; Randall et al., 2011). Alternatively, some studies conclude that only this northeasternmost region experienced block rotation at all, and the majority of the present-day MFS experienced distributed shear before transitioning to the modern pattern of strike-slip faulting (Little and Roberts, 1997; Hall et al., 2004).

In the central and western MFS, Cenozoic cover is not preserved, or may never have existed, and rocks suitable for paleomagnetic studies are sparse or absent (Rattenbury et al., 2006). There is therefore less direct evidence with which to constrain the tectonic history of this area. In contrast to the eastern MFS, the western MFS is not underlain by the Pacific slab, and based on block models it is a region that would have had to shear extensively to link the block-rotation domain with the Alpine fault. Therefore, several studies hypothesize that distributed dextral shear occurred on kilometer-scale blocks (Lamb, 1988; Hall et al., 2004; Lamb, 2011; Randall et al., 2011). Throughout most of the MFS the Torlesse basement dips steeply, and shear

between bedding planes could have played a significant role (Rattenbury et al., 2006; Randall et al., 2011).

Many workers place the boundary between the eastern large-block-rotation domain and the western small-block/distributed-shear domain in the center of the MFS, though there is little paleomagnetic data from this area with which to determine the location precisely (Lamb, 1988; Lamb and Bibby, 1989; Townsend, 2001; Randall et al., 2011). This boundary coincides with the Awatere, Clarence, and Hope/Jordan/Kekerengu faults' change in strike from 070° in the southwest to 055° in the northeast, and also approximately with the edge of the subducted Pacific slab at the time (Lamb, 1988; Lamb and Bibby, 1989; Randall et al., 2011). If the block boundaries extended down to the slab, which was itself rotating with the subduction zone, the blocks' rotation could have been driven by either basal traction from the slab, or shear imposed at the boundaries of the block-rotation domain, or likely by a combination of the two (Lamb, 1994; Hall et al., 2004; Lamb, 2011; Randall et al., 2011).

Before and during this period of rotation, the eastern portions of at least some of the Marlborough faults are widely believed to have acted as thrust or reverse faults. Earlier in their history of rotation, the faults would have been oriented more parallel to the trench, favoring reverse motion (Lamb and Bibby, 1989; Townsend, 2001). In areas where Cretaceous-Cenozoic cover rocks are preserved, there is also ample evidence of associated folding and thrusting (Browne, 1992;, Lamb and Bibby, 1989; Townsend, 2001; Rattenbury et al., 2006). Other structures than the modern-day Marlborough faults were involved in this folding and thrusting; the Flags Creek thrust fault system accommodated about 20 km of shortening before being incorporated into the Ben More Anticline and becoming inactive (Townsend, 2001). The Early to Middle Miocene Great Marlborough Conglomerate is thought to reflect sedimentation associated

with uplift and erosion of basement rocks. It consists of debris-flow conglomerates containing clasts of Cretaceous-Paleogene cover rocks, as well as basement Torlesse (Browne, 1995; Rattenbury, 2006). Previous authors have investigated the exhumation and uplift history of the Inland and Seaward Kaikōura ranges using low-temperature thermochronology. Baker and Seward (1996) found evidence of rapid exhumation of the Inland Kaikōura range around 22 Ma. Collett et al. (2019) found Clarence-fault-hanging-wall focused exhumation in the Inland Kaikōura range beginning 35-40 Ma, followed by Jordan-thrust-hanging-wall-focused exhumation in the Seaward Kaikōura range beginning aroung 19 Ma. These findings both support the model of thrust faulting in this area of the MFS. Collett et al. (2019) also found a later, more general pattern of rapid exhumation throughout the southeastern MFS within the last 4-5 Ma, strongly suggesting a change in accommodation of plate boundary deformation that time.

After block rotation ceased in most of the MFS, plate boundary slip began to be accommodated more through strike-slip faulting on the MFS faults. The history of the western Awatere, Clarence and Hope faults, including the age of these structures, is much less well-studied than the eastern segments. Some paleomagnetic studies of rotation in eastern Marlborough infer that the western MFS faults are newer structures than their eastern counterparts, and formed after rotation was largely complete in order to link strike-slip motion in the east with the Alpine fault (e.g., Randall et al., 2011). Wallace et al. (2007) suggest that as the Hikurangi Subduction Zone has migrated southward, it has initiated motion on each of these three faults in turn, between 7 Ma and 1 Ma, as a means to transfer the majority of plate boundary slip to the Alpine fault, just as the Hope fault transmits the majority of slip through the MFS today. A study of the eastern Awatere fault supports this general timing – it first became

active as a strike-slip fault between ~5-7.5 Ma – but does not directly constrain the age of the western Awatere fault (Little and Jones, 1998). Direct geological evidence for the ages of the western faults has not yet been documented. As the Hikurangi subduction zone continues to migrate south, pinned to the northern edge of the Chatham Rise, it may be in the process of initiating a new fault south of the MFS in the Porters Pass-Amberly fault zone (PPAFZ; Cowan et al., 1996).

1.2 Primer on Methods

1.2.1 *Low-temperature Thermochronology*

In two chapters of this thesis, I use apatite and zircon (U-Th)/He and apatite fission-track thermochronology (AHe, ZHe and AFT, respectively) to investigate the exhumation history of the MFS. All of these methods measure an accumulated decay product that is retained in an apatite or zircon crystal only below a closure temperature, and thus determine the time since that degree of cooling was achieved. In geological applications this cooling is either the initial cooling of an igneous rock, or exhumation toward the Earth's surface from a burial depth great enough that the closure temperature was exceeded. If exhumation toward the surface is assumed to be due to the linked processes of rock uplift and surface erosion, and a geothermal gradient is known or assumed, exhumation and/or uplift rates can be determined. Low-temperature thermochronology has been used in many geologic settings to unravel tectonic histories by determining and interpreting patterns and chronologies of exhumation (e.g., Dokka et al., 1986; Tagami et al., 1988; Fitzergald et al., 1995; Colgan et al., 2006; Benowitz et al., 2011; Duvall et al., 2013).

In apatite and zircon crystals, ^{238}U, ^{235}U, and ^{232}Th continually decay to ^{206}Pb, ^{207}Pb, and ^{208}Pb going through several instances of alpha decay in the process, and ^{147}Sm undergoes alpha

decay to ^{143}Nd. During alpha decay, the nucleus of the parent isotope releases an alpha particle, which is a ^{4}He nucleus (Farley, 2000; Braun et al., 2006). The equation for ^{4}He production over time for either system is:

$$^{4}He = 8 \times {}^{238}U\left(e^{\lambda_{238}t} - 1\right) + 7 \times \frac{^{238}U}{137.88}\left(e^{\lambda_{235}t} - 1\right) + 6 \times {}^{232}Th\left(e^{\lambda_{232}t} - 1\right)$$

where λ values are decay constants for each parent isotope: $\lambda_{238} = 1.55 \times 10^{-10}$, $\lambda_{235} = 9.85 \times 10^{-10}$, and $\lambda_{232} = 4.95 \times 10^{-11}$, and all isotopes in the equation are the abundances of each in the sample (Braun et al., 2006). Decay of ^{147}Sm is very minimal in apatite and zircon, so it is not typically included in the equation above (Farley, 2000). At high temperatures, ^{4}He can easily diffuse out of the crystal lattice, but it is retained below temperatures of ~40-90° C for apatite and ~140-220° C for zircon (Flowers et al., 2009; Guenthner et al., 2013). Depending on the complexity of the assumed thermal history, an analytical or numerical solution for closure age can be found (Braun et al., 2006). Variations in closure temperature can be caused by radiation damage to the crystal lattice, but this can be accounted for when determining the thermal history of a sample (Flowers et al., 2009; Guenthner et al., 2013).

In apatite fission track dating, the decay products are the physical damage tracks created when ^{238}U decays through spontaneous fission. Because the rate of decay by fission is much smaller than the rate of alpha decay – its decay constant is more than six orders of magnitude smaller than the alpha-decay constant – individual fission tracks in a crystal can be counted (Braun et al., 2006). Fission tracks in apatite anneal over time at higher temperatures- relatively slowly within the partial annealing zone, and rapidly enough at temperatures above the PAZ that tracks are annealed as fast as they are produced – but are retained at low temperatures. The

closure temperature of the AFT system is approximately 100-160° C (Ketcham et al., 1999). The chemical composition of apatite can affect the rate of track annealing and therefore the closure temperature of an individual grain (Green et al., 1989; Ketcham et al., 1999). The apatite fission track age is a function of the track density and the rate of ^{238}U decay by fission:

$$t = \frac{1}{\lambda_D} \ln\left(\frac{\lambda_D}{\lambda_f}\frac{N_s}{^{238}U} + 1\right)$$

where λ_D is the total decay constant for ^{238}U, λ_f is the spontaneous fission decay constant for ^{238}U, N_s is the number of spontaneous fission tracks in the sample, and ^{238}U is the number of ^{238}U atoms in the sample (Braun et al., 2006). Our fission track measurements were performed using the LA-ICP-MS (laser-ablation inductively-coupled mass spectrometry), ζ-calibration method. The age equation then becomes:

$$t = \frac{1}{\lambda_D} \ln\left(\lambda_d \zeta_{MS} g \frac{\rho_s}{\mathcal{P}} + 1\right)$$

where ζ_{MS} is a calibration based on measurements of standards, g is a geometry factor, ρ_s is spontaneous track density and $\mathcal{P}$ is a calibrated abundance of ^{238}U ($\mathcal{P}$ = ^{238}U/^{43}Ca for apatite) (Donelick et al., 2005). Age is calculated for each of multiple grains per sample, but sample age is then reported as a mean, pooled, or central age (Braun et al., 2006).

1.2.2 *Landscape Evolution Modeling*

In the final chapter of this thesis, I use a landscape evolution model to simulate the development of topography in the region surrounding a strike-slip fault. Most landscape evolution models numerically solve a set of geomorphic transport functions across discretized space and time. In

the model used in Chapter 4, the basic equation governing the elevation of the land surface over time is:

$$\frac{\partial h}{\partial t} = U - V\frac{\partial h}{\partial x} - E_f - E_h$$

Where h is land surface elevation, t is time, U is rock uplift rate, V is lateral fault slip rate, E_f is fluvial erosion rate, and E_h is hillslope erosion rate (Tucker et al., 2001). This formulation illustrates the adaptability of a landscape evolution model. Different expressions may be used to define different input variables: for instance, rates of tectonic movement may vary over time; hillslope erosion may be modeled by linear or nonlinear soil creep; fluvial erosion may be modeled by simple stream power, or may be modulated by sediment flux; and diffusivity/erodibility parameters within the geomorphic transport laws may vary to simulate different lithologies or climates (Tucker and Hancock, 2010). The specific model configuration that I use is discussed in detail in Chapter 4 and in the appendix to Chapter 4.

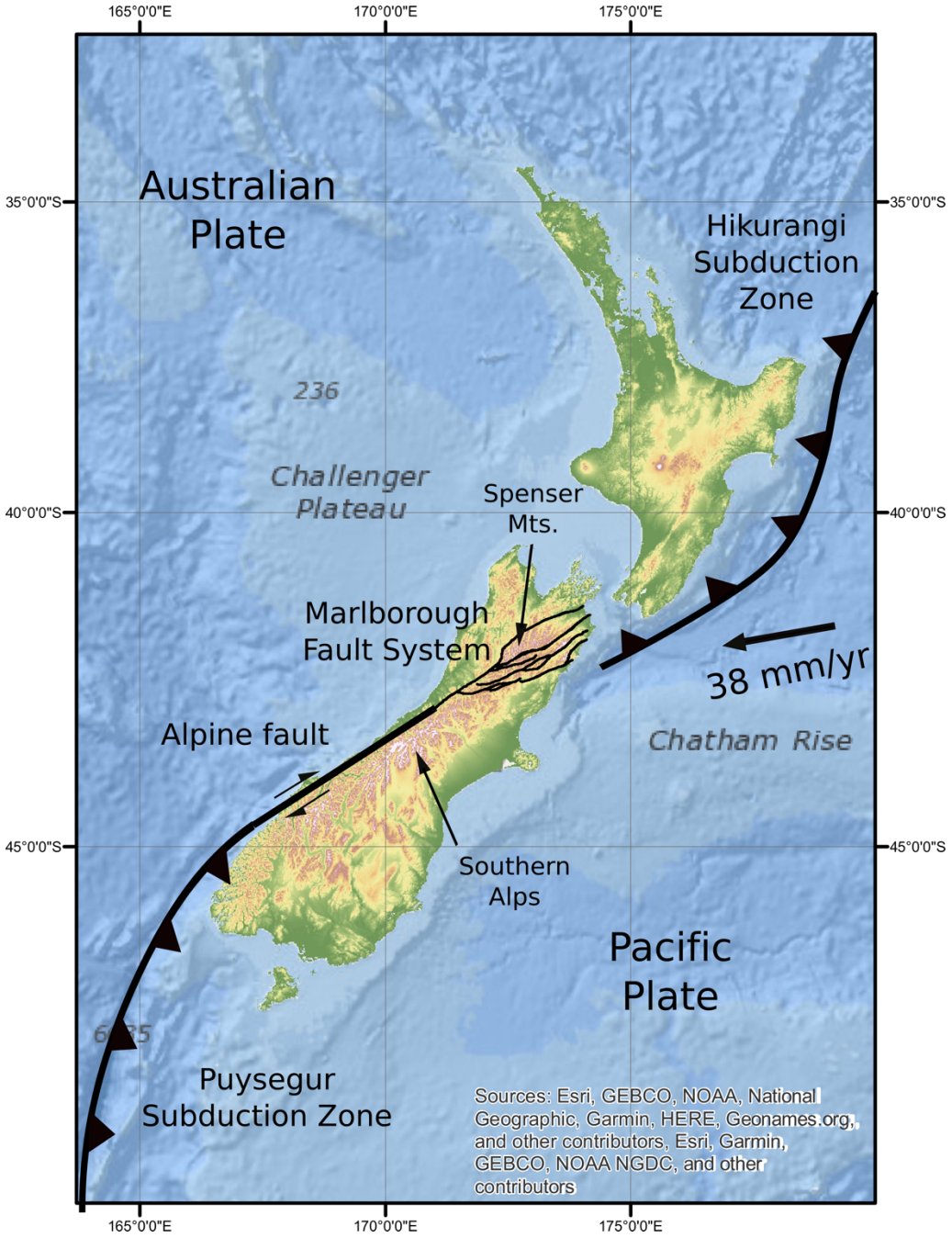

Figure 1.1. Tectonic setting of New Zealand. Land elevation data in this figure only is a 3 arc second digital elevation model from the Shuttle Radar Topography Mission (Farr et al., 2007). Bathymetry data is from the Esri Ocean basemap (Esri, 2012).

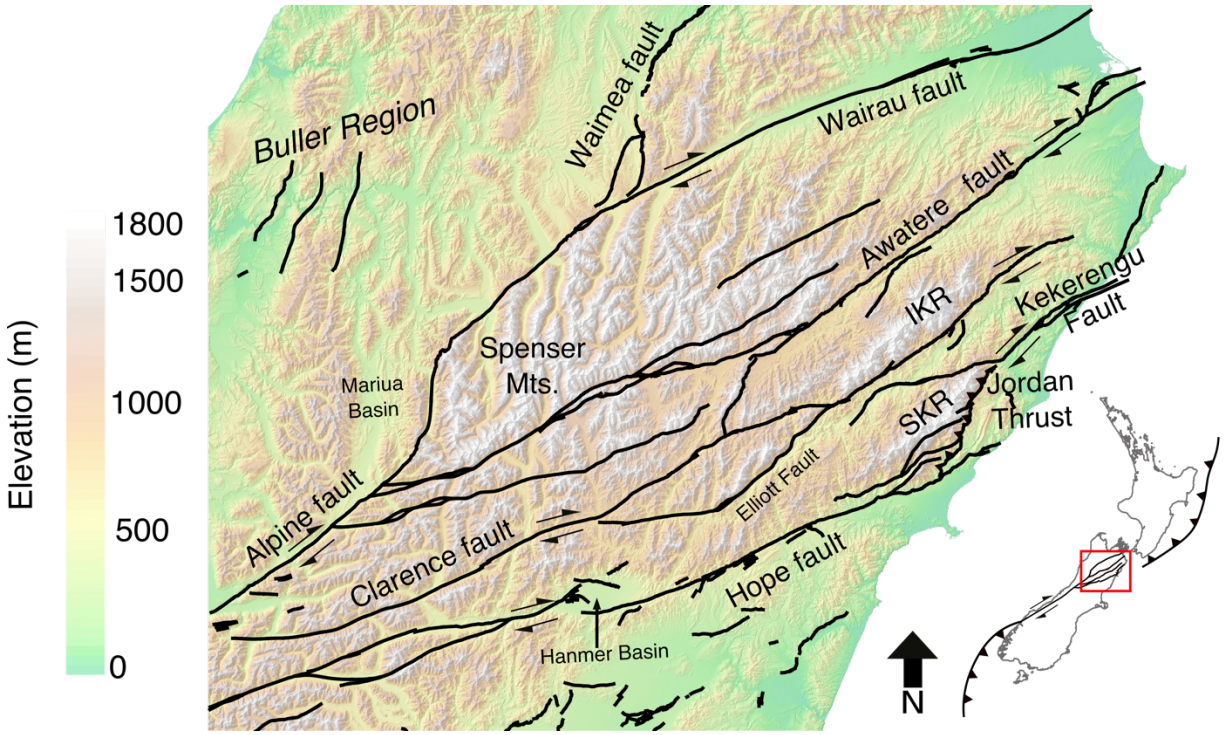

Figure 1.2. The Marlborough Fault System. IKR = Inland Kaikōura Range; SKR = Seaward Kaikōura Range. Faults pictured (black lines) are Quaternary active faults from geologic maps of Rattenbury et al. (1998), Nathan et al. (2002), and Rattenbury et al. (2006). Topography is a 15m digital elevation model (NZDEM SoS v1.0; Columbus et al., 2011).

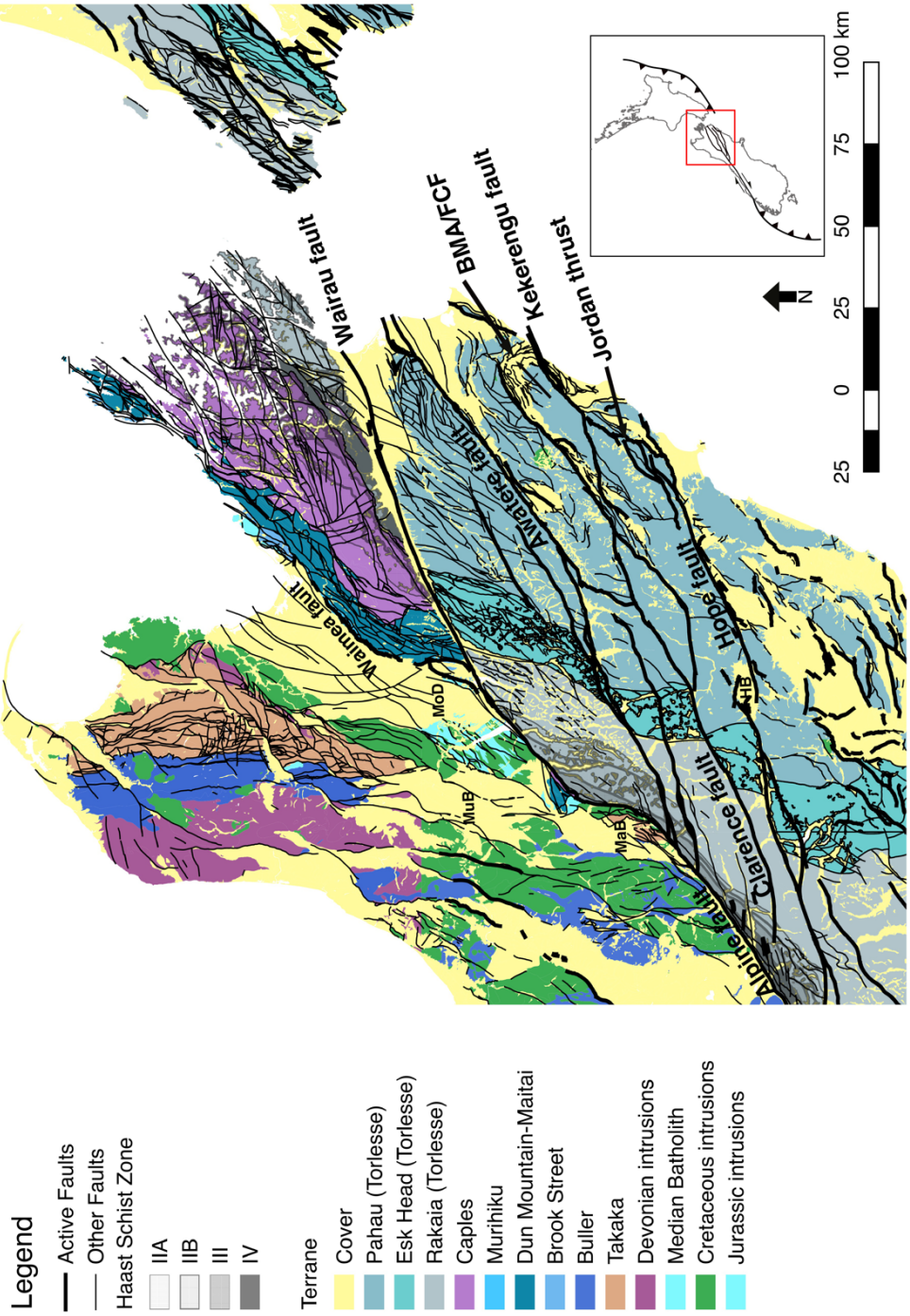

Figure 1.3. Geologic map of the Marlborough Fault System. BMA = Ben More Anticline; FCF = Flags Creek thrust fault. Geology simplified from Rattenbury et al. (1998), Begg et al. (2000), Nathan et al. (2002) and Rattenbury et al. (2006); faults from the same sources.

1.3 CHAPTER 1 REFERENCES

Amos, C. B., & Burbank, D. W. (2007). Channel width response to differential uplift. *Journal of Geophysical Research: Earth Surface*, *112*(F2).

Bacon, S. N., Chinn, T. J., Van Dissen, R. J., Tillinghast, S. F., Goldstein, H. L., & Burke, R. M. (2001). Paleo-equilibrium line altitude estimates from late Quaternary glacial features in the Inland Kaikoura Range, South Island, New Zealand. *New Zealand Journal of Geology and Geophysics*, *44*(1), 55-67.

Baker, J., & Seward, D. (1996). Timing of Cretaceous extension and Miocene compression in northeast South Island, New Zealand: Constraints from Rb-Sr and fission-track dating of an igneous pluton. *Tectonics*, *15*(5), 976-983.

Barnes, P. M., Lépinay, B. M., Collot, J. Y., Delteil, J., & Audru, J. C. (1998). Strain partitioning in the transition area between oblique subduction and continental collision, Hikurangi margin, New Zealand. *Tectonics, 17*(4), 534-557.

Barrell, D. J. A. (2011). Quaternary glaciers of New Zealand. *Developments in Quaternary Sciences, 15*, 1047-1064.

Batt, G. E., Baldwin, S. L., Cottam, M. A., Fitzgerald, P. G., Brandon, M. T., & Spell, T. L. (2004). Cenozoic plate boundary evolution in the South Island of New Zealand: New thermochronological constraints. *Tectonics, 23*(4).

Beavan, J., Tregoning, P., Bevis, M., Kato, T., & Meertens, C. (2002). Motion and rigidity of the Pacific Plate and implications for plate boundary deformation. *Journal of Geophysical Research: Solid Earth*, *107*(B10), ETG-19.

Begg, J.G.; Johnston, M.R. (compilers) (2000). Geology of the Wellington area: scale 1:250,000. Lower Hutt: Institute of Geological & Nuclear Sciences. Institute of Geological & Nuclear Sciences 1:250,000 geological map 10. 64 p. + 1 sheet.

Benowitz, J. A., Layer, P. W., Armstrong, P., Perry, S. E., Haeussler, P. J., Fitzgerald, P. G., & VanLaningham, S. (2011). Spatial variations in focused exhumation along a continental-scale strike-slip fault: The Denali fault of the eastern Alaska Range. *Geosphere, 7*(2), 455-467.

Benson, A. M., Little, T. A., Van Dissen, R. J., Hill, N., & Townsend, D. B. (2001). Late Quaternary paleoseismic history and surface rupture characteristics of the eastern Awatere strike-slip fault, New Zealand. *Geological Society of America Bulletin*, *113*(8), 1079-1091.

Blake, M. C., & Landis, C. A. (1973). The Dun Mountain ultramafic belt–Permian oceanic crust and upper mantle in New Zealand. *Journal of Research of the United States Geological Survey*, *1*, 529-534.

Braun, J., Van Der Beek, P., & Batt, G. (2006). Quantitative thermochronology: Numerical methods for the interpretation of thermochronological data. Cambridge University Press.

Browne, G. H. (1992). The northeastern portion of the Clarence Fault: tectonic implications for the late Neogene evolution of Marlborough, New Zealand. *New Zealand Journal of Geology and Geophysics, 35*(4), 437-445.

Browne, G. H. (1995). Sedimentation patterns during the Neogene in Marlborough, New Zealand. *Journal of the Royal Society of New Zealand, 25*(4), 459-483.

Campbell, J. K., Pettinga, J. R., & Jongens, R. (2012). The tectonic and structural setting of the 4 September 2010 Darfield (Canterbury) earthquake sequence, New Zealand. *New Zealand Journal of Geology and Geophysics, 55*(3), 155-168.

Carter, R. M., & Carter, L. (1982). The Motunau Fault and other structures at the southern edge of the Australian-Pacific plate boundary, offshore Marlborough, New Zealand. *Tectonophysics*, *88*(1-2), 133-159.

Cashman, S. M., Kelsey, H. M., Erdman, C. F., Cutten, H. N., & Berryman, K. R. (1992). Strain partitioning between structural domains in the forearc of the Hikurangi subduction zone, New Zealand. *Tectonics, 11*(2), 242-257.

Castelltort, S., Goren, L., Willett, S. D., Champagnac, J. D., Herman, F., & Braun, J. (2012). River drainage patterns in the New Zealand Alps primarily controlled by plate tectonic strain. *Nature Geoscience*, *5*(10), 744.

Chappell, P.R. (2016). The climate and weather of Marlborough. NIWA Science and Technology Series 69.

Colgan, J. P., Dumitru, T. A., Reiners, P. W., Wooden, J. L., & Miller, E. L. (2006). Cenozoic tectonic evolution of the Basin and Range Province in northwestern Nevada. *American Journal of Science, 306(*8), 616-654.

Collett, C. M., Duvall, A. R., Flowers, R. M., Tucker, G. E., & Upton, P. (2019). The Timing and Style of Oblique Deformation Within New Zealand's Kaikōura Ranges and Marlborough Fault System Based on Low-Temperature Thermochronology. *Tectonics*, *38*(4), 1250-1272.

Columbus, J., Sirguey, P., & Tenzer, R. (2011). A free, fully assessed 15-m DEM for New Zealand. *Survey Quarterly 66*, 16-19.

Cooper, A. F., Barreiro, B. A., Kimbrough, D. L., & Mattinson, J. M. (1987). Lamprophyre dike intrusion and the age of the Alpine fault, New Zealand. *Geology*, *15*(10), 941-944.

Cowan, H., Nicol, A., & Tonkin, P. (1996). A comparison of historical and paleoseismicity in a newly formed fault zone and a mature fault zone, North Canterbury, New Zealand. *Journal of Geophysical Research: Solid Earth, 101(*B3), 6021-6036.

Crampton, J. S., & Laird, M. G. (1997). Burnt Creek Formation and Late Cretaceous basin development in Marlborough, New Zealand. *New Zealand Journal of Geology and Geophysics, 40*(2), 199-222.

Crampton, J. S., Laird, M., Nicol, A., Hollis, C. J., & Van Dissen, R. J. (1998). Geology at the northern end of the Clarence Valley, Marlborough; a complete record spanning the Rangitata to Kaikoura orogenies. In *Geological Society of New Zealand, New Zealand Geophysical Society 1998 Joint Annual Conference* (Vol. 30).

Craw, D., Burridge, C. P., Upton, P., Rowe, D. L., & Waters, J. M. (2008). Evolution of biological dispersal corridors through a tectonically active mountain range in New Zealand. *Journal of Biogeography, 35*(10), 1790-1802.

Craw, D., Upton, P., Horton, T., & Williams, J. (2013). Migration of hydrothermal systems in an evolving collisional orogen, New Zealand. *Mineralium Deposita, 48*(2), 233-248.

Davy, B., Hoernle, K., & Werner, R. (2008). Hikurangi Plateau: Crustal structure, rifted formation, and Gondwana subduction history. *Geochemistry, Geophysics, Geosystems, 9*(7).

Davy, B. (2014). Rotation and offset of the Gondwana convergent margin in the New Zealand region following Cretaceous jamming of Hikurangi Plateau large igneous province subduction. *Tectonics*, *33*(8), 1577-1595.

DeMets, C., Gordon, R. G., Argus, D. F., & Stein, S. (1994). Effect of recent revisions to the geomagnetic reversal time scale on estimates of current plate motions. *Geophysical research letters*, *21*(20), 2191-2194.

DeMets, C., Gordon, R. G., & Argus, D. F. (2010). Geologically current plate motions. *Geophysical Journal International*, *181*(1), 1-80.

Dokka, R. K., Mahaffie, M. J., & Snoke, A. W. (1986). Thermochronologic evidence of major tectonic denudation associated with detachment faulting, northern Ruby Mountains-East Humboldt Range, Nevada. *Tectonics*, *5*(7), 995-1006.

Donelick, R. A., O'Sullivan, P. B., & Ketcham, R. A. (2005). Apatite fission-track analysis. *Reviews in Mineralogy and Geochemistry*, *58*(1), 49-94.

Duvall, A., Kirby, E., & Burbank, D. (2004). Tectonic and lithologic controls on bedrock channel profiles and processes in coastal California. *Journal of Geophysical Research: Earth Surface*, *109*(F3).

Duvall, A. R., Clark, M. K., Kirby, E., Farley, K. A., Craddock, W. H., Li, C., & Yuan, D. Y. (2013). Low-temperature thermochronometry along the Kunlun and Haiyuan Faults, NE Tibetan Plateau: Evidence for kinematic change during late-stage orogenesis. *Tectonics*, *32*(5), 1190-1211.

Duvall, A.R., Harbert, S.A., Upton, P., Tucker, G.E., Flowers, R.M., & Collett, C. (2019). River patterns reveal landscape evolution at the edge of subduction, Marlborough Fault System, New Zealand. Manuscript submitted for publication.

Esri. (2012). Ocean [basemap]. https://www.arcgis.com/home/item.html?id=8adf6db6ca5f4140b73b3a2e053753e6

Farley, K. A. (2000). Helium diffusion from apatite: General behavior as illustrated by Durango fluorapatite. *Journal of Geophysical Research: Solid Earth*, *105*(B2), 2903-2914.

Farr, T.G., Rosen, P.A., Caro, E., Crippen, R., Duren, R., Hensley, S., Kobrick, M., Paller, M., Rodriguez, E., Roth, L., Seal, D., Shaffer, S., Shimada, J., Umland, J., Werner, M., Oskin, M., Burbank, D., Alsdorf, D. (2007), The Shuttle Radar Topography Mission, *Reviews of Geophysics, 45*(2), RG2004.

Fitzgerald, P. G., Sorkhabi, R. B., Redfield, T. F., & Stump, E. (1995). Uplift and denudation of the central Alaska Range: A case study in the use of apatite fission track thermochronology to determine absolute uplift parameters. *Journal of Geophysical Research: Solid Earth, 100*(B10), 20175-20191.

Flowers, R. M., Ketcham, R. A., Shuster, D. L., & Farley, K. A. (2009). Apatite (U–Th)/He thermochronometry using a radiation damage accumulation and annealing model. *Geochimica et Cosmochimica Acta, 73*(8), 2347-2365.

Furlong, K. P., & Kamp, P. J. (2009). The lithospheric geodynamics of plate boundary transpression in New Zealand: Initiating and emplacing subduction along the Hikurangi margin, and the tectonic evolution of the Alpine Fault system. *Tectonophysics*, *474*(3-4), 449-462.

Furlong, K. P., & Kamp, P. J. (2013). Changes in plate boundary kinematics: Punctuated or smoothly varying—Evidence from the Mid-Cenozoic transition from lithospheric extension to shortening in New Zealand. *Tectonophysics, 608*, 1328-1342.

Ghisetti, F. C., & Sibson, R. H. (2006). Accommodation of compressional inversion in north-western South Island (New Zealand): Old faults versus new? *Journal of Structural Geology, 28*(11), 1994-2010.

Gray, H. J., Shobe, C. M., Hobley, D. E., Tucker, G. E., Duvall, A. R., Harbert, S. A., & Owen, L. A. (2017). Off-fault deformation rate along the southern San Andreas fault at Mecca Hills, southern California, inferred from landscape modeling of curved drainages. *Geology*, *46*(1), 59-62.

Green, P. F., Duddy, I. R., Laslett, G. M., Hegarty, K. A., Gleadow, A. W., & Lovering, J. F. (1989). Thermal annealing of fission tracks in apatite 4. Quantitative modelling techniques and extension to geological timescales. *Chemical Geology: Isotope Geoscience Section, 79*(2), 155-182.

Guenthner, W. R., Reiners, P. W., Ketcham, R. A., Nasdala, L., & Giester, G. (2013). Helium diffusion in natural zircon: Radiation damage, anisotropy, and the interpretation of zircon (U-Th)/He thermochronology. *American Journal of Science, 313*(3), 145-198.

Hall, L. S., Lamb, S. H., & Mac Niocaill, C. (2004). Cenozoic distributed rotational deformation, South Island, New Zealand. *Tectonics, 23*(2), TC2002.

Hamling, I. J., Hreinsdóttir, S., Clark, K., Elliott, J., Liang, C., Fielding, E., Litchfield, N., Villamor, P., Wallace, L., Wright, T.J., D'Anastasio, E., Bannister, S., Burbidge, D., Denys, P., Gentle, P., Howarth, J., Mueller, C., Palmer, N., Pearson, C., Power, W., Barnes, P., Barrell, D.J.A., Van Dissen, R., Langridge, R., Little, T., Nicol, A., Pettinga, J., Rowland, J., & Stirling, M. (2017). Complex multifault rupture during the 2016 M w 7.8 Kaikōura earthquake, New Zealand. *Science, 356*(6334), eaam7194.

Hilley, G. E., & Arrowsmith, J. R. (2008). Geomorphic response to uplift along the Dragon's Back pressure ridge, Carrizo Plain, California. *Geology*, *36*(5), 367-370.

Howell, D. G. (1981). Submarine fan facies in the Torlesse terrane, New Zealand. *Journal of the Royal Society of New Zealand, 11*(2), 113-122.

Howard, M., Nicol, A., Campbell, J., & Pettinga, J. (2003). Recent Paleoearthquakes of the Porters Pass Fault and Hazard Posed to Christchurch, New Zealand. In *Proceedings of the Pacific Conference on Earthquake Engineering*, *69,* 1-8.

Keller, E. A., Bonkowski, M. S., Korsch, R. J., & Shlemon, R. J. (1982). Tectonic geomorphology of the San Andreas fault zone in the southern Indio Hills, Coachella Valley, California. *Geological Society of America Bulletin*, *93*(1), 46-56.

Keller, E. A. (1986). Investigation of active tectonics: use of surficial earth processes. In *Active Tectonics*, 136-147.

Kamp, P. J. (1986). The mid-Cenozoic Challenger Rift System of western New Zealand and its implications for the age of Alpine fault inception. *Geological Society of America Bulletin*, *97*(3), 255-281.

Kamp, P. J. J. (1987). Age and origin of the New Zealand orocline in relation to Alpine Fault movement. *Journal of the Geological Society, 144*(4), 641-652.

Ketcham, R. A., Donelick, R. A., & Carlson, W. D. (1999). Variability of apatite fission-track annealing kinetics: III. Extrapolation to geological time scales. *American Mineralogist, 84*(9), 1235-1255.

King, P. R. (2000). Tectonic reconstructions of New Zealand: 40 Ma to the present. *New Zealand Journal of Geology and Geophysics*, *43*(4), 611-638.

Laird, M. G., & Bradshaw, J. D. (2004). The break-up of a long-term relationship: The Cretaceous separation of New Zealand from Gondwana. *Gondwana Research, 7*(1), 273-286.

Lamb, S. H. (1988). Tectonic rotations about vertical axes during the last 4 Ma in part of the New Zealand plate-boundary zone. *Journal of Structural Geology, 10*(8), 875-893.

Lamb, S. H., & Bibby, H. M. (1989). The last 25 Ma of rotational deformation in part of the New Zealand plate-boundary zone. *Journal of Structural Geology, 11*(4), 473-492.

Lamb, S. (2011). Cenozoic tectonic evolution of the New Zealand plate-boundary zone: A paleomagnetic perspective. *Tectonophysics*, *509*(3-4), 135-164.

Lamb, S., Mortimer, N., Smith, E., & Turner, G. (2016). Focusing of relative plate motion at a continental transform fault: Cenozoic dextral displacement >700 km on New Zealand's Alpine Fault, reversing >225 km of Late Cretaceous sinistral motion. *Geochemistry, Geophysics, Geosystems, 17*(3), 1197-1213.

Langridge, R., Campbell, J., Hill, N., Pere, V., Pope, J., Pettinga, J., Estrada, B., & Berryman, K. (2003). Paleoseismology and slip rate of the Conway Segment of the Hope Fault at Greenburn Stream, South Island, New Zealand. *Annals of Geophysics, 46*(5), 1119-1139.

Lewis, D. W., Laird, M. G., & Powell, R. D. (1980). Debris flow deposits of early Miocene age, Deadman stream, Marlborough, New Zealand. *Sedimentary Geology*, *27*(2), 83-118.

Lewis, D. W. (1992). Anatomy of an unconformity on mid-Oligocene Amuri Limestone, Canterbury, New Zealand. New Zealand *Journal of Geology and Geophysics, 35*(4), 463-475.

Litchfield, N. J., Van Dissen, R., Sutherland, R., Barnes, P. M., Cox, S. C., Norris, R., Beavan, R.J., Langridge, R., Villamor, P., Berryman, K., Stirling, M., Nicol, A., Nodder, S., Lamarche, G., Barrell, D.J.A., Pettinga, J.R., Little, T., Ponard, N., Mountjoy, J.J., & Clark, K. (2014). A model of active faulting in New Zealand. *New Zealand Journal of Geology and Geophysics, 57*(1), 32-56.

Little, T. A., & Roberts, A. P. (1997). Distribution and mechanism of Neogene to present-day vertical axis rotations, Pacific-Australian plate boundary zone, South Island, New Zealand. *Journal of Geophysical Research: Solid Earth, 102*(B9), 20447-20468.

Little, T. A., Mortimer, N., & McWilliams, M. (1999). An episodic Cretaceous cooling model for the Otago-Marlborough Schist, New Zealand, based on 40Ar/39Ar white mica ages. *New Zealand Journal of Geology and Geophysics, 42*(3), 305-325.

Little, T. A., & Mortimer, N. (2001). Rotation of ductile fabrics across the Alpine Fault and Cenozoic bending of the New Zealand orocline. *Journal of the Geological Society*, *158*(5), 745-756.

Macara, G.R. (2016a). The climate and weather of Nelson and Tasman. NIWA Science and Technology Series 71..

Macara, G.R. (2016b). The climate and weather of West Coast. NIWA Science and Technology Series 72.

MacKinnon, T. C. (1983). Origin of the Torlesse terrane and coeval rocks, South Island, New Zealand. *Geological Society of America Bulletin, 94*(8), 967-985.

Mason, D. P., Little, T. A., & Van Dissen, R. J. (2006). Rates of active faulting during late Quaternary fluvial terrace formation at Saxton River, Awatere fault, New Zealand. *Geological Society of America Bulletin*, *118*(11-12), 1431-1446.

Merritts, D., & Vincent, K. R. (1989). Geomorphic response of coastal streams to low, intermediate, and high rates of uplift, Medocino triple junction region, northern California. *Geological Society of America Bulletin*, *101*(11), 1373-1388.

Molnar, P., Atwater, T., Mammerickx, J., & Smith, S. M. (1975). Magnetic anomalies, bathymetry and the tectonic evolution of the South Pacific since the Late Cretaceous. *Geophysical Journal International*, *40*(3), 383-420.

Mortimer, N. (2004). New Zealand's geological foundations. *Gondwana Research, 7*(1), 261-272.

Mortimer, N., & Cooper, A. F. (2004). U-Pb and Sm-Nd ages from the Alpine Schist, New Zealand. *New Zealand Journal of Geology and Geophysics, 47*(1), 21-28.

Mortimer, N. (2014). The oroclinal bend in the South Island, New Zealand. *Journal of Structural Geology, 64*, 32-38.

Münker, C., & Cooper, R. (1999). The Cambrian arc complex of the Takaka Terrane, New Zealand: an integrated stratigraphical, paleontological and geochemical approach. *New Zealand Journal of Geology and Geophysics*, *42*(3), 415-445.

Nathan, S.; Rattenbury, M.S.; Suggate, R.P. (compilers) (2002). Geology of the Greymouth area: scale 1:250,000. Lower Hutt: Institute of Geological & Nuclear Sciences. Institute of Geological & Nuclear Sciences 1:250,000 geological map 12. 58 p. + 1 sheet.

Nicol, A., & Van Dissen, R. (2002). Up-dip partitioning of displacement components on the oblique-slip Clarence Fault, New Zealand. *Journal of Structural Geology, 24*(9), 1521-1535.

Norris, R. J., Koons, P. O., & Cooper, A. F. (1990). The obliquely-convergent plate boundary in the South Island of New Zealand: Implications for ancient collision zones. *Journal of Structural Geology, 12*(5-6), 715-725.

Norris, R. J., & Cooper, A. F. (2001). Late Quaternary slip rates and slip partitioning on the Alpine Fault, New Zealand. *Journal of Structural Geology*, *23*(2-3), 507-520.

Norris, R. J., & Toy, V. G. (2014). Continental transforms: A view from the Alpine Fault. *Journal of Structural Geology, 64*, 3-31.

Orr, T. O. H., Korsch, R. J., & Foley, L. A. (1991). Structure of melange and associated units in the Torlesse accretionary wedge, Tararua Range, New Zealand. *New Zealand Journal of Geology and Geophysics*, *34*(1), 61-72.

Ouchi, S. (2005). Development of offset channels across the San Andreas fault. *Geomorphology*, *70*(1-2), 112-128.

Rait, G., Chanier, F., & Waters, D. W. (1991). Landward-and seaward-directed thrusting accompanying the onset of subduction beneath New Zealand. *Geology*, *19*(3), 230-233.

Randall, K., Lamb, S., & Mac Niocaill, C. (2011). Large tectonic rotations in a wide zone of Neogene distributed dextral shear, northeastern South Island, New Zealand. *Tectonophysics, 509*(3-4), 165-180.

Rattenbury, M.S.; Cooper, R.A.; Johnston, M.R. (compilers) (1998). Geology of the Nelson area: scale 1:250,000. Lower Hutt: Institute of Geological & Nuclear Sciences Limited. Institute of Geological & Nuclear Sciences 1:250,000 geological map 9. 67 p. + 1 sheet.

Rattenbury, M. S., Townsend, D. B., and Johnston, M. R. (compilers), (2006). Geology of the Kaikoura area. Lower Hutt: Institute of Geological and Nuclear Sciences Limited. 1:250000 geological map 13. 70 p. +1 sheet.

Reyners, M., Eberhart-Phillips, D., & Bannister, S. (2011). Tracking repeated subduction of the Hikurangi Plateau beneath New Zealand. *Earth and Planetary Science Letters*, *311*(1-2), 165-171.

Reyners, M., Eberhart-Phillips, D., & Bannister, S. (2017). Subducting an old subduction zone sideways provides insights into what controls plate coupling. *Earth and Planetary Science Letters*, *466*, 53-61.

Rose, R. V. (1986). Structure and metamorphism of the Haast Schist and Torlesse Zones between the Alpine Fault and the D'urville Valley, South Nelson. (Masters thesis, University of Canterbury).

Roy, S. G., Koons, P. O., Osti, B., Upton, P., & Tucker, G. E. (2016). Multi-scale characterization of topographic anisotropy. *Computers & Geosciences, 90*, 102-116.

Schoenbohm, L. M., Whipple, K. X., Burchfiel, B. C., & Chen, L. (2004). Geomorphic constraints on surface uplift, exhumation, and plateau growth in the Red River region, Yunnan Province, China. *Geological Society of America Bulletin*, *116*(7-8), 895-909.

Schwartz, D. P., & Coppersmith, K. J. (1984). Fault behavior and characteristic earthquakes: Examples from the Wasatch and San Andreas fault zones. *Journal of Geophysical Research: Solid Earth*, *89*(B7), 5681-5698.

Silberling, N. J., Nichols, K. M., Bradshaw, J. D., & Blome, C. D. (1988). Limestone and chert in tectonic blocks from the Esk Head subterrane, South Island, New Zealand. *Geological Society of America Bulletin*, 100(8), 1213-1223.

Snyder, N. P., Whipple, K. X., Tucker, G. E., & Merritts, D. J. (2000). Landscape response to tectonic forcing: Digital elevation model analysis of stream profiles in the Mendocino triple junction region, northern California. *Geological Society of America Bulletin*, *112*(8), 1250-1263.

Spandler, C., Worden, K., Arculus, R., & Eggins, S. (2005). Igneous rocks of the Brook Street Terrane, New Zealand: implications for Permian tectonics of eastern Gondwana and magma genesis in modern intra-oceanic volcanic arcs. *New Zealand Journal of Geology and Geophysics, 48*(1), 167-183.

Stirling, M. W., Litchfield, N. J., Villamor, P., Van Dissen, R. J., Nicol, A., Pettinga, J., Mountjoy, J., Ries, W.F., Rowland, J., Fenton, C., Hamling, I., Asher, C., Barrier, A., Benson, A., Bischoff, A., Borella, J., Carne, R., Cochran, U.A., Cockroft, M., Cox, S.C., Duke, G., Fenton, F., Gasston., C., Grimshaw, C., Hale, D., Hall, B., Hao, K.X., Hatem, A., Hemphill-Haley, M., Heron, D.W., Howarth, J., Juniper, Z., Kane, T., Kearse, J., Khajavi, N., Lamarche, G., Lawson, S., Lukovic, B., Madugo, C., Manousakis, J., McColl, S., Noble, D., Pedley, K., Sauer, K., Stahl, T., Strong, D.T., Townsend, D.B., Toy, V., Villenueve, M., Wandres, A., Williams, J., Woelz, S., & Zinke, R. (2017). The Mw 7.8 2016 Kaikōura earthquake: Surface fault rupture and seismic hazard context. *Bulletin of the New Zealand Society for Earthquake Engineering*, *50*, 73-84.

Strogen, D. P., Seebeck, H., Nicol, A., & King, P. R. (2017). Two-phase Cretaceous–Paleocene rifting in the Taranaki Basin region, New Zealand: Implications for Gondwana break-up. *Journal of the Geological Society*, *174*(5), 929-946.

Suggate, R. P. (1979). The Alpine Fault bends and the Marlborough faults. *Royal Society of New Zealand Bulletin, 18*, 67-72.

Sutherland, R. (1994). Displacement since the Pliocene along the southern section of the Alpine Fault, New Zealand. *Geology*, *22*(4), 327-330.

Sutherland, R. (1999). Cenozoic bending of New Zealand basement terranes and Alpine Fault displacement: a brief review. *New Zealand Journal of Geology and Geophysics*, *42*(2), 295-301.

Sutherland, R., Davey, F., & Beavan, J. (2000). Plate boundary deformation in South Island, New Zealand, is related to inherited lithospheric structure. *Earth and Planetary Science Letters*, *177*(3-4), 141-151.

Sutherland, R., Collot, J., Bache, F., Henrys, S., Barker, D., Browne, G. H., Lawrence, M.F.J., Morgans, H.E.G., Hollis, C.J., Clowes, C., Mortimer, N., Rouillard, P., Gurnis, M., Etienne, S., & Stratford, W. (2017). Widespread compression associated with Eocene Tonga-Kermadec subduction initiation. *Geology, 45*(4), 355-358.

Sylvester, A. G. (1988). Strike-slip faults. *Geological Society of America Bulletin, 100*(11), 1666-1703.

Tagami, T., Lal, N., Sorkhabi, R. B., & Nishimura, S. (1988). Fission track thermochronologic analysis of the Ryoke belt and the Median Tectonic Line, Southwest Japan. *Journal of Geophysical Research: Solid Earth, 93*(B11), 13705-13715.

Townsend, D. B. (2001). Neogene evolution of the Pacific-Australia plate boundary zone in NE Marlborough, South Island, New Zealand. (Doctoral dissertation, Victoria University of Wellington).

Tucker, G., Lancaster, S., Gasparini, N., & Bras, R. (2001). The channel-hillslope integrated landscape development model (CHILD). In *Landscape Erosion and Evolution Modeling,* 349-388.

Tucker, G.E., and Hancock, G.R. (2010). Modeling landscape evolution. *Earth Surface Processes and Landforms*, *35*(1), 28-50.

Turnbull, I. M., & Forsyth, P. J. (1986). Schist structure east of the Alpine Fault bends, southeast Nelson, New Zealand. *New Zealand Journal of Geology and Geophysics, 29*(2), 165-177.

University of Otago – National School of Surveying. (2011). NZ_SoS_DEM v1.0. University of Otago – National School of Surveying.

Van Dissen, R., & Yeats, R. S. (1991). Hope fault, Jordan thrust, and uplift of the seaward Kaikoura Range, New Zealand. *Geology*, *19*(4), 393-396.

Vickery, S., & Lamb, S. (1995). Large tectonic rotations since the Early Miocene in a convergent plate-boundary zone, South Island, New Zealand. *Earth and Planetary Science Letters*, *136*(1-2), 43-59.

Vry, J. K., Baker, J., Maas, R., Little, T. A., Grapes, R., & Dixon, M. (2004). Zoned (Cretaceous and Cenozoic) garnet and the timing of high grade metamorphism, Southern Alps, New Zealand. *Journal of Metamorphic Geology, 22*(3), 137-157.

Walcott, R. I. (1987). Geodetic strain and the deformational history of the North Island of New Zealand during the late Cainozoic. *Philosophical Transactions of the Royal Society of London. Series A, Mathematical and Physical Sciences, 321*(1557), 163-181.

Walcott, R. I. (1998). Modes of oblique compression: Late Cenozoic tectonics of the South Island of New Zealand. *Reviews of Geophysics*, *36*(1), 1-26.

Walker, F., & Allen, M. B. (2012). Offset rivers, drainage spacing and the record of strike-slip faulting: The Kuh Banan Fault, Iran. *Tectonophysics*, *530*, 251-263.

Walker, R., & Jackson, J. (2002). Offset and evolution of the Gowk fault, SE Iran: a major intra-continental strike-slip system. *Journal of Structural Geology*, *24*(11), 1677-1698.

Wallace, R. E. (1968). Notes on stream channels offset by the San Andreas fault, southern Coast Ranges, California. In *Conference on Geologic Problems of the San Andreas Fault System. Stanford University Publication in Geological Sciences, 11*, 6-21.

Wallace, R. E. (1990). *The San Andreas fault system, California* (No. 1515). US Government Printing Office.

Wallace, L. M., Beavan, J., McCaffrey, R., Berryman, K., & Denys, P. (2007). Balancing the plate motion budget in the South Island, New Zealand using GPS, geological and seismological data. *Geophysical Journal International*, *168*(1), 332-352.

Wallace, L. M., Barnes, P., Beavan, J., Van Dissen, R., Litchfield, N., Mountjoy, J., Langridge, R., Lamarche, G., & Pondard, N. (2012). The kinematics of a transition from subduction to strike-slip: An example from the central New Zealand plate boundary. *Journal of Geophysical Research: Solid Earth*, *117*(B2), B02405.

Whipple, K. X., & Tucker, G. E. (1999). Dynamics of the stream-power river incision model: Implications for height limits of mountain ranges, landscape response timescales, and research needs. *Journal of Geophysical Research: Solid Earth*, *104*(B8), 17661-17674.

White, S. H., & Green, P. F. (1986). Tectonic development of the Alpine fault zone, New Zealand: A fission-track study. *Geology*, *14*(2), 124-127.

Wobus, C., Whipple, K. X., Kirby, E., Snyder, N., Johnson, J., Spyropolou, K., Crosby, B., & Sheehan, D. (2006). Tectonics from topography: Procedures, promise, and pitfalls. *Geological Society of America Special Papers*, *398*, 55-74.

Zachariasen, J., Berryman, K., Langridge, R., Prentice, C., Rymer, M., Stirling, M., & Villamor, P. (2006). Timing of late Holocene surface rupture of the Wairau fault, Marlborough, New Zealand. *New Zealand Journal of Geology and Geophysics, 49*(1), 159-174.

Chapter 2. MID-MIOCENE DEVELOPMENT OF ALPINE FAULT RESTRAINING BEND FROM LOW-TEMPERATURE THERMOCHRONOLOGY[1]

The restraining bend of the Alpine-Wairau fault is a site of high, steep topography in New Zealand's Spenser Mountains. Here we present new apatite and zircon (U-Th)/He and apatite fission-track low-temperature thermochronology along the Alpine-Wairau fault, close to this prominent restraining bend, in order to investigate the timing and style of mountain building. Our results show the onset of rapid cooling on the Pacific plate side of the fault starting around 10-13 Ma. Rates and total amounts of exhumation are greatest farther south along the Alpine-Wairau fault and taper off to the north, before eventually falling below the amount of exhumation necessary for reset zircon (U-Th)/He ages. We attribute the onset of exhumation to the increasingly convergent motion across the plate boundary over this time interval, the initiation of the Wairau splay of the Alpine fault, and the resultant development of the restraining bend. The bend has a broad area of influence, reflected in our thermochronology and in topography and stream channel steepness, which results from the 60° dip of the Alpine/Wairau fault into the bend and the 70-85° dip of the fault for ~80 km away from the bend.

2.1 INTRODUCTION

Restraining bends on large strike-slip faults, such as the San Andreas and Denali faults, are commonly sites of rapid uplift and high topography (Cunningham and Mann, 2007). Previous

[1] This chapter is in prep for submission to *Geology* with authors S. Harbert, A. Duvall, R. Flowers, P. Upton, and P. O'Sullivan. Harbert conceived of and designed the study. Harbert selected sample sites and conducted the sampling. Harbert and O'Sullivan did the mineral separation. Harbert selected and prepared grains for (U-Th)/He analysis. Flowers conducted the (U-Th)/He analysis. O'Sullivan conducted the apatite fission track analysis. Harbert conducted the QTQt modeling. Harbert and Duvall interpreted the results. Harbert wrote the manuscript. All authors reviewed the manuscript.

studies focusing on the development of such topography have revealed important information about deformation and seismicity within restraining bends as well as the regional tectonics underlying their formation (e.g., Crowell, 1979; Mann et al., 1991; Fitzgerald et al., 1993; Bürgmann et al., 1994; Elias et al., 2007; Dair and Cooke, 2009; Benowitz et al., 2011; Gudmundsdottir et al., 2013).

The Alpine fault is a prominent, dextral-reverse, plate-bounding fault that links two Australia-Pacific plate subduction zones with opposite senses of vergence (Fig. 2.1A). Transpression on the central and southern Alpine fault is responsible for creating the Southern Alps, a high-relief, fast-exhuming mountain range spanning the western spine of New Zealand's South Island. At its northern end, the Alpine fault meets the ~150 km wide Marlborough Fault System (MFS). The MFS splays northeastward from the Alpine fault and includes four main, dextral faults: the Hope, Clarence, Awatere, and Alpine-Wairau faults, from south to north, respectively. Near its intersection with the Awatere fault, the Alpine fault jogs to the north in a large restraining bend that offsets its trace by about 20 km and differs in strike from the rest of the fault by about 45° (Fig. 2.1B). The fault continues on as the Wairau after the bend.

Despite interest in the Alpine fault bend (Suggate, 1979; Rose, 1986; Turnbull and Forsyth, 1986; Yeats and Berryman, 1987; Cutten et al., 2006; Sagar, 2014), the timing, style, extent, and drivers of its formation remain poorly constrained. Here we use low-temperature thermochronology and landscape analysis to determine the timing of development of the Alpine fault bend and associated mountain building and exhumation. Similar studies have used cooling ages and erosion rates from thermochronology (Fitzgerald et al., 1993; Bürgmann et al., 1994; Spotila et al., 1998; 2001; Benowitz et al., 2011; Duvall et al., 2013; Niemi et al., 2013) or from cosmogenic radionuclides (Gudmundsdottir et al., 2013) to define the timing, extent, and rates of

uplift associated with compressional fault bends. These studies also use patterns in erosion to assess the nature of asymmetry in restraining bend deformation and on which side of the fault crust is advected through the bend versus fixed in a zone of contraction. In this paper, we assess spatial patterns in cooling and topography near the Alpine fault bend using low-temperature thermochronology and landscape analysis, and place our results in the context of the timing of Southern Alps, MFS, and AUS-PAC plate boundary evolution.

2.2 Geologic History and Sample Site Descriptions

The Alpine fault is thought to have initiated as a through-going transform plate boundary structure around 20-25 Ma, possibly located at the site of a much older structure (Kamp, 1986; White and Green, 1986; Sutherland et al., 2000; Batt et al., 2004). After initiation it was a more or less purely dextral fault until a gradual increase in plate convergence beginning 11 Ma or earlier caused it to become more oblique to plate motion vectors (Cande and Stock, 2004). Many authors attribute the birth of the Southern Alps to this increase in convergence and resulting increase in reverse motion on the Alpine fault, as well as off-fault deformation; however, major exhumation lagged behind plate convergence by several million years (e.g., Tippett and Kamp, 1993; Walcott, 1998; Batt et al., 2004). The earliest signal of possible Southern Alps exhumation occurs at 12-8 Ma in the southern end of the range, and an increase in hanging wall exhumation rate occurs along most of the Alpine fault by 5 Ma (Kamp et al., 1989; Tippett and Kamp, 1993; Sutherland, 1996; Batt et al., 2004; Jiao et al., 2017), possibly indicating a spatial progression in range development.

However, less is known about the timing and amount of exhumation along the northern sections of the Alpine fault, especially where it splays into the MFS and along its restraining bend. Recent thermochronology from the eastern MFS (Collett et al., 2019) indicates that the

Inland and Seaward Kaikōura mountain ranges developed in the early Miocene and that exhumation, and by proxy faulting and uplift, became more widespread by 5 Ma. These data provide important information about the plate boundary history, but the sample sites are located well east of the Alpine fault bend and thus are likely controlled by the local influence of the proto-MFS faults (Collett et al., 2019) rather than the Alpine fault.

In this study, we use apatite and zircon (U-Th)/He and apatite fission-track thermochronology to constrain the history of exhumation along the Alpine-Wairau fault from samples collected near the restraining bend. These low-temperature thermochronology techniques determine the time at which a sample cooled below a closure temperature (~40-90° C for apatite (U-Th)/He, ~140-220° C for zircon (U-Th)/He, and ~100-160° C for apatite fission-track) (Ketcham et al., 1999; Flowers et al., 2009; Guenthner et al., 2013). Suites of ages from multiple thermochronometers can provide a more detailed exhumation history,

In order to help guide our sampling strategy, we used topography and river morphology to define a probable zone of uplift associated with bend deformation. The Spenser Mountains and neighboring ranges occupy the interior of the restraining bend in an elongate zone of topography between the Alpine-Wairau and Awatere faults, a width of 20-30 km, for a distance of about 80 km along strike. In this region, peak elevations and mean elevations are higher than regions either to the north of the Wairau fault or to the south, between the Awatere and Hope faults. Stream channel steepness indices (k_{sn}) are markedly higher in this large bend region than most other areas of the northern South Island (Fig. 2.2). These values are comparable to those in the Inland and Seaward Kaikōura mountains, and the Southern Alps. High steepness index values often correspond to areas of high uplift rate, as stream channels incise to keep pace with rock uplift (e.g., Wobus et al., 2006). Based on these landscape patterns, we interpret the

formation of this topography in relation to transpression from the Alpine fault bend. We then test this hypothesis through low-temperature thermochronology analysis of samples collected across this zone.

2.3 Thermochronologic Ages and Modeled Cooling Histories

We performed apatite and zircon (U-Th)/He and apatite fission-track thermochronology on 16 bedrock samples, sandstones and schists from the Rakaia, Esk Head, and Pahau subterranes on the hanging wall (east / south side) of the Alpine-Wairau fault, and Median Batholith diorites and Caples terrane and Rakaia subterrane schists north of the Wairau fault (footwall). We sampled one vertical transect (labeled "VT" in Fig. 2.3), covering vertical relief of 890 meters with five samples. Other sampling locations were single samples on which we used 1-3 thermochronometers. See Figure 2.3 and Tables 2.1, 2.2, and 2.3 for sample information.

To better constrain the probable time-temperature paths of our samples as they exhumed and cooled, we modeled their cooling histories with QTQt, a Bayesian transdimensional Markov chain Monte Carlo model (Gallagher, 2012). In some models, we supplemented our data with zircon fission track ages from Kao (2002), if those samples were within a few kilometers of and were not redundant with our samples, and if the cooling ages were based on at least 10 crystals. Models were given prior time and temperature ranges reflecting the deposition or emplacement of the rock, and, where necessary, a temperature window reflecting metamorphic grade. Samples from sedimentary rocks were allowed to have a time-temperature history prior to their depositional age, as radiation damage accumulated earlier in a detrital crystal's history could have an impact on its cooling age (e.g., Fox et al., 2019). This option was used unless it reduced the model goodness-of-fit. See Section 2.8.3 for QTQt model inputs. Some samples could not produce a satisfactory model, either because their ages were unreset or because dispersion among

replicate grains was very large, resulting in poor model convergence and/or a poor fit to the data. Here we present both raw cooling ages and modeled time-temperature paths.

In most of the field area, our samples from the Pacific plate side of the bend are much younger than those from the Australian plate side (Fig. 2.3). Near the southern end of the bend on the Pacific plate all three of our thermochronometers have ages < 4 Ma, which suggests rapid cooling over the last several million years. Moving out of the bend to the northeast, along the Wairau fault, Pacific plate cooling ages show a general increase. Four of the five ZHe samples in our vertical transect have ages within error of each other, ranging from 8-14 Ma, suggesting rapid cooling over this time interval. By 80-100 km along strike, ZHe ages are unreset - older than the depositional age of the rocks - indicating that since the deposition of the Pahau subterrane ~140-100 Ma these samples have remained at less than the ~6-8 km depth required to reset zircon (or have not otherwise been heated to an equivalent temperature). On the Australian Plate, the ZHe samples decrease in age northeastward along the Wairau fault, but are nowhere younger than 24 Ma.

Modeled cooling histories show many samples, especially those closest to the Wairau fault on the interior (hanging wall) of the bend, beginning to cool at a similar time, about ~10-13 Ma. The sample ~80 km east of the bend, 15mfs07, has a wider and possibly earlier range of timing, but the uncertainty on this sample is larger than those adjacent to it (Figures 2.3 and 2.4). Among our hanging wall samples, total cooling in the last 10-13 Ma decrease northward from ~400 degrees very near to the bend to only ~150 degrees, ~80 km from the bend. Samples south of the Alpine fault, west of the bend, begin to cool somewhat later (See Figures 2.3 and 2.4). Therefore, cooling rates over this interval also decrease northward along strike. Samples north of

the Wairau fault have cooled very little within the last 25 Ma, and our single-thermochronometer samples at many locations make it difficult to discern subtle changes in rate during that interval.

2.4 DISCUSSION

Low-temperature thermochronology from samples along the Alpine fault bend interior consistently shows onset of rapid cooling starting around 10-13 Ma (Fig. 2.3). We attribute this cooling to the onset of exhumation in this area caused by the interrelated processes of increasingly convergent plate motion and the resultant formation of the Alpine fault restraining bend. The region affected by a synchronous increase in cooling is broad, extending up to 80 km northeastward and eastward from the bend. The fastest rates of cooling are close to the interior corners of the bend, with total cooling and cooling rate decreasing with distance. These patterns suggest a close relationship between the bend and cooling/exhumation. This spatial extent also corresponds well with the zone of high topography and steep channels that occupies the interior of the bend (Fig. 2.2), between the Alpine-Wairau and Awatere faults. There, stream channel steepness indices are greater than in most other parts of the MFS, which have the same bedrock unit. High topography is also prevalent here, with many peaks of 1800-2000 m; south of the bend along the Alpine fault, comparable peak elevations are not reached until south of the Hope fault, in the Southern Alps proper (Suggate, 1979).

Zones of uplift and deformation associated with strike-slip restraining bends range from narrow to wide due to contrasts in lithological strength, structural complexity of the fault zone and the geometry of the bend itself (e.g., Burgmann et al, 1994; Spotila et al., 2001; Niemi et al., 2013; Fitzgerald et al., 2014). Gentle restraining bends commonly develop higher topography and more extensive zones of fault-related deformation as compared to sharp bends, where deformation is more focused (Crowell, 1974). The Alpine fault bend is likely too sharp to

explain the wide zone of exhumation and uplift. Instead, we propose that the large extent of Alpine fault restraining bend formed in response to its dip toward the Pacific plate, a geometry that helps to maintain the high, steep topography of the Spenser Mountains and surrounding region. The dip of the fault is 60° E at the bend, 70° S, SE for 35-40 km along strike from the north end of the bend, and 85° S, SE for a further 45 km before finally becoming vertical (Rattenbury et al., 2006). Bends on dipping strike-slip faults form broader zones of uplift than bends along vertical faults, as has been shown along the southern San Andreas fault (Storti et al., 2003; Dair and Cooke, 2009). Still, the very great along-strike extent of exhumation between the Alpine and Wairau faults suggests that in the distal, more slowly-exhuming areas, the development of a dipping fault alone may be causing the exhumation; these eastern samples may not yet "feel" the restraining bend.

The east / south dip on the Alpine fault could explain why deformation is focused on the Pacific plate side of the bend. This asymmetry may also relate to bend kinematics. We propose that the east (Pacific plate) side rather than the west (Australian plate) side of the fault remains fixed to the bend in a zone of long-lived contraction, uplift, and exhumation. We base this interpretation on asymmetric patterns in topography, river channel steepness, thermochronology ages, and metamorphic rocks. The east side of the Alpine fault bend is characterized by high topography, steep rivers, young thermochronology ages, and a < 2 km-wide band of garnet to biotite zone Alpine (Haast) Schist along the fault, all of which provide evidence for greater uplift and exhumation here (Rose, 1986; Turnbull and Forsyth, 1986). On the Australian plate side, topography is generally more subdued and rivers are less steep. More deeply-exhumed metamorphic rocks are not present preferentially along the Alpine fault, and thermochronology ages are older (Rattenbury et al., 2006; Sagar, 2014).

We suggest that crustal material of the Australian plate is advected through the bend with time, experiencing some shortening and basin inversions involving many NE-SW-trending faults, but experiencing much less exhumation than the Pacific plate side (Lihou, 1992; Reilly et al., 2015; Ghisetti et al., 2016). Meanwhile, crustal material on the Pacific plate is shortened, thickened and uplifted in a stationary zone. Foliation orientations in the Alpine Schist within the bend do not show evidence of the rotation expected if Pacific Plate crust were "flowing" through the bend (Rose, 1986; Turnbull and Forsyth, 1986). Also, a signal of earlier exhumation would be expected south of the bend along the Alpine fault, in rocks that had moved through and out of the bend, but our samples from this area (15MFS09, 17MFS18, 17MFS19) do not show earlier exhumation. These geologic patterns and interpretations are analogous to the Northern and Southern Santa Cruz Mountains, on either side of the San Andreas fault restraining bend, near Loma Prieta, CA (Anderson, 1990; Valensise and Ward, 1991; Bürgmann et al., 1994; Gudmundsdottir et al., 2013).

We might expect to find thrust or reverse faults that accommodate crustal shortening within the Pacific plate side of the Alpine fault bend, similar to the numerous faults and folds mapped along San Andreas fault bends (Davis, 1983; Namson and Davis, 1988; McLaughlin et al., 1988; Spotila and Sieh, 2000; Plesch et al., 2007; Cooke and Dair, 2011) and at other large restraining bends around the world (Mann et al., 1991; Ben-Avraham and Lyakhovsky, 1992; Elias et al., 2007). On the Australian plate, previous studies document tens of kilometers of shortening via folding and reverse faulting near to the bend, starting in the early Miocene with a possible slight acceleration toward the present (Kamp et al., 1996; Ghisetti and Sibson, 2006; Ghisetti et al., 2014). On the Pacific plate, however, there are few mapped faults and shear zones to accommodate compression in the bend and those present are short and discontinuous.

(Turnbull and Forsyth, 1986; Rattenbury et al., 2006). The area is heavily vegetated, largely roadless, and extensively deformed by at least one prior phase of folding, so it is reasonable to speculate that shortening in the bend is accommodated at least partially on unknown folds or faults, on older structures thought to be inactive, or on blind structures at depth (Turnbull and Forsyth, 1986). It is also possible that shortening is accommodated primarily by oblique slip faulting on the Alpine fault rather than partitioned across numerous strike-slip and dip-slip faults within the bend.

Several mechanisms have been proposed for formation of the Alpine fault bend, all of which implicate an increase in plate convergence that had begun by 10-15 Ma (Cande and Stock, 2004). We rule out the development of the bend during the initial propagation of the Alpine fault at ~23 Ma based on the timing of rapid cooling from our thermochronology. If the bend were an original feature of the early Miocene Alpine fault, we would expect deeper exhumation within the bend starting not long after that time, which is not observed. Therefore, we conclude that the bend is a younger feature. Some authors contend that a formerly straight Alpine fault was deflected to the northwest due to approximately 30 km of NW-SE shortening that occurred northwest of the fault in the Buller region around 12-13 Ma (Anderson et al., 1993; Walcott, 1998; Lamb et al., 2016). However, this model implies that the bend is fixed to the Australian plate. Another mechanism, compatible with a Pacific-plate-fixed bend, is that of Suggate (1979). In this model, increasing convergence causes part of the Alpine fault to be offset to the north on a preexisting cross fault. Suggate (1979) suggested the Waimea fault, the western boundary of the Brook Street terrane, as the offsetting structure, but the latest Miocene timing implied timing of this scenario does not agree with our thermochronology. Still, the same general mechanism could have formed the bend.

We propose an alternative scenario: that the Wairau fault is a primary splay of the Alpine fault (Scholz et al., 2010), and that it, and the bend that connects it to the Alpine fault, formed around 12-13 Ma. When an existing strike-slip fault becomes misaligned with the regional stress field, as might happen when relative plate motion changes, a splay fault can form at an orientation parallel to the plate motion vector (Du and Aydin, 1995; Scholz et al., 2010). In this way, the Wairau fault could have propagated from or toward the tip of the Alpine fault at a more preferable angle to plate motion, similar to what has been proposed for the formation of the other Marlborough fault splays (Little and Jones, 1998). The sharpness of restraining bend itself probably indicates that the Wairau splay took advantage of a preexisting structure during propagation, or that the Alpine fault had done so during its own earlier development. We suggest that prior to the development of the Wairau fault at 12-13 Ma, deformation between the tip of the Alpine fault (in the modern-day bend region) and the Hikurangi subduction zone was accommodated through distributed shear. Little and Mortimer (2001) suggest that distributed shear, on elongate crustal blocks in a zone up to 100 km wide, took place before and possibly during initial northward propagation of the Alpine fault. This process could have continued, accommodating deformation beyond the Alpine fault tip, until development of the Wairau fault.

Once the Wairau fault developed, the bend between the two fault segments became a site of convergence, uplift and exhumation, as indicated by our thermochronology. As plate motion continued to become more convergent, additional primary fault splays – the Awatere, Clarence and Hope faults – developed, at a more preferable, strike-slip orientation to the plate motion vector (Little and Jones, 1998; Scholz et al., 2010). These faults took up plate boundary slip, reducing the slip rate of the Wairau fault. Our proposed timing of Wairau fault initiation around 12-13 Ma fits well with the 140 km of offset of the Esk Head subterrane (or more generally, the

Rakaia-Pahau subterrane transition) across the Wairau fault – much less than the total of ~480 km of offset across the Alpine fault (Little and Jones, 1998; Rattenbury et al., 2006). For the first 3-5 Ma of its existence the Wairau fault could have accommodated ~25 mm/yr of slip, approximately the total Alpine fault slip rate, before being reduced to its current 3-5 mm/yr (Zachariasen et al., 2006). Previous studies have shown a tendency for bends to evolve toward a straighter geometry with the formation of new splays or fault rotations through time (e.g., Crowell, 1979; Elias et al., 2007; Cooke and Dair, 2009) or to migrate along strike with increased fault displacement (Cunningham and Mann, 2007). Here, however, the transfer of slip southward onto the other MFS faults arrested or reduced the need for changes in fault-bend geometry, so the bend has remained a site of uplift and exhumation.

Because of changing plate motions, the mid-late Miocene was an important time for the development of this plate boundary. As the MFS developed into its modern form, farther to the south the Alpine fault was becoming more transpressive. Along some parts of the Alpine fault, associated foreland thrusting and shortening began around this time, though it would be several million years before the onset of major exhumation in the hanging wall of the Alpine fault (Kamp et al., 1992; Sutherland, 1996; Ring and Bernet, 2010). Our thermochronology therefore shows one early manifestation of a plate-boundary-wide transition toward more transpressive tectonics.

2.5 CONCLUSIONS

Low-temperature thermochronology along the Alpine-Wairau fault through its restraining bend shows hanging wall exhumation beginning at 10-13 Ma. The zone of exhumation, and associated high topography and steep river channels, is especially large because of the dip of the Alpine-Wairau fault into the bend. We propose that this exhumation reflects a long-lived zone of

contraction related to the formation of the Wairau fault as a primary splay of the Alpine fault at or slightly earlier than this time in response to an increase in plate convergence. This timing is earlier than the onset of major exhumation along the central and southern Alpine fault and earlier than the onset of dextral motion on the main Marlborough faults. We view this development as an early manifestation of transpression at the plate boundary.

2.6 ACKNOWLEDGEMENTS

This work was made possible through generous support from the National Science Foundation (grants EAR-132859 and -1321735 to Duvall and Flowers, and -1126991 to Flowers). Upton was supported by the New Zealand Ministry for Business Innovation and Employment (grant C05X1103). We thank Jim Metcalf at CU Boulder TRaIL lab for (U-Th)/He analyses. We gratefully acknowledge the New Zealand Department of Conservation and Mount Ella Station for sampling permission. We thank Sean LaHusen, Philip Schoettle-Greene, and Camille Collett for field and sampling assistance and Gabrielle Alampay for lab assistance.

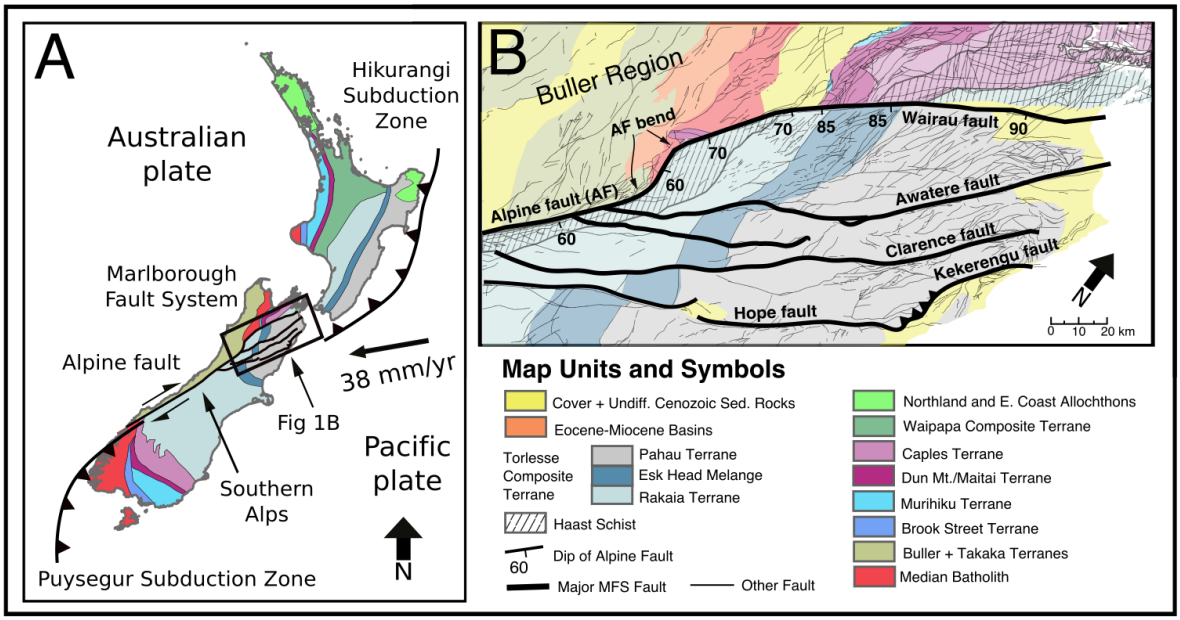

Figure 2.1. Geologic setting of Ch. 2. A.) Geology and major tectonic features of New Zealand. B.) Geologic map of study area, including bend region of the Alpine fault. Geologic units adapted and simplified from Rattenbury et al. (2006) and Mortimer (2004). Faults from Nathan et al. (2002) and Rattenbury et al. (2006). Heavy black lines represent main Marlborough faults. “Other faults” shown in gray includes both active and inactive faults.

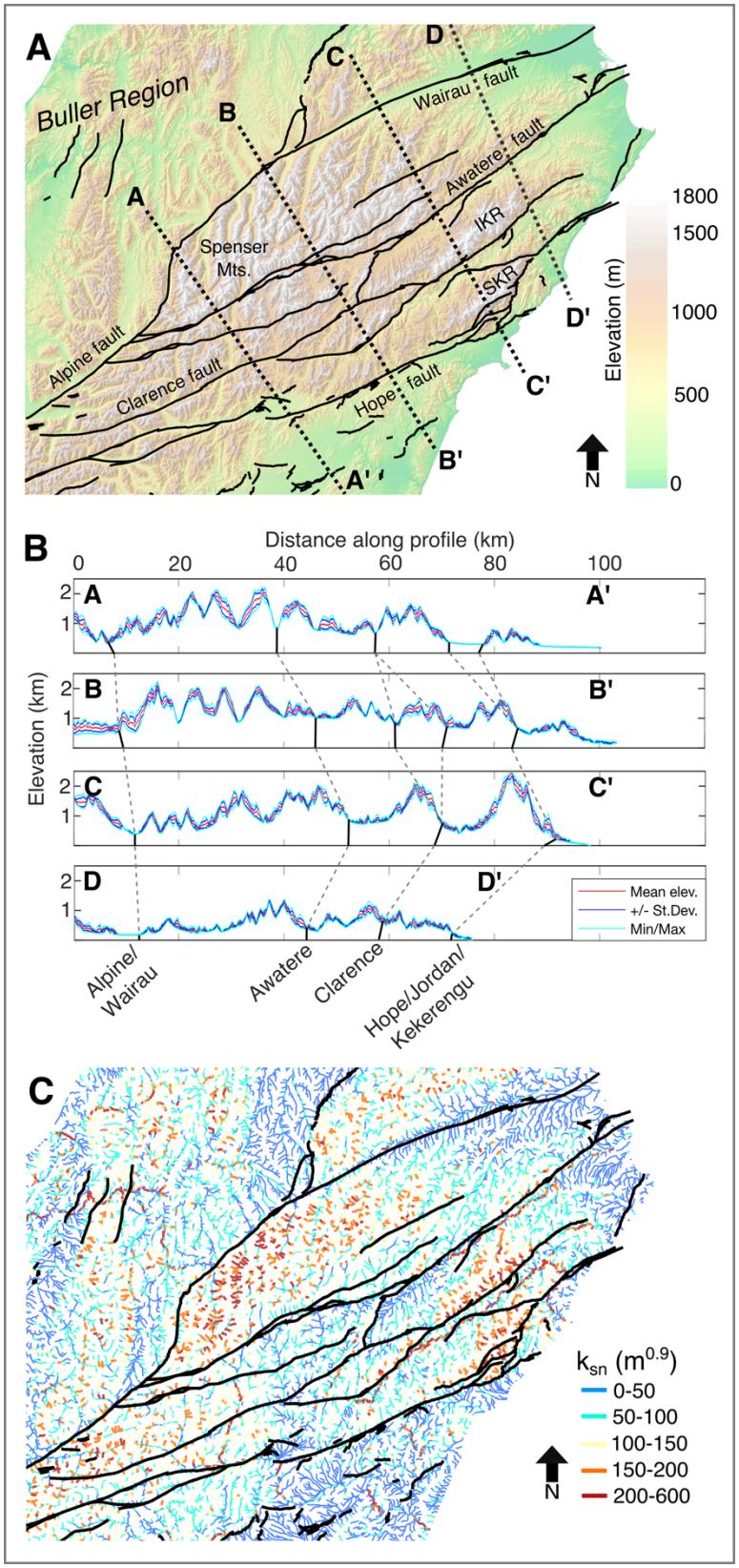

Figure 2.2. Geomorphology of bend region/MFS. A.) Shaded relief map of Marlborough Fault System (MFS) and surrounding area made from 15m digital elvation model NZDEM SoS v1.0; this DEM was used for all topographic analysis in this chapter. (Columbus et al., 2011). IKR = Inland Kaikōura Range, SKR = Seaward Kaikōura Range. B.) Topographic swath profiles at transects shown in panel A. Dashed lines correlate faults; where dashed lines diverge, faults splay. Topographic swath profiles are 10 km wide. C.) Map of channel steepness index (k_{sn}) with θ_{ref} = 0.45. Faults in panels A and C are active faults from Nathan et al. (2002) and Rattenbury et al. (1998; 2006). Topographic swath profiles and k_{sn} map were made using TopoToolbox 2 (Schwanghart and Scherler, 2014).

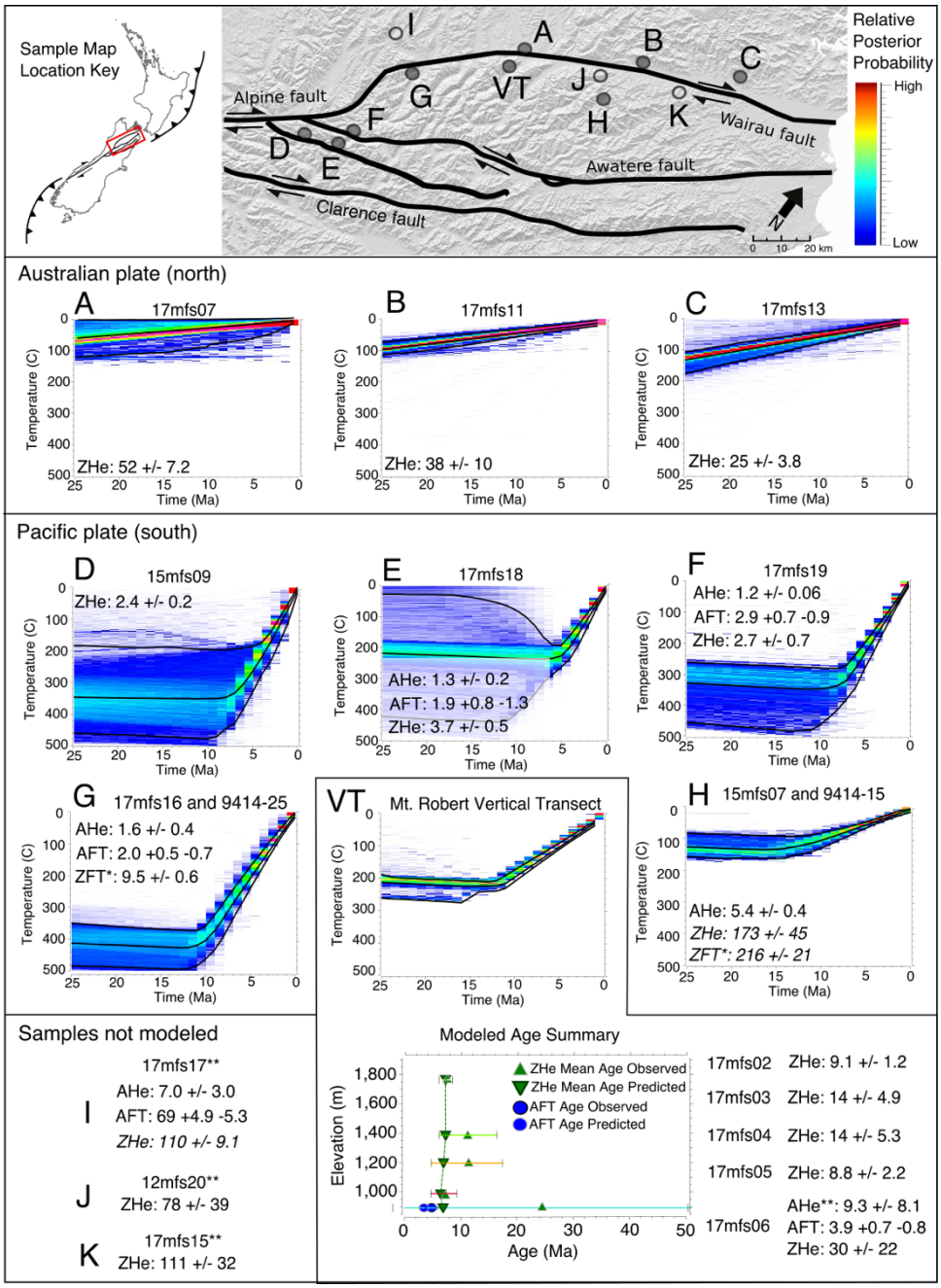

Figure 2.3. QTQt modeling results, Ch. 2. Top panel: sample locations. Open circles and ** symbol indicate samples that were not modeled successfully, or individual ages that were not included in models due to poor model convergence or poor reproduction of observed data (see data repository for details). Time-temperature plots show heat maps of probability density. Black lines on time-temperature plots are the expected model – a weighted mean, weighted by posterior probability of each model – with the 95% credible interval bounds above and below it. * Indicates zircon fission track ages from Kao (2002) that were added to the QTQt models. Italics indicate ages that are considered unreset. All ages and uncertainties are given in Ma. Uncertainties are one standard deviation. QTQt model described in Gallagher (2012).

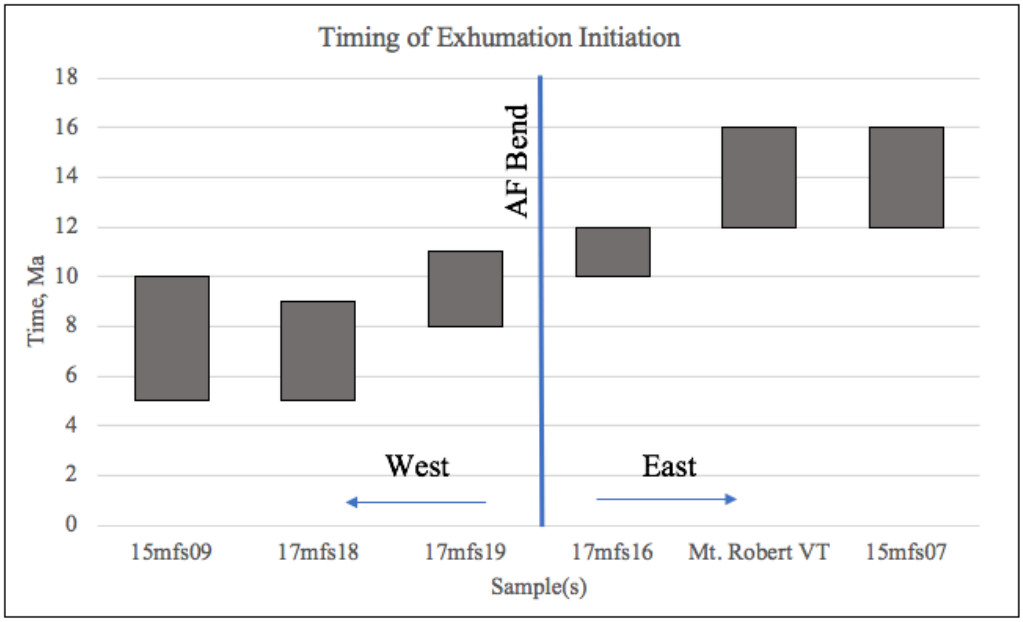

Figure 2.4. Boxplot of exhumation initiation. Plot shows timing of increase in cooling/exhumation rate of samples on the south side of the Alpine-Wairau fault. Timing windows for each sample are taken from the breaks in slope in the minimum and maximum 95% credible intervals given by the QTQt models shown in Figure 2.3.

2.7 CHAPTER 2 REFERENCES

Anderson, R. S. (1990). Evolution of the northern Santa Cruz Mountains by advection of crust past a San Andreas fault bend. *Science*, *249*(4967), 397-401.

Anderson, H., Webb, T., & Jackson, J. (1993). Focal mechanisms of large earthquakes in the South Island of New Zealand: implications for the accommodation of Pacific-Australia plate motion. *Geophysical journal international, 115*(3), 1032-1054.

Batt, G. E., Baldwin, S. L., Cottam, M. A., Fitzgerald, P. G., Brandon, M. T., & Spell, T. L. (2004). Cenozoic plate boundary evolution in the South Island of New Zealand: New thermochronological constraints. *Tectonics, 23*(4).

Ben-Avraham, Z., & Lyakhovsky, V. (1992). Faulting processes along the northern Dead Sea transform and the Levant margin. *Geology*, *20*(12), 1139-1142.

Benowitz, J. A., Layer, P. W., Armstrong, P., Perry, S. E., Haeussler, P. J., Fitzgerald, P. G., & VanLaningham, S. (2011). Spatial variations in focused exhumation along a continental-scale strike-slip fault: The Denali fault of the eastern Alaska Range. *Geosphere, 7*(2), 455-467.

Bürgmann, R., Arrowsmith, R., Dumitru, T., & McLaughlin, R. (1994). Rise and fall of the southern Santa Cruz Mountains, California, from fission tracks, geomorphology, and geodesy. *Journal of Geophysical Research: Solid Earth*, *99*(B10), 20181-20202.

Cande, S. C., & Stock, J. M. (2004). Pacific—Antarctic—Australia motion and the formation of the Macquarie Plate. *Geophysical Journal International, 157*(1), 399-414.

Collett, C. M., Duvall, A. R., Flowers, R. M., Tucker, G. E., & Upton, P. (2019). The Timing and style of oblique deformation within New Zealand's Kaikōura Ranges and Marlborough Fault System based on low-temperature thermochronology. *Tectonics*, *38*(4), 1250-1272.

Columbus, J., Sirguey, P., & Tenzer, R. (2011). A free, fully assessed 15-m DEM for New Zealand. *Survey Quarterly 66*, 16-19.

Cooke, M. L., & Dair, L. C. (2011). Simulating the recent evolution of the southern big bend of the San Andreas fault, southern California. *Journal of Geophysical Research: Solid Earth, 116*(B4).

Crowell, J. C. (1974). Sedimentation along the San Andreas fault, California. In *Modern and Ancient Geosynclinal Sedimentation*, 292-303.

Crowell, J. C. (1979). The San Andreas fault system through time. *Journal of the Geological Society*, *136*(3), 293-302.

Cunningham, W. D., & Mann, P. (2007). Tectonics of strike-slip restraining and releasing bends. *Geological Society, London, Special Publications*, *290*(1), 1-12.

Cutten, H. N. C., Korsch, R. J., & Roser, B. P. (2006). Using geochemical fingerprinting to determine transpressive fault movement history: Application to the New Zealand Alpine Fault. *Tectonics*, *25*(4).

Dair, L., & Cooke, M. L. (2009). San Andreas fault geometry through the San Gorgonio Pass, California. *Geology, 37*(2), 119-122.

Davis, T. L. (1983). Late Cenozoic structure and tectonic history of the western" Big Bend" of the San Andreas fault and adjacent San Emigdio Mountains. (Doctoral dissertation, University of California, Santa Barbara).

Donelick, R. A., & Miller, D. S. (1991). Enhanced TINT fission track densities in low spontaneous track density apatites using 252Cf-derived fission fragment tracks: A model and experimental observations. *International Journal of Radiation Applications and Instrumentation. Part D. Nuclear Tracks and Radiation Measurements, 18*(3), 301-307.

Donelick, R. A., Ketcham, R. A., & Carlson, W. D. (1999). Variability of apatite fission-track annealing kinetics: II. Crystallographic orientation effects. *American Mineralogist, 84*(9), 1224-1234.

Du, Y., & Aydin, A. (1995). Shear fracture patterns and connectivity at geometric complexities along strike-slip faults. *Journal of Geophysical Research: Solid Earth*, *100*(B9), 18093-18102.

Duvall, A. R., Clark, M. K., Kirby, E., Farley, K. A., Craddock, W. H., Li, C., & Yuan, D. Y. (2013). Low-temperature thermochronometry along the Kunlun and Haiyuan Faults, NE Tibetan Plateau: Evidence for kinematic change during late-stage orogenesis. *Tectonics*, *32*(5), 1190-1211.

Elias, A., Tapponnier, P., Singh, S. C., King, G. C., Briais, A., Daëron, M., ... & Klinger, Y. (2007). Active thrusting offshore Mount Lebanon: Source of the tsunamigenic AD 551 Beirut-Tripoli earthquake. *Geology, 35*(8), 755-758.

Fox, M., Dai, J. G., & Carter, A. (2019). Badly behaved detrital (U-Th)/He ages: Problems with He diffusion models or geological models? *Geochemistry, Geophysics, Geosystems, 20*, 2418-2432.

Fitzgerald, P. G., Stump, E., & Redfield, T. F. (1993). Late Cenozoic uplift of Denali and its relation to relative plate motion and fault morphology. *Science, 259*(5094), 497-499.

Fitzgerald, P. G., Roeske, S. M., Benowitz, J. A., Riccio, S. J., Perry, S. E., & Armstrong, P. A. (2014). Alternating asymmetric topography of the Alaska range along the strike-slip Denali fault: Strain partitioning and lithospheric control across a terrane suture zone. *Tectonics, 33*(8), 1519-1533.

Flowers, R. M., Ketcham, R. A., Shuster, D. L., & Farley, K. A. (2009). Apatite (U–Th)/He thermochronometry using a radiation damage accumulation and annealing model. *Geochimica et Cosmochimica Acta*, *73*(8), 2347-2365.

Gallagher, K. (2012). Transdimensional inverse thermal history modeling for quantitative thermochronology. *Journal of Geophysical Research: Solid Earth, 117*(B2).

Ghisetti, F. C., & Sibson, R. H. (2006). Accommodation of compressional inversion in north-western South Island (New Zealand): Old faults versus new? *Journal of Structural Geology, 28*(11), 1994-2010.

Ghisetti, F. C., Barnes, P. M., & Sibson, R. H. (2014). Deformation of the top basement unconformity west of the Alpine Fault (South Island, New Zealand): seismotectonic implications. *New Zealand Journal of Geology and Geophysics, 57*(3), 271-294.

Green, P. F., Duddy, I. R., Laslett, G. M., Hegarty, K. A., Gleadow, A. W., & Lovering, J. F. (1989). Thermal annealing of fission tracks in apatite 4. Quantitative modelling techniques and extension to geological timescales. *Chemical Geology: Isotope Geoscience Section, 79*(2), 155-182.

Gudmundsdottir, M. H., Blisniuk, K., Ebert, Y., Levine, N. M., Rood, D. H., Wilson, A., & Hilley, G. E. (2013). Restraining bend tectonics in the Santa Cruz Mountains, California, imaged using 10Be concentrations in river sands. *Geology*, *41*(8), 843-846.

Guenthner, W. R., Reiners, P. W., Ketcham, R. A., Nasdala, L., & Giester, G. (2013). Helium diffusion in natural zircon: Radiation damage, anisotropy, and the interpretation of zircon (U-Th)/He thermochronology. *American Journal of Science*, *313*(3), 145-198.

Hasebe, N., Tamura, A., & Arai, S. (2013). Zeta equivalent fission-track dating using LA-ICP-MS and examples with simultaneous U–P b dating. *Island Arc, 22*(3), 280-291.

Jiao, R., Herman, F., & Seward, D. (2017). Late Cenozoic exhumation model of New Zealand: Impacts from tectonics and climate. Earth-science reviews, 166, 286-298.

Kao, Ming-Hung. (2002). Thermo-tectonic implications of zircon and apatite FT data of the Marlborough Region, South Island, New Zealand. *Terrestrial, Atmospheric and Oceanic Sciences, 13*(2), 109-124.

Kamp, P. J. (1986). The mid-Cenozoic Challenger Rift System of western New Zealand and its implications for the age of Alpine fault inception. *Geological Society of America Bulletin*, *97*(3), 255-281.

Kamp, P. J., Green, P. F., & White, S. H. (1989). Fission track analysis reveals character of collisional tectonics in New Zealand. *Tectonics*, *8*(2), 169-195.

Kamp, P. J., Green, P. F., & Tippett, J. M. (1992). Tectonic architecture of the mountain front-foreland basin transition, South Island, New Zealand, assessed by fission track analysis. *Tectonics, 11*(1), 98-113.

Ketcham, R. A., Donelick, R. A., & Carlson, W. D. (1999). Variability of apatite fission-track annealing kinetics: III. Extrapolation to geological time scales. *American Mineralogist, 84*(9), 1235-1255.

Ketcham, R. A. (2005). The role of crystallographic angle in characterizing and modeling apatite fission-track length data. *Radiation Measurements, 39*(6), 595-601.

Ketcham, R. A., Carter, A., Donelick, R. A., Barbarand, J., & Hurford, A. J. (2007). Improved modeling of fission-track annealing in apatite. *American Mineralogist, 92*(5-6), 799-810.

Ketcham, R. A., Gautheron, C., & Tassan-Got, L. (2011). Accounting for long alpha-particle stopping distances in (U–Th–Sm)/He geochronology: Refinement of the baseline case. *Geochimica et Cosmochimica Acta, 75*(24), 7779-7791.

Lamb, S., Mortimer, N., Smith, E., & Turner, G. (2016). Focusing of relative plate motion at a continental transform fault: Cenozoic dextral displacement> 700 km on New Zealand's Alpine Fault, reversing> 225 km of Late Cretaceous sinistral motion. *Geochemistry, Geophysics, Geosystems, 17*(3), 1197-1213.

Lihou, J. C. (1992). Reinterpretation of seismic reflection data from the Moutere depression, Nelson region, South Island, New Zealand. *New Zealand Journal of Geology and Geophysics, 35*(4), 477-490.

Little, T. A., & Jones, A. (1998). Seven million years of strike-slip and related off-fault deformation, northeastern Marlborough fault system, South Island, New Zealand. *Tectonics, 17*(2), 285-302.

Little, T. A., & Mortimer, N. (2001). Rotation of ductile fabrics across the Alpine Fault and Cenozoic bending of the New Zealand orocline. *Journal of the Geological Society, 158*(5), 745-756.

Little, T. A., Holcombe, R. J., & Ilg, B. R. (2002). Ductile fabrics in the zone of active oblique convergence near the Alpine Fault, New Zealand: identifying the neotectonic overprint. *Journal of Structural Geology, 24*(1), 193-217.

Mann, P., Tyburski, S. A., & Rosencrantz, E. (1991). Neogene development of the Swan Islands restraining-bend complex, Caribbean Sea. *Geology, 19*(8), 823-826.

McLaughlin, R. J., Blake Jr, M. C., Griscom, A., Blome, C. D., & Murchey, B. (1988). Tectonics of formation, translation, and dispersal of the Coast Range ophiolite of California. *Tectonics*, *7*(5), 1033-1056.

Mitchell, S. G., & Reiners, P. W. (2003). Influence of wildfires on apatite and zircon (U-Th)/He ages. *Geology, 31*(12), 1025-1028.

Namson, J., & Davis, T. (1988). Structural transect of the western Transverse Ranges, California: Implications for lithospheric kinematics and seismic risk evaluation. *Geology*, *16*(8), 675-679.

Nathan, S.; Rattenbury, M.S.; Suggate, R.P. (compilers) (2002). Geology of the Greymouth area: scale 1:250,000. Lower Hutt: Institute of Geological & Nuclear Sciences. Institute of Geological & Nuclear Sciences 1:250,000 geological map 12. 58 p. + 1 sheet.

Niemi, N. A., Buscher, J. T., Spotila, J. A., House, M. A., & Kelley, S. A. (2013). Insights from low-temperature thermochronometry into transpressional deformation and crustal exhumation along the San Andreas fault in the western Transverse Ranges, California. *Tectonics, 32(*6), 1602-1622.

Plesch, A., Shaw, J. H., Bryant, W. A., Carena, S., Cooke, M. L., Dolan, J. F., Fuis, G. S., Gath, E. M., Grant Ludwig, L. B., Hauksson, E., Jordan, T. H., Kamerling, M. J., Legg, M. R., Lindvall, S. C., Magistrale, H., Nicholson, C., Niemi, N. A., Oskin, M. E., Perry, S. C., Planansky, G., Rockwell, T. K., Shearer, P. M., Sorlien, C. C., Suess, M., Suppe, J., Treiman, J. A., & Yeats, R. S. (2007). Community Fault Model (CFM) for Southern California. *Bulletin of the Seismological Society of America, 97*(6), 1793-1802. doi: 10.1785/0120050211.

Rattenbury, M.S.; Cooper, R.A.; Johnston, M.R. (compilers) (1998). Geology of the Nelson area: scale 1:250,000. Lower Hutt: Institute of Geological & Nuclear Sciences Limited. Institute of Geological & Nuclear Sciences 1:250,000 geological map 9. 67 p. + 1 sheet.

Rattenbury, M. S., Townsend, D. B., and Johnston, M. R. (compilers), (2006). Geology of the Kaikoura area. Lower Hutt: Institute of Geological and Nuclear Sciences Limited. 1:250000 geological map 13. 70 p. + 1 sheet.

Reilly, C., Nicol, A., Walsh, J. J., & Seebeck, H. (2015). Evolution of faulting and plate boundary deformation in the Southern Taranaki Basin, New Zealand. *Tectonophysics*, 651, 1-18.

Ring, U., & Bernet, M. (2010). Fission-track analysis unravels the denudation history of the Bonar Range in the footwall of the Alpine Fault, South Island, New Zealand. *Geological Magazine, 147(*6), 801-813.

Rogers, G. M., Walker, S., Basher, L. M., & Lee, W. G. (2007). Frequency and impact of Holocene fire in eastern South Island, New Zealand. *New Zealand Journal of Ecology 31*(2), 129-142.

Rose, R. V. (1986). Structure and metamorphism of the Haast Schist and Torlesse Zones between the Alpine Fault and the D'urville Valley, South Nelson. (Masters thesis, University of Canterbury).

Ross, S. M. (2003). Peirce's criterion for the elimination of suspect experimental data. *Journal of Engineering Technology, 20*(2), 38-41.

Sagar, M. W. (2014). Geology, petrology and thermochronology of the Glenroy Complex and associated granitoids, southeast Nelson, New Zealand (Doctoral dissertation, University of Otago).

Scholz, C. H., Ando, R., & Shaw, B. E. (2010). The mechanics of first order splay faulting: The strike-slip case. *Journal of Structural Geology*, *32*(1), 118-126.

Schwanghart, W., & Scherler, D. (2014). TopoToolbox 2–MATLAB-based software for topographic analysis and modeling in Earth surface sciences. *Earth Surface Dynamics*, *2*(1), 1-7.

Seward, D., & Tulloch, A. J. (1991). Fission-track analysis of Tertiary uplift history of granitic basement in the Victoria Range, West Coast, New Zealand. *New Zealand Journal of Geology and Geophysics, (*2), 115-120.

Spotila, J. A., Farley, K. A., & Sieh, K. (1998). Uplift and erosion of the San Bernardino Mountains associated with transpression along the San Andreas fault, California, as constrained by radiogenic helium thermochronometry. *Tectonics*, *17*(3), 360-378.

Spotila, J. A., & Sieh, K. (2000). Architecture of transpressional thrust faulting in the San Bernardino Mountains, southern California, from deformation of a deeply weathered surface. *Tectonics, 19(*4), 589-615.

Spotila, J. A., Farley, K. A., Yule, J. D., & Reiners, P. W. (2001). Near-field transpressive deformation along the San Andreas fault zone in southern California, based on exhumation constrained by (U-Th)/He dating. *Journal of Geophysical Research: Solid Earth, 106*(B12), 30909-30922.

Spotila, J. A., House, M. A., Niemi, N. A., Brady, R. C., Oskin, M., Buscher, J. T., ... & Foster, D. A. (2007). Patterns of bedrock uplift along the San Andreas fault and implicatios for mechanisms of transpression. *Special Papers-Geological Society of America,* 434, 15.

Storti, F., Holdsworth, R. E., & Salvini, F. (2003). Intraplate strike-slip deformation belts. *Geological Society, London, Special Publications, 210*(1), 1-14.

Suggate, R. P. (1979). The Alpine Fault bends and the Marlborough faults. *Royal Society of New Zealand Bulletin*, 18, 67-72.

Sutherland, R. (1996). Transpressional development of the Australia-Pacific boundary through southern South Island, New Zealand: Constraints from Miocene-Pliocene sediments, Waiho-1 borehole, South Westland. *New Zealand Journal of Geology and Geophysics*, *39*(2), 251-264.

Sutherland, R., Davey, F., & Beavan, J. (2000). Plate boundary deformation in South Island, New Zealand, is related to inherited lithospheric structure. *Earth and Planetary Science Letters, 177*(3-4), 141-151.

Tippett, J. M., & Kamp, P. J. (1993). Fission track analysis of the late Cenozoic vertical kinematics of continental Pacific crust, South Island, New Zealand. *Journal of Geophysical Research: Solid Earth, 98*(B9), 16119-16148.

Tulloch, A. J., & Campbell, J. K. (1993). Clinoenstatite-bearing buchites possibly from combustion of hydrocarbon gases in a major thrust zone: Glenroy Valley, New Zealand. *The Journal of Geology, 101*(3), 404-412.

Turnbull, I. M., & Forsyth, P. J. (1986). Schist structure east of the Alpine Fault bends, southeast Nelson, New Zealand. *New Zealand Journal of Geology and Geophysics, 29*(2), 165-177.

University of Otago – National School of Surveying. (2011). NZ_SoS_DEM v1.0. University of Otago – National School of Surveying.

Valensise, G., & Ward, S. N. (1991). Long-term uplift of the Santa Cruz coastline in response to repeated earthquakes along the San Andreas fault. *Bulletin of the Seismological Society of America*, *81*(5), 1694-1704.

Vry, J. K., Baker, J., Maas, R., Little, T. A., Grapes, R., & Dixon, M. (2004). Zoned (Cretaceous and Cenozoic) garnet and the timing of high grade metamorphism, Southern Alps, New Zealand. *Journal of Metamorphic Geology, 22*(3), 137-157.

Walcott, R. I. (1998). Modes of oblique compression: Late Cenozoic tectonics of the South Island of New Zealand. *Reviews of Geophysics, 36*(1), 1-26.

White, S. H., & Green, P. F. (1986). Tectonic development of the Alpine fault zone, New Zealand: A fission-track study. *Geology*, *14*(2), 124-127.

Wobus, C., Whipple, K. X., Kirby, E., Snyder, N., Johnson, J., Spyropolou, K., Crosby, B., & Sheehan, D. (2006). Tectonics from topography: Procedures, promise, and pitfalls. *Geological Society of America Special Papers*, *398*, 55-74.

Yeats, R. S., & Berryman, K. R. (1987). South Island, New Zealand, and transverse ranges, California: A seismotectonic comparison. *Tectonics, 6*(3), 363-376.

Zachariasen, J., Berryman, K., Langridge, R., Prentice, C., Rymer, M., Stirling, M., & Villamor, P. (2006). Timing of late Holocene surface rupture of the Wairau fault, Marlborough, New Zealand. *New Zealand Journal of Geology and Geophysics, 49*(1), 159-174.

2.8 APPENDIX TO CHAPTER 2

2.8.1 *Supplementary Text*

2.8.1.1 Thermochronology Methods

We collected 16 samples from bedrock outcrops on both sides of the Alpine-Wairau fault. The outer 5cm of rock were not included in the samples in order to avoid any possible resetting of apatite ages caused by forest or brush fires (Mitchell and Reiners, 2003; Rogers et al, 2007). Apatite and zircon were separated from the samples at GeoSep services in Moscow, Idaho using standard magnetic and heavy liquid mineral separation procedures.

2.8.1.1.1 Apatite Fission Track

Apatite fission-track analysis was carried out at GeoSep Services. 30-40 individual grains were analyzed for fission track age per sample and 17-125 track lengths were measured per sample. Grains were mounted and polished (etched) before fission tracks were counted. Tracks were enhanced by exposing the samples to Cf irradiation before etching (Donelick and Miller, 1991). For track length measurements, angle to the crystal's c-axis was measured. D_{par} was also measured for each grain; this is a kinetic parameter related to apatite composition, which is important because resistance to annealing varies with composition, resulting in closure temperature variability (Green et al., 1989; Ketcham et al., 1999). ^{238}U content was measured using an LA-ICP-MS, and the zeta calibration method was used to determine ages; ζ was 8.2727 (Hasebe et al., 2013).

2.8.1.1.2 (U-Th)/He Thermochronology

Individual apatite and zircon grains for (U-Th)/He analysis were handpicked at the University of Washington using a Leica M205C binocular microscope with transmitted and polarized light and equipped with a calibrated digital camera. Selected grains were screened to ensure that they were

free of cracks and inclusions and were of sufficient size. Aliquots of five grains (apatite) and three grains (zircon) represented each sample. Each grain was measured and photographed before being packed into a Nb foil tube. Apatite and zircon grains were then sent to the CU-TRaIL (Thermochronology Research and Instrumentation Laboratory) at the University of Colorado, Boulder for (U-Th)/He analysis. There, each grain (still inside its Nb tube) was heated with a 25W diode laser in order to degas and measure the radiogenic ^{4}He. This procedure was repeated at least once to ensure complete degassing and, in apatite, to determine whether zircon inclusions may have been present in the grain (discussed further below). After degassing, grains (still in Nb tubes) were dissolved in acid: apatite in HNO_3 at 80° C, and zircon in a multi-step acid-vapor dissolution process involving HF, HCl and HNO_3. Once dissolved, the samples were analyzed for U, Th and Sm content on an ICP-MS. Apatite and zircon (U-Th)/He cooling ages were then calculated using methods described in Ketcham (2011).

After (U-Th)/He analysis was complete, we screened the data and ultimately excluded 6 grains from further analysis for one or more of the following reasons. First, we excluded any apatite grains that both degassed less than 95% of its total helium content during the first heating and had a total volume of measured ^{4}He greater than 0.01 ncc, as this could indicate the presence of inclusions. If less-soluble zircon inclusions were present in an apatite crystal, "parentless" ^{4}He could be measured and the cooling age for the crystal could be erroneously old. We also excluded grains that had effective uranium (eU) < 5 ppm. We then performed the Peirce outlier test and excluded grains deemed outliers within each sample (Ross, 2003). We also examined each apatite and zircon sample, and then the apatite and zircon data as a whole, for a relationship between age and eU, and between age and grain size, but found no substantial trends.

2.8.1.2 Modeling of Cooling Histories

We modeled our data using QTQt, a software package that uses a Bayesian transdimensional Markov Chain Monte Carlo (MCMC) method to invert thermochronology ages and other samples characteristics for time-temperature histories (Gallagher, 2012). In most cases, we modeled individual samples with 1-3 thermochronometers. At Mt. Robert we modeled several samples together in a vertical transect. We also included zircon fission-track data from Kao (2002), in QTQt models of samples 17mfs16 and 15mfs07.

Inputs to apatite- and zircon-helium QTQt models included uncorrected age and one-sigma analytical uncertainty, grain dimensions and number of terminations, eU, and sample elevation. For apatite-helium samples 3-5 grains were used, and for zircon-helium samples 3 grains were used. We used the radiation damage models of Flowers et al. (2009) and Guenthner et al. (2013) for AHe and ZHe models, respectively. Grains were modeled as spheres. Error on apatite- and zircon-helium ages was resampled during each of the model runs, as we felt that the analytical error on individual grain ages may not adequately capture the entire possible error. This method uses MCMC to resample a distribution from 0.1x to 10x the given error (Gallagher, 2012).

Model inputs for apatite fission track ages were: number of spontaneous tracks per crystal; fission track age and -95% confidence interval; the kinetic parameter D_{par}; angle to crystal c-axis, and zeta (8.2727 for all of our AFT samples) (Donelick et al., 1999; Ketcham et al., 1999; Ketcham et al., 2005; Gallagher, 2012). When 0 spontaneous tracks were measured for a crystal and the age and -95% confidence value for that crystal was therefore 0, we used the (usually large) +95% confidence interval as the error input for that crystal instead of -95%. In other words, crystal ages of 0 were treated as having large uncertainty. We excluded the very rare crystals that had an age and both lower and upper 95% confidence bounds of 0, or that had

an extremely large +95% confidence interval (e.g., 10^9 years). These exclusions totaled 2 or fewer grains per sample.

We also used track length data in the QTQt models for all of our AFT samples. Observed track lengths are the product of "fresh" track lengths that are subsequently reduced by partial annealing; the distribution of track lengths can provide additional information about the rate of cooling, as well as about the potential for multiple stages of cooling (Gleadow et al., 1986). Length inputs were track length, angle to crystal c-axis, and D_{par} (Ketcham et al., 1999; Ketcham et al., 2005; Ketcham et al., 2007). We used the annealing model of Ketcham et al. (2007).

Model runs were set up with general priors of temperature and time ranges (See Section 2.8.3 for QTQt model run inputs). In most cases, these parameters were constrained by the thermochronometers and the ages represented by the samples involved. However, the time-temperature window was expanded if preliminary model runs showed that most thermal history paths were forced against extreme edge of the available time-temperature space. In addition to this general available time-temperature space, models were given other time-temperature priors based on known information about each sample. All models of samples from sedimentary rock were given a prior time-temperature range of 10±10° C at the time of deposition. Sedimentary rocks were allowed to have one time-temperature point prior to their depositional age, as radiation damage accumulated earlier in a detrital grain's history can persist and affect its cooling age even after heating above the closure temperature (e.g., Fox et al., 2019). This option was used unless it reduced the model goodness-of-fit. Our two igneous samples, both diorites, were given prior time-temperature ranges of 900±100° C at the time of emplacement, in order to reflect the closure temperature of the U-Pb system that was used to date these plutons. Models of samples from metamorphic rocks were given an additional constraint of a broad temperature

range corresponding to metamorphic grade. The time window when this temperature could have been attained was very broad, between 1 Ma and shortly after protolith deposition, in order to force the sample to heat sufficiently but not unduly constrain the model. Models of multiple samples at a range of elevations were given a prior geothermal gradient of 25±25° C/km and an ending temperature gradient, based on the adiabatic lapse rate, of 7±5° C/km. The geothermal gradient was allowed to vary over time.

Models were run until the likelihood and posterior chains each converged, with neither having any apparent trend. This was accomplished with either 20,000 burn-in iterations and 100,000 post-burn-in iterations, or if necessary, 100,000 burn-in and 500,000 post-burn-in iterations. Interpretation of model results was based on both the expected model, which is a mean model weighted by each model's posterior probability, the 95% credible interval around the expected model, and on a heat map of all time-temperature models (Gallagher, 2012).

2.8.2 *Supplementary Tables: Thermochronology Data*

Table 2.1. Thermochronology samples.

Sample	Lithology	Longitude	Latitude	Elevation (m)	# AHe	# ZHe	# AFT
North Side of Alpine-Wairau fault (Footwall)							
17mfs17	Diorite of Median Batholith (unit uncertain)	172.4785	-41.9010	402	3	3	30
17mfs07	Buller diorite	172.8169	-41.7832	607	-	3	-
17mfs11	Caples schist	173.2364	-41.6362	318	-	3	-
17mfs13	Marlborough (Haast) schist overprint of Rakaia greywacke	173.6273	-41.4838	487	-	3	-
South Side of Alpine-Wairau fault (Hanging Wall)							
15mfs09	Alpine (Haast) schist overprint of Rakaia greywacke	172.2772	-42.3843	608	-	3	-
17mfs18	Rakaia greywacke	172.4318	-42.3290	927	5	3	40
17mfs19	Rakaia greywacke	172.4529	-42.3014	1064	4	3	39
17mfs16	Rakaia greywacke	172.5200	-42.0189	420	5	-	40
12mfs20	Esk Head greywacke	173.1908	-41.6841	381	-	3	-
15mfs07	Pahau greywacke	173.2172	-41.7811	928	4	3	-
17mfs15	Pahau greywacke	173.4108	-41.6323	490	-	3	-
Mt. Robert Vertical Transect							
17mfs02	Rakaia greywacke	172.7733	-41.8607	1763	-	3	-
17mfs03	Rakaia greywacke	172.8096	-41.8323	1387	-	3	-
17mfs04	Rakaia greywacke	172.8112	-41.8281	1197	-	3	-
17mfs05	Rakaia greywacke	172.8114	-41.8247	989	-	3	-
17mfs06	Rakaia greywacke	172.8121	-41.8232	892	3	3	39

Table 2.2. Apatite (U-Th)/He data.

Sample	Grain	Mass (µg)	r[a] (µm)	T[b]	He (nmol/g)	U (ppm)	Th (ppm)	Sm (ppm)	eU[c] (ppm)	Th/U	Raw Date (Ma)	Ft[d]	Date (Ma)	2σ[e] (Ma)
North Side of Alpine-Wairau fault (Footwall)														
17mfs17														
Diorite of Median Batholith, Emplacement 140 ±40 Ma, -41.9010°, 172.4785°														
	a	3.4	53.2	0	0.12	4.5	15.8	15.1	8.2	3.5	2.76	0.73	3.78	0.43
	b[g]	*3.4*	*55.7*	*1*	*5.9*	*45.4*	*58.2*	*18.5*	*59.0*	*1.3*	*18.37*	*0.75*	*24.59*	*0.92*
	c	2.9	47.8	0	1.4	34.8	51.0	18.5	46.8	1.5	5.49	0.71	7.78	0.33
	d	2.9	50.3	0	0.54	8.4	26.2	15.9	14.6	3.1	6.82	0.71	9.53	0.66
	e[g]	*6.9*	*65.7*	*0*	*1.7*	*11.4*	*38.0*	*14.0*	*20.3*	*3.3*	*15.21*	*0.78*	*19.56*	*0.57*
Mean: 7.03 ± 2.95 Ma														
South side of Alpine-Wairau fault (hanging wall)														
17mfs18														
Rakaia Subterrane (Torlesse Supergroup), Deposition 227 ± 21 Ma, -42.3290°, 172.4318°														
	a	0.7	32.5	1	0.10	16.5	36.2	52.3	25.0	2.2	0.74	0.58	1.28	0.44
	b	0.7	32.2	1	0.77	199.8	298.7	27.3	270.0	1.5	0.53	0.57	0.93	0.08
	c	0.7	31.4	1	0.63	124.2	27.7	16.4	130.7	0.2	0.89	0.58	1.54	0.13
	d	1.3	40.2	1	0.093	14.5	27.2	13.7	20.9	1.9	0.82	0.65	1.25	0.25
	e	2.6	48.6	0	0.10	15.1	23.2	10.0	20.6	1.5	0.90	0.71	1.27	0.12
Mean: 1.25 ± 0.22 Ma														
17mfs19														
Rakaia Subterrane (Torlesse Supergroup), Deposition 227 ± 21 Ma, -42.3014°, 172.4529°														
	a	1.4	40.3	1	0.18	36.2	34.9	11.0	44.5	1.0	0.76	0.66	1.15	0.15
	b[h]	*1.1*	*37.9*	*1*	*0.078*	*9.7*	*24.7*	*52.9*	*15.5*	*2.5*	*0.91*	*0.62*	*1.44*	*0.25*
	c	2.6	49.0	0	0.063	9.1	17.1	10.7	13.1	1.9	0.89	0.71	1.24	0.22
	d	0.8	33.3	1	0.082	13.4	28.7	15.9	20.1	2.1	0.75	0.59	1.28	0.74
	e	1.3	39.7	1	0.58	123.9	28.3	76.5	130.5	0.2	0.82	0.66	1.23	0.12
Mean: 1.27 ± 0.11 Ma														
17mfs16														
Alpine (Haast) Schist overprint of Rakaia Subterrane (Torlesse Supergroup), Deposition 227 ± 21 Ma, -42.0189°, 172.5200°														
	a	0.6	28.5	0	0.031	6.0	19.6	5.0	10.6	3.3	0.53	0.52	1.02	2.39
	b	1.1	38.0	1	0.075	10.3	10.7	22.3	12.8	1.0	1.07	0.64	1.67	0.62
	c	1.3	38.6	0	0.060	5.7	17.6	3.5	9.9	3.1	1.11	0.63	1.76	0.66
	d	2.3	45.4	0	0.33	54.8	38.8	8.1	64.0	0.7	0.95	0.70	1.36	0.13
	e	1.3	38.7	0	0.11	7.8	30.6	11.8	15.0	3.9	1.34	0.63	2.13	0.44
Mean: 1.59 ± 0.42 Ma														
17mfs06														
Rakaia Subterrane (Torlesse Supergroup), Deposition 227 ± 21 Ma, -41.8232°, 172.8121°														
	a[f]	*3.1*	*51.9*	*0*	*0.13*	*2.5*	*7.7*	*28.4*	*4.3*	*3.1*	*5.43*	*0.72*	*7.41*	*0.85*
	b	1.1	36.2	0	0.66	32.8	19.3	48.7	37.3	0.6	3.24	0.63	5.15	0.31
	c	3.4	50.2	1	1.3	6.1	49.5	25.4	17.7	8.1	13.04	0.70	18.67	0.73
	d	1.3	38.2	0	0.23	7.6	36.1	6.3	16.1	4.8	2.60	0.62	4.17	0.48
	e[g]	*2.1*	*44.1*	*0*	*0.27*	*8.1*	*20.9*	*12.7*	*13.0*	*2.6*	*3.86*	*0.68*	*5.67*	*0.41*
Mean: 9.33 ± 8.1 Ma														

15mfs07

Pahau Subterrane (Torlesse Supergroup), Deposition 120 ± 22 Ma, -41.7811°, 173.2172°

a	1.1	32.8	0	0.2	10.6	9.1	20.9	12.8	0.9	3.52	0.60	5.86	0.63
b	1.5	37.6	0	0.3	7.5	36.2	38.2	16.0	4.8	3.12	0.62	4.97	0.44
c[g]	*0.9*	*35.6*	*1*	*1.3*	*34.8*	*12.8*	*27.6*	*37.8*	*0.4*	*6.13*	*0.62*	*9.82*	*1.04*
d	0.7	32.2	1	0.4	10.7	42.2	28.9	20.6	3.9	3.21	0.56	5.67	0.70
e	1.9	42.6	1	0.5	13.7	50.3	22.1	25.5	3.7	3.39	0.66	5.14	0.26

Mean: 5.41 ± 0.42 Ma

---

[a] equivelent spherical radius

[b]F T indicates grain terminus. 0: Both tips broken. 1:One tip broken. 2: Whole grain.

[c]eU - effective uranium concentration, weights U and Th for their alpha productivity, computed as [U] + 0.235 * [Th]

[d]Ft is alpha-ejection correction of Farley et al [2002]

[e]Analytical uncertainty based on U, Th, He, and grain length measurements

Grains in italics were not included in means, plots or models and were excluded for the following reasons:

[f] Grains less than 5ppm eU

[g] Apatite grains with He re-extraction < 95% and He > 0.01 ncc

[h] Grains that failed the Peirce outlier test (Ross, 2003)

Table 2.3. Zircon (U-Th)/He data.

Sample	Grain	Mass (μg)	r[a] (μm)	T[b]	He (nmol/g)	U (ppm)	Th (ppm)	Sm (ppm)	eU[c] (ppm)	Th/U	Raw Date (Ma)	Ft[d]	Date (Ma)	2σ[e] (Ma)
North Side of Alpine-Wairau fault (Footwall)														
17mfs17														
Diorite of Median Batholith, Emplacement 140 ± 40 Ma, -41.9010°, 172.4785°														
	a	15.2	79.9	2	152.4	225	201	0.3	272	0.89	103.08	0.85	120.58	3.92
	b	14.4	73.4	1	82.1	142	134	0.5	174	0.94	87.04	0.84	103.26	10.32
	c	28.3	93.2	1	146.6	240	205	0.3	288	0.86	93.65	0.87	106.96	2.25
Mean: 110.27 ± 9.12 Ma														
17mfs07														
Buller Diorite (Median Batholith), Emplacement 147 ± 21 Ma, -41.7832°, 172.8169°														
	a	2.1	40.8	2	52.8	279	31	0.3	286	0.11	34.18	0.73	46.82	1.58
	b	2.6	43.7	2	54.6	273	39	0.3	282	0.14	35.84	0.75	48.00	1.18
	c	3.0	46.4	2	76.0	307	7	0.1	309	0.02	45.51	0.76	59.74	1.16
Mean: 51.52 ± 7.15 Ma														
17mfs11														
Marlborough (Haast) Schist overprint of Caples Terrane, Deposition 248 ± 42 Ma, -41.6362°, 173.2364°														
	a	2.7	40.6	1	20.8	138	93	0.5	159	0.67	24.10	0.73	33.19	1.15
	b	5.0	51.6	1	51.6	215	141	0.6	248	0.66	38.46	0.78	49.23	2.83
	c	2.0	39.4	2	7.3	52	44	0.01	63	0.85	21.49	0.71	30.07	2.14
Mean: 37.50 ± 10.28 Ma														
17mfs13														
Marlborough (Haast) Schist overprint of Rakaia Suberrane (Torlesse Supergroup), Deposition 227 ± 21 Ma, -41.4838°, 173.6273°														
	a	2.4	43.7	2	44.6	496	171	0.5	536	0.34	15.42	0.74	20.70	0.75
	b	3.3	47.8	2	39.5	295	188	0.5	339	0.64	21.53	0.76	28.22	0.71
	c	2.2	40.0	2	34.1	300	168	0.2	339	0.56	18.64	0.72	25.86	1.34
Mean: 24.93 ± 3.84 Ma														
South Side of Alpine-Wairau fault (Hanging Wall)														
15mfs09														

Alpine (Haast) Schist overprint of Rakaia Subterrane (Torlesse Supergroup), Deposition 227 ± 21 Ma, -42.3843°, 172.2772°

a	5.3	53.0	1	8.914	900	196	0.48	946	0.22	1.75	0.79	2.22	0.18
b	3.8	49.6	2	4.005	371	215	1.88	422	0.58	1.76	0.77	2.28	0.68
c	5.1	55.0	2	10.695	775	765	1.36	955	0.99	2.08	0.79	2.63	0.09

Mean: 2.38 ± 0.22 Ma

17mfs18

Rakaia Subterrane (Torlesse Supergroup), Deposition 227 ± 21 Ma, -42.3290°, 172.4318°

a	3.4	46.6	2	10.565	822	74	0.25	840	0.09	2.34	0.76	3.07	0.11
b	2.5	41.7	2	10.184	595	215	1.01	646	0.36	2.92	0.73	3.99	0.14
c	2.9	45.6	2	7.747	404	355	0.85	488	0.88	2.94	0.75	3.92	0.10

Mean: 3.66 ± 0.51 Ma

17mfs19

Rakaia Subterrane (Torlesse Supergroup), Deposition 227 ± 21 Ma, -42.3014°, 172.4529°

a	1.9	39.5	2	3.1	372	272	0.8	436	0.73	1.33	0.72	1.86	0.08
b	2.3	43.0	2	15.5	1096	865	1.4	1299	0.79	2.21	0.74	3.00	0.05
c	5.5	53.4	1	4.7	295	264	1.1	357	0.89	2.44	0.79	3.10	0.10

Mean: 2.65 ± 0.69 Ma

12mfs20

Esk Head (Torlesse Supergoup), Deposition 227 ± 21 Ma, -41.6841°, 173.1908°

a	2.0	40.3	2	33.7	245	85	0.02	264	0.35	23.57	0.72	32.53	0.74
b	2.3	42.0	2	139.2	322	164	0.5	361	0.51	71.19	0.73	96.91	4.10
c	6.2	57.4	2	204.7	416	144	1.8	450	0.34	83.76	0.80	104.24	2.26

Mean: 77.89 ± 39.46 Ma

15mfs07

Pahau Subterrane (Torlesse Supergroup), Deposition 120 ± 22 Ma, -41.7811°, 173.2172°

a	3.2	47.4	2	158.5	232	152	0.5	267	0.66	108.89	0.76	142.76	3.99
b	5.7	54.2	2	245.2	319	232	0.5	373	0.73	120.50	0.79	152.45	3.49
c	3.3	48.0	2	294.5	275	159	0.5	312	0.58	172.43	0.76	224.67	6.62

Mean: 173.29 ± 44.75 Ma

17mfs15

Pahau Subterrane (Torlesse Supergroup), Deposition 120 ± 22 Ma, -41.6323°, 173.4108°

a	2.0	40.8	2	197.2	285	267	1.1	347	0.94	104.31	0.72	143.90	3.11
b	2.7	44.8	2	100.7	207	80	0.3	226	0.39	82.08	0.75	109.18	5.27
c	2.6	45.2	2	62.7	157	165	0.7	196	1.06	59.13	0.75	79.01	2.50

Mean: 110.70 ± 32.47 Ma

Mt. Robert Vertical Transect

17mfs02
Rakaia Subterrane (Torlesse Supergroup), Deposition 227 ± 21 Ma, -41.8607°, 172.7733°

a	3.6	49.7	1	32.5	716	236	0.6	772	0.33	7.81	0.77	10.10	0.33
b	6.2	56.0	1	21.1	589	177	0.3	630	0.30	6.20	0.80	7.75	0.36
c	5.1	55.0	2	10.7	222	164	0.3	260	0.74	7.59	0.79	9.58	0.30

Mean: 9.14 ± 1.23 Ma

17mfs03
Rakaia Subterrane (Torlesse Supergroup), Deposition 227 ± 21 Ma, -41.8323°, 172.8096°

a	15.0	78.8	2	15.4	269	255	0.6	329	0.95	8.68	0.85	10.20	0.33
b	6.6	57.2	1	8.2	140	86	0.3	161	0.61	9.44	0.80	11.78	0.29
c	5.2	53.6	2	47.0	529	180	0.2	571	0.34	15.26	0.79	19.34	0.55

Mean: 13.77 ± 4.88 Ma

17mfs04
Rakaia Subterrane (Torlesse Supergroup), Deposition 227 ± 21 Ma, -41.8281°, 172.8112°

a	6.0	58.1	2	16.5	288	138	0.4	321	0.48	9.52	0.80	11.84	0.59
b	3.6	47.4	2	15.4	380	38	0.3	389	0.10	7.35	0.76	9.61	0.37
c	7.6	59.6	2	82.4	884	313	0.4	958	0.35	15.94	0.81	19.70	0.79

Mean: 13.72 ± 5.30 Ma

17mfs05
Rakaia Subterrane (Torlesse Supergroup), Deposition 227 ± 21 Ma, -41.8247°, 172.8114°

a	4.5	52.8	2	39.9	1407	194	0.3	1452	0.14	5.10	0.79	6.47	0.28
b	4.9	52.9	2	26.2	595	364	0.4	680	0.61	7.14	0.78	9.10	0.32
c	3.4	46.1	2	10.5	228	36	0.4	237	0.16	8.27	0.76	10.91	0.63

Mean: 8.83 ± 2.23 Ma

17mfs06
Rakaia Subterrane (Torlesse Supergroup), Deposition 227 ± 21 Ma, -41.8232°, 172.8121°

a	8.1	62.2	2	99.3	344	257	0.7	404	0.75	45.39	0.81	55.69	1.25
b	6.8	57.5	1	26.5	318	235	0.5	374	0.74	13.16	0.80	16.41	0.41
c	2.2	40.8	2	39.7	513	153	0.9	549	0.30	13.42	0.73	18.44	0.38

Mean: 30.18 ± 22.12 Ma

[a] equivelent spherical radius
[b]F T indicates grain terminus. 0: Both tips broken. 1:One tip broken. 2: Whole grain.
[c]eU - effective uranium concentration, weights U and Th for their alpha productivity, computed as [U] + 0.235 * [Th]
[d]Ft is alpha-ejection correction of Farley et al [2002]
[e]Analytical uncertainty based on U, Th, He, and grain length measurements

Grains in italics were not included in means, plots or models and were excluded for the following reasons:
[f] Grains less than 5ppm eU
[g] Apatite grains with He re-extraction < 95% and He > 0.01 ncc
[h] Grains that failed the Peirce outlier test (Ross, 2003)

2.8.3 *Supplementary Tables: QTQt Modeling Inputs*

2.8.3.1 Mt. Robert Vertical Transect

Table 2.4. Data inputs for Mt. Robert vertical transect.

Sample #	Elev. (m)	Unit + Strat. or Emplacement Age	Temp. (°C)	Systems used	Pre-dep. History?
17mfs02	1763	Rakaia (Torlesse) greywacke, 227 ± 21 Ma	10 ± 10	ZHe	Yes
17mfs03	1387	Rakaia (Torlesse) greywacke, 227 ± 21 Ma	10 ± 10	Zhe	Yes
17mfs04	1197	Rakaia (Torlesse) greywacke, 227 ± 21 Ma	10 ± 10	Zhe	Yes
17mfs05	989	Rakaia (Torlesse) greywacke, 227 ± 21 Ma	10 ± 10	Zhe	Yes
17mfs06	892	Rakaia (Torlesse) greywacke, 227 ± 21 Ma	10 ± 10	Zhe, AFT	Yes

Table 2.5. Thermal history constraints for Mt. Robert vertical transect.

Range for Time (m.y.) general prior	Range for Temp (°C) general prior	Temp Gradient (°C/km)	Present Day Surface Temp (°C)	Present Day Temp Offset (°C)	Max. $\partial T/\partial t$ (°C/m.y.)
150 ± 150	250 ± 250	25 ± 25	10 ± 10	7 ± 5	1000

Table 2.6. Zircon-helium inputs to Mt. Robert vertical transect.

Raw Age (Ma)	Error (Ma)	eU (ppm)	Grain length (microns)	Grain width (microns)	Grain thickness (microns)
Sample 17mfs02					
7.81	0.13	771.7	155	95	85
6.20	0.14	630.4	172.5	100	95
7.59	0.12	260.5	185	100	90
Sample 17mfs03					
8.68	0.14	328.8	265	150	125
9.44	0.12	160.6	175	105	95
15.26	0.21	571.0	205	90	85
Sample 17mfs04					
9.52	0.24	320.8	195	100	100
7.35	0.14	388.7	180	75	80
15.94	0.32	957.6	245	95	95

Sample 17mfs05					
5.10	0.11	1452.5	175	100	85
7.14	0.12	680.1	195	85	90
8.27	0.24	236.5	180	80	70
Sample 17mfs06					
45.39	0.51	404.2	235	95	110
13.16	0.17	373.7	175	115	90
13.42	0.14	548.8	150	70	65

Table 2.7. Apatite fission track data for Mt. Robert vertical transect.

Ns	**Age (Ma)**	**Age‡ Error (Ma)**	**Dpar (microns)**	**Zeta**
Sample 17mfs06 (AFT)				
9	5.01	2.45	1.72	8.2727
6	4.13	2.31	1.67	8.2727
2	6.97	5.27	1.63	8.2727
1	4.62	3.99	1.91	8.2727
2	8.48	6.42	1.73	8.2727
4	5.25	3.32	1.93	8.2727
2	15.79	11.95	1.78	8.2727
1	0.95	0.82	1.65	8.2727
4	1.22	0.77	1.9	8.2727
4	1.59	1.01	2.09	8.2727
6	12.97	7.28	1.8	8.2727
1	5.72	4.94	2.32	8.2727
3	2.27	1.56	1.94	8.2727
2	11.77	8.91	1.78	8.2727
1	2.31	2	1.71	8.2727
1	2.65	2.29	1.72	8.2727
0	0	33.47	1.44	8.2727
0	0	3.59	1.95	8.2727
7	4.49	2.39	1.8	8.2727
6	4.34	2.43	1.68	8.2727
12	4.1	1.81	1.68	8.2727
*1**	*0**	*0**	*1.79**	*8.2727**
3	12.88	8.83	1.82	8.2727
6	12.99	7.29	1.99	8.2727
4	4.94	3.12	1.61	8.2727
3	19.03	13.04	1.52	8.2727
1	25.57	22.11	1.97	8.2727
0	0	14.75	1.9	8.2727
0	0	10.06	2.14	8.2727

2	4.43	3.35	1.68	8.2727
1	13.24	11.45	1.52	8.2727
1	4.89	4.23	1.85	8.2727
1	3.66	3.17	1.92	8.2727
1	1.03	0.89	1.72	8.2727
1	1.79	1.55	1.97	8.2727
10	6.65	3.12	2.41	8.2727
1	1.9	1.64	1.73	8.2727
1	4.11	3.55	1.89	8.2727
2	5.49	4.16	1.79	8.2727
1	5.99	5.18	2.07	8.2727

*Italics indicate data not used because age and both positive and negative error = 0

Table 2.8. Apatite fission track length data inputs to model for Mt. Robert vertical transect.

Length (microns)	**C-axis Angle (°)**	**Dpar (microns)**
Sample 17mfs06 (AFT length)		
13.78	43.00	2.37
15.67	27.52	2.37
12.16	75.21	2.23
14.04	74.68	2.85
14.07	82.84	2.22
16.29	18.89	2.22
12.22	72.78	1.80
14.80	34.02	1.80
13.00	24.04	1.80
13.80	47.02	1.80
13.81	52.60	2.19
15.39	58.52	2.19
12.98	67.01	1.99
15.91	38.75	2.20
9.86	64.21	2.17
11.06	51.98	2.17
12.34	47.79	2.34
14.09	23.33	2.34
14.76	32.22	3.03
13.51	71.23	1.99
13.41	38.21	1.99
13.12	67.29	1.74
12.11	48.71	1.87
14.63	33.10	1.87
18.10	35.90	1.87
16.11	29.10	1.87
14.77	11.48	2.24
10.61	69.09	2.24
14.58	36.51	2.93

13.85	74.68	2.21
9.64	57.96	2.21
15.35	72.59	2.58
15.20	75.73	2.58
15.41	25.65	2.58
15.57	33.58	2.99
13.81	79.75	2.99
11.30	63.77	2.99
12.74	68.43	2.17
15.77	35.14	2.17
11.64	55.46	2.37
12.42	67.63	2.22
14.28	66.03	2.22
14.21	52.35	2.49
13.28	47.74	2.49
12.82	50.37	2.36
12.48	57.03	2.36
14.46	28.15	2.45
13.65	61.21	1.99
15.16	28.13	1.99
14.64	76.02	1.99
15.58	24.07	1.99
13.83	39.04	1.99
14.88	32.81	2.01
13.31	66.84	2.09
7.74	81.09	2.73
13.24	77.53	1.62
13.92	36.77	2.11
11.11	83.92	2.11
13.38	68.58	2.24
15.65	21.47	2.24
14.76	30.99	2.11
14.90	49.46	2.21
14.68	71.29	2.10
15.02	29.67	2.27
13.80	76.66	2.14
14.54	77.85	2.14
13.95	31.06	2.51
13.75	72.06	2.07
15.95	50.52	2.07
14.33	54.45	2.05
15.31	30.62	1.76
14.72	53.44	2.48
14.80	40.56	2.31

2.8.3.2 Sample 15mfs09.

Table 2.9. Thermal history constraints for model for 15mfs09.

Range for Time (m.y.) general prior	Range for Temp (°C) general prior	Geologic unit and depositional or emplacement age	Temp at Deposition (°C)	Present Day Surface Temp (°C)	Max. ∂T/∂t (°C/m.y.)	Pre-dep. History?
25 ± 25	250 ± 250	Alpine (Haast) Schist overprint of Rakaia Subterrane (Torlesse): 227 ± 21 Ma	10 ± 10	10 ± 10	1000	No

Additional time/temperature constraint: 375 ± 75° C at 114 ± 114 Ma to reflect metamorphic conditions

Table 2.10. Zircon-helium inputs to model for 15mfs09.

Raw Age (Ma)	Error (Ma)	eU (ppm)	Grain length (microns)	Grain width (microns)	Grain thickness (microns)
Sample 15mfs09					
1.75	0.07	946.1	165	85	100
1.76	0.26	421.6	170	90	80
2.08	0.04	954.8	185	90	100

2.8.3.3 Sample 17mfs18.

Table 2.11. Thermal history constraints for model for 17mfs18.

Range for Time (m.y.) general prior	Range for Temp (°C) general prior	Geologic unit and depositional or emplacement age	Temp at Deposition (°C)	Present Day Surface Temp (°C)	Max. ∂T/∂t (°C/m.y.)	Pre-dep. History?
10 ± 10	250 ± 250	Rakaia (Torlesse): 227 ± 21 Ma	10 ± 10	10 ± 10	1000	No

Table 2.12. Apatite- and zircon-helium inputs to model for 17mfs18.

Raw Age (Ma)	Error (Ma)	eU (ppm)	Grain length (microns)	Grain width (microns)	Grain thickness (microns)
Sample 17mfs18 (apatite)					
0.74	0.13	25.0	70	95	80
0.53	0.02	270.0	100	70	60
0.89	0.04	130.7	90	75	60
0.82	0.08	20.9	100	115	80
0.90	0.04	20.6	110	110	100
Sample 17mfs18 (zircon)					
2.34	0.04	839.6	175	85	70
2.92	0.05	646.1	160	80	60
2.94	0.04	487.7	150	85	75

Table 2.13. Apatite fission track data inputs to model for 17mfs18.

Ns	Age (Ma)	Age‡ Error (Ma)	Dpar (microns)	Zeta
Sample 17mfs18 (AFT)				
1	2.28	1.97	1.61	8.2727
0	0	30.31	2.05	8.2727
0	0	17.08	2.02	8.2727
1	5.62	4.86	1.9	8.2727
0	0	8.65	1.87	8.2727
0	0	13.72	1.78	8.2727
0	0	28.02	1.99	8.2727
0	0	6.8	1.57	8.2727
2	2.59	1.96	1.58	8.2727
0	0	26.99	1.69	8.2727
2	25.01	18.93	1.62	8.2727
1	20.34	17.59	1.78	8.2727
2	6.38	4.83	1.82	8.2727
0	0	26.29	1.49	8.2727
1	1.57	1.36	1.62	8.2727
0	0	81.01	1.88	8.2727
0	0	9.07	1.76	8.2727
0	0	19.06	1.58	8.2727
1	10.96	9.48	2.09	8.2727
1	2.5	2.16	1.68	8.2727
0	0	13.54	1.78	8.2727

1	5.24	4.53	1.82	8.2727
0	0	8.79	1.41	8.2727
0	0	46.07	2.09	8.2727
0	0	58.58	1.52	8.2727
0	0	37.24	1.56	8.2727
0	0	64.7	1.78	8.2727
0	0	50	1.73	8.2727
0	0	11.2	1.27	8.2727
0	0	67.27	1.59	8.2727
0	0	24.75	1.59	8.2727
0	0	19.07	1.71	8.2727
1	13.45	11.63	2.49	8.2727
0	0	136.61	1.68	8.2727
1	2.53	2.18	1.96	8.2727
0	0	24.71	1.93	8.2727
0	0	18.21	1.86	8.2727
1	1.55	1.34	1.89	8.2727
0	0	337.62	1.82	8.2727
0	0	45.51	2.2	8.2727

Table 2.14. Apatite fission track length data inputs to model for 17mfs18.

Length (microns)	**C-axis Angle (°)**	**Dpar (microns)**
Sample 17mfs18 (AFT length)		
15.20	39.52	2.35
14.17	62.12	2.35
9.94	63.74	2.63
13.13	63.76	2.03
15.62	27.07	2.03
14.33	18.50	2.20
15.25	30.79	2.49
15.12	34.32	2.31
15.09	26.32	2.31
11.54	65.46	2.59
13.21	67.43	2.02
15.57	30.11	2.02
14.45	19.12	2.07
15.17	33.48	2.40
15.11	32.98	2.36
14.32	64.21	2.36
12.87	64.26	2.48
13.59	61.11	1.96
15.76	19.89	1.96
14.09	21.42	2.23
15.33	29.59	2.53

2.8.3.4 Sample 17mfs19

Table 2.15. Thermal history constraints for model for 17mfs19.

Range for Time (m.y.) general prior	Range for Temp (°C) general prior	Geologic unit and depositional or emplacement age	Temp at Deposition (°C)	Present Day Surface Temp (°C)	Max. ∂T/∂t (°C/m.y.)	Pre-dep. History?
10 ± 10	250 ± 250	Rakaia (Torlesse): 227 ± 21 Ma	10 ± 10	10 ± 10	1000	No

Table 2.16. Apatite- and zircon-helium inputs to model for 17mfs19.

Raw Age (Ma)	Error (Ma)	eU (ppm)	Grain length (microns)	Grain width (microns)	Grain thickness (microns)
Sample 17mfs19 (apatite)					
0.76	0.05	44.5	85	100	110
0.89	0.08	13.1	90	100	120
0.75	0.23	20.1	70	90	90
0.82	0.04	130.5	90	110	90
Sample 17mfs19 (zircon)					
1.33	0.03	436.2	130	90	60
2.21	0.02	1299.2	130	85	75
2.44	0.04	357.4	170	100	85

Table 2.17. Apatite fission track data inputs to model for 17mfs19.

Ns	Age (Ma)	Age‡ Error (Ma)	Dpar (microns)	Zeta
Sample 17mfs19 (AFT)				
1	1.93	1.66	2.07	8.2727
1	1.07	0.93	1.98	8.2727
0	0	19.78	1.97	8.2727
0	0	97.81	2.14	8.2727
2	1.98	1.5	1.8	8.2727
1	0.94	0.81	1.88	8.2727
0	0	44.73	1.76	8.2727
2	1.21	0.92	2.1	8.2727
1	0.68	0.59	1.72	8.2727
0	0	46.8	2.01	8.2727

2	2.89	2.19	2.07	8.2727
1	2.42	2.1	2.08	8.2727
2	1.26	0.96	1.75	8.2727
3	2.32	1.59	1.61	8.2727
*0**	*0**	*0**	*1.88**	*8.2727**
0	0	67.09	1.82	8.2727
3	2.17	1.48	1.88	8.2727
0	0	14.87	1.66	8.2727
0	0	14.31	1.7	8.2727
0	0	7.09	1.94	8.2727
1	3.65	3.16	1.77	8.2727
1	0.94	0.81	1.73	8.2727
1	5.09	4.4	2.18	8.2727
0	0	67.86	1.84	8.2727
1	4.11	3.55	2.04	8.2727
2	2.76	2.09	1.99	8.2727
1	33.76	29.19	1.77	8.2727
0	0	25.42	1.5	8.2727
1	6.92	5.98	1.62	8.2727
2	2.02	1.53	1.99	8.2727
0	0	130.55	1.65	8.2727
0	0	26.97	1.54	8.2727
1	3.74	3.24	2.09	8.2727
0	0	39.24	1.82	8.2727
0	0	24.41	1.44	8.2727
0	0	21.8	1.83	8.2727
3	54.89	37.6	1.8	8.2727
1	1.05	0.91	1.88	8.2727
23	54.15	18.59	2.09	8.2727
0	0	7.44	1.82	8.2727

*Italics indicate data not used because age and both positive and negative error = 0

Table 2.18. Apatite fission track length data inputs to model for 17mfs19.

Length (microns)	**C-axis Angle (°)**	**Dpar (microns)**
Sample 17mfs19 (AFT length)		
13.27	31.03	1.84
15.32	22.83	2.21
14.34	52.74	1.97
13.86	49.84	2.29
15.39	41.34	1.93
13.27	72.17	2.27
13.80	52.61	2.19
12.84	49.39	2.15
14.67	49.55	1.59
15.23	47.91	2.00

14.96	63.61	2.24
14.63	63.29	2.33
13.92	66.46	2.24
15.62	53.07	1.85
15.62	35.94	1.90
16.86	54.27	1.90
15.52	44.84	1.90
13.84	85.81	1.95
12.60	73.08	1.95
15.58	26.65	2.51
15.13	43.90	1.94
14.87	64.60	2.26
14.56	62.26	2.37
13.89	61.47	2.29
15.54	54.04	1.86
13.78	86.83	1.92
12.54	78.06	1.92
15.48	24.62	2.49
13.12	38.01	1.83
15.28	20.81	2.15
14.27	52.72	1.95
13.69	41.83	2.27
15.08	40.32	1.92
13.03	76.14	2.26
13.59	53.60	2.15
12.98	47.37	2.13
14.55	45.53	1.56

2.8.3.5 Sample 17mfs16

Table 2.19. Data inputs for 17mfs16.*

Sample #	Elev. (m)	Unit + Strat. or Emplacement Age	Temp. (°C)	Systems used	Pre-dep. History?
17mfs16	420	Rakaia (Torlesse) greywacke, 227 ± 21 Ma	10 ± 10	AHe, AFT	No
9414-25**	540	Rakaia (Torlesse) greywacke, 227 ± 21 Ma	10 ± 10	ZFT	No

*Modeled as a vertical transect because samples had slightly different elevations
**Legacy data from Kao (2002).

Table 2.20. Thermal history constraints for 17mfs16.

Range for Time (m.y.) general prior	Range for Temp (°C) general prior	Temp Gradient (°C/km)	Present Day Surface Temp (°C)	Present Day Temp Offset (°C)	Max. ∂T/∂t (°C/m.y.)
20 ± 20	250 ± 250	25 ± 25	10 ± 10	7 ± 5	1000

Additional time/temperature constraint: 375 ± 75° C at 124 ± 123 Ma to reflect metamorphic conditions

Table 2.21. Apatite-helium inputs to model for 17mfs16.

Raw Age (Ma)	Error (Ma)	eU (ppm)	Grain length (microns)	Grain width (microns)	Grain thickness (microns)
Sample 17mfs16 (apatite)					
0.53	0.62	10.6	60	75	60
1.07	0.20	12.8	105	85	75
1.11	0.20	9.9	90	80	80
0.95	0.04	64.0	110	110	90
1.34	0.13	15.0	100	70	80

Table 2.22. Apatite fission track data inputs to model for 17mfs16.

Ns	Age (Ma)	Age‡ Error (Ma)	Dpar (microns)	Zeta
Sample 17mfs16 (AFT)				
1	5.78	5	1.76	8.2727
1	5.06	4.37	1.67	8.2727
0	0	34.81	2.04	8.2727
1	0.87	0.75	1.65	8.2727
0	0	61.34	2.21	8.2727
1	15.83	13.69	1.71	8.2727
0	0	148.12	1.84	8.2727
2	6.19	4.69	1.7	8.2727
0	0	54.61	1.94	8.2727
0	0	18.73	1.74	8.2727
2	1.07	0.81	1.54	8.2727
1	2.2	1.9	2.05	8.2727
1	5	4.33	1.52	8.2727
3	4.66	3.2	1.9	8.2727
0	0	5.08	1.36	8.2727

1	1.62	1.41	1.44	8.2727
1	7.76	6.71	1.82	8.2727
2	5.45	4.13	1.6	8.2727
2	6.75	5.11	1.8	8.2727
0	0	3.91	1.56	8.2727
2	1.72	1.3	1.64	8.2727
4	1.83	1.16	1.97	8.2727
0	0	65.97	2.02	8.2727
0	0	55.98	1.27	8.2727
1	5.77	4.99	1.91	8.2727
2	3.06	2.35	2.18	8.2727
4	3.92	2.48	1.72	8.2727
0	0	10.29	1.77	8.2727
0	0	4.52	1.5	8.2727
1	8.2	7.09	1.5	8.2727
1	5.08	4.39	1.81	8.2727
0	0	7.6	1.8	8.2727
0	0	14.08	1.72	8.2727
2	1.92	1.45	1.5	8.2727
0	0	6.2	1.75	8.2727
1	1.1	0.95	1.98	8.2727
2	1.68	1.27	1.68	8.2727
1	3.4	2.94	1.59	8.2727
2	1.47	1.11	2.1	8.2727
1	1.34	1.16	1.8	8.2727

Table 2.23. Apatite fission track length data inputs to model for 17mfs16.

Length (microns)	**C-axis Angle (°)**	**Dpar (microns)**
Sample 17mfs16 (AFT length)		
14.81	22.64	1.97
14.28	52.16	2.33
13.02	67.11	2.04
14.17	61.98	1.69
13.78	49.56	2.19
14.62	47.14	1.98
11.63	68.14	1.98
14.34	30.29	2.12
14.22	39.77	2.12
14.64	31.05	2.13
14.28	54.07	1.85
13.44	61.87	1.90
14.27	21.54	1.95
14.09	53.28	2.39
13.89	65.09	2.11
14.32	67.78	1.68

13.69	44.13	2.16
14.76	42.43	1.94
11.63	68.14	1.94
14.46	31.68	2.19
14.22	39.77	2.19
14.54	35.33	2.16
14.58	52.16	1.89
13.33	66.66	1.82

Table 2.24. Zircon fission track inputs to model for 17mfs16.

Ns	Ni	Age (Ma)	Age Error (Ma)	Zeta
Sample 9414-25†				
9	87.219	6.23	2.184	140.2
21	125.471	10.1	2.391	140.2
9	55.251	9.83	3.539	140.2
21	144.67	8.76	2.054	140.2
19	105.662	10.85	2.713	140.2
15	121.402	7.46	2.047	140.2
23	144.675	9.59	2.163	140.2
14	77.315	10.92	3.182	140.2
22	150.57	8.82	2.021	140.2
15	78.69	11.5	3.249	140.2
31	115.555	16.18	3.291	140.2
13	105.54	7.43	2.191	140.2
16	108.288	8.92	2.396	140.2
14	68.382	12.35	3.633	140.2
12	80.978	8.94	2.773	140.2
15	117.963	7.67	2.11	140.2
15	145.727	6.21	1.69	140.2
14	73.761	11.45	3.347	140.2
20	120.838	9.99	2.42	140.2
18	106.044	10.24	2.62	140.2

†Legacy data from Kao (2002) input to QTQt using “resample age/count data” option

2.8.3.1 Sample 15mfs07

Table 2.25. Data inputs for 15mfs07.*

Sample #	Elev. (m)	Unit + Strat. or Emplacement Age	Temp. (°C)	Systems used	Pre-dep. History?
15mfs07	930	Pahau (Torlesse) greywacke, 120 ± 22 Ma	10 ± 10	AHe, ZHe	Yes
9414-15**	520	Pahau (Torlesse) greywacke, 120 ± 22 Ma	10 ± 10	ZFT	Yes

*Modeled as a vertical transect because samples had different elevations
**Legacy data from Kao (2002).

Table 2.26. Thermal history constraints for 15mfs07.

Range for Time (m.y.) general prior	Range for Temp (°C) general prior	Temp Gradient (°C/km)	Present Day Surface Temp (°C)	Present Day Temp Offset (°C)	Max. ∂T/∂t (°C/m.y.)
219 ± 219*	200 ± 200	25 ± 25	10 ± 10	7 ± 5	1000

*Oldest single-grain age ± itself

Table 2.27. Apatite- and zircon-helium inputs to model for 15mfs07.

Raw Age (Ma)	Error (Ma)	eU (ppm)	Grain length (microns)	Grain width (microns)	Grain thickness (microns)
Sample 15mfs07 (apatite)					
3.52	0.20	12.8	95	110	65
3.12	0.15	16.0	75	140	85
3.21	0.21	20.6	80	90	65
3.39	0.09	25.5	145	110	75
Sample 15mfs07 (zircon)					
108.89	1.54	267.5	155	95	75
120.50	1.37	373.5	220	95	80
172.43	2.55	312.1	155	90	80

Table 2.28. Zircon fission track inputs to model for 15mfs07.

Ns	Ni	Age (Ma)	Age Error (Ma)	Zeta
Sample 9414-15†				
113	39.811	234.66	43.453	140.2
128	48.413	218.85	37.134	140.2
85	35.719	197.31	39.503	140.2
112	38.101	242.87	45.757	140.2
61	27.579	183.59	42.255	140.2
116	34.108	280.17	54.802	140.2
73	35.774	169.56	34.739	140.2
125	46.936	220.42	37.94	140.2
77	21.634	292.91	71.469	140.2
108	46.88	191.11	33.6	140.2
111	35.434	258.5	50.093	140.2
142	61.111	192.73	29.688	140.2

†Legacy data from Kao (2002) input to QTQt using “resample age/count data” option

2.8.3.2 Sample 17mfs07

Table 2.29. Thermal history constraints for model for 17mfs07.

Range for Time (m.y.) general prior	Range for Temp (°C) general prior	Geologic unit and depositional or emplacement age	Temp at Emplacement (°C)	Present Day Surface Temp (°C)	Max. ∂T/∂t (°C/m.y.)	Pre-dep. History?
45.51 ± 45.51*	100 ± 100	Buller Diorite: 147 ± 21 Ma	900 ± 100	10 ± 10	1000	N/A (plutonic)

* Oldest single-grain age ± itself

Table 2.30. Zircon-helium inputs to model for 17mfs07.

Raw Age (Ma)	Error (Ma)	eU (ppm)	Grain length (microns)	Grain width (microns)	Grain thickness (microns)
Sample 17mfs07 (zircon)					
34.18	0.58	285.8	140	65	75
35.84	0.44	281.8	150	80	70
45.51	0.44	308.8	155	80	80

2.8.3.3 Sample 17mfs11

Table 2.31. Thermal history constraints for model for 17mfs11.

Range for Time (m.y.) general prior	Range for Temp (°C) general prior	Geologic unit and depositional or emplacement age	Temp at Deposition (°C)	Present Day Surface Temp (°C)	Max. ∂T/∂t (°C/m.y.)	Pre-dep. History?
150 ± 150	250 ± 250	Caples Schist: 248 ± 42 Ma	10 ± 10	10 ± 10	1000	Yes

Table 2.32. Zircon-helium inputs to model for 17mfs11.

Raw Age (Ma)	Error (Ma)	eU (ppm)	Grain length (microns)	Grain width (microns)	Grain thickness (microns)
Sample 17mfs11 (zircon)					
24.10	0.42	159.5	150	75	60
38.46	1.10	248.0	170	90	85
21.49	0.77	62.6	140	75	60

2.8.3.4 Sample 17mfs13

Table 2.33. Thermal history constraints for model for 17mfs13.

Range for Time (m.y.) general prior	Range for Temp (°C) general prior	Geologic unit and depositional or emplacement age	Temp at Deposition (°C)	Present Day Surface Temp (°C)	Max. $\partial T/\partial t$ (°C/m.y.)	Pre-dep. History?
150 ± 150	250 ± 250	Marlborough (Haast) Schist overprint of Rakaia (Torlesse): 227 ± 21 Ma	10 ± 10	10 ± 10	1000	Yes

Table 2.34. Zircon-helium inputs to model for 17mfs13.

Raw Age (Ma)	Error (Ma)	eU (ppm)	Grain length (microns)	Grain width (microns)	Grain thickness (microns)
Sample 17mfs13 (zircon)					
15.42	0.28	535.6	135	75	85
21.53	0.27	339.4	160	85	80
18.64	0.48	339.3	155	65	65

2.8.4 *Supplementary Tables: Equivalent QTQt Inputs for Unmodelled Samples*

2.8.4.1 Sample 12mfs20

Table 2.35. Zircon-helium data for sample 12mfs20.

Raw Age (Ma)	Error (Ma)	eU (ppm)	Grain length (microns)	Grain width (microns)	Grain thickness (microns)
Sample 12mfs20 (zircon)					
23.57	0.27	264.5	135	65	75
71.19	1.51	360.5	145	65	80
83.76	0.91	450.1	210	95	95

2.8.4.2 Sample 17mfs06 AHe

Table 2.36. Apatite-helium data for 17mfs06.

Raw Age (Ma)	Error (Ma)	eU (ppm)	Grain length (microns)	Grain width (microns)	Grain thickness (microns)
Sample 17mfs06 (apatite)					
3.24	0.10	37.3	95	80	70
2.60	0.14	16.1	90	75	80
13.04	0.26	17.7	210	110	85

2.8.4.3 Sample 17mfs15

Table 2.37. Zircon-helium data for sample 17mfs15.

Raw Age (Ma)	Error (Ma)	eU (ppm)	Grain length (microns)	Grain width (microns)	Grain thickness (microns)
Sample 17mfs15 (zircon)					
104.31	1.14	347.4	130	75	70
82.08	1.98	225.9	150	80	75
59.13	0.95	195.5	135	90	80

2.8.4.4 Sample 17mfs17

Table 2.38. Apatite- and zircon-helium data for 17mfs17.

Raw Age (Ma)	Error (Ma)	eU (ppm)	Grain length (microns)	Grain width (microns)	Grain thickness (microns)
Sample 17mfs17 (apatite)					
2.76	0.15	8.2	120	95	120
5.49	0.12	46.8	135	120	90
6.82	0.23	14.6	115	105	105
Sample 17mfs17 (zircon)					
103.08	1.68	271.8	260	140	140
87.04	4.33	173.6	240	130	120
93.65	0.98	287.9	285	165	160

Table 2.39. Apatite fission track data inputs to model for 17mfs17.

Ns	Age (Ma)	Age‡ Error (Ma)	Dpar (microns)	Zeta
Sample 17mfs17 (AFT)				
116	48.36	8.58	1.68	8.2727
12	49.45	22.06	1.99	8.2727
152	127.68	19.98	2.21	8.2727
40	76.57	20.94	1.98	8.2727
56	76.09	18.16	2.47	8.2727
35	165.72	56.76	2.11	8.2727
15	41.88	16.96	2.31	8.2727
56	40.53	9.76	2.24	8.2727
8	56.13	28.47	2.52	8.2727
9	69.54	33.86	1.84	8.2727
14	74.82	31.03	2.23	8.2727
48	51.18	12.99	2.12	8.2727
15	65.82	26.69	2.05	8.2727
12	90.67	39.92	2.09	8.2727
12	85.8	37.76	2.08	8.2727
28	139.53	44.2	2.34	8.2727
56	60.34	14.53	2.12	8.2727
84	122.56	25.53	2.32	8.2727
3	55.47	38	2.46	8.2727
12	58.84	25.94	2.53	8.2727
5	42.64	25.25	2.35	8.2727
34	46.34	13.68	2.65	8.2727

31	67.19	20.8	2.69	8.2727
16	106.84	42.21	2.15	8.2727
11	47.68	21.69	2.22	8.2727
6	63.39	35.37	2.04	8.2727
12	64.17	28.19	2.58	8.2727
9	97.14	47.22	2.26	8.2727
5	69.1	40.82	2.31	8.2727
42	58.92	15.88	2.41	8.2727

Table 2.40. Apatite fission track length data for 17mfs17.

Length (microns)	**C-axis Angle (°)**	**Dpar (microns)**
Sample 17mfs17 (AFT length)		
14.32	53.85	2.56
14.00	55.32	2.12
13.53	68.37	2.12
11.08	69.38	2.12
14.24	33.73	2.31
11.91	60.36	2.31
14.66	64.64	2.31
13.04	48.93	2.31
13.49	71.38	2.31
14.85	58.38	2.31
13.28	38.82	2.70
15.89	42.95	2.70
16.35	48.10	2.70
13.32	38.54	2.70
15.14	45.83	2.70
9.72	72.53	2.39
15.06	39.60	2.39
11.84	63.26	2.39
11.26	69.08	2.39
11.43	52.73	2.39
11.86	65.33	2.45
12.49	51.16	2.45
13.93	62.81	2.65
12.12	73.96	2.65
11.17	40.10	2.65
13.19	75.38	2.05
13.59	74.66	2.05
13.56	42.48	2.05
14.83	47.26	2.05
12.37	85.32	2.52
16.34	52.52	2.52
10.58	54.81	2.52
15.11	20.11	2.52

14.43	56.67	2.52
12.41	53.96	2.52
12.51	79.76	2.59
12.71	60.35	2.80
15.03	37.39	2.80
12.77	33.37	2.80
12.54	74.26	2.80
13.54	72.72	2.43
15.37	36.65	2.43
13.62	81.92	2.37
13.28	85.23	2.60
14.18	88.46	2.47
15.61	38.30	2.81
16.32	45.40	2.81
14.97	49.22	2.81
9.91	86.32	2.81
14.33	53.19	2.81
15.26	40.40	2.83
13.13	43.42	2.83
14.31	49.89	2.83
12.10	54.06	2.66
13.17	59.10	2.62
13.75	42.46	2.62
14.03	54.48	1.92
12.90	71.42	1.93
14.22	26.84	1.93
12.87	81.24	1.91
13.74	44.64	1.91
15.04	57.41	2.72
12.81	79.08	2.72
15.05	32.22	2.72
13.51	45.62	2.72
13.36	41.17	2.72
14.05	52.07	2.92
13.58	46.86	3.02
14.44	53.93	3.02
14.68	32.42	3.02
14.01	61.48	3.02
15.22	47.23	2.35
12.32	56.89	2.30
12.07	69.36	2.30
12.99	44.49	2.30
13.00	88.58	2.30
13.75	37.04	2.30
14.37	65.79	2.30
11.74	47.55	2.30
13.14	49.15	2.30
14.48	37.94	2.69
12.67	61.98	2.69

11.17	70.67	2.69
15.31	60.85	2.69
13.88	59.69	2.69
13.81	76.30	2.69
14.63	54.96	2.02
10.23	85.67	2.02
11.22	77.95	2.02
15.32	45.75	2.02
14.85	69.03	2.02
13.23	75.16	2.02
13.15	71.41	2.02
13.87	34.59	2.02
15.13	57.68	2.02
12.07	51.46	2.69
12.42	55.29	2.69
15.11	42.04	2.69
14.23	43.22	2.69
14.08	55.09	2.69
13.71	44.74	2.63
13.93	25.09	2.63
11.49	63.51	2.63
13.40	44.42	2.26
13.38	68.66	2.26
13.50	27.42	2.51
10.63	66.56	2.51
14.26	70.50	2.51
14.27	32.96	2.73
11.68	85.51	2.73
14.20	45.45	2.58
11.55	20.88	2.58
13.63	44.99	2.48
11.88	46.76	2.48
14.26	40.84	2.48
15.94	18.25	2.46
13.51	50.36	2.46
14.59	59.24	2.46
14.29	44.22	2.46
13.47	73.66	2.46
13.68	42.01	2.46
14.76	32.62	2.46
13.36	78.82	2.50
9.66	66.27	2.50
13.64	71.69	2.09

Chapter 3. LOW-TEMPERATURE THERMOCHRONOLOGY REVEALS A MULTI-STAGE TECTONIC HISTORY IN THE MARLBOROUGH FAULT SYSTEM, NEW ZEALAND[2]

The Marlborough Fault System (MFS) on the South Island of New Zealand has been evolving tectonically throughout the Cenozoic, resulting in diverse patterns of faulting, deformation, and mountain building. Here we present new apatite and zircon (U-Th)/He and apatite fission track low-temperature thermochronology data that sheds light on patterns of exhumation, and inferred tectonics, across this landscape. We also use the GLIDE model to invert our data, as well as legacy thermochronology data, for exhumation rates across the MFS over time. Our results show that the eastern Awatere fault had experienced a phase of dip-slip motion beginning 40-60 Ma, the earliest known manifestation of the Early Kaikōura Orogeny. On the other hand, the Early Kaikōura Orogeny did not extend into the western MFS, where the Marlborough faults do not control patterns of exhumation; instead, this area experienced spatially and temporally irregular exhumation while in a state of distributed dextral shear. Closer to the present, the western MFS faults still do not exert an influence on patterns of exhumation, supporting the idea that they are purely strike-slip. Exhumation "hot spots" over the last 4 Ma include the Alpine fault, near its intersections with the MFS faults (exhumation rates up to 3.0-3.6 mm/yr), the restraining bend of

[2] This chapter is in prep for submission to *Tectonics* with authors S. Harbert, A. Duvall, R. Flowers, P. Upton, G. Tucker, P. O'Sullivan, C. Collett, M. Fox, and F. Herman. Author contributions were as follows: Duvall, Flowers and Tucker conceived of the study. Harbert assisted with design of the study. Harbert and Collett chose sampling sites. Harbert, Duvall, and Collett conducted the sampling with assistance from Flowers, Tucker and Upton. Harbert and O'Sullivan conducted the mineral separation. Harbert selected and prepared grains for (U-Th)/He analysis. Flowers conducted the apatite and zircon (U-Th)/He analysis. O'Sullivan conducted the apatite fission track analysis. Harbert conducted the QTQt thermal modeling. Fox and Herman developed the GLIDE model; Harbert implemented the GLIDE model on these data with assistance from Fox and Herman. Harbert interpreted the results and wrote the manuscript.

the Alpine-Wairau fault (rates of 1.2-1.7 mm/yr) and the Seaward Kaikōura range (rates of 0.9-1.4 mm/yr).

3.1 INTRODUCTION

The Marlborough Fault System (MFS) is a complex part of the plate boundary between the Australian and Pacific Plates on New Zealand's South Island where the Hikurangi Subduction Zone transitions to dextral-reverse motion on the Alpine fault, building the Southern Alps. In the MFS, plate boundary oblique convergence is distributed onto four major and several minor faults, which are primarily dextral. While the entire MFS is mountainous, the eastern and western region have different spatial patterns of topography. In the east, several of the major faults bound parallel mountain ranges, which are separated by large river valleys. In the western MFS there is also considerable relief, but individual ranges are smaller in areal extent and not preferentially aligned with the faults.

This difference in landscape character has been proposed to relate to a difference in tectonic history (Duvall et al., *in review*). The MFS has been evolving for at least the last 25 Ma as the orientation between the Hikurangi subduction zone and the single-strand transform margin has changed; rotation of the subduction zone about its southern end has driven about 100 degrees of clockwise, vertical-axis block rotation in the eastern MFS (Walcott, 1987; Lamb, 1988; Lamb and Bibby, 1989; Furlong and Kamp, 2009; Randall et al., 2011). Early in this period of rotation, the eastern Marlborough faults may have been oriented more parallel to the subduction zone and acted as thrust faults during the Early Kaikōura Orogeny (Lamb and Bibby, 1989; Vickery and Lamb, 1995). This phase of deformation set up the modern relief structure in the eastern MFS (Duvall et al., *in review*). Where Cretaceous and later cover rocks are preserved in the eastern MFS – in the Inland and Seaward Kaikōura mountains, and southeast of these ranges – there is

ample evidence for this rotation, folding and thrusting, and exhumation (Lamb and Bibby, 1989; Collett et al., 2019). The corresponding history of the western MFS is much less well constrained, but this area is thought to have undergone Miocene distributed shear without major mountain building (Randall et al., 2011). Between the western Wairau and Awatere faults, the Spenser Mountains reflect the initiation of the Wairau fault around 12-13 Ma and resultant development of the restraining bend between the Alpine and Wairau faults (Chapter 2, this dissertation). As the Hikurangi Subduction Zone and the Marlborough faults attained their present orientations and stopped or greatly slowed their rotation, the Marlborough faults became connected to the Alpine fault. This likely occurred in a north-to-south progression between ~7-8 Ma and as recently as 1 Ma (Carter and Carter, 1982; Wood et al., 1994; Little and Jones, 1998; Wallace et al., 2007). Currently, the southern end of the Hikurangi Subduction zone is migrating southward (Wallace et al., 2007). As it does so, the locus of motion on the plate boundary has moving southward as well, and the majority of plate motion is now transmitted through the southernmost MFS faults and in newer, developing fault zones to the south (Carter and Carter, 1982; Cowan et al., 1996).

Because much of the MFS has relatively uniform lithology and a great deal of Mesozoic deformation, it can be difficult to parse the relatively recent tectonic history of the broad region solely through structural mapping. In this study I use apatite and zircon (U-Th)/He and apatite fission-track low-temperature thermochronology to examine timing, magnitude, and when possible, rates, of exhumation throughout the MFS, including the western region, where few other data exist. Interpreted in spatial relation to each other, these patterns shed light on the tectonic processes that drive exhumation through rock uplift and erosion. This work addresses three main questions:

1. What is the northern extent of Oligocene-early Miocene Early Kaikōura Orogeny thrusting beyond the areas determined by previous workers?
2. Have the western MFS faults been important for accommodating oblique convergence via dip-slip motion, either during the Early Kaikōura Orogeny or more recently?
3. Over the last few million years, which areas have experienced the fastest exhumation, and what drives these spatial patterns?

3.2 Background/Prior Work

3.2.1 *The Modern Plate Boundary*

The Australian-Pacific plate boundary through New Zealand comprises two subduction zones of opposite vergence connected by the Alpine fault transform margin. In the north, the Pacific plate subducts beneath the Australian plate at the Hikurangi Subduction Zone. The Marlborough Fault System connects the southern end of this subduction zone to the dextral-reverse Alpine fault, where oblique continental collision is taking place. Beginning at the southern end of the South Island, the Australian plate subducts under the Pacific plate at the Puysegur subduction zone. The modern relative motion at the New Zealand plate boundary ranges from ~45 mm/yr off the North Island to ~37 mm/yr along the central Alpine fault (Beavan et al., 2002; Wallace et al., 2007, 2012; De Mets et al., 1994, 2010).

3.2.2 *The Marlborough Fault System*

At the Marlborough Fault System, plate boundary slip is partitioned primarily onto four major faults: from north to south, these are the Wairau (3-8 mm/yr), Awatere (~5 mm/yr), Clarence (~ 5 mm/yr) and Hope/Kekerengu faults (~20 mm/yr) (Benson et al., 2001; Nicol and Van Dissen, 2002; Langridge et al., 2003; Zachariasen et al., 2006; Wallace et al., 2007). The Hope, Clarence

and Awatere faults connect with the Alpine fault; the Wairau fault is the continuation of the Alpine fault within the MFS and northeast of its restraining bend. The Hope and Kekerengu faults are linked by the more northerly-striking Jordan thrust, which because of its orientation is the only major fault in the MFS to accommodate significant convergence through oblique slip (Van Dissen and Yeats, 1991). Models using GPS velocities, earthquake slip vector azimuths, and published fault slip rates to balance the plate motion budget across the Marlborough Fault System conclude that the major Marlborough faults (Wairau, Awatere, Clarence and Hope) are mostly strike-slip at present (Wallace et al., 2007, 2012).

Directly to the south of the MFS in the North Canterbury domain, and farther to the south in the Porters Pass-Amberley fault zone (PPAFZ), are complex areas of dextral and reverse faulting which have experienced significant recent seismicity, such as the 2016 M_w 7.8 Kaikōura earthquake and the four 2010-2011 Christchurch earthquakes (e.g., Cowan et al., 1996; Campbell et al., 2012; Hamling et al., 2017). These areas illustrate the general trend of southward migration of the MFS, and of the majority of plate boundary slip in this area (Carter and Carter, 1982; Cowan et al., 1996; Litchfield et al., 2014).

3.2.3 *Regional Geology*

The bedrock in the majority of the Marlborough Fault System is made up of the Torlesse Supergroup, an imbricated accretionary complex deposited at the subduction margin of Gondwana (Fig. 1.3). The Torlesse is divided into the Permian-Triassic Rakaia Subterrane in the west and the early Cretaceous Pahau Subterrane in the east (Rattenbury et al., 2006). Both subterranes are composed mainly of greywacke, and of alternating greywacke and siltstone turbidite deposits (MacKinnon, 1983; Mortimer, 2004; Rattenbury et al., 2006). In the westernmost MFS, the Rakaia subterrane has been metamorphosed to become the Haast schist

(Little et al., 1999; Rattenbury et al., 2006). The Rakaia and Pahau subterranes are separated by the Esk Head Subterrane, a belt of tectonic mélange (Silberling et al., 1988). The Esk Head is one of the only markers of total offset across the Hope, Clarence, and Awatere faults, as the Pahau and Rakaia contain few continuous marker beds, and units younger than the Torlesse are only present in the eastern MFS (Rattenbury et al., 2006). North of the Alpine-Wairau fault, the bedrock is composed of many Devonian-Jurassic accreted terranes, including the Buller, Takaka, Brook Street, Dun Mt.-Maitai, and Caples terranes, as well as the Triassic-Cretaceous Median Batholith (Mortimer, 2004).

Cenozoic sedimentary rocks are largely absent from the western MFS. In the eastern MFS, the Pahau subterrane is overlain by a spatially discontinuous Cretaceous-Pliocene sequence of marine sedimentary rocks (Rattenbury et al, 2006). After about 25 Ma, the coarse fan-delta Great Marlborough Conglomerate was deposited; this unit consists largely of clasts of Torlesse greywacke, indicating uplift and erosion of the basement (Browne 1995). After the deposition of the Great Marlborough Conglomerate, the sedimentary record reflects shallowing water and a trend toward terrestrial depositional environments (Lewis et al., 1980; Rait et al., 1991; Browne, 1995; Randall et al., 2011).

3.2.4 *Plate Boundary Evolution*

Present-day New Zealand rifted away from Gondwana around 100-80 Ma after subduction at its margin ceased (e.g., Laird and Bradshaw, 2004; Strogen et al., 2017). This, in turn, occurred around 100 Ma when the Hikurangi Plateau, a part of the ~120 Ma Ontong-Java/Manihiki/Hikurangi Plateau large igneous province, entered the subduction zone but was unable to fully subduct because it was thick, young and buoyant (Davy et al., 2008). The leading slab broke off and the Hikurangi Plateau remained partly underplated to the overriding plate at

the Chatham Rise (Fig. 1.1; Davy et al., 2008). This area – of continental crust attached to an oceanic plateau – defines the southern end of the Hikurangi Subduction Zone, as the Chatham Rise does not easily subduct beneath the Australian plate (Barnes et al., 1998).

Modern subduction of the Pacific Plate beneath the Australian Plate began north of New Zealand at the Tonga-Kermadec trench at around 50-55 Ma, then propagated south, reaching the modern North Island by ~25 Ma (e.g., King, 2000; Furlong and Kamp, 2009; Sutherland et al., 2017). At around 23 Ma, the Alpine fault initiated in response to increasingly convergent plate motion; it linked preexisting transtensional features into a strike-slip fault (Kamp, 1986; Cooper et al., 1987; King, 2000; Batt et al., 2004; Furlong and Kamp, 2013). Since that time, it has accumulated about 480 km of dextral offset (e.g.,Kamp, 1987; Hall et al., 2004).

3.2.5 *Early History of the Marlborough Fault System*

Between 25 and 8 Ma, the Hikurangi Subduction Zone rotated clockwise about its southern end (Walcott, 1987; Furlong and Kamp, 2009). In present-day eastern MFS, this rotation resulted in clockwise vertical-axis block rotations of about 100°. This history of Miocene rotation has been well constrained by many paleomagnetic studies, although there are several different models for number and geometry of blocks (e.g., Lamb, 1988; Lamb and Bibby, 1989; Vickery and Lamb, 1995; Little and Roberts, 1997; Hall et al., 2004; Lamb, 2011; Randall et al., 2011). Rotation is best-constrained toward the east, where igneous rocks and sedimentary rocks conducive to paleomagnetic studies are preserved (e.g., Lamb, 1988; Little and Roberts, 1997; Townsend, 2001; Randall et al., 2011).

The eastern portions of at least some of the Marlborough faults are widely believed to be reactivated Miocene thrust or reverse faults (Lamb and Bibby, 1989; Baker and Seward, 1996; Collett et al., 2019). During the Early to Middle Miocene and earlier, the faults would have been

oriented more favorably for trenchward-verging folding and thrusting, an episode called the Early Kaikōura Orogeny (Lamb and Bibby, 1989; Townsend, 2001; Collett et al., 2019). Some of these faults were localized at zones of still earlier deformation: the Clarence fault is immediately bordered by a several-hundred-meter wide zone of intense brittle deformation of Cretaceous or older age, which may reflect normal faulting as New Zealand rifted away from Gondwana (Crampton et al., 1998; Nicol and Van Dissen, 2002). Folded and faulted Cretaceous-Cenozoic cover rocks provide evidence of this deformation, as do now-inactive faults from this phase, such as the Flags Creek thrust fault (Lamb and Bibby, 1989; Browne, 1992; Townsend, 2001; Rattenbury et al., 2006). The Early to Middle Miocene Great Marlborough Conglomerate also reflects uplift and erosion of basement rocks: it consists of debris-flow conglomerates containing clasts of both Cretaceous-Paleogene cover rocks and basement Torlesse (Browne, 1995; Rattenbury, 2006). Altogether, the eastern MFS is thought to have experienced an episode of uplift and exhumation, focused in the hanging walls of thrust faults, during the Oligocene-early Miocene.

The western MFS is generally thought to have not experienced large-block rotation, and therefore not to have experienced the folding, thrusting and mountain-building that the eastern MFS did. However, rocks suitable for paleomagnetic analysis are not present in this area, so direct evidence for the spatial extent of the Early Kaikōura Orogeny is lacking (Lamb and Bibby, 1989; Randall et al., 2011). Many authors place the boundary between these tectonic domains at the Awatere, Clarence, and Hope/Jordan/Kekerengu faults' change in strike (from 070° in the west to 055° in the east), which also coincides with the edge of the subducted Pacific slab during the Miocene (Lamb, 1988; Lamb and Bibby, 1989; Randall et al., 2011). Since the western MFS was not underlain by the Pacific slab during the Miocene, and based on block models is a region

that would have had to shear extensively to link the block-rotation domain with the Alpine fault, several studies hypothesize that distributed dextral shear occurred on kilometer-scale blocks in the western MFS (Lamb, 1988; Hall et al., 2004; Lamb, 2011; Randall et al., 2011). Slip on small, preexisting faults, and shear between planes of the steeply-dipping Torlesse bedding, could have both contributed to accommodating this distributed shear (Rattenbury et al., 2006; Randall et al., 2011).

Paleomagnetic studies show that after about 8 Ma rates of block rotation were greatly reduced in the eastern MFS, as the elongate blocks between the eastern MFS faults were no longer oriented favorably for continued rotation (Hall et al., 2004). Plate boundary slip then began to be accommodated mainly through strike-slip faulting on the MFS faults. For example, the eastern Awatere fault first became active as a strike-slip fault between 7.4-6.4 Ma (Little and Jones, 1998). The history of the western Awatere, Clarence and Hope faults is much less well-studied. Some paleomagnetic studies of rotation in the eastern MFS infer that the western MFS faults are newer structures than their eastern counterparts, formed after rotation was largely complete, and linked strike-slip motion in the east with the Alpine fault (e.g., Little and Roberts, 1997; Randall et al., 2011). Wallace et al. (2007) suggest that as the Hikurangi Subduction Zone has migrated southward, it has initiated motion on each of these three faults in turn, between 7 Ma and 1 Ma, as a means to transfer the majority of plate boundary slip to the Alpine fault (just as the Hope fault transmits the majority of slip through the MFS today). This process likely started even earlier, around 12 Ma, with the initiation of the Wairau fault as such as linking structure (Ch. 2 of this dissertation). Thus, the western MFS faults would not be expected to control patterns of mountain-building or exhumation.

3.2.6 *Previous Low-Temperature Thermochronology*

Low-temperature thermochronology can be used to infer tectonic histories via interpretation of patterns of exhumation-driven cooling. Previous thermochronology studies have identified periods of exhumation that were associated with the Oligocene-early Miocene period of thrusting in the Inland and Seaward Kaikōura ranges. Baker and Seward (1996) used apatite fission track thermochronology to study the exhumation of the Tapue-o-uenuku igneous complex, which intruded the Torlesse basement at 90 Ma and now comprises the highest peak in the Inland Kaikōura Mountains, and found that it experienced rapid exhumation around 22 Ma, which they attributed to this thrusting phase. Collett et al. (2019) identified hanging-wall-focused exhumation propagating southward, initiating across the Clarence fault beginning around 35-40 Ma, across the Jordan thrust around 19 Ma, and across the Hope fault, further to the southwest, around 8-5 Ma. They termed the former two episodes the "Early Kaikōura Orogeny" and attributed them to the Oligocene-Miocene thrusting phase. However, they attributed the 8-5 Ma exhumation in the Amuri range (the hanging wall of the Hope fault) to the initiation of the Hope fault. Collett et al. (2019) also found rapid exhumation that was not confined to fault hanging walls (the "Late Kaikōura Orogeny") across their study area by 4-5 Ma, which they attributed to both an increase in plate convergence around 4 Ma and the ongoing translation of relatively thick continental crust into the space above the Pacific plate slab (Walcott, 1998; Eberhart-Phillips and Bannister, 2010; Jiao et al., 2017).

3.3 METHODS

3.3.1 *Low-Temperature Thermochronology*

We use apatite and zircon (U-Th)/He and apatite fission-track thermochronology (AHe, ZHe and AFT, respectively) to investigate the exhumation history of the entire MFS. All of these methods measure an accumulated decay product that is only retained in an apatite or zircon crystal below an effective closure temperature, and thus determine the time since that level of cooling was achieved. In geological applications this cooling is either the initial cooling of an igneous rock, or exhumation toward the Earth's surface, by erosion or by normal faulting, from a burial depth great enough that the closure temperature was exceeded.

In apatite and zircon crystals, ^{238}U, ^{235}U, and ^{232}Th continually decay to ^{206}Pb, ^{207}Pb, and ^{208}Pb, going through several instances of alpha decay in the process, and ^{147}Sm undergoes alpha decay to ^{143}Nd. During alpha decay, the nucleus of the parent isotope releases an alpha particle, which is a ^{4}He nucleus (Braun et al., 2006). At high temperatures ^{4}He can easily diffuse out of the crystal lattice, but it is retained below temperatures of ~40-90° C for apatite and ~140-220° C for zircon (Flowers et al., 2009; Guenthner et al., 2013). Variations in closure temperature can be caused by radiation damage to the crystal lattice; this effect varies with concentration of radiogenic isotopes.

In apatite fission track dating, the decay products are the physical damage tracks created when ^{238}U decays through spontaneous fission. Above the closure temperature window, or partial annealing zone, tracks are annealed as quickly as they are produced, but at lower temperatures, tracks anneal very slowly. The chemical composition of apatite can also affect the rate of track annealing and therefore the closure temperature of an individual grain (discussed further below;

Green et al., 1989). The apatite fission track age is a function of the track density and the rate of ^{238}U decay by fission.

The partial retention zone (or partial annealing zone for AFT) refers to the range of depths in the crust that correspond to the closure temperature window of a particular system. If a geothermal gradient is measured or assumed, the partial retention zone can be assigned a depth and an exhumation rate can be calculated. Low-temperature thermochronology is often used to study histories of tectonic uplift (e.g., Dokka et al., 1986; Tagami et al., 1988; Fitzergald et al., 1995; Colgan et al., 2006; Benowitz et al., 2011; Duvall et al., 2013). The key assumption in such studies is that exhumation from depth is due to surficial erosion, which is acting in response to rock uplift and generally keeping pace with it.

Most of our samples are from sedimentary rocks. For all thermochronometers, an age greater than the depositional age of the rock is referred to as "unreset" and indicates that the sedimentary rock was never heated above the closure temperature of that particular system. With assumptions about geothermal gradient, unreset ages can be used to constrain the maximum burial depth of a sample, and so the maximum exhumation that has occurred at that site. (However, an unreset apatite age, for example, still allows for repeated burial by and erosion of < ~1-2 km of sediment, so the latter assumption must be made carefully if the application deals with sediment flux or a question other than net rock uplift).

3.3.1.1 Sampling

For this study we collected 46 new bedrock samples from outcrops across the Marlborough Fault System in 2012, 2015 and 2017. Due to limitations on target mineral abundance, crystal size, and crystal quality, we were unable to use every thermochronometer at every sample location and ultimately used 24 samples for AHe, 44 for ZHe and 10 for AFT. Samples were generally taken

in pairs on either side of major faults, at similar elevations when possible. With this sampling scheme we covered as much of the MFS not previously sampled as possible. We also took samples in three vertical transects: at Mt. Robert, near the restraining bend of the Alpine/Wairau fault (discussed in Ch. 2 of this dissertation); at Black Birch, a mountain on the north side of the eastern end of the Awatere fault; and at Mt. Murphy, just north of the stepover from the Molesworth section to the Eastern section of the Awatere fault. These vertical transects spanned 890, 580, and 770 meters of elevation, respectively, and were each adjacent to a sample on the opposite side of a fault. Taking samples for low-temperature thermochronology from a range of elevations within a short horizontal space allows for the construction of an age-elevation plot (Fitzgerald et al., 1995). An apparent exhumation rate can be found by fitting a line to the age-elevation plot. With enough samples, changes in rate may be found. A similar, though lower-resolution strategy can be used on a single sample by analyzing it using multiple thermochronometers.

Most of the samples were from the Torlesse Supergroup, including the Pahau, Esk Head and Rakaia subterranes and the Haast Schist overprint of the Rakaia subterrane. One sample north of the Alpine fault was taken from the Haast Schist overprint of the Caples terrane. One sample was taken from the Late Cretaceous Burnt Creek formation, between the Clarence and Kekerengu faults. Two samples were taken from diorites of the late Triassic-early Cretaceous Median Batholith north of the Alpine fault. In all cases, the outer 5cm of rock were not included in the samples in order to avoid any possible resetting of apatite ages caused by forest or brush fires (Mitchell and Reiners, 2003; Rogers et al., 2007).

3.3.1.2 Analytical Methods: Apatite and Zircon (U-Th)/He

Apatite and zircon were separated from the bulk rock samples at GeoSep Services using heavy liquid and magnetic separation techniques. Individual apatite and zircon crystals for (U-Th)/He thermochronology were handpicked at the University of Washington under a Leica M205C binocular microscope with transmitted and polarized light and equipped with a calibrated digital camera. Each sample consisted of an aliquot of five grains (for apatite) or three grains (for zircon). The grains were screened for quality, including size, crystal shape, and the presence of inclusions. The grains were measured and characterized before each grain was packed into a small Nb foil tube, which was sealed by crimping both ends. Apatite and zircon grains were then sent to CU-TRaIL (Thermochronology Research and Instrumentation Laboratory) at the University of Colorado, Boulder, for (U-Th)/He analysis. The analysis performed by CU-TRaIL was as follows:

The Nb packet was loaded into an ASI Alphachron He extraction and measurement line. The packet was placed in the UHV extraction line (~3 X 10^{-8} torr) and heated with a 25W diode laser to ~800-1100°C for 5 to 10 minutes to extract the radiogenic ^{4}He. The degassed ^{4}He was then spiked with approximately 13 ncc of pure ^{3}He, cleaned via interaction with two SAES getters, and analyzed on a Balzers PrismaPlus QME 220 quadrupole mass spectrometer. This procedure was repeated at least once for each grain to ensure complete mineral degassing. Degassed grains were then removed from the line and taken to a Class 10 clean lab for dissolution.

Apatite grains, still enclosed in the Nb tubes, were each placed in 1.5 mL Cetac vials, spiked with a ^{235}U - ^{230}Th - ^{145}Nd tracer in HNO_3, capped, and baked in a lab oven at 80°C for 2 hours. Zircon grains were dissolved using Parr large-capacity dissolution vessels in a multi-step acid-vapor dissolution process. Zircon grains (including the Nb tube) were placed in Ludwig-

style Savillex vials, spiked with a ^{235}U - ^{230}Th - ^{145}Nd tracer, and mixed with 200 µl of Optima grade HF. The vials were then capped, stacked in a 125 mL Teflon liner, placed in a Parr dissolution vessel, and baked at 220°C for 72 hours. After cooling, the zircon vials were uncapped and dried down on a 90°C hot plate until dry. The vials then underwent a second round of acid-vapor dissolution, this time with 200 µl of 6N Optima grade HCl in each vial that is baked at 200°C for 24 hours. Vials were then dried down a second time on a hot plate. Once dry, 200 µL of a 7:1 HNO_3: HF mixture was added to each vial, and the vial was capped and cooked on the hot plate at 90°C for 4 hours. Once the minerals were dissolved, regardless of the dissolution process, they were diluted with 1 to 3 mL of doubly-deionized water and taken to the ICP-MS lab for analysis. Sample solutions, along with normal solutions and blanks, were analyzed for U, Th, and Sm content using either a Thermo Element 2 magnetic sector ICP-MS or an Agilent 7900 quadrupole ICP-MS. After the U, Th, and Sm contents were measured, He dates and all associated data were calculated on a custom spreadsheet using the methods described in Ketcham et al. (2011). The natural occurring $^{238}U/^{235}U$ ratio used in data reduction is 137.818 after Hiess et al. (2012). Every batch of samples included standards run sporadically throughout the process to monitor procedures and maintain consistency from run to run. Long term averages of Fish Canyon Tuff zircons and Durango fluorapatites run in the CU TRaIL are 28.7 ± 1.8 Ma (n=150) and 31.1 ± 2.1 (n=85), respectively.

We excluded from our analysis any apatite grains that had both a re-extract percentage less than 95% and a total volume of measured 4He greater than 0.01 ncc, as this indicates the presence of inclusions which could have contributed "parentless" ^{4}He to our ^{4}He measurement. We also excluded any grains with effective uranium (eU) < 5 ppm. After excluding these grains, we performed the Peirce outlier test on each sample to exclude and remove any outliers (Ross,

2003). Next, we examined each apatite and zircon aliquot, and then the apatite and zircon data as a whole, for a relationship between age and eU, and between age and grain size, but found no significant trends.

3.3.1.3 Analytical Methods: Apatite Fission-Track

Apatite separates were sent to GeoSep Services for apatite fission-track dating. 30-40 individual grains were analyzed for fission track age per sample and 17-125 fission track lengths were measured per sample. Grains were mounted and polished (etched) before fission tracks were counted. Tracks were enhanced by exposing the samples to Cf irradiation before etching (Donelick and Miller, 1991). For track length measurements, angle to the crystal's c-axis was measured. D_{par} was also measured for each grain; this is a kinetic parameter related to apatite composition, which is important because resistance to annealing varies with composition, resulting in closure temperature variability (Green et al., 1989, Ketcham et al., 1999). ^{238}U content was measured using an LA-ICP-MS, and the zeta calibration method was used to determine ages; ζ was 8.2727 (Hasebe et al., 2013).

3.3.2 *QTQt Modeling of Thermal Histories*

We modeled our data using QTQt, a software package that uses a Bayesian transdimensional Markov Chain Monte Carlo (MCMC) method to invert thermochronology ages and other samples characteristics for time-temperature histories (Gallagher, 2012). In most cases, we modeled individual samples with 1-3 thermochronometers. At Mt. Robert, Black Birch, and Mt. Murphy, we modeled several samples together in a vertical transect. Where a vertical transect crossed a fault, we modeled each side separately, because both sides of a fault cannot be assumed to have the same thermal history.

Inputs to apatite- and zircon-helium models included uncorrected age and one-sigma analytical uncertainty, grain dimensions and number of terminations, eU, and sample elevation. For apatite-helium samples, 3-5 grains were used, and for zircon-helium samples, 3 grains were used. We used the radiation damage models of Flowers et al. (2009) and Guenthner et al. (2013) for AHe and ZHe models, respectively. Grains were modeled as spheres. Error on apatite- and zircon-helium ages was resampled during each of the model runs, because the analytical error on individual grain ages may not adequately capture the entire possible error. This method uses MCMC to resample a distribution from 0.1x to 10x the given error (Gallagher, 2012).

Model inputs for apatite fission track ages included: number of spontaneous tracks per crystal; fission track age and -95% confidence interval; D_{par}; angle to crystal c-axis, and ζ (8.2727 for all of our AFT samples; Donelick et al., 1999; Ketcham et al., 1999, 2005; Gallagher, 2012). When 0 spontaneous tracks were measured for a certain crystal and the age and -95% confidence value for that crystal was therefore 0, we used the (usually large) +95% confidence interval for that crystal instead of -95%. In other words, crystal ages of 0 were treated as having large uncertainty. We excluded the very rare crystals that had an age and both lower and upper 95% confidence bounds of 0, or that had an extremely large +95% confidence interval (e.g., 10^8 years). These exclusions totaled fewer than 2 grains per sample.

We also used track length data in the QTQt models for all of our AFT samples. Observed track lengths are the product of "fresh" track lengths that are subsequently reduced by partial annealing of tracks; the distribution of track lengths can provide additional information about the rate of cooling, as well as about the potential for multiple stages of cooling (Gleadow et al., 1986). Length inputs were track length, angle to crystal c-axis, and D_{par} (Ketcham et al., 1999, 2005, 2007). We used the annealing model of Ketcham et al. (2007).

Model runs were set up with general priors of temperature and time ranges (See Section 3.9.3 for QTQt model run inputs). In most cases, these parameters were constrained by the thermochronometers and the ages represented by the samples involved. However, the time-temperature window was expanded if preliminary model runs showed that thermal history paths were forced to have a break in slope at the extreme edge of the available time-temperature space. In addition to this general time-temperature space, models were given other time-temperature priors based on known geologic information about each sample. All models of samples from sedimentary rock were given a prior time-temperature range of 10±10° C at the time of deposition. Sedimentary rocks were allowed to have one time-temperature point prior to their depositional age, as radiation damage accumulated earlier in a detrital grain's history can persist and affect its cooling age even after heating above the closure temperature (e.g., Fox et al., 2019). This option was used unless it reduced the model goodness-of-fit. Our two igneous samples, both diorites, were given prior time-temperature ranges of 900±100° C at the time of emplacement, in order to reflect the closure temperature of the U-Pb system that was used to date these plutons (Kimbrough et al., 1994; Lee et al., 1997). Models of samples from metamorphic rocks were given an additional constraint of a broad temperature range corresponding to metamorphic grade. The time window when this temperature could have been attained was very broad, between 1 Ma and shortly after protolith deposition, in order to force the sample to heat sufficiently but not unduly constrain the model. Modeled vertical transects were given a prior geothermal gradient of 25±25° C/km and an ending temperature gradient, based on the adiabatic lapse rate, of 7±5° C/km. The geothermal gradient was allowed to vary over time.

Models were run until the likelihood and posterior chains each converged, with neither having any apparent trend. This was accomplished with either 20,000 burn-in iterations and

100,000 post-burn-in iterations, or if necessary, 100,000 burn-in and 500,000 post-burn-in iterations. Interpretation of model results was based on both the expected model, which is a mean model weighted by each model's posterior probability, and on a heat map of all time-temperature models (Gallagher, 2012).

3.3.3 *Inversion of Data for Temporal and Spatial Distribution of Exhumation Rates*

In order to convert our large thermochronology dataset into a more integrated picture of exhumation rate over time, we modeled it using the GLIDE model (Gaussian Linear Inversion of Data to Exhumation rate) developed by Fox et al. (2014). This model takes a large dataset of thermochronometric ages, ideally with good spatial and elevation coverage, and inverts it for exhumation rates over space and time. A detailed description of the GLIDE model is available in Fox et al. (2014), but the general method is as follows. Here we use the same notation as Fox et al. (2014) for clarity.

For each sample, the isotherm corresponding to the closure temperature of the relevant mineral is interpreted to be the integral of the exhumation rate at that point, from the present to the cooling (closure) age:

$$\int_0^{\tau} \dot{e} dt = z_c$$

where τ is cooling age, $\dot{e}$ is exhumation rate, t is time, and z_c is depth of closure temperature isotherm. Where there are multiple samples and/or multiple chronometers at a single location, the above equation is applied to each, resulting in a linear system of equations. This system is discretized by dividing time into intervals of Δt selected by the user. However, unless there are

more cooling ages than time intervals, the problem is non-unique. The model uses a linear inversion method in which data and model parameters are Gaussian probability densities, characterized by a mean and variance. A mean and variance for a priori exhumation rate ($\dot{e}$ prior) and geothermal gradient (used to determine closure temperature isotherm depths) are specified by the user.

When samples are distributed in space as well as in elevation, a spatial correlation function is imposed so that exhumation rate varies smoothly in space. However, time intervals are independent; exhumation rate may vary sharply over time. Exhumation rates are correlated in space according to the exponential function:

$$\rho(u) = \exp\left(-\frac{u}{\phi}\right)$$

where $\rho(u)$ is the spatial correlation between a pair of points, u is the separation distance between the points and ϕ is the user-specific correlation length scale. Any areas of the model domain that are not within the correlation length scale of any data will have no result.

GLIDE also includes a thermal model, which determines the depth to closure temperature isotherm for the various thermochronometers, accounts for any temporal or spatial changes to isotherms that may occur as the result of fast exhumation, and also accounts for spatial perturbations to isotherms caused by surface topography. Mean temperature with depth is found by solving the heat transfer equation:

$$\frac{\partial T}{\partial t} - \dot{e}\frac{\partial T}{\partial z} = \kappa\nabla^2 T$$

where $T(x,y,z,t)$ is temperature and κ is thermal diffusivity. Boundary conditions of this problem are the temperature of the land surface (T_0 at the average surface elevation of the model domain, which is considered by the thermal model to be z=0) and the heat flow at the base of the modeled crustal thickness, all of which are user inputs. These inputs together can be thought of as a prior geothermal gradient. The methods for calculating perturbations to isotherms by surface topography, and the numerical implementation of calculating isotherms and solving for exhumation rates, are described in detail in Fox et al. (2014).

GLIDE can incorporate user-defined discontinuities across which exhumation rates are not spatially correlated. These boundaries are "faults" in the sense that each side is considered to have an independent thermal history, but they are not assigned a slip rate, and they all function as discontinuities for the entire duration of the model run. All discontinuities have vertical dips and extend through the entire thickness of the model domain.

The dataset used in our model consisted of 414 ages, 278 of which were within the 40-million-year time domain of our model. It consisted of the 78 new ages from this study and Ch. 2; all ages from Collett et al. (2019); all AFT and ZFT ages from Baker and Seward (1996); apatite and zircon fission track ages from Kao (2001; 2002) that were based on 10 or more crystals; and a subset of the amalgamated data from Jiao et al. (2017) that was in or near to our study area (sources of this data were White and Green, 1986; Kamp et al., 1989; Seward, 1989; Seward and Tulloch, 1991; Kamp et al., 1992; Seward and White, 1992; Gibson, 1993; Tippett and Kamp, 1993a and 1993b; Kamp et al., 1996; Schulte et al, 2014; and unpublished data from Seward and Sagar). See Section 3.9.5 for all data used in the inversion. We used a portion of the

GEBCO_08 30 arc-second digital elevation model of modern-day topography and bathymetry as our land surface input ("The GEBCO_08 Grid").

We ran versions of the GLIDE model with and without fault blocks in order to test whether these faults have a significant influence on spatial patterns of exhumation. In both cases we used a spatial correlation distance of 20 km, although in the fault-block model this distance could be truncated by the faults. Block boundaries were generally the Marlborough faults and the Alpine fault. The blocks between the Wairau and Awatere, Awatere and Clarence, and Clarence and Hope faults were each divided into an eastern and western half, approximately at the location where those faults change strike. Our placement of this middle boundary is not meant to imply an assertion of an active fault at that exact location; rather, it is to test the hypothesis that the eastern and western MFS faults have behaved differently during their history, or may have differences in slip sense due to their differences in strike. This central region is relatively data-poor, so the precise location of the boundary is not critical to our analysis. Locations of block boundaries and data are shown in Figure 3.2.

We tested $\dot{e}_{pr}$ of 0.1 mm/yr and 0.5 mm/yr, each ± 7 mm/yr, and ran the model for a total of 40 Ma with a time step of 2 Ma. Our starting geothermal gradient was 26° C/km. In models with $\dot{e}_{pr}$ = 0.1 mm/yr, the ending geothermal gradient was 28° C/km, and in models with $\dot{e}_{pr}$ = 0.5 mm/yr, the ending geothermal gradient was 33° C/km. We use geothermal parameters similar to those used by Jiao et al. (2017) in an inversion of thermochronology data from the North and South Islands. Our model inputs are summarized in Table 3.1. Output of the model includes exhumation rate over space and time; reduction in variance over space and time; and time-temperature histories of user-selected control points. Output is written to a grid of 16,770 nodes with spacing of 1.5 km, as well as 20 "control points" selected for their proximity to ample data.

3.4 RESULTS

3.4.1 *Thermochronology Ages*

Some general patterns are apparent from the thermochronology ages (Fig. 3.3). First, all of the analyzed apatite (U-Th)/He samples are reset and all sample means are younger than 20 Ma. Most are younger than ~6 Ma. Much of the MFS has therefore experienced at least 2-3 km of exhumation since deposition of the Torlesse, and in much of the field area this much exhumation has occurred since the late Miocene.

Some of the zircon samples are reset and younger than ~20 Ma, and others are completely unreset. However, zircon ages tend to exhibit a wide range of single-grain ages per sample. In some samples, some grains may have cooling ages within the depositional age range of the rock, while others are somewhat younger. This may indicate that the sample represents an exhumed partial retention zone. Zircon (U-Th)/He age dispersion can also result from the interaction of eU and resulting radiation damage, and the thermal history of the sample. Although we see no robust eU-age trends in our data, when modeling our data in QTQt we allow for the possibility that radiation damage influences cooling ages (Guenthner et al., 2013).

Patterns of unreset and reset ages on either side of a fault can shed light on relative amounts of exhumation, and therefore on possible dip-slip motion. We see this pattern across the eastern Awatere and Wairau faults, as well as across the Hope fault at Hanmer Basin. The north side of the Awatere fault has slightly younger AHe ages than the south side, but the difference is not extreme; ages range from 3-9 Ma on the north side and 6-16 Ma on the south side. This pattern suggests that dip-slip motion on the Awatere fault may have persisted until at least within the last several million years.

Our youngest ages for all thermochronometers are focused in a few key locations. Closest to the Alpine fault and its restraining bend, all thermochronometers have cooling ages < ~4 Ma. In the southwest corner of our field area, young (<10 Ma) AHe ages extend farther from the Alpine fault than young ZHe ages do, likely indicating rapid, but lower-magnitude, exhumation here. Very young AHe ages (<2 Ma) are also found between the Clarence and Kekerengu faults at river level in the Clarence River gorge.

3.4.2 *QTQt Time-Temperature Model Results*

3.4.2.1 Awatere Fault

Results from QTQt models near the eastern Awatere fault are summarized in Figure 3.4 (Locations of figures 3.4, 3.5, and 3.7 are shown in Fig. 3.1). We modeled samples 17mfs08 (AHe and ZHe), 17mfs09 (ZHe), and 17mfs10 (ZHe) as a vertical transect (VT) on Black Birch, a mountain on the north side of the eastern Awatere fault. Results frm this model are similar to those at other samples on the north side of the Awatere fault, 17mfs30 and 15mfs05. These models show gradual heating after Torlesse (Pahau) deposition, followed by monotonic cooling. The timing of cooling initiation is highly uncertain but occurred before 40 Ma, possibly as early as 50-60 Ma, based on sample 17mfs30 and the Black Birch vertical transect. The QTQt model for sample 15mfs05 shows an even earlier onset of cooling, possibly as early as 80 Ma, which is unexpected because this sample is located between the other two. All of these samples (Black Birch VT, 15mfs05, and 17mfs30) then cooled at a rate of ~5-6° C/Ma until the present. However, since we do not have AHe or AFT for 15mfs05 or 17mfs30, we cannot resolve any changes in cooling rate that may have occurred since the samples cooled below the ZHe closure temperature. Sample 15mfs04, located about 9 km northwest of 15mfs05 and farther from the Awatere fault, shows later but faster cooling, starting 16-18 and at a rate of 9-10° C/Ma.

Samples in the footwall of the Awatere fault generally show less total cooling than those in the hanging wall. Samples 17mfs31, 17mfs29, 12mfs02 and 12mfs03 all heated gradually since deposition, then cooled from 100-150 degrees to surface temperatures starting about 18-35 Ma. These samples were exhumed as the Inland Kaikōura Range (IKR) grew; this timing and amount of cooling is later and less than that found by Collett et al. (2019) immediately adjacent to the Clarence fault, which is to be expected if the sample were located farther from the Clarence fault in the more gently-dipping limb of a fault-propagation fold, or if the Inland Kaikōura mountains grew due to vertical deformation distributed off of the main fault (Van Dissen and Yeats, 1991; Nicol and Van Dissen, 2002). We attribute the timing of exhumation in the footwall of the Awatere fault to the growth of the Inland Kaikōura mountains and resultant piggyback uplift inboard of the Clarence fault.

We modeled samples 17mfs33 (Zhe), 17mfs34 (Zhe), 17mfs35 (Zhe) and 15mfs02 (AHe) as a VT on Mt. Murphy. This mountain sits just north of the Awatere fault and just west of the stepover between the eastern and Molesworth sections of the fault (notation from McCalpin, 1996). Our QTQt model shows that this area experienced gradual heating from Torlesse (Pahau) deposition until around 9-12 Ma, when it began cooling from about 130-140 degrees at a rate of about 12° C/Ma. The sample across the Awatere fault from Mt. Murphy, 17mfs32, cooled a similar amount but much started much earlier, around 55 Ma. This sample may be far enough away from the IKR that it was not affected by the Clarence fault stage of the Early Kaikōura Orogeny.

Modeled thermal histories from the eastern Awatere fault are very different from those along strike to the west. We therefore draw a distinction between the cooling and tectonic history

of the eastern Awatere fault and the Molesworth section, and place the boundary between the two just east of the stepover between fault segments.

3.4.2.2 Central MFS

Our modeled cooling histories from the western MFS show many samples beginning to cool, after gradual heating since Torlesse deposition, within the last 25 Ma (See Figure 3.5). Our analysis is limited in some parts of this region by the thermochronometers that we were able to use on each sample. For instance, samples 17mfs22 and 17mfs36 were only analyzed using ZHe and both yielded unreset or very old ages. These samples are therefore unable to reveal information about any heating or cooling of less that ~200 degrees that may have occurred. QTQt models of unreset samples tend to show the sample remaining at surface temperatures for the entire model duration, but such results should not be taken literally in the absence of a lower-temperature thermochronometer. QTQt models of partially reset samples, or reset but very old samples, tend to show a period of heating close in time to the cooling age, followed by gradual cooling to the present. This history may or may not be complete, but we have no constraint more recently in time than the ZHe age.

Some samples with reset-but-old ZHe ages occur in the Esk Head subterrane of the Torlesse: 17mfs22, 17mfs25, and 17mfs26. The Esk Head is a belt of mélange consisting of disrupted tectonic blocks of material from the Rakaia and possibly the Pahau, and also of limestones, cherts and basalts interpreted to be from the plate subducting at the Gondwana margin (Silberling et al., 1988). Silberling et al. (1988) suggest that the Esk Head was accreted to the Gondwana margin through underplating, then later rapidly exhumed by thrust faulting within the growing accretionary prism. Our individual grain ages within the Esk Head are too dispersed, and some are too young, to definitively correlate them with this event. However, it is fair to

conclude that the early thermal history of our samples from the Esk Head may be complex, and not entirely captured by a depositional age similar to the Rakaia. Our samples in the western MFS generally may also be affected by periods of low-grade metamorphism and subsequent cooling of the Rakaia subterrane, if patterns found in the Rakaia of the North Island were widespread (Adams and Graham, 1996).

Of our sample pair on the western Awatere fault, the northern sample, 17mfs26, was unfortunately limited to a ZHe sample with very large dispersion between replicate ages. The QTQt model of this sample was unable to "choose" between several time-temperature paths, each of which fit a subset of the replicates. However, modeling the sample on the south side of the western Awatere fault, 17mfs25, yielded a more conclusive cooling history. This sample cooled from ~150-190 degrees to surface temperatures starting sometime between 8-13 Ma, at a rate of ~12° C/Ma. This history is remarkably similar to that at Mt. Murphy, which is about 35 km away and on the opposite side of the Awatere fault (see Figure 3.6).

The modern western MFS faults, thought to have initiated from ~7-8 Ma to perhaps as recently as 1 Ma, have not had a strong control on our thermochronology dates or modeled cooling histories (Little and Jones, 1988; Wood et al., 1994; Little and Roberts, 1997, Collett et al., 2019). For example, samples 17mfs20 and 17mfs21, on either side of the Hope fault at Hanmer Basin, have a similar timing of cooling/exhumation initiation, though the north side of the fault has experienced approximately an extra 20° C of cooling. Sample 17mfs37, on the south side of the Elliott fault, shows an earlier onset of cooling and at least 150° C more cooling than samples 17mfs21 and 17mfs23, which are only 10-15km from it and not separated from it by any modern faults. At other location pairs, such as samples 17mfs22 and 17mfs23 on either side of

the Clarence fault, our thermal models are not directly comparable because we were not able to use equivalent thermochronometers on either side of the fault.

The southwestern part of the field area has some of our youngest AHe ages. For example, sample 12mfs25 has a young, very precise AHe age of 1.8 ± 0.035 Ma, but an older, much more dispersed ZHe age of 50 ± 29 Ma. The QTQt model of sample 12mfs25 shows rapid cooling from 70° C over the last 2 Ma, equivalent to an apparent exhumation rate of more than 1 mm/yr, but is unable to pinpoint the onset of this cooling or determine an earlier cooling rate (Fig. 3.7).

3.4.3 *GLIDE Inversion Results*

With our dataset, the GLIDE model has the most utility as a way to elucidate recent patterns of exhumation, as opposed to a comprehensive tectonic history. Because so many of the ages in our dataset are very young, and the model has information only about a point at times after its cooling age, exhumation farther back in time than a few million years ago is poorly resolved. Thus, we present results from 4-2 Ma and from 2 Ma to the present. (See variance plots accompanying Figures 3.8 and 3.9, and section 3.10.1; when the variance is still close to 1, the exhumation rate at that location is not well resolved and is likely to simply be $\dot{e}$ prior.)

In all models, the fastest rates of exhumation are in the western MFS immediately adjacent to the Alpine fault, particularly in the area near the Alpine fault-Awatere fault junction. Peak rates of exhumation at the Alpine-Awatere junction area within the last 2 Ma range from 3.0 – 3.6 mm/yr, depending on model parameters. Peak exhumation rates vary between low $\dot{e}$ prior and high $\dot{e}$ prior runs, but the general patterns are the same (see Figure 3.10). In the runs with fault blocks (1 and 2), the high rates of exhumation are sharply truncated by the Alpine fault. Rapid exhumation in the last 2 Ma, at rates of ~0.9-1.4 mm/yr, is also found in the Seaward Kaikōura range in both block and non-block models (See Figure 3.11), and in the restraining

bend of the Alpine-Wairau fault (1.2-1.7 mm/yr; Fig. 3.12). Exhumation in the Inland Kaikōura Range does differ depending on whether fault blocks are used. In both models without blocks, exhumation rates increase sharply in the last 2 Ma to ~0.5-0.7 mm/yr, but in models with blocks, the rates in the last 2 Ma are only 0.2-0.3 mm/yr, and do not show a sudden increase in the last 2 Ma (See Figure 3.13). The apparent increase in exhumation rate in the non-block model may not be a real phenomenon, but may appear because the Inland Kaikōura mountains are within the spatial correlation distance of other areas, such as the Seaward Kaikōura Mountains, which have younger thermochronology ages and faster exhumation rates.

The choice of $\dot{e}$ prior can affect exhumation rate results. When data is sparse at a location, that location tends to have an exhumation rate equal to $\dot{e}$ prior, particularly at the beginning of its "existence" in the model (the first few time steps after the thermochronometric age of that data). In subsequent time steps, $\dot{e}$ near that data may increase or decrease from $\dot{e}$ prior. In data-rich locations, $\dot{e}$ may differ between model runs with different $\dot{e}$ prior, but not systemically, e.g. when comparing model runs 1 ($\dot{e}$ prior = 0.5 mm/yr) and 2 ($\dot{e}$ prior = 0.1 mm/yr), exhumation rates at control points differ between runs, but are not always higher in run 1. Due to uncertainty in the selection of $\dot{e}$ prior, and the fact that the single $\dot{e}$ prior imposed across the whole model domain is likely to approximate the true prior exhumation rate in better in some areas than in others, we interpret a suite of model results rather than one single model.

In some parts of our field area, particularly the south and southeast, neither the non-block model nor the multi-block model may truly represent the relationship between exhumation histories at our sample sites. Some faults – for example, the Jordan thrust – do certainly exhibit dip-slip motion, and thus crustal blocks on either side experience different exhumation rates and histories. However, superimposed on that behavior is broader-scale contraction, which seems

based on recent research (Barnes et al., 1998; Hamling et al., 2017; Collett et al., 2019) to involve many possibly imbricated structures. In this way, crustal blocks on either side of a fault such as the Jordan thrust may have integrated exhumation histories involving some of the same forcings, and some differential forcings. Recovering the correct exhumation histories on each side of such a complicated fault zone would be achievable in our GLIDE block model if we had a great deal more data, with ages from many thermochronometers covering every time step – but as it is, drawing a hard boundary between blocks hampers our ability to glean relevant information from data that may have a partially similar history.

3.5 Discussion

Our results show that the eastern Awatere fault played a role in the Early Kaikōura Orogeny. We draw the boundary of this pattern of deformation at the fault's change in strike and the stepover between the eastern and Molesworth sections; our vertical transect just west of this junction, at Mt. Murphy, shows less and later exhumation than our samples in the eastern hanging wall. The onset of hanging-wall-focused exhumation is highly uncertain – between approximately 40 and 60 Ma, or even earlier – but it is clear that the total exhumation in the hanging wall has been greater than in the footwall. In the footwall of the eastern Awatere fault, exhumation started later, around 20-30 Ma. We interpret footwall exhumation to be caused by the inception of the proto-Clarence fault and the growth of the Inland Kaikōura mountains. At this time, footwall samples attained similar exhumation rates to hanging wall samples; both sides of the fault exhumed together.

Our finding here fits with the conceptual model of Collett et al. (2019). Their study made the interpretation that reverse faulting/hanging wall exhumation propagated toward the plate margin, with the proto-Clarence fault being active before the proto-Jordan. Our study adds an

earlier phase of the Early Kaikōura Orogeny, farther inboard from the plate margin. This timing of exhumation on the north side of the Awatere fault predates estimates of the Hikurangi subduction zone's extension southward toward our field area (King, 2000; Furlong and Kamp, 2009). It is possible that this exhumation reflects deformation in advance of subduction initiation at this part of the plate margin. After subduction reached the area, exhumation in the Inland and especially the Seaward Kaikōura ranges proceeded at a greater rate.

At Mt. Murphy and the Awatere fault segment stepover, the increase in exhumation rate around 8-13 Ma found in our QTQt models appears to be fault-controlled. However, because it also occurs at 17mfs25, on the opposite side of the fault, we do not tie this change to the inception of the modern Awatere fault. Instead, we suggest that exhumation increased sometime between 8-13 Ma due to the formation of the restraining bend of the Alpine-Wairau fault. As discussed in further detail in Chapter 2, the formation of the bend created a large area of high topography extending ~80 km along strike of the Wairau fault; in that chapter, our most distal evidence of the exhumation increase was at sample 15mfs07. In the area of Mt. Murphy, some of the associated convergence could have been accommodated through reverse motion on the western end of the eastern Awatere fault, or on an incipient western (Molesworth) section of the fault, which was at the time limited in extent.

We find that the western MFS was not involved in the broad-scale thrusting and range building of the Early Kaikōura Orogeny. Instead of large-scale block rotation, folding, and thrusting, this area was thought to have undergone distributed shear on many small crustal blocks beginning with or possibly slightly before the initiation of the Alpine fault at ~23 Ma, and ending with the initiation of the western MFS faults (Lamb, 1988; Hall et al., 2004; Lamb, 2011; Randall et al., 2011). We therefore suggest that our discontinuous pattern of ~20-25 Ma

exhumation initiation in the southwestern MFS is an amalgamation of local effects of this pattern. As the region was under transpression, patterns of exhumation that were discontinuous in space and time could have occurred due to the complex arrangement of block boundaries, which could have had differences in shape and alignment. Despite the fact that patterns of stress should have been changing as blocks rotated, ultimately driven by the rotating plate boundary to the north, our model results generally show unchanging exhumation rates to the present. It is reasonable for exhumation to continue, as the plate boundary has only become more convergent since ~10 Ma (Cande and Stock, 2004). We note that at most of these locations we do not have the temporal resolution (i.e. many chronometers covering the time since 10 Ma) to discern exhumation rate changes over this time.

Samples near to the Clarence River (15cla04 and 15cla06) show very rapid cooling (30-40°C/Ma) beginning 2-4 Ma; these samples reflect widespread exhumation of the Late Kaikōura Orogeny (Collett et al., 2019). Nearby sample 12mfs13 shows somewhat earlier and slower cooling. All of these samples are, broadly, in the hanging wall of the Kekerengu fault and near the locus of modern plate boundary deformation. The entire region experienced uplift during the 2016 Kaikōura earthquake, which ruptured the Kekerengu fault (Hamling et al., 2017). Other faults outboard of the Kekerengu may also be contributing to uplift in the region, including offshore thrust faults (Barnes et al., 1998; Collett et al., 2019). We conclude that the modeled thermal histories of these three samples all show a response to this relatively recent rock uplift, and that samples 15cla04 and 15cla06 show faster cooling rates because the large, incisive Clarence River may be responding to even greater, more recent uplift than the surrounding landscape has yet been able to.

The results of the GLIDE inversion show that the fastest rates of exhumation in our study area over the last 2-4 Ma are near the MFS faults' junctions with the Alpine fault; in the bend of the Alpine-Wairau fault; and in the Seaward Kaikōura mountains. These areas all have young thermochronology ages, and all host steep river channels (Figure 2.2). However, while exhumation rates are about twice as fast near the Alpine fault as in the Alpine-Wairau fault restraining bend, both elevations and stream channel steepness indices (k_{sn}) are lower in the former area (Figure 2.2). This pattern is unexpected, as steeper channels generally correlate with faster uplift rates, and there is no difference in rock type between the two regions that could account for the difference (Figure 1.3; e.g. Wobus et al., 2006). Both areas have a similar history of glaciation (Barrell, 2011). We suggest that the difference is caused by anisotropy of erodibility of the regional bedrock. In the restraining bend region, higher-order drainages generally follow the regional strike of the steeply-dipping bedrock, which is also the trend of pre-MFS faults in the region. Near the Alpine fault, drainages cut across this trend (Figure 2.2). Preexisting strength contrasts in the landscape, such as those caused by fractures, joints, or fault damage zones, can make fluvial or glacial incision much more efficient in some parts of the landscape (Roy et al., 2015, 2016). In the restraining bend, higher-order channels and glaciers have taken advantage of such strength contrasts and incised greatly, causing a pattern of less-steep main channels fed by many steep, orthogonal tributaries (Figure 2.2; Roy et al., 2015). In the Alpine fault area, rivers do not follow the pattern of the regional bedrock, incision has been more uniform across the landscape, and a pattern of overall lower, less dramatically bimodal k_{sn} has resulted (Figure 2.2).

3.6 CONCLUSIONS

We used apatite and zircon (U-Th)/He and apatite fission track thermochronology to examine patterns of exhumation across the Marlborough Fault System of New Zealand. We extended the capabilities of our dataset by modeling thermal histories of single locations using QTQt, and by inverting our entire dataset and legacy data for spatially correlated exhumation rates across the MFS over time. We found that the eastern Awatere fault experienced north-side-up differential exhumation in the early Eocene and perhaps as early as the late Paleocene, a finding that extends the timing and spatial extent of the Early Kaikōura Orogeny thrust faults. The western (Molesworth) segment of the Awatere fault was not involved in this deformation, but later accommodated increased plate boundary convergence around 8-13 Ma through increased exhumation in the (broadly-defined) Alpine-Wairau restraining bend area. In the west-central MFS, most sample sites experienced exhumation after 25 Ma, but timing and rate was highly spatially variable and was not controlled by the modern-day MFS faults. We interpret this pattern to a period of distributed shear on small, rotating crustal blocks, where local transpression could have occurred depending on orientations of individual block boundaries. In the last several million years, the most rapidly exhuming parts of our study area have been the southern MFS – both the southeast, with rates of ~1-1.5 mm/yr near areas that experienced uplift during the 2016 M_w 7.8 Kaikōura earthquake, and the southwest, with rates of ~3.0-3.5 mm/yr closer to the influence of the Alpine fault and the rapidly exhuming Southern Alps. This pattern is related to the southward migration of the majority of plate boundary motion over time, as well as to the obliquity of the Alpine fault to plate motion.

3.7 ACKNOWLEDGEMENTS

This work was made possible by support from the National Science Foundation (grants EAR-132859 and -1321735 to Duvall and Flowers, and -1126991 to Flowers). Harbert received research support from the Geological Society of American graduate student research grant and from the University of Washington department of earth and space sciences. Upton was supported by the New Zealand Ministry for Business Innovation and Employment (grant C05X1103). We thank Jim Metcalf at CU Boulder TRaIL lab for (U-Th-Sm)/He analyses. We gratefully acknowledge the New Zealand Department of Conservation, Ngāi Tahu Iwi, and the following landowners for sampling permission: Muller Sation, Ranui Station, Mt. Gladstone Station, Upcot Station, Stronvar, Christopher and Deborah Schollum, and Frank Prouting. We thank Sean LaHusen, Philip Schoettle-Greene, Jody Bourgeois, Jenny Knuth, and Grant South/Hidden Valleys Rafting Co. for field and sampling assistance, and Gabrielle Alampay for lab assistance.

Table 3.1. GLIDE model run inputs.

Run	**Blocks?**	**$\dot{e}_{pr}$, mm/yr**	**Time Step, Ma**	**Model Duration, Ma**	**Starting Geotherm, °C/km**	**Ending Geotherm, °C/km**	**Spatial Correlation Distance, km**
1	Yes	0.5	2	40	26	33	20
2	Yes	0.1	2	40	26	28	20
3	No	0.5	2	40	26	33	20
4	No	0.1	2	40	26	28	20

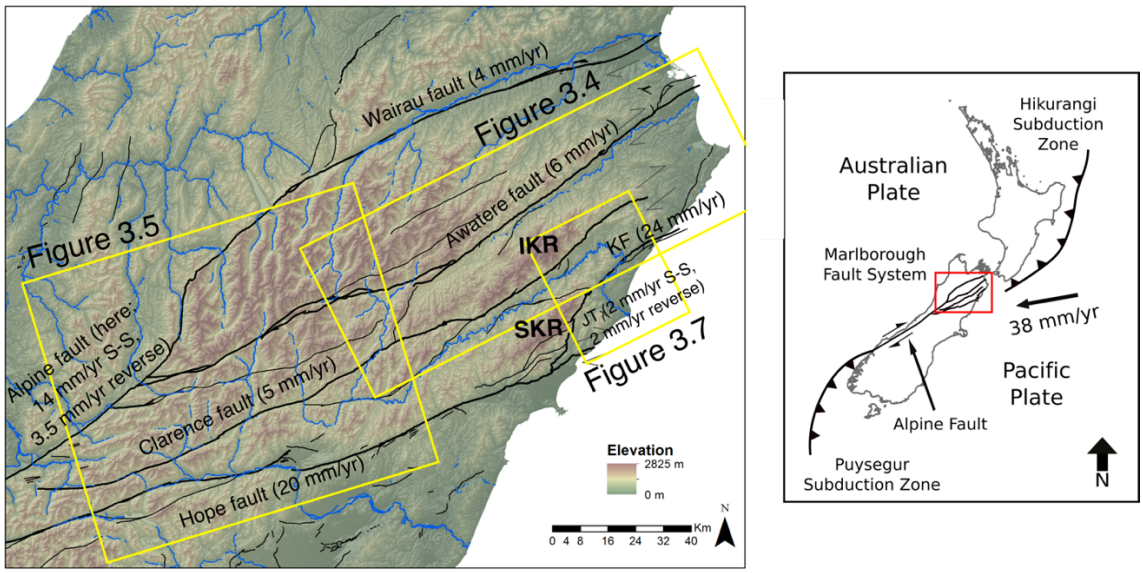

Figure 3.1. Marlborough Fault System, with locations of Figures 3.4, 3.5, and 3.7. IKR = Inland Kaikōura Range. JT = Jordan thrust. KF = Kekerengu fault. SKR = Seaward Kaikōura Range. Topography from 15m NZDEM SoS v1.0 (Columbus et al., 2011). Faults are Quaternary active faults from Nathan et al. (2002) and Rattenbury et al. (1998; 2006).

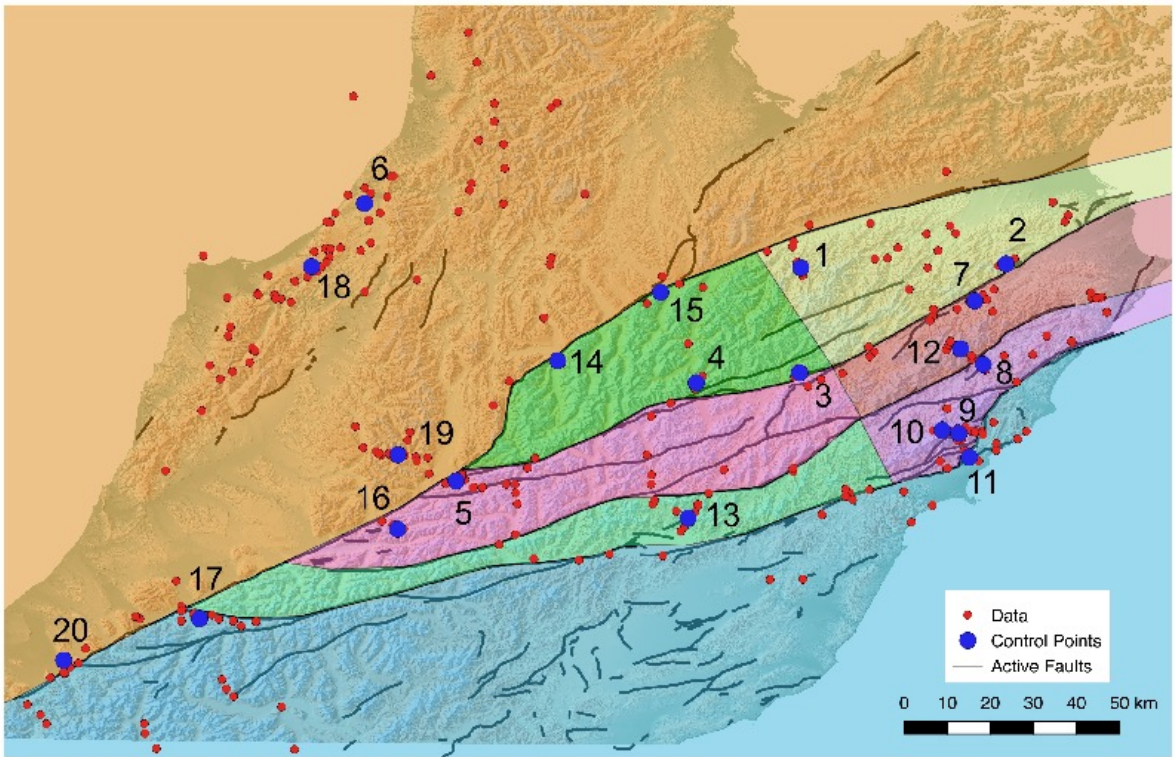

Figure 3.2. Map of GLIDE model inputs. Locations of thermochronology data (red) and output control points (blue) for GLIDE model. Output time-temperature paths for all control points are shown in Section 3.10.2. Also shown are block boundaries, used in model runs 1 and 2 but not in runs 3 and 4. Topography from 15m NZDEM SoS v1.0 (Columbus et al., 2011). Faults are Quaternary active faults from Nathan et al. (2002) and Rattenbury et al. (1998; 2006).

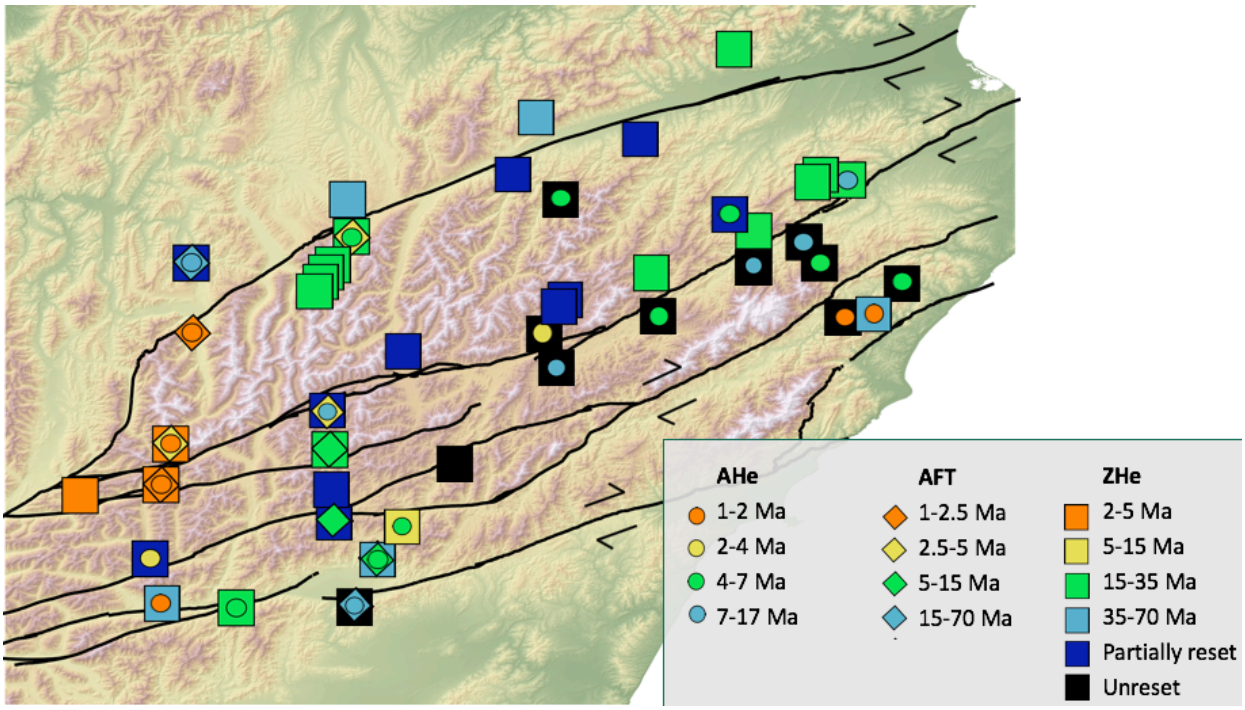

Figure 3.3. Low-temperature thermochronology ages. Topography from 15m NZDEM SoS v1.0 (Columbus et al., 2011). Faults are simplified from Quaternary active faults of Nathan et al. (2002) and Rattenbury et al. (1998; 2006).

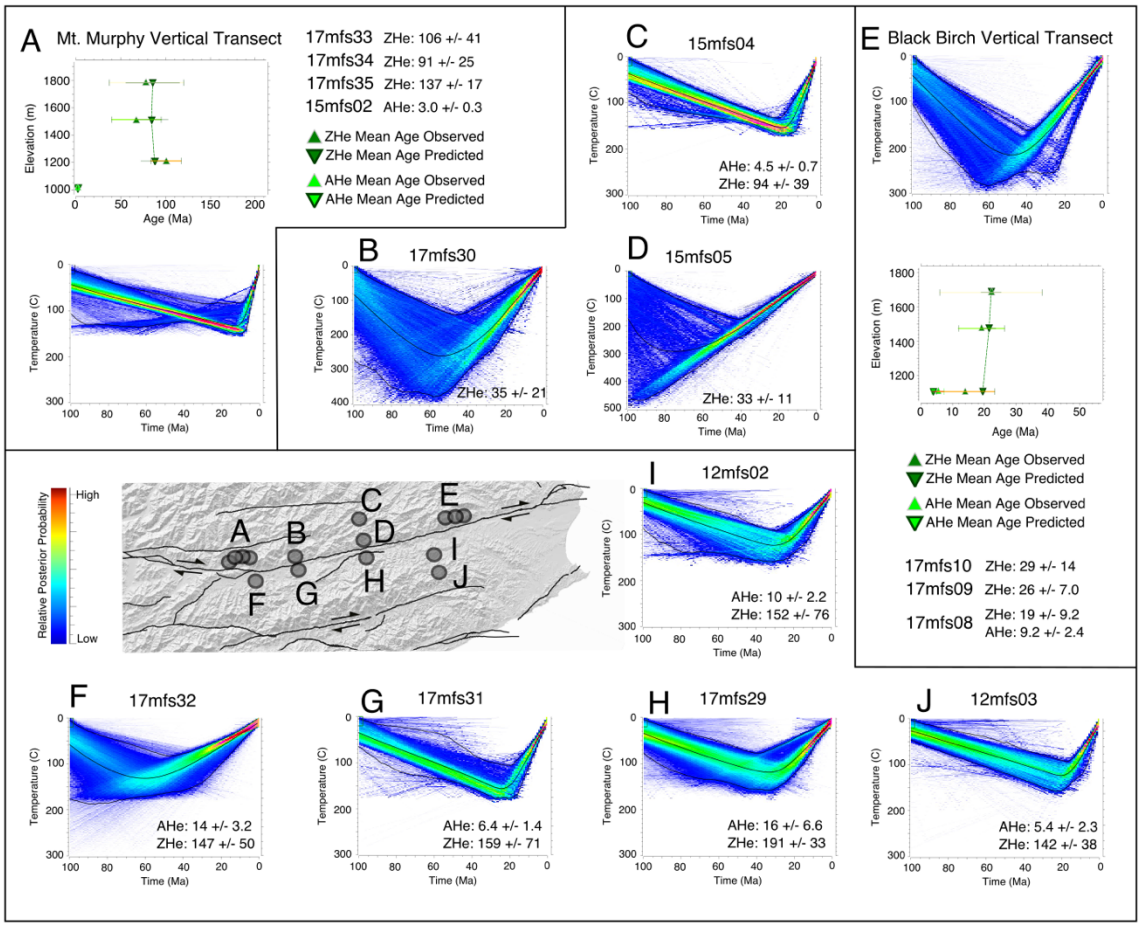

Figure 3.4. Awatere fault QTQt results. Modeled time-temperature histories for samples along the Awatere fault created using QTQt. Letters on map refer to time-temperature plots on this figure only. On each plot, black lines are the "expected" (weighted mean) path, with the 95% credible interval on either side. Topography from 15m NZDEM SoS v1.0 (Columbus et al., 2011).

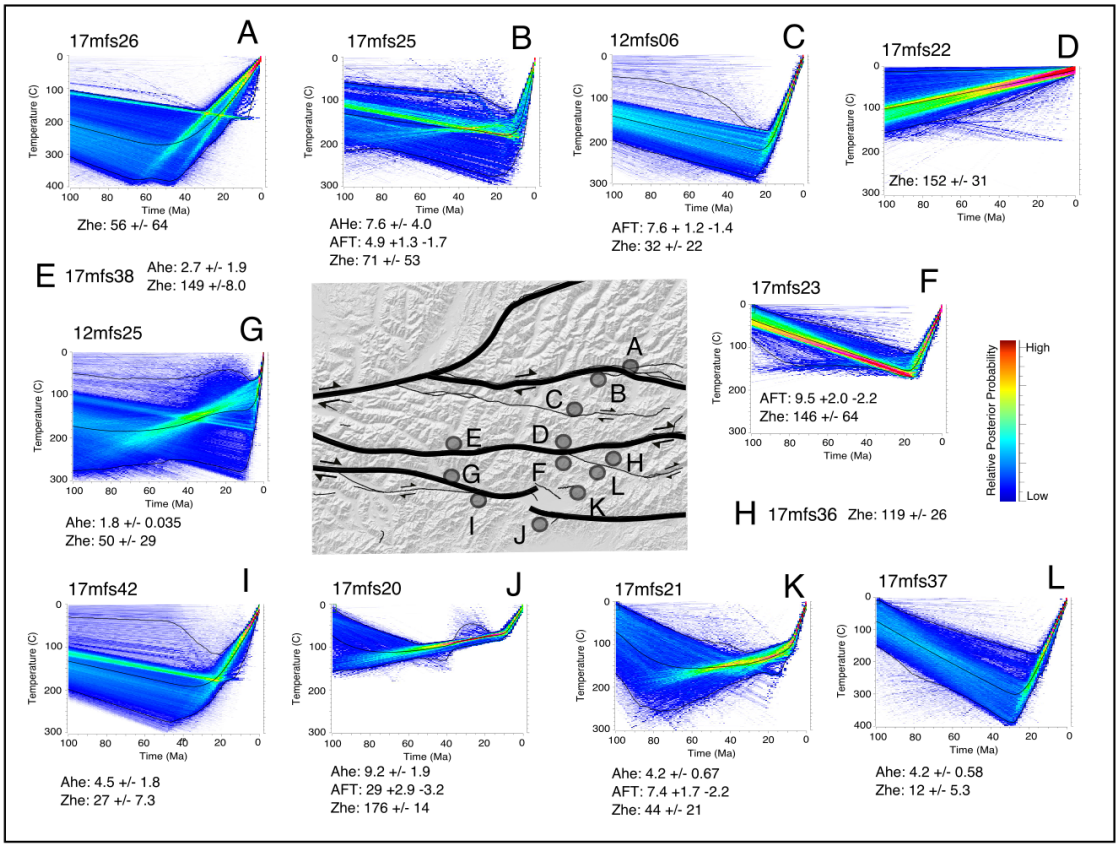

Figure 3.5. Central MFS QTQt results. Modeled time-temperature histories for samples along in the western MFS created using QTQt. Letters on map refer to time-temperature plots on this figure only. On each plot, black lines are the "expected" (weighted mean) path, with the 95% credible interval on either side. Topography from 15m NZDEM SoS v1.0 (Columbus et al., 2011).

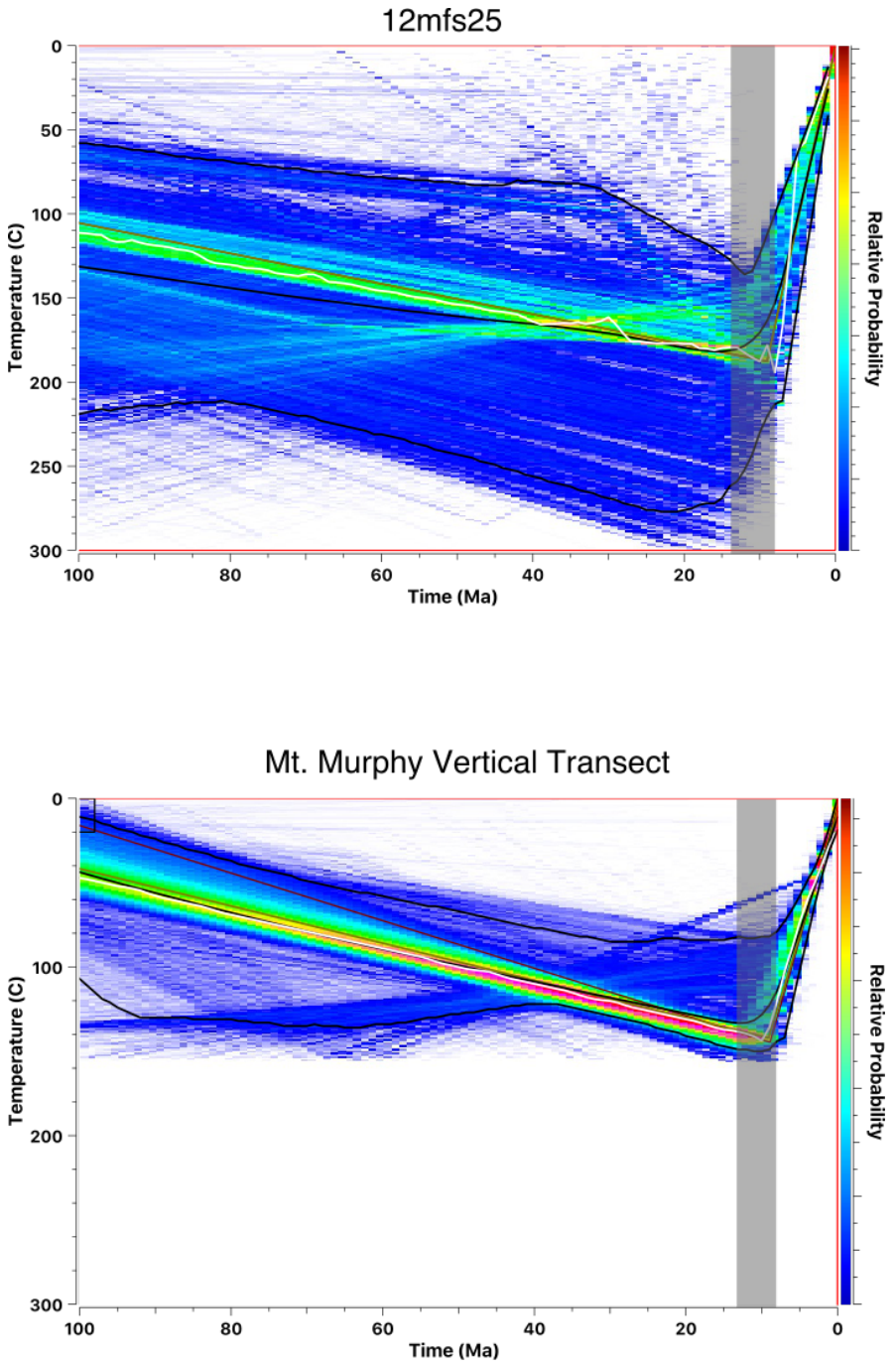

Figure 3.6. Comparison: 12mfs25 and Mt. Murphy vertical transect. Comparison of QTQt models from samples on the south side of the western Awatere fault (top) and on the north side of the central Awatere fault (bottom). Grey shaded bar shows timing of onset of exhumation.

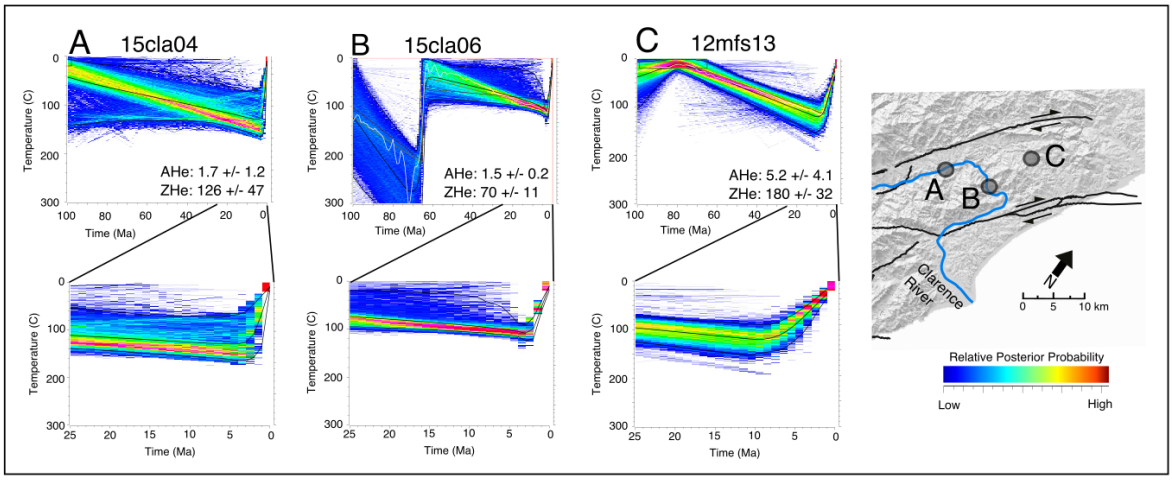

Figure 3.7. Southeastern MFS QTQt results. Modeled time-temperature histories for samples along in the southeastern field area, near the Clarence River, created using QTQt. Letters on map refer to time-temperature plots on this figure only. On each plot, black lines are the "expected" (weighted mean) path, with the 95% credible interval on either side. Bottom plots zoom in on last 25 Ma. Topography from 15m NZDEM SoS v1.0 (Columbus et al., 2011).

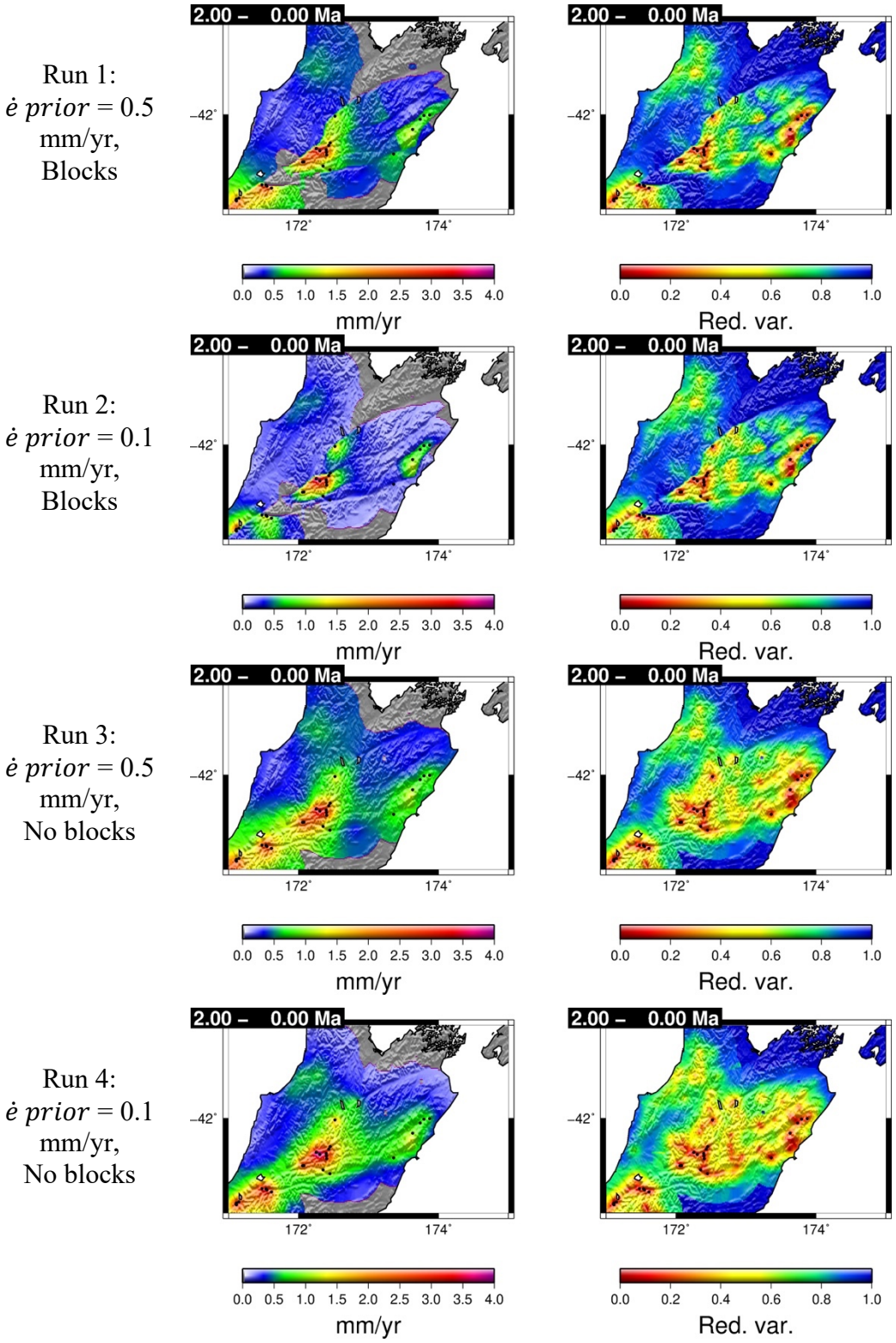

Figure 3.8. GLIDE results: 0-2 Ma. Maps of exhumation rate (left) and reduction in variance (left) for period of 0-2 Ma in each GLIDE model run. When variance is low, modeled exhumation rate is better constrained; when it is high, modeled exhumation rate is more likely to default to $\dot{e}\ prior$.

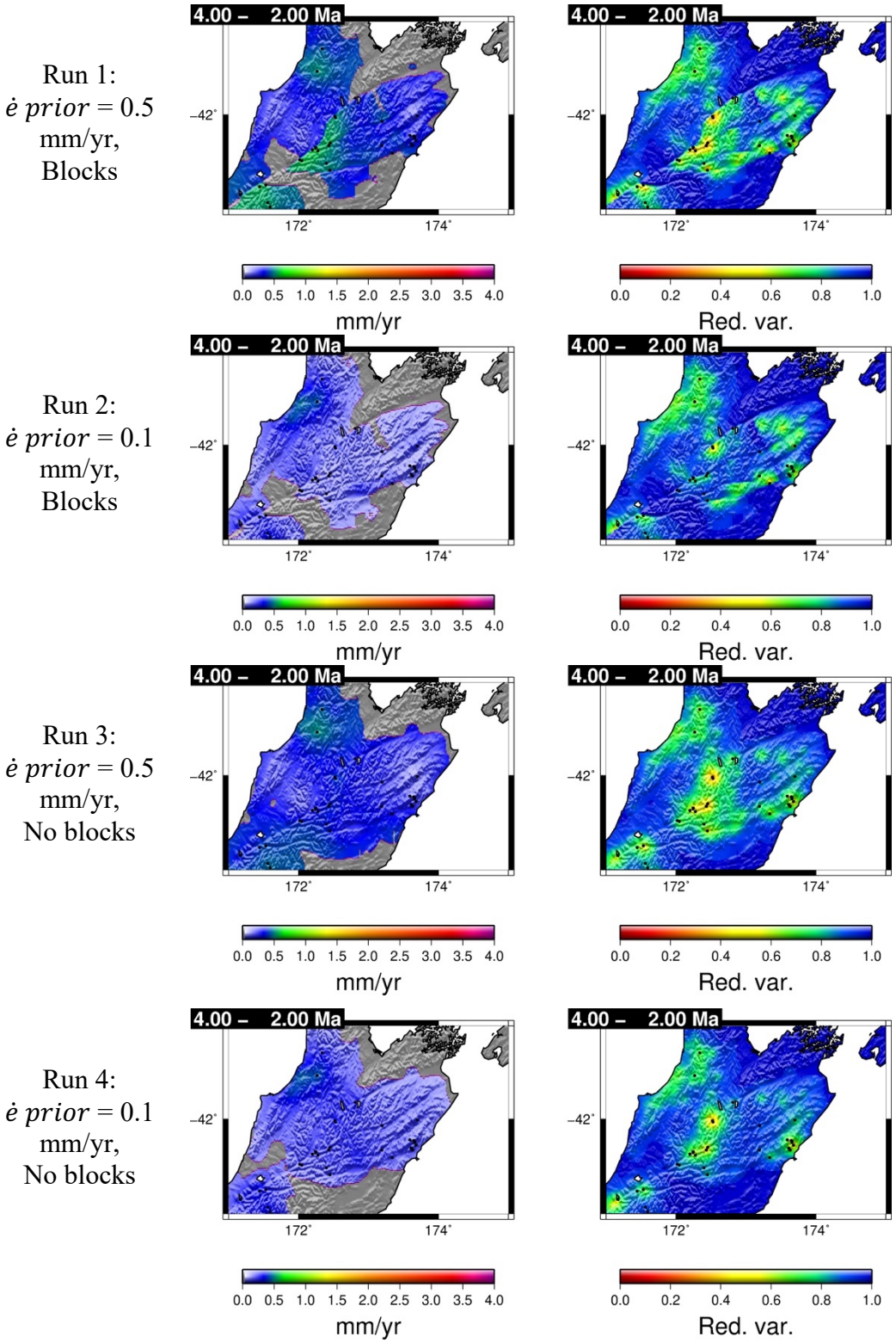

Figure 3.9. GLIDE results: 2-4 Ma. Maps of exhumation rate (left) and reduction in variance (left) for period of 2-4 Ma in each GLIDE model run. Note that exhumation rates are generally much lower (closer to $\dot{e}\ prior$) and variance is generally much higher in this time step than in 0-2 Ma time step.

Control Point #5

	$\dot{e}\ prior$ = 0.5 mm/yr	$\dot{e}\ prior$ = 0.1 mm/yr
Blocks	Run 1	Run 2
No Blocks	Run 3	Run 4

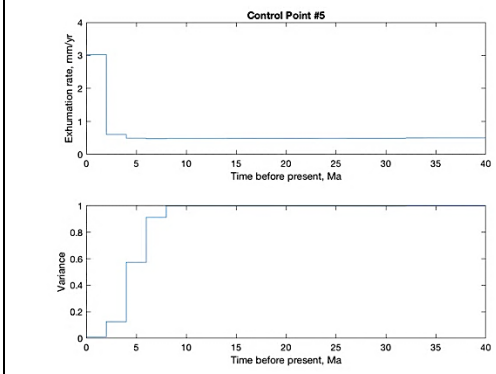

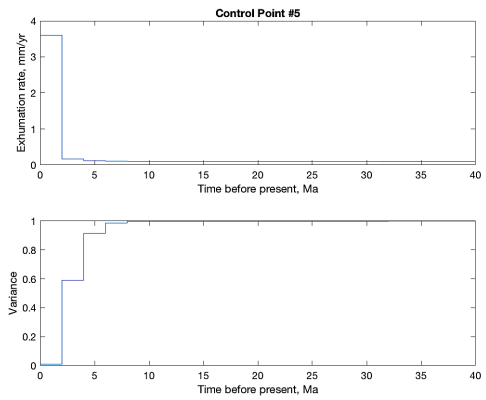

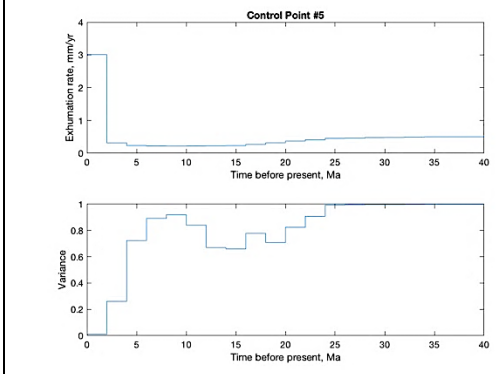

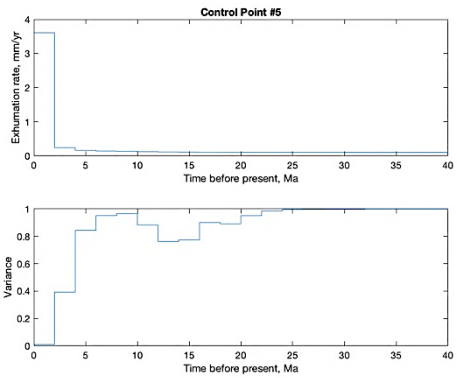

Figure 3.10. Time-temperature paths for control point #5. Time-temperature paths from GLIDE for control point 5, near the junction between the Alpine and Awatere faults. Top plot in each pair is modeled exhumation rate at each time step (time steps are 2 Ma long). Bottom plot in each pair is reduction in variance at each time step; the lower the variance, the better-constrained the exhumation rate at that time.

Control Point #10

	$\dot{e}$ *prior* = 0.5 mm/yr	$\dot{e}$ *prior* = 0.1 mm/yr
Blocks	Run 1	Run 2
No Blocks	Run 3	Run 4

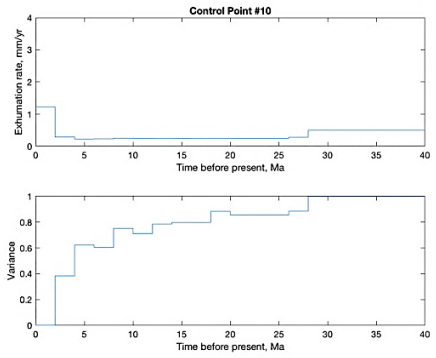

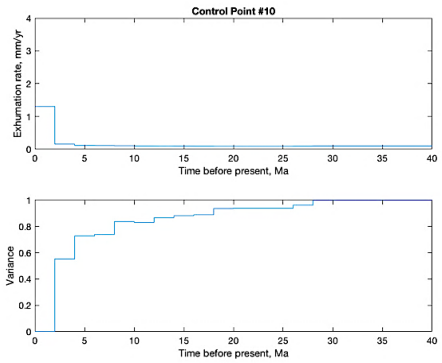

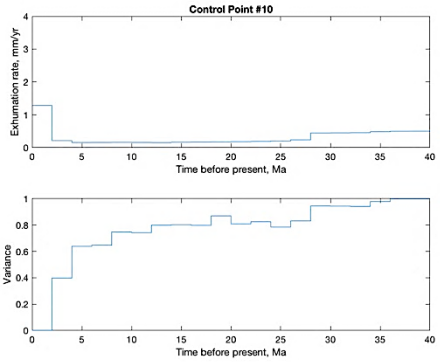

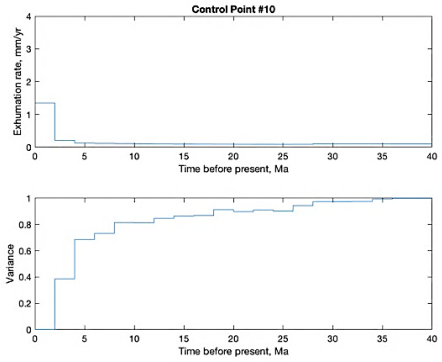

Figure 3.11. Time-temperature paths for control point #10. Time-temperature paths from GLIDE for control point 10, in the Seaward Kaikōura range. Top plot in each pair is modeled exhumation rate at each time step (time steps are 2 Ma long). Bottom plot in each pair is reduction in variance at each time step; the lower the variance, the better-constrained the exhumation rate at that time.

Control Point #14

	$\dot{e}\ prior$ = 0.5 mm/yr	$\dot{e}\ prior$ = 0.1 mm/yr
Blocks	Run 1	Run 2
No Blocks	Run 3	Run 4

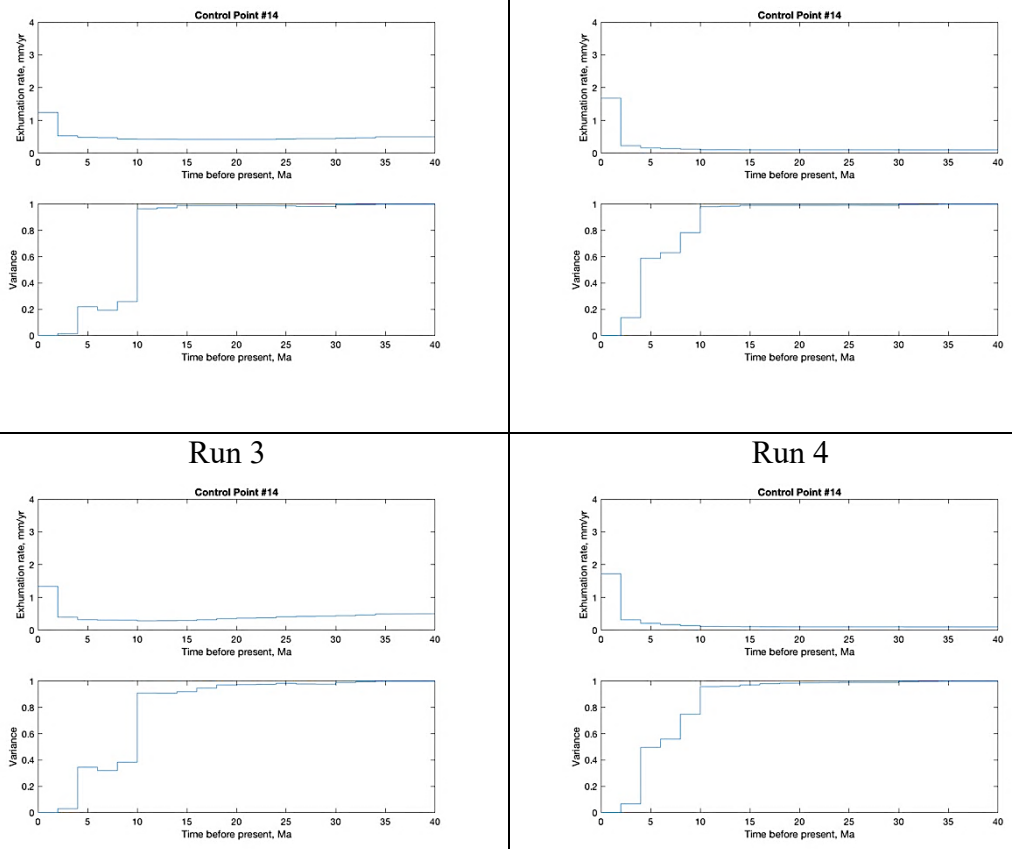

Figure 3.12. Time-temperature paths for control point #14. Time-temperature paths from GLIDE for control point 14, in the Alpine-Wairau fault restraining bend. Top plot in each pair is modeled exhumation rate at each time step (time steps are 2 Ma long). Bottom plot in each pair is reduction in variance at each time step; the lower the variance, the better-constrained the exhumation rate at that time.

Control Point #12

	$\dot{e}$ $prior$ = 0.5 mm/yr	$\dot{e}$ $prior$ = 0.1 mm/yr
Blocks	Run 1 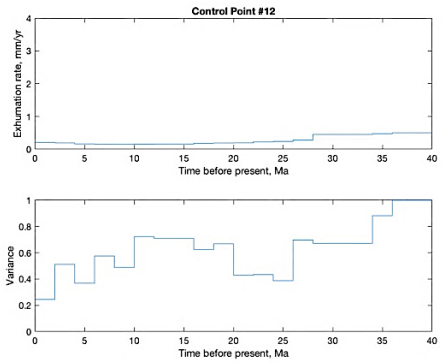	Run 2 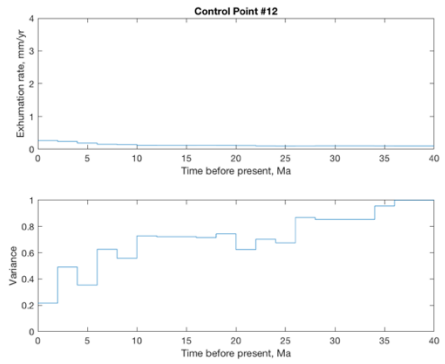
No Blocks	Run 3 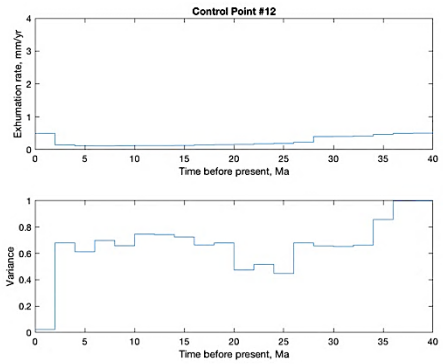	Run 4 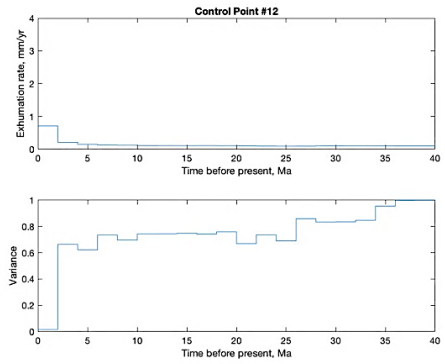

Figure 3.13. Time-temperature paths for control point #12. Time-temperature paths from GLIDE for control point 12, in the Inland Kaikōura range. Top plot in each pair is modeled exhumation rate at each time step (time steps are 2 Ma long). Bottom plot in each pair is reduction in variance at each time step; the lower the variance, the better-constrained the exhumation rate at that time.

3.8 CHAPTER 3 REFERENCES

Adams, C. J., & Graham, I. J. (1996). Metamorphic and tectonic geochronology of the Torlesse terrane, Wellington, New Zealand. *New Zealand Journal of Geology and Geophysics, 39*(2), 157-180.

Baker, J., & Seward, D. (1996). Timing of Cretaceous extension and Miocene compression in northeast South Island, New Zealand: Constraints from Rb-Sr and fission-track dating of an igneous pluton. *Tectonics*, *15*(5), 976-983.

Barnes, P. M., Lépinay, B. M., Collot, J. Y., Delteil, J., & Audru, J. C. (1998). Strain partitioning in the transition area between oblique subduction and continental collision, Hikurangi margin, New Zealand. *Tectonics, 17*(4), 534-557.

Barrell, D. J. A. (2011). Quaternary glaciers of New Zealand. *Developments in Quaternary Sciences, 15*, 1047-1064.

Batt, G. E., Baldwin, S. L., Cottam, M. A., Fitzgerald, P. G., Brandon, M. T., & Spell, T. L. (2004). Cenozoic plate boundary evolution in the South Island of New Zealand: New thermochronological constraints. *Tectonics, 23*(4).

Beanland, S. (1995). The North Island Dextral Fault Belt, Hikurangi Subduction Margin, New Zealand: A Thesis Submitted for the Degree of Doctor of Philosophy [in Geology], Victoria University of Wellington (Doctoral dissertation, Victoria University of Wellington).

Beavan, J., Tregoning, P., Bevis, M., Kato, T., & Meertens, C. (2002). Motion and rigidity of the Pacific Plate and implications for plate boundary deformation. *Journal of Geophysical Research: Solid Earth*, *107*(B10), ETG-19.

Benowitz, J. A., Layer, P. W., Armstrong, P., Perry, S. E., Haeussler, P. J., Fitzgerald, P. G., & VanLaningham, S. (2011). Spatial variations in focused exhumation along a continental-scale strike-slip fault: The Denali fault of the eastern Alaska Range. *Geosphere, 7*(2), 455-467.

Benson, A. M., Little, T. A., Van Dissen, R. J., Hill, N., & Townsend, D. B. (2001). Late Quaternary paleoseismic history and surface rupture characteristics of the eastern Awatere strike-slip fault, New Zealand. *Geological Society of America Bulletin*, *113*(8), 1079-1091.

Braun, J., Van Der Beek, P., & Batt, G. (2006). Quantitative thermochronology: Numerical methods for the interpretation of thermochronological data. Cambridge University Press.

Browne, G. H. (1992). The northeastern portion of the Clarence Fault: tectonic implications for the late Neogene evolution of Marlborough, New Zealand. *New ZealandJ Journal of Geology and Geophysics, 35*(4), 437-445.

Browne, G. H. (1995). Sedimentation patterns during the Neogene in Marlborough, New Zealand. *Journal of the Royal Society of New Zealand, 25*(4), 459-483.

Campbell, J. K., Pettinga, J. R., & Jongens, R. (2012). The tectonic and structural setting of the 4 September 2010 Darfield (Canterbury) earthquake sequence, New Zealand. *New Zealand Journal of Geology and Geophysics, 55*(3), 155-168.

Cande, S. C., & Stock, J. M. (2004). Pacific—Antarctic—Australia motion and the formation of the Macquarie Plate. *Geophysical Journal International, 157*(1), 399-414.

Carter, R. M., & Carter, L. (1982). The Motunau Fault and other structures at the southern edge of the Australian-Pacific plate boundary, offshore Marlborough, New Zealand. *Tectonophysics*, *88*(1-2), 133-159.

Colgan, J. P., Dumitru, T. A., Reiners, P. W., Wooden, J. L., & Miller, E. L. (2006). Cenozoic tectonic evolution of the Basin and Range Province in northwestern Nevada. *American Journal of Science*, *306*(8), 616-654.

Collett, C. M., Duvall, A. R., Flowers, R. M., Tucker, G. E., & Upton, P. (2019). The timing and style of oblique deformation within New Zealand's Kaikōura Ranges and Marlborough Fault System based on low-temperature thermochronology. *Tectonics*, *38*(4), 1250-1272.

Columbus, J., Sirguey, P., & Tenzer, R. (2011). A free, fully assessed 15-m DEM for New Zealand. *Survey Quarterly* 66, 16-19.

Cooper, A. F., Barreiro, B. A., Kimbrough, D. L., & Mattinson, J. M. (1987). Lamprophyre dike intrusion and the age of the Alpine fault, New Zealand. *Geology*, *15*(10), 941-944.

Cowan, H., Nicol, A., & Tonkin, P. (1996). A comparison of historical and paleoseismicity in a newly formed fault zone and a mature fault zone, North Canterbury, New Zealand. *Journal of Geophysical Research: Solid Earth, 101*(B3), 6021-6036.

Crampton, J. S., Laird, M., Nicol, A., Hollis, C. J., & Van Dissen, R. J. (1998). Geology at the northern end of the Clarence Valley, Marlborough; a complete record spanning the Rangitata to Kaikoura orogenies. In *Geological Society of New Zealand, New Zealand Geophysical Society 1998 Joint Annual Conference* (Vol. 30).

Davy, B., Hoernle, K., & Werner, R. (2008). Hikurangi Plateau: Crustal structure, rifted formation, and Gondwana subduction history. *Geochemistry, Geophysics, Geosystems, 9*(7).

DeMets, C., Gordon, R. G., Argus, D. F., & Stein, S. (1994). Effect of recent revisions to the geomagnetic reversal time scale on estimates of current plate motions. *Geophysical Research Letters, 21*(20), 2191-2194.

DeMets, C., Gordon, R. G., & Argus, D. F. (2010). Geologically current plate motions. *Geophysical Journal International, 181*(1), 1-80.

Dokka, R. K., Mahaffie, M. J., & Snoke, A. W. (1986). Thermochronologic evidence of major tectonic denudation associated with detachment faulting, northern Ruby Mountains-East Humboldt Range, Nevada. *Tectonics*, *5*(7), 995-1006.

Donelick, R. A., & Miller, D. S. (1991). Enhanced TINT fission track densities in low spontaneous track density apatites using 252Cf-derived fission fragment tracks: A model and experimental observations. *International Journal of Radiation Applications and Instrumentation. Part D. Nuclear Tracks and Radiation Measurements, 18*(3), 301-307.

Donelick, R. A., Ketcham, R. A., & Carlson, W. D. (1999). Variability of apatite fission-track annealing kinetics: II. Crystallographic orientation effects. *American Mineralogist, 84*(9), 1224-1234.

Duvall, A. R., Clark, M. K., Kirby, E., Farley, K. A., Craddock, W. H., Li, C., & Yuan, D. Y. (2013). Low-temperature thermochronometry along the Kunlun and Haiyuan Faults, NE Tibetan Plateau: Evidence for kinematic change during late-stage orogenesis. *Tectonics*, *32*(5), 1190-1211.

Duvall, A.R., Harbert, S.A., Upton, P., Tucker, G.E., Flowers, R.M., & Collett, C. (2019). River patterns reveal landscape evolution at the edge of subduction, Marlborough Fault System, New Zealand. Manuscript submitted for publication.

Eberhart-Phillips, D., & Bannister, S. (2010). 3-D imaging of Marlborough, New Zealand, subducted plate and strike-slip fault systems. *Geophysical Journal International*, *182*(1), 73-96.

Fitzgerald, P. G., Sorkhabi, R. B., Redfield, T. F., & Stump, E. (1995). Uplift and denudation of the central Alaska Range: A case study in the use of apatite fission track thermochronology to determine absolute uplift parameters. *Journal of Geophysical Research: Solid Earth*, *100*(B10), 20175-20191.

Flowers, R. M., Ketcham, R. A., Shuster, D. L., & Farley, K. A. (2009). Apatite (U–Th)/He thermochronometry using a radiation damage accumulation and annealing model. *Geochimica et Cosmochimica Acta*, *73*(8), 2347-2365.

Fox, M., Herman, F., Willett, S. D., & May, D. A. (2014). A linear inversion method to infer exhumation rates in space and time from thermochronometric data. *Earth Surface Dynamics*, *2*(1), 47.

Fox, M., Dai, J. G., & Carter, A. (2019). Badly behaved detrital (U-Th)/He ages: Problems with He diffusion models or geological models? *Geochemistry, Geophysics, Geosystems, 20*, 2418-2432.

Furlong, K. P., & Kamp, P. J. (2009). The lithospheric geodynamics of plate boundary transpression in New Zealand: Initiating and emplacing subduction along the Hikurangi margin, and the tectonic evolution of the Alpine Fault system. *Tectonophysics*, *474*(3-4), 449-462.

Furlong, K. P., & Kamp, P. J. (2013). Changes in plate boundary kinematics: Punctuated or smoothly varying—Evidence from the Mid-Cenozoic transition from lithospheric extension to shortening in New Zealand. *Tectonophysics, 608*, 1328-1342.

Ketcham, R. A., Carter, A., Donelick, R. A., Barbarand, J., & Hurford, A. J. (2007). Improved modeling of fission-track annealing in apatite. *American Mineralogist, 92*(5-6), 799-810.

Gallagher, K. (2012). Transdimensional inverse thermal history modeling for quantitative thermochronology. *Journal of Geophysical Research: Solid Earth, 117*(B2).

The GEBCO_08 Grid, version 20100927, http://www.gebco.net.

Gleadow, A. J. W., Duddy, I. R., Green, P. F., & Lovering, J. F. (1986). Confined fission track lengths in apatite: a diagnostic tool for thermal history analysis. *Contributions to Mineralogy and Petrology, 94*(4), 405-415.

Green, P. F., Duddy, I. R., Laslett, G. M., Hegarty, K. A., Gleadow, A. W., & Lovering, J. F. (1989). Thermal annealing of fission tracks in apatite 4. Quantitative modelling techniques and extension to geological timescales. *Chemical Geology: Isotope Geoscience Section, 79*(2), 155-182.

Guenthner, W. R., Reiners, P. W., Ketcham, R. A., Nasdala, L., & Giester, G. (2013). Helium diffusion in natural zircon: Radiation damage, anisotropy, and the interpretation of zircon (U-Th)/He thermochronology. *American Journal of Science*, *313*(3), 145-198.

Hamling, I. J., Hreinsdóttir, S., Clark, K., Elliott, J., Liang, C., Fielding, E., Litchfield, N., Villamor, P., Wallace, L., Wright, T.J., D'Anastasio, E., Bannister, S., Burbidge, D., Denys, P., Gentle, P., Howarth, J., Mueller, C., Palmer, N., Pearson, C., Power, W., Barnes, P., Barrell, D.J.A., Van Dissen, R., Langridge, R., Little, T., Nicol, A., Pettinga, J., Rowland, J., & Stirling, M. (2017). Complex multifault rupture during the 2016 M w 7.8 Kaikōura earthquake, New Zealand. *Science, 356*(6334), eaam7194.

Hall, L. S., Lamb, S. H., & Mac Niocaill, C. (2004). Cenozoic distributed rotational deformation, South Island, New Zealand. *Tectonics, 23*(2).

Hasebe, N., Tamura, A., & Arai, S. (2013). Zeta equivalent fission-track dating using LA-ICP-MS and examples with simultaneous U–P b dating. *Island Arc, 22*(3), 280-291.

Jiao, R., Herman, F., & Seward, D. (2017). Late Cenozoic exhumation model of New Zealand: Impacts from tectonics and climate. *Earth-Science Reviews, 166*, 286-298.

Kamp, P. J. (1986). The mid-Cenozoic Challenger Rift System of western New Zealand and its implications for the age of Alpine fault inception. *Geological Society of America Bulletin*, *97*(3), 255-281.

Kamp, P. J. J. (1987). Age and origin of the New Zealand orocline in relation to Alpine Fault movement. *Journal of the Geological Society*, *144*(4), 641-652.

Kamp, P. J., Webster, K. S., & Nathan, S. (1996). Thermal history analysis by integrated modelling of apatite fission track and vitrinite reflectance data: Application to an inverted basin (Buller Coalfield, New Zealand). *Basin Research, 8*(4), 383-402.

Kao, Ming-Hung. (2002). Thermo-tectonic implications of zircon and apatite FT data of the Marlborough Region, South Island, New Zealand. *Terrestrial, Atmospheric and Oceanic Sciences, 13*(2), 109-124.

Ketcham, R. A., Donelick, R. A., & Carlson, W. D. (1999). Variability of apatite fission-track annealing kinetics: III. Extrapolation to geological time scales. *American Mineralogist, 84*(9), 1235-1255.

Ketcham, R. A. (2005). The role of crystallographic angle in characterizing and modeling apatite fission-track length data. *Radiation Measurements, 39*(6), 595-601.

Ketcham, R. A., Carter, A., Donelick, R. A., Barbarand, J., & Hurford, A. J. (2007). Improved modeling of fission-track annealing in apatite. *American Mineralogist, 92*(5-6), 799-810.

Ketcham, R. A., Gautheron, C., & Tassan-Got, L. (2011). Accounting for long alpha-particle stopping distances in (U–Th–Sm)/He geochronology: Refinement of the baseline case. *Geochimica et Cosmochimica Acta, 75*(24), 7779-7791.

Kimbrough, D. L., Tulloch, A. J., Coombs, D. S., Landis, C. A., Johnston, M. R., & Mattinson, J. M. (1994). Uranium-lead zircon ages from the Median Tectonic Zone, New Zealand. *New Zealand Journal of Geology and Geophysics, 37*(4), 393-419.

King, P. R. (2000). Tectonic reconstructions of New Zealand: 40 Ma to the present. *New Zealand Journal of Geology and Geophysics*, *43*(4), 611-638.

Laird, M. G., & Bradshaw, J. D. (2004). The break-up of a long-term relationship: The Cretaceous separation of New Zealand from Gondwana. *Gondwana Research, 7*(1), 273-286.

Lamb, S. H. (1988). Tectonic rotations about vertical axes during the last 4 Ma in part of the New Zealand plate-boundary zone. *Journal of Structural Geology, 10*(8), 875-893.

Lamb, S. H., & Bibby, H. M. (1989). The last 25 Ma of rotational deformation in part of the New Zealand plate-boundary zone. *Journal of Structural Geology, 11*(4), 473-492.

Lamb, S. (2011). Cenozoic tectonic evolution of the New Zealand plate-boundary zone: A paleomagnetic perspective. *Tectonophysics*, *509*(3-4), 135-164.

Langridge, R., Campbell, J., Hill, N., Pere, V., Pope, J., Pettinga, J., Estrada, B., & Berryman, K. (2003). Paleoseismology and slip rate of the Conway Segment of the Hope Fault at Greenburn Stream, South Island, New Zealand. *Annals of Geophysics, 46*(5), 1119-1139.

Lee, J. K., Williams, I. S., & Ellis, D. J. (1997). Pb, U and Th diffusion in natural zircon. *Nature*, *390*(6656), 159.

Lewis, D. W., Laird, M. G., & Powell, R. D. (1980). Debris flow deposits of early Miocene age, Deadman stream, Marlborough, New Zealand. *Sedimentary Geology*, *27*(2), 83-118.

Lewis, D. W. (1992). Anatomy of an unconformity on mid-Oligocene Amuri Limestone, Canterbury, New Zealand. *New Zealand Journal of Geology and Geophysics, 35*(4), 463-475.

Litchfield, N. J., Van Dissen, R., Sutherland, R., Barnes, P. M., Cox, S. C., Norris, R., ... & Stirling, M. (2014). A model of active faulting in New Zealand. *New Zealand Journal of Geology and Geophysics, 57*(1), 32-56.

Little, T. A., & Jones, A. (1998). Seven million years of strike-slip and related off-fault deformation, northeastern Marlborough fault system, South Island, New Zealand. *Tectonics, 17*(2), 285-302.

Little, T. A., Mortimer, N., & McWilliams, M. (1999). An episodic Cretaceous cooling model for the Otago-Marlborough Schist, New Zealand, based on 40Ar/39Ar white mica ages. *New Zealand Journal of Geology and Geophysics, 42*(3), 305-325.

Little, T. A., & Roberts, A. P. (1997). Distribution and mechanism of Neogene to present-day vertical axis rotations, Pacific-Australian plate boundary zone, South Island, New Zealand. *Journal of Geophysical Research: Solid Earth, 102*(B9), 20447-20468.

MacKinnon, T. C. (1983). Origin of the Torlesse terrane and coeval rocks, South Island, New Zealand. *Geological Society of America Bulletin, 94*(8), 967-985.

McCalpin, J. P. (1996). Tectonic geomorphology and Holocene paleoseismicity of the Molesworth section of the Awatere fault, South Island, New Zealand. *New Zealand Journal of Geology and Geophysics, 39*(1), 33-50.

Mitchell, S. G., & Reiners, P. W. (2003). Influence of wildfires on apatite and zircon (U-Th)/He ages. *Geology*, *31*(12), 1025-1028.

Mortimer, N. (2004). New Zealand's geological foundations. *Gondwana Research, 7*(1), 261-272.

Nathan, S.; Rattenbury, M.S.; Suggate, R.P. (compilers) (2002). Geology of the Greymouth area: scale 1:250,000. Lower Hutt: Institute of Geological & Nuclear Sciences. Institute of Geological & Nuclear Sciences 1:250,000 geological map 12. 58 p. + 1 sheet.

Nicol, A., & Van Dissen, R. (2002). Up-dip partitioning of displacement components on the oblique-slip Clarence Fault, New Zealand. *Journal of Structural Geology, 24*(9), 1521-1535.

Rait, G., Chanier, F., & Waters, D. W. (1991). Landward-and seaward-directed thrusting accompanying the onset of subduction beneath New Zealand. *Geology*, *19*(3), 230-233.

Randall, K., Lamb, S., & Mac Niocaill, C. (2011). Large tectonic rotations in a wide zone of Neogene distributed dextral shear, northeastern South Island, New Zealand. *Tectonophysics, 509*(3-4), 165-180.

Rattenbury, M.S.; Cooper, R.A.; Johnston, M.R. (compilers) (1998). Geology of the Nelson area: scale 1:250,000. Lower Hutt: Institute of Geological & Nuclear Sciences Limited. Institute of Geological & Nuclear Sciences 1:250,000 geological map 9. 67 p. + 1 sheet.

Rattenbury, M. S., Townsend, D. B., and Johnston, M. R. (compilers), (2006). Geology of the Kaikoura area. Lower Hutt: Institute of Geological and Nuclear Sciences Limited. 1:250000 geological map 13. 70 p. + 1 sheet.

Rogers, G. M., Walker, S., Basher, L. M., & Lee, W. G. (2007). Frequency and impact of Holocene fire in eastern South Island, New Zealand. *New Zealand Journal of Ecology, (31)*2, 129-142.

Ross, S. M. (2003). Peirce's criterion for the elimination of suspect experimental data. *Journal of Engineering Technology, 20*(2), 38-41.

Roy, S. G., Koons, P. O., Upton, P., & Tucker, G. E. (2015). The influence of crustal strength fields on the patterns and rates of fluvial incision. *Journal of Geophysical Research: Earth Surface*, *120*(2), 275-299.

Roy, S. G., Koons, P. O., Osti, B., Upton, P., & Tucker, G. E. (2016). Multi-scale characterization of topographic anisotropy. *Computers & Geosciences, 90*, 102-116.

Silberling, N. J., Nichols, K. M., Bradshaw, J. D., & Blome, C. D. (1988). Limestone and chert in tectonic blocks from the Esk Head subterrane, South Island, New Zealand. *Geological Society of America Bulletin, 100*(8), 1213-1223.

Strogen, D. P., Seebeck, H., Nicol, A., & King, P. R. (2017). Two-phase Cretaceous–Paleocene rifting in the Taranaki Basin region, New Zealand; implications for Gondwana break-up. *Journal of the Geological Society, 174*(5), 929-946.

Sutherland, R., Collot, J., Bache, F., Henrys, S., Barker, D., Browne, G. H., Lawrence, M.F.J., Morgans, H.E.G., Hollis, C.J., Clowes, C., Mortimer, N., Rouillard, P., Gurnis, M., Etienne, S., & Stratford, W. (2017). Widespread compression associated with Eocene Tonga-Kermadec subduction initiation. *Geology, 45*(4), 355-358.

Tagami, T., Lal, N., Sorkhabi, R. B., & Nishimura, S. (1988). Fission track thermochronologic analysis of the Ryoke belt and the Median Tectonic Line, Southwest Japan. *Journal of Geophysical Research: Solid Earth*, *93*(B11), 13705-13715.

Tippett, J. M., & Kamp, P. J. (1993). Fission track analysis of the late Cenozoic vertical kinematics of continental Pacific crust, South Island, New Zealand. *Journal of Geophysical Research: Solid Earth, 98*(B9), 16119-16148.

Townsend, D. B. (2001). Neogene evolution of the Pacific-Australia plate boundary zone in NE Marlborough, South Island, New Zealand. (Doctoral dissertation, Victoria University of Wellington).

University of Otago – National School of Surveying. (2011). NZ_SoS_DEM v1.0. University of Otago – National School of Surveying.

Van Dissen, R., & Yeats, R. S. (1991). Hope fault, Jordan thrust, and uplift of the seaward Kaikoura Range, New Zealand. *Geology*, *19*(4), 393-396.

Vickery, S., & Lamb, S. (1995). Large tectonic rotations since the Early Miocene in a convergent plate-boundary zone, South Island, New Zealand. *Earth and Planetary Science Letters*, *136*(1-2), 43-59.

Walcott, R. I. (1987). Geodetic strain and the deformational history of the North Island of New Zealand during the late Cainozoic. Philosophical Transactions of the Royal Society of London. *Series A, Mathematical and Physical Sciences, 321*(1557), 163-181.

Walcott, R. I. (1998). Modes of oblique compression: Late Cenozoic tectonics of the South Island of New Zealand. *Reviews of Geophysics, 36*(1), 1-26.

Wallace, L. M., Beavan, J., McCaffrey, R., Berryman, K., & Denys, P. (2007). Balancing the plate motion budget in the South Island, New Zealand using GPS, geological and seismological data. *Geophysical Journal International*, *168*(1), 332-352.

Wallace, L. M., Barnes, P., Beavan, J., Van Dissen, R., Litchfield, N., Mountjoy, J., Langridge, R., Lamarche, G., & Pondard, N. (2012). The kinematics of a transition from subduction to strike-slip: An example from the central New Zealand plate boundary. *Journal of Geophysical Research: Solid Earth*, *117*(B2), B02405.

Wobus, C., Whipple, K. X., Kirby, E., Snyder, N., Johnson, J., Spyropolou, K., Crosby, B., & Sheehan, D. (2006). Tectonics from topography: Procedures, promise, and pitfalls. *Geological Society of America Special Papers*, *398*, 55-74.

Wood, R. A., Pettinga, J. R., Bannister, S., Lamarche, G., & McMorran, T. J. (1994). Structure of the Hanmer strike-slip basin, Hope fault, New Zealand. *Geological Society of America Bulletin, 106*(11), 1459-1473.

Zachariasen, J., Berryman, K., Langridge, R., Prentice, C., Rymer, M., Stirling, M., & Villamor, P. (2006). Timing of late Holocene surface rupture of the Wairau fault, Marlborough, New Zealand. *New Zealand Journal of Geology and Geophysics, 49*(1), 159-174.

3.9 SUPPLEMENTARY TABLES

3.9.1 *Thermochronology Sample Locations*

Table 3.2. Thermochronology samples for Chapter 3.

Thermochronology Samples from Marlborough Fault System

Sample	Lithology	Longitude	Latitude	Elevation (m)	# AHe	# ZHe	# AFT
Black Birch Vertical Transect							
17mfs08	Pahau greywacke	173.8220	-41.7325	1104	3	3	-
17mfs09	Pahau greywacke	173.7950	-41.7458	1474	-	3	-
17mfs10	Pahau greywacke	173.7758	-41.7533	1685	-	3	-
Mt. Murphy Vertical Transect							
15mfs02	Pahau greywacke	173.1934	-42.0698	1016	4	-	-
17mfs33	Pahau greywacke	173.2196	-42.0496	1784	-	3	-
17mfs34	Pahau greywacke	173.2039	-42.0488	1513	-	3	-
17mfs35	Pahau greywacke	173.1971	-42.0570	1211	-	3	-
Other Samples							
12mfs02	Pahau greywacke	173.7433	-41.8494	480	5	3	-
12mfs03	Pahau greywacke	173.7604	-41.8842	851	5	3	-
12mfs06	Esk Head greywacke	172.7729	-42.2923	997	-	3	40
12mfs13	Burnt Creek Fm. conglomerate	173.9145	-41.9528	469	4	3	-
12mfs25	Esk Head greywacke	172.4497	-42.5884	446	3	3	-
15cla04	Pahau greywacke	173.7925	-42.0101	243	4	3	-
15cla06	Pahau greywacke	173.8741	-42.0056	163	5	3	-
15mfs04	Pahau greywacke	173.5209	-41.8204	948	4	3	-
15mfs05	Pahau greywacke	173.5907	-41.8772	901	-	3	-
17mfs20	Pahau conglomerate	172.8184	-42.5797	501	5	3	39
17mfs21	Pahau greywacke	172.8696	-42.5100	491	5	3	39
17mfs22	Esk Head greywacke	172.7844	-42.3757	1009	-	3	-
17mfs23	Pahau greywacke	172.7895	-42.4324	986	-	3	38
17mfs25	Esk Head greywacke	172.7849	-42.1822	1218	4	3	40
17mfs26	Esk Head greywacke	172.9094	-42.1032	975	-	3	-
17mfs29	Pahau greywacke	173.5808	-41.9101	536	4	3	-
17mfs30	Pahau greywacke	173.4051	-41.9843	837	-	3	-
17mfs31	Pahau siltstone	173.4087	-42.0126	755	4	3	-
17mfs32	Pahau greywacke	173.2328	-42.0966	963	4	3	-
17mfs36	Pahau greywacke	172.9924	-42.3343	758	-	3	-
17mfs37	Pahau siltstone	172.9189	-42.4333	746	5	3	-

17mfs38	Rakaia greywacke	172.3974	-42.5196	598	3	3	-
17mfs42	Pahau greywacke	172.5783	-42.5917	421	5	3	-

3.9.2 *Thermochronology Data*

Table 3.3. Apatite (U-Th)/He data.

Sample	Grain	Mass (µg)	r[a] (µm)	T[b]	He (nmol/g)	U (ppm)	Th (ppm)	Sm (ppm)	eU[c] (ppm)	Th/U	Raw Date (Ma)	Ft[d]	Date (Ma)	2σ[e] (Ma)
12mfs02														
Pahau Subterrane (Torlesse Supergroup), Deposition 120 ± 22 Ma														
	a	0.67	32.1	0	6.26	201.0	219.2	79.38	253	1.09	4.58	0.58	7.94	0.36
	b	1.55	41.6	1	0.81	13.32	42.90	12.70	23.4	3.22	6.40	0.66	9.73	0.84
	c	1.76	39.8	0	0.30	3.25	12.95	40.92	6.3	3.98	8.49	0.64	12.99	1.32
	d	1.44	41.8	1	0.57	11.39	32.96	9.18	19.1	2.89	5.45	0.66	8.27	0.97
	e	1.72	41.1	0	0.32	3.28	16.22	44.50	7.1	4.94	7.91	0.65	12.00	1.68
Mean: 10.18 ± 2.24 Ma														
12mfs03														
Pahau Subterrane (Torlesse Supergroup), Deposition 120 ± 22 Ma														
	a	1.08	35.7	0	0.18	15.48	29.57	33.16	22.4	1.91	1.44	0.61	2.35	0.44
	b	0.99	36.1	1	0.23	9.23	32.75	52.03	16.9	3.55	2.43	0.60	4.00	0.62
	c	0.90	37.0	2	0.30	8.17	28.87	19.04	15.0	3.53	3.65	0.61	5.99	0.62
	d	0.66	32.2	1	1.14	38.56	82.01	42.28	57.8	2.13	3.63	0.57	6.35	0.37
	e	1.03	37.4	1	0.30	4.72	24.14	20.47	10.4	5.11	5.18	0.61	8.39	0.81
Mean: 5.41 ± 2.32 Ma														
12mfs13														
Burnt Creek Formation, Deposition 82 ± 17 Ma														
	a	0.84	34.2	1	0.41	26.49	100.77	34.68	50.2	3.80	1.48	0.58	2.54	0.25
	b	1.29	39.4	1	0.71	12.17	23.89	27.34	17.8	1.96	7.26	0.64	11.26	0.98
	c	0.89	36.7	2	0.34	18.98	45.46	78.42	29.7	2.40	2.08	0.61	3.38	0.28
	d	2.02	44.6	0	0.16	7.42	17.68	37.20	11.6	2.38	2.54	0.68	3.70	0.39
	e[h]	*1.67*	*40.4*	*1*	*5.53*	*15.03*	*36.72*	*50.24*	*23.7*	*2.44*	*42.36*	*0.64*	*65.32*	*2.05*
Mean: 5.22 ± 4.06 Ma														
12mfs25														
Esk Head Mélange (Torlesse Supergroup), Deposition 227 ± 21 Ma														
	a[h]	*0.47*	*28.7*	*1*	*0.62*	*72.68*	*89.84*	*31.06*	*93.8*	*1.24*	*1.22*	*0.53*	*2.30*	*0.32*
	b	1.28	36.9	0	0.17	21.83	19.73	44.30	26.5	0.90	1.17	0.63	1.84	0.19
	c	0.77	30.8	0	0.07	6.46	24.31	22.68	12.2	3.76	1.03	0.55	1.87	0.77
	d	1.59	39.7	0	0.08	5.70	27.73	31.90	12.2	4.86	1.15	0.63	1.80	0.38
	e[h]	*0.93*	*35.0*	*1*	*0.10*	*16.86*	*40.51*	*11.39*	*26.4*	*2.40*	*0.72*	*0.59*	*1.21*	*0.33*
Mean: 1.84 ± 0.035 Ma														
15cla04														
Pahau Subterrane (Torlesse Supergroup), Deposition 120 ± 22 Ma														
	a	1.46	41.5	1	0.44	24.60	43.61	34.93	34.8	1.77	2.33	0.66	3.50	0.27

b	0.82	34.4	1	0.06	8.08	24.75	60.42	13.9	3.06	0.76	0.59	1.27	0.59
c[h]	*2.21*	*46.4*	*1*	*0.36*	*7.89*	*32.40*	*20.49*	*15.5*	*4.10*	*4.25*	*0.68*	*6.20*	*0.43*
d	0.69	32.4	1	0.06	10.87	28.05	62.38	17.5	2.58	0.58	0.57	1.01	0.81
e	2.35	48.0	1	0.09	7.74	53.85	49.84	20.4	6.96	0.76	0.69	1.09	0.17

Mean: 1.72 ± 1.19 Ma

15cla06

Pahau Subterrane (Torlesse Supergroup), Deposition 120 ± 22 Ma

a	0.91	35.8	1	0.13	10.76	45.50	79.31	21.4	4.23	1.06	0.60	1.74	0.44
b	1.36	39.9	1	0.16	16.70	53.58	8.59	29.3	3.21	1.02	0.64	1.60	0.26
c	1.48	39.8	0	0.05	4.89	15.70	21.59	8.6	3.21	0.98	0.64	1.51	0.67
d	1.51	42.2	1	0.17	20.70	74.53	75.10	38.2	3.60	0.83	0.66	1.25	0.19
e	2.66	51.4	1	0.05	4.89	19.93	42.26	9.6	4.07	0.94	0.71	1.30	0.28

Mean: 1.48 ± 0.20 Ma

15mfs02

Pahau Subterrane (Torlesse Supergroup), Deposition 120 ± 22 Ma

a	1.41	39.9	0	0.06	3.18	9.88	36.43	5.5	3.11	1.89	0.64	2.88	0.55
b	0.61	31.2	1	0.27	23.63	25.25	23.18	29.6	1.07	1.66	0.57	2.90	0.46
c[h]	*0.78*	*31.5*	*0*	*0.09*	*2.64*	*19.26*	*26.06*	*7.2*	*7.30*	*2.22*	*0.54*	*4.03*	*1.22*
d	0.67	32.4	1	0.10	4.23	23.06	34.43	9.6	5.45	1.93	0.56	3.40	0.76
e	0.91	34.3	0	0.18	8.49	53.30	10.67	21.0	6.28	1.55	0.58	2.65	0.27

Mean: 2.96 ± 0.32 Ma

15mfs04

Pahau Subterrane (Torlesse Supergroup), Deposition 120 ± 22 Ma

a[h]	*0.60*	*29.2*	*0*	*0.28*	*5.73*	*19.03*	*39.00*	*10.2*	*3.32*	*4.88*	*0.53*	*9.06*	*1.11*
b	0.99	34.2	0	0.24	10.20	21.63	11.66	15.3	2.12	2.84	0.59	4.77	0.70
c	1.27	38.5	0	0.15	9.98	9.32	32.50	12.2	0.93	2.23	0.65	3.43	0.61
d	0.55	28.5	0	0.47	20.76	47.22	41.80	31.9	2.27	2.73	0.53	5.15	0.68
e	0.58	31.1	1	0.18	5.50	32.25	46.87	13.1	5.87	2.50	0.55	4.48	0.74

Mean: 4.46 ± 0.74 Ma

17mfs08

Pahau Subterrane (Torlesse Supergroup), Deposition 120 ± 22 Ma

a	0.75	33.2	1	0.47	9.53	37.78	19.25	18.4	3.97	4.65	0.57	8.15	0.96
b	0.90	34.7	1	0.42	5.06	26.18	9.30	11.2	5.17	6.92	0.58	11.84	1.41
c	0.74	33.4	1	1.47	51.08	42.72	20.57	61.1	0.84	4.44	0.59	7.48	0.44
d[g]	*1.24*	*37.5*	*0*	*1.06*	*28.86*	*27.83*	*27.84*	*35.4*	*0.96*	*5.50*	*0.64*	*8.62*	*0.58*
e[h]	*0.57*	*29.3*	*0*	*0.48*	*2.47*	*12.98*	*13.97*	*5.5*	*5.26*	*15.60*	*0.52*	*29.66*	*3.42*

Mean: 9.16 ± 2.35 Ma

17mfs20

Pahau Subterrane (Torlesse Supergroup), Deposition 120 ± 22 Ma

a	0.96	35.9	1	0.52	6.52	34.94	19.25	14.7	5.36	6.42	0.60	10.71	1.03
b	1.11	38.4	1	1.07	29.64	71.60	18.94	46.5	2.42	4.25	0.63	6.71	0.31
c	0.93	36.0	1	1.06	23.78	65.09	17.09	39.1	2.74	4.98	0.61	8.19	0.58
d	0.64	29.9	0	0.79	15.71	65.68	26.39	31.1	4.18	4.66	0.53	8.71	0.78
e	2.15	47.6	1	0.90	10.89	41.97	13.02	20.8	3.86	7.97	0.69	11.48	0.65

Mean: 9.16 ± 1.93 Ma

17mfs21

Pahau Subterrane (Torlesse Supergroup), Deposition 120 ± 22 Ma

a	1.54	41.0	0	0.07	2.55	14.66	13.76	6.0	5.74	2.17	0.65	3.34	0.56
b	2.12	45.0	0	0.07	2.95	9.61	9.90	5.2	3.25	2.59	0.68	3.79	0.77
c	1.52	40.7	0	0.23	8.69	24.63	8.85	14.5	2.84	2.87	0.65	4.39	0.48
d	1.71	44.0	1	0.16	4.87	15.01	17.46	8.4	3.08	3.39	0.67	5.02	0.80
e	0.93	33.9	1	0.33	17.00	18.72	60.22	21.4	1.10	2.78	0.59	4.64	0.41

Mean: 4.23 ± 0.67 Ma

17mfs25

Esk Head Mélange (Torlesse Supergroup), Deposition 227 ± 21 Ma

a	0.87	33.6	0	1.00	14.41	37.18	25.75	23.2	2.58	7.89	0.59	13.36	1.30
b	0.50	31.2	2	1.37	74.88	17.30	68.76	78.9	0.23	3.20	0.57	5.54	0.41
c	0.99	37.1	1	0.27	6.74	17.94	19.58	11.0	2.66	4.54	0.62	7.28	0.85
d[h]	*3.76*	*55.1*	*0*	*4.40*	*3.23*	*12.58*	*22.80*	*6.2*	*3.90*	*126.71*	*0.74*	*170.4*	*6.20*
e	1.99	43.5	0	0.37	15.32	34.02	15.74	23.3	2.22	2.95	0.68	4.36	0.24

Mean: 7.64 ± 4.00 Ma

17mfs29

Pahau Subterrane (Torlesse Supergroup), Deposition 120 ± 22 Ma

a	2.34	45.4	0	2.52	55.51	42.7	28.1	65.5	0.77	7.09	0.70	10.16	0.36
b	1.46	40.6	1	0.58	6.22	35.5	20.8	14.6	5.71	7.24	0.64	11.31	0.70
c	2.16	44.1	0	1.81	11.00	47.9	48.5	22.2	4.35	14.77	0.67	21.89	1.03
d[g]	1.71	43.6	1	0.06	3.37	9.0	14.1	5.5	2.67	1.98	0.67	2.94	0.65
e	0.56	32.2	2	0.90	6.63	25.5	69.3	12.6	3.84	12.59	0.55	22.19	2.15

Mean: 16.39 ± 6.55 Ma

17mfs31

Pahau Subterrane (Torlesse Supergroup), Deposition 120 ± 22 Ma

a	3.05	53.5	1	0.44	8.89	34.2	31.5	16.9	3.85	4.76	0.73	6.52	0.46
b	1.63	42.4	1	1.38	28.11	82.0	19.7	47.4	2.92	5.37	0.66	8.11	0.41
c	1.77	45.0	1	0.22	6.40	24.0	35.5	12.0	3.75	3.22	0.68	4.71	0.44
d[h]	1.80	44.2	1	0.55	5.55	23.3	30.9	11.0	4.19	8.94	0.67	13.24	1.53
e	0.65	31.8	1	0.79	22.04	81.1	31.4	41.1	3.68	3.54	0.56	6.29	0.49

Mean: 6.41 ± 1.39 Ma

17mfs32

Pahau Subterrane (Torlesse Supergroup), Deposition 120 ± 22 Ma

a	0.68	30.8	0	0.23	3.43	8.9	18.3	5.5	2.60	7.57	0.55	13.45	4.48
b	0.39	26.9	1	1.00	15.05	28.9	34.6	21.8	1.92	8.36	0.50	16.46	2.37
c	0.68	31.7	1	0.80	15.40	50.7	25.2	27.3	3.30	5.37	0.55	9.68	1.57
d	1.09	36.3	0	0.80	7.66	28.3	37.7	14.3	3.69	10.12	0.61	16.46	1.39
e[f]	*1.35*	*37.5*	*0*	*0.22*	*1.52*	*4.1*	*12.0*	*2.5*	*2.70*	*16.02*	*0.63*	*25.20*	*4.14*

Mean: 14.01 ± 3.22 Ma

17mfs37

Pahau Subterrane (Torlesse Supergroup), Deposition 120 ± 22 Ma

a	0.53	29.7	1	0.17	5.67	22.5	47.3	11.0	3.96	2.70	0.53	4.99	1.68
b	0.60	29.6	0	0.15	6.87	17.2	34.8	10.9	2.51	2.44	0.54	4.47	1.65
c	0.50	29.4	1	0.19	9.91	37.0	36.3	18.6	3.74	1.82	0.53	3.43	1.30
d	0.63	31.2	1	0.16	7.88	23.1	47.6	13.3	2.93	2.20	0.55	3.94	1.28
e	0.61	30.8	1	0.15	6.02	23.9	30.6	11.6	3.96	2.32	0.54	4.23	1.20

Mean: 4.21 ± 0.58 Ma

17mfs38

Rakaia Subterrane (Torlesse Supergroup), Deposition 227 ± 21 Ma

a[g]	*8.45*	*71.96*	*0*	*0.14*	*7.36*	*29.0*	*8.8*	*14.2*	*3.94*	*1.81*	*0.79*	*2.28*	*0.12*
b	1.43	38.91	0	0.16	14.91	48.0	13.0	26.2	3.22	1.14	0.63	1.80	0.25
c	4.73	59.32	0	0.15	2.80	20.5	6.4	7.6	7.32	3.64	0.75	4.86	0.42
d[g]	*3.06*	*54.50*	*2*	*0.24*	*14.27*	*61.8*	*13.7*	*28.8*	*4.33*	*1.56*	*0.73*	*2.15*	*0.15*
e	1.30	40.27	1	0.12	11.80	59.6	27.4	25.8	5.06	0.87	0.64	1.36	0.26

Mean: 2.68 ± 1.91 Ma

17mfs42

Pahau Subterrane (Torlesse Supergroup), Deposition 120 ± 22 Ma

a	1.23	38.1	0	0.28	9.06	47.2	8.0	20.2	5.21	2.57	0.62	4.13	0.49
b	0.65	31.9	1	1.51	51.76	99.9	18.7	75.3	1.93	3.70	0.57	6.48	0.51
c	0.87	35.7	1	0.31	25.25	51.5	21.8	37.4	2.04	1.53	0.62	2.46	0.32
d	1.00	34.4	1	0.17	3.46	22.1	38.9	8.7	6.40	3.57	0.57	6.09	0.88
e	1.80	43.0	0	0.08	2.47	18.0	27.3	6.7	7.27	2.09	0.66	3.13	0.63

Mean: 4.46 ± 1.78 Ma

---

[a] equivelent spherical radius

[b]F T indicates grain terminus. 0: Both tips broken. 1:One tip broken. 2: Whole grain.

[c]eU - effective uranium concentration, weights U and Th for their alpha productivity, computed as [U] + 0.235 * [Th]

[d]Ft is alpha-ejection correction of Farley et al [2002]

[e]Analytical uncertainty based on U, Th, He, and grain length measurements

Grains in italics were not included in means, plots or models and were excluded for the following reasons:

[f] Grains less than 5ppm eU

[g] Apatite grains with He re-extraction < 95% and He > 0.01 ncc

[h] Grains that failed the Peirce outlier test (Ross, 2003)

Table 3.4. Zircon (U-Th)/He data.

Sample	Grain	Mass (μg)	r[a] (μm)	T[b]	He (nmol/g)	U (ppm)	Th (ppm)	Sm (ppm)	eU[c] (ppm)	Th/U	Raw Date (Ma)	Ft[d]	Date (Ma)	2σ[e] (Ma)
12mfs02														
Pahau Subterrane (Torlesse Supergroup), Deposition 120 ± 22 Ma														
	a	6.43	59.5	2	159	164	102	0.62	188	0.62	154.91	0.81	191.29	6.40
	b	2.71	44.4	2	34.1	112	75.8	0.65	130	0.68	48.44	0.75	64.90	3.06
	c	4.87	54.5	2	151	159	61.3	0.15	174	0.39	159.11	0.79	200.21	3.72
Mean: 152.13 ± 75.68 Ma														
12mfs03														
Pahau Subterrane (Torlesse Supergroup), Deposition 120 ± 22 Ma														
	a	3.01	44.0	1	204	428	349	1.00	510	0.82	73.62	0.74	98.70	1.86
	b	3.71	46.0	1	136	170	92.5	0.42	191	0.55	130.75	0.76	172.22	5.57
	c	3.12	45.4	2	112	171	20.9	0.03	175	0.12	117.11	0.75	154.63	8.26
Mean: 141.85 ± 38.39 Ma														
12mfs06														
Esk Head Mélange (Torlesse Supergroup), Deposition 227 ± 21 Ma														
	a	5.06	54.3	2	61.7	229	114	0.34	256	0.50	44.59	0.79	56.36	1.53
	b	4.19	46.7	1	42.8	366	156	0.24	403	0.43	19.67	0.76	25.86	0.79
	c	4.89	52.2	1	18.0	251	205	1.26	299	0.82	11.17	0.78	14.27	1.27
Mean: 32.16 ± 21.74 Ma														
12mfs13														
Burnt Creek Formation, Deposition 82 ± 17 Ma														
	a	2.34	42.7	2	179	228	132	0.30	259	0.58	126.81	0.74	171.51	9.52
	b	2.35	41.9	2	137	133	106	0.28	158	0.80	158.49	0.73	216.02	10.13
	c	3.10	46.0	2	221	313	149	0.74	348	0.48	116.29	0.75	153.52	4.99
Mean: 180.35 ± 32.17 Ma														
12mfs25														
Esk Head Mélange (Torlesse Supergroup), Deposition 227 ± 21 Ma														
	a	2.08	40.9	2	13.2	86.2	78.0	0.28	105	0.90	23.28	0.72	32.16	1.53
	b	1.90	39.5	2	180	488	282	0.80	554	0.58	59.93	0.72	83.46	7.48

c	2.53	44.6	2	54.6	302	381	1.13	392	1.26	25.72	0.74	34.59	5.50

Mean: 50.07 ± 28.94 Ma

15cla04

Pahau Subterrane (Torlesse Supergroup), Deposition 120 ± 22 Ma

a	12.69	72.7	2	217	230	144	0.29	264	0.63	150.46	0.84	178.53	6.16
b	14.16	75.2	2	227	408	227	0.65	461	0.56	90.64	0.85	106.95	2.05
c	4.11	50.8	2	104	249	90.3	0.46	271	0.36	71.12	0.78	91.27	2.39

Mean: 125.58 ± 46.52 Ma

15cla06

Pahau Subterrane (Torlesse Supergroup), Deposition 120 ± 22 Ma

a	4.46	51.7	2	106	299	224	0.88	351	0.75	55.56	0.78	71.24	3.15
b	2.88	45.3	2	168	454	260	0.68	515	0.57	60.18	0.75	79.98	1.95
c	6.85	61.7	2	120	390	305	1.26	462	0.78	47.96	0.81	58.95	1.03

Mean: 70.06 ± 10.57 Ma

15mfs04

Pahau Subterrane (Torlesse Supergroup), Deposition 120 ± 22 Ma

a	1.48	37.2	2	344	670	335	0.57	749	0.50	84.56	0.70	120.20	3.33
b	2.14	38.9	1	27.0	114	118	0.36	142	1.03	35.26	0.71	49.46	3.29
c	3.15	44.4	1	144	275	152	0.14	310	0.56	85.24	0.75	113.58	2.60

Mean: 94.41 ± 39.07 Ma

15mfs05

Pahau Subterrane (Torlesse Supergroup), Deposition 120 ± 22 Ma

a	3.92	48.9	2	19.9	149	153	0.36	185	1.03	19.86	0.76	25.95	0.66
b	4.90	54.6	2	42.5	315	182	1.49	358	0.58	21.96	0.79	27.74	1.65
c	2.34	41.7	2	62.6	325	89.9	0.86	346	0.28	33.43	0.73	45.57	2.04

Mean: 33.09 ± 10.85 Ma

17mfs08

Pahau Subterrane (Torlesse Supergroup), Deposition 120 ± 22 Ma

a	1.45	36.7	2	44.1	668	112	1.83	695	0.17	11.76	0.70	16.78	0.71
b	3.12	47.4	2	11.7	211	128	0.39	241	0.60	9.01	0.76	11.83	0.32
c	1.87	40.1	2	32.1	239	166	1.35	279	0.70	21.35	0.72	29.62	2.15

Mean: 19.41 ± 9.18 Ma

17mfs09

Pahau Subterrane (Torlesse Supergroup), Deposition 120 ± 22 Ma

	a	5.16	49.9	1	68.6	523	214	0.56	573	0.41	22.17	0.77	28.59	1.05
	b	2.60	43.7	2	60.7	811	187	0.52	855	0.23	13.17	0.75	17.66	0.68
	c	1.78	37.8	2	66.5	528	157	0.75	565	0.30	21.81	0.71	30.80	1.11

Mean: 25.68 ± 7.03 Ma

17mfs10

Pahau Subterrane (Torlesse Supergroup), Deposition 120 ± 22 Ma

	a	2.43	41.5	2	31.5	598	113	0.02	624	0.19	9.37	0.73	12.78	0.44
	b	2.58	42.7	2	35.7	222	169	0.62	261	0.76	25.28	0.73	34.38	1.55
	c	4.98	56.0	2	74.1	402	143	0.27	435	0.36	31.48	0.80	39.43	1.81

Mean: 28.87 ± 14.16 Ma

17mfs20

Pahau Subterrane (Torlesse Supergroup), Deposition 120 ± 22 Ma

	a	5.25	55.7	2	142	140	135	0.59	172	0.96	151.83	0.79	190.89	7.35
	b	10.86	67.2	1	190	235	96.6	0.30	258	0.41	135.33	0.83	162.58	6.46
	c	8.24	61.5	1	221	246	167	0.27	285	0.68	141.81	0.81	173.71	3.78

Mean: 175.73 ± 14.26 Ma

17mfs21

Pahau Subterrane (Torlesse Supergroup), Deposition 120 ± 22 Ma

	a	5.41	51.7	1	103	423	304	0.35	494	0.72	38.50	0.78	49.28	1.07
	b	2.56	42.4	2	127	436	327	0.86	513	0.75	45.70	0.73	62.22	1.94
	c	3.44	47.9	2	5.8	59.8	29.1	0.53	67	0.49	16.16	0.76	21.14	1.09

Mean 44.22 ± 21.00 Ma

17mfs22

Esk Head Mélange (Torlesse Supergroup), Deposition 227 ± 21 Ma

	a	2.62	43.9	2	272	342	258	0.29	403	0.75	123.94	0.74	166.38	4.29
	b	3.21	45.0	2	60.9	113	68.3	0.26	129	0.60	86.89	0.75	115.72	7.64
	c	3.74	47.7	1	61.4	78.8	24.5	0.07	85	0.31	133.03	0.77	172.90	9.04

Mean: 151.67 ± 31.30 Ma

17mfs23

Pahau Subterrane (Torlesse Supergroup), Deposition 120 ± 22 Ma

	a	4.03	50.2	2	124	160	174	0.53	200	1.09	114.03	0.77	147.60	6.02
	b	3.32	48.5	2	40.7	103	73.4	0.34	120	0.71	62.35	0.77	81.33	3.44
	c	3.86	48.0	2	339	364	95.9	0.67	386	0.26	160.66	0.77	208.76	5.98

Mean: 145.90 ± 63.73 Ma

17mfs25
Esk Head Mélange (Torlesse Supergroup), Deposition 227 ± 21 Ma

a	4.82	54.0	2	25.4	114	82.8	0.26	134	0.73	35.22	0.79	44.66	1.59
b	2.97	46.3	2	63.4	374	237	0.40	430	0.63	27.29	0.76	36.09	1.15
c	2.46	43.7	2	251	403	291	0.50	471	0.72	98.18	0.74	132.03	3.03

Mean: 70.93 ± 53.09 Ma

17mfs26
Esk Head Mélange (Torlesse Supergroup), Deposition 227 ± 21 Ma

a	5.68	52.7	1	21.6	288	202	0.34	335	0.70	11.96	0.78	15.25	0.38
b	5.27	56.4	2	35.0	330	130	0.52	360	0.39	18.00	0.80	22.53	0.64
c	4.97	51.3	1	141	215	181	1.03	257	0.84	100.85	0.78	129.29	4.65

Mean: 55.69 ± 63.85 Ma

17mfs29
Pahau Subterrane (Torlesse Supergroup), Deposition 120 ± 22 Ma

a	9.75	64.6	1	552	500	298	0.48	570	0.60	176.87	0.82	214.24	7.84
b	2.60	43.7	2	163	233	122	0.58	262	0.53	114.45	0.74	153.58	9.18
c	4.09	48.1	2	171	162	158	0.83	200	0.97	157.12	0.76	205.43	7.40

Mean: 191.08 ± 32.78 Ma

17mfs30
Pahau Subterrane (Torlesse Supergroup), Deposition 120 ± 22 Ma

a	1.90	39.0	2	32.9	309	171	0.16	349	0.55	17.42	0.71	24.40	1.90
b	4.19	48.6	1	42.4	481	141	0.43	514	0.29	15.27	0.77	19.81	0.82
c	5.96	57.5	2	145	613	276	1.01	678	0.45	39.53	0.80	49.25	1.56

Mean: 31.15 ± 15.84 Ma

17mfs31
Pahau Subterrane (Torlesse Supergroup), Deposition 120 ± 22 Ma

a	4.12	50.5	2	334	546	205	0.37	594	0.38	103.37	0.78	132.80	4.07
b	4.42	49.1	2	418	351	266	0.78	413	0.76	184.76	0.77	239.62	10.65
c	2.57	43.9	2	161	327	238	0.61	383	0.73	77.42	0.74	104.05	4.39

Mean: 158.82 ± 71.43 Ma

17mfs32
Pahau Subterrane (Torlesse Supergroup), Deposition 120 ± 22 Ma

a	1.40	36.7	2	284	550	388	2.93	641	0.71	81.61	0.70	116.83	4.61
b	1.72	36.1	1	257	290	167	0.54	329	0.57	142.86	0.70	204.34	6.79
c	1.60	37.0	2	170	315	266	0.49	378	0.84	82.94	0.70	118.66	7.54

Mean: 146.61 ± 50.01 Ma

17mfs33

Pahau Subterrane (Torlesse Supergroup), Deposition 120 ± 22 Ma

a	6.07	55.8	1	286	493	229	0.40	547	0.46	96.06	0.80	120.20	5.02
b	1.51	36.0	2	391	663	396	0.80	756	0.60	95.15	0.69	137.14	5.30
c	3.12	45.4	2	17.9	60.4	55.7	0.32	73	0.92	45.05	0.75	60.10	2.43

Mean: 105.81 ± 40.49 Ma

17mfs34

Pahau Subterrane (Torlesse Supergroup), Deposition 120 ± 22 Ma

a	2.24	41.9	2	85.2	225	157	0.55	262	0.70	59.88	0.73	81.75	4.48
b	3.25	45.7	2	318	591	259	1.11	652	0.44	89.86	0.75	118.91	5.53
c	2.91	43.8	1	36.4	109	74.1	0.34	126	0.68	53.18	0.74	71.30	1.57

Mean: 90.65 ± 25.02 Ma

17mfs35

Pahau Subterrane (Torlesse Supergroup), Deposition 120 ± 22 Ma

a	6.07	55.8	1	250	386	205	0.51	434	0.53	106.13	0.80	132.84	3.52
b	1.51	36.0	2	463	743	174	1.55	783	0.23	108.58	0.69	155.61	7.10
c	1.69	37.4	2	184	328	269	0.45	391	0.82	86.77	0.70	123.54	7.39

Mean: 137.33 ± 16.50 Ma

17mfs36

Pahau Subterrane (Torlesse Supergroup), Deposition 120 ± 22 Ma

a	3.07	46.9	2	177	367	361	0.76	452	0.98	72.20	0.76	95.33	1.53
b	4.23	48.4	2	190	277	129	2.62	307	0.47	113.41	0.77	147.55	4.09
c	2.99	45.0	2	224	418	262	1.07	480	0.63	85.87	0.75	114.39	3.22

Mean: 119.09 ± 26.43 Ma

17mfs37

Pahau Subterrane (Torlesse Supergroup), Deposition 120 ± 22 Ma

a	5.36	57.2	2	3.9	88	60.3	0.42	102	0.69	7.18	0.80	8.98	0.29
b	1.62	37.9	2	4.0	113	73.6	0.35	130	0.65	5.67	0.70	8.04	0.21
c	1.66	37.9	2	10.8	138	98.4	0.46	161	0.71	12.49	0.70	17.71	0.47

Mean: 11.58 ± 5.33 Ma

17mfs38

Rakaia Subterrane (Torlesse Supergroup), Deposition 227 ± 21 Ma

a	3.79	49.6	2	442	635	353	0.87	718	0.56	113.07	0.77	146.17	4.92
b	6.72	59.7	2	234	311	272	0.82	375	0.88	114.84	0.81	142.07	2.88
c	6.35	60.2	2	286	341	296	0.81	410	0.87	127.62	0.81	157.56	5.15

Mean: 148.60 ± 8.02 Ma

17mfs42

Pahau Subterrane (Torlesse Supergroup), Deposition 120 ± 22 Ma

a	2.41	42.6	2	27.5	171	129	0.31	202	0.75	25.20	0.73	34.27	1.09
b	2.42	40.6	1	14.9	167	107	0.49	193	0.64	14.32	0.73	19.72	0.57
c	2.08	40.9	2	29.7	240	141	0.55	273	0.59	20.16	0.73	27.75	0.69

Mean: 27.25 ± 7.29 Ma

---

[a] equivelent spherical radius

[b]F T indicates grain terminus. 0: Both tips broken. 1:One tip broken. 2: Whole grain.

[c]eU - effective uranium concentration, weights U and Th for their alpha productivity, computed as [U] + 0.235 * [Th]

[d]Ft is alpha-ejection correction of Farley et al [2002]

[e]Analytical uncertainty based on U, Th, He, and grain length measurements

3.9.3 *QTQt Modeling Inputs*

3.9.3.1 Black Birch Vertical Transect

Table 3.5. Data inputs for Black Birch vertical transect.

Sample #	Elev. (m)	Unit + Strat. or Emplacement Age	Temp. (°C)	Systems used	Pre-dep. History?
17mfs08	1104	Pahau (Torlesse) greywacke, 120 ± 22 Ma	10 ± 10	ZHe, AHe	Yes
17mfs09	1474	Pahau (Torlesse) greywacke, 120 ± 22 Ma	10 ± 10	Zhe	Yes
17mfs010	1685	Pahau (Torlesse) greywacke, 120 ± 22 Ma	10 ± 10	Zhe	Yes

Table 3.6. Thermal history constraints for Black Birch vertical transect.

Range for Time (m.y.) general prior	Range for Temp (°C) general prior	Temp Gradient (°C/km)	Present Day Surface Temp (°C)	Present Day Temp Offset (°C)	Max. ∂T/∂t (°C/m.y.)
100 ± 100	150 ± 150	25 ± 25	10 ± 10	7 ± 5	1000

Table 3.7. Apatite-helium inputs to Black Birch vertical transect.

Raw Age (Ma)	Error (Ma)	eU (ppm)	Grain length (microns)	Grain width (microns)	Grain thickness (microns)
Sample 17mfs08					
4.65	0.27	18.4	95.0	70.0	65.0
6.92	0.42	11.2	105.0	80.0	65.0
4.44	0.13	61.1	90.0	65.0	70.0

Table 3.8. Zircon-helium inputs to Black Birch vertical transect.

Raw Age (Ma)	Error (Ma)	eU (ppm)	Grain length (microns)	Grain width (microns)	Grain thickness (microns)
Sample 17mfs08					
11.76	0.25	694.8	115	75	60
9.01	0.12	241.1	150	80	90
21.35	0.78	278.6	125	75	70
Sample 17mfs09					
22.17	0.40	573.3	200	80	80

13.17	0.26	855.0	150	70	80
21.81	0.39	564.8	140	65	60
Sample 17mfs10					
9.37	0.16	624.2	160	65.0	70.0
25.28	0.57	261.4	160	70.0	70.0
31.48	0.74	435.4	165	110.0	100.0

3.9.3.2 Mt. Murphy Vertical Transect

Table 3.9. Data inputs for Mt. Murphy vertical transect.

Sample #	Elev. (m)	Unit + Strat. or Emplacement Age	Temp. (°C)	Systems used	Pre-dep. History?
17mfs33	1784	Pahau (Torlesse) greywacke, 120 ± 22 Ma	10 ± 10	ZHe	No
17mfs34	1513	Pahau (Torlesse) greywacke, 120 ± 22 Ma	10 ± 10	ZHe	No
17mfs35	1211	Pahau (Torlesse) greywacke, 120 ± 22 Ma	10 ± 10	ZHe	No
15mfs02	1016	Pahau (Torlesse) greywacke, 120 ± 22 Ma	10 ± 10	AHe	No

Table 3.10. Thermal history constraints for Mt. Murphy vertical transect.

Range for Time (m.y.) general prior	Range for Temp (°C) general prior	Temp Gradient (°C/km)	Present Day Surface Temp (°C)	Present Day Temp Offset (°C)	Max. $\partial T/\partial t$ (°C/m.y.)
100 ± 100	200 ± 200	25 ± 25	10 ± 10	7 ± 5	1000

Table 3.11. Apatite-helium inputs to Mt. Murphy vertical transect.

Raw Age (Ma)	Error (Ma)	eU (ppm)	Grain length (microns)	Grain width (microns)	Grain thickness (microns)
Sample 15mfs02					
1.89	0.17	5.5	80.0	75.0	95.0
1.66	0.14	29.6	80.0	90.0	60.0
1.93	0.21	9.6	75.0	60.0	85.0
1.55	0.07	21.0	70.0	60.0	85.0

Table 3.12. Zircon-helium inputs to Mt. Murphy vertical transect.

Raw Age (Ma)	Error (Ma)	eU (ppm)	Grain length (microns)	Grain width (microns)	Grain thickness (microns)
Sample 17mfs33					
96.06	2.00	547.1	170.0	95.0	100.0
95.15	1.84	756.4	130.0	60.0	60.0
45.05	0.91	73.5	170.0	80.0	70.0
Sample 17mfs34					
59.88	1.65	262.4	140.0	70.0	75.0
89.86	2.08	651.6	175.0	80.0	70.0
53.18	0.58	126.5	130.0	80.0	75.0
Sample 17mfs35					
106.13	1.40	433.6	170.0	95.0	100.0
108.58	2.47	783.4	130.0	60.0	60.0
86.77	2.60	390.8	135.0	60.0	65.0

3.9.3.3 Sample 12mfs02

Table 3.13. Thermal history constraints for model for 12mfs02.

Range for Time (m.y.) general prior	Range for Temp (°C) general prior	Geologic unit and depositional or emplacement age	Temp at Deposition (°C)	Present Day Surface Temp (°C)	Max. ∂T/∂t (°C/m.y.)	Pre-dep. History?
100 ± 100	100 ± 100	Pahau (Torlesse): 120 ± 22 Ma	10 ± 10	10 ± 10	1000	Yes

Table 3.14. Apatite- and zircon-helium inputs to model for 12mfs02.

Raw Age (Ma)	Error (Ma)	eU (ppm)	Grain length (microns)	Grain width (microns)	Grain thickness (microns)
Sample 12mfs02 (apatite)					
4.58	0.12	252.5	90	110	95
6.40	0.29	23.4	120	120	75
8.49	0.44	6.3	100	125	80
5.45	0.31	19.1	110	80	90
7.91	0.55	7.1	105	100	80
Sample 12mfs02 (zircon)					
154.91	2.59	188.1	200	100	105
48.44	1.15	129.9	150	85	70
159.11	1.48	173.6	180	100	90

3.9.3.4 Sample 12mfs03

Table 3.15. Thermal history constraints for model for 12mfs03.

Range for Time (m.y.) general prior	Range for Temp (°C) general prior	Geologic unit and depositional or emplacement age	Temp at Deposition (°C)	Present Day Surface Temp (°C)	Max. $\partial T/\partial t$ (°C/m.y.)	Pre-dep. History?
100 ± 100	150 ± 150	Pahau (Torlesse): 120 ± 22 Ma	10 ± 10	10 ± 10	1000	Yes

Table 3.16. Apatite- and zircon-helium inputs to model for 12mfs03.

Raw Age (Ma)	Error (Ma)	eU (ppm)	Grain length (microns)	Grain width (microns)	Grain thickness (microns)
Sample 12mfs03 (apatite)					
1.44	0.13	22.4	90	80	70
2.43	0.18	16.9	110	70	70
3.65	0.19	15.0	120	65	75
3.63	0.10	57.8	80	70	70
5.18	0.25	10.4	95	80	80
Sample 12mfs03 (zircon)					
73.62	0.69	509.9	135	85	70
130.75	2.10	191.4	160	70	85
117.11	3.11	175.5	170	80	70

3.9.3.5 Sample 12mfs06

Table 3.17. Thermal history constraints for 12mfs06.

Range for Time (m.y.) general prior	Range for Temp (°C) general prior	Geologic unit and depositional or emplacement age	Temp at Deposition (°C)	Present Day Surface Temp (°C)	Max. ∂T/∂t (°C/m.y.)	Pre-dep. History?
44.59 ± 44.59*	150 ± 150	Esk Head (Torlesse): 227 ± 21 Ma	10 ± 10	10 ± 10	1000	No

*Oldest single-grain age ± itself

Table 3.18. Zircon-helium inputs to model for 12mfs06.

Raw Age (Ma)	Error (Ma)	eU (ppm)	Grain length (microns)	Grain width (microns)	Grain thickness (microns)
Sample 12mfs06 (zircon)					
44.59	0.61	255.6	190	85	100
19.67	0.30	403.0	185	75	75
11.17	0.50	298.8	150	105	85

Table 3.19. Apatite fission track inputs to model for 12mfs06.

Ns	Age (Ma)	Age Error (Ma)	Dpar (microns)	Zeta
Samples 12mfs06 (AFT)				
12	12.55	5.54	2.07	8.2727
4	5.27	3.33	1.99	8.2727
28	6.86	2.19	2.42	8.2727
2	3.14	2.38	1.49	8.2727
10	23.23	10.95	2.43	8.2727
1	1.31	1.15	1.93	8.2727
1	15.58	13.47	1.98	8.2727
0	0	129.16	2.08	8.2727
1	12.23	10.58	2.39	8.2727
4	5.39	3.41	2.14	8.2727
0	0	35.32	1.75	8.2727
3	22.37	15.32	1.74	8.2727
2	3.92	2.97	1.96	8.2727
4	7.34	4.65	2.12	8.2727
6	4.91	2.75	2.23	8.2727
1	3.3	2.85	2.03	8.2727
1	23.47	20.29	2.54	8.2727
3	8.43	5.78	1.78	8.2727
1	12.86	11.12	1.88	8.2727
0	0	168.27	1.52	8.2727
0	0	32.08	1.27	8.2727
3	29.65	20.31	2.06	8.2727
0	0	49.68	2.02	8.2727
4	11.56	7.32	1.78	8.2727
5	8.51	5.04	2.02	8.2727
7	26.75	14.22	2.09	8.2727
10	12.82	6.03	1.93	8.2727
0	0	31.13	1.55	8.2727
1	3.91	3.38	1.6	8.2727
1	5.95	5.14	2.22	8.2727
1	14.89	12.88	1.74	8.2727
0	0	6.41	1.26	8.2727
0	0	38.08	1.89	8.2727
0	0	33.52	1.51	8.2727
1	35.96	31.09	1.86	8.2727
15	4.84	1.96	2.03	8.2727
2	9.5	7.19	1.68	8.2727
3	14.08	9.64	1.64	8.2727
11	13.58	6.17	1.87	8.2727
3	14.82	10.15	1.81	8.2727

Table 3.20. Apatite fission track length data inputs to model for 12mfs06.

Length (microns)	C-axis Angle (°)	Dpar (microns)
Sample 12mfs06 (AFT length)		
14.67	50.98	1.71
12.72	66.71	2.69
15.41	27.29	2.69
14.15	39.21	2.69
14.97	30.99	2.69
13.00	60.21	2.38
14.38	54.21	2.87
9.82	61.11	3.01
11.52	70.41	3.01
12.84	79.47	2.01
10.85	69.54	1.94
11.75	41.01	1.94
10.27	65.44	1.94
14.19	22.43	1.94
13.37	82.62	1.94
12.37	66.86	1.94
13.79	32.88	1.94
12.22	57.42	1.94
9.22	61.60	1.94
10.53	80.95	1.94
12.10	43.02	2.97
11.60	43.34	1.98
14.02	24.82	1.98
13.53	63.67	1.91
14.84	35.89	2.17
11.33	54.53	2.10
16.98	49.60	2.78
14.81	46.76	2.58
13.92	60.81	2.04
12.95	53.13	2.13
13.74	43.90	2.17
14.04	29.20	2.17
14.52	9.80	2.85
14.26	36.79	2.06
14.40	34.71	3.31
14.33	31.27	3.31
14.11	56.39	2.04
14.96	56.88	2.25
14.78	34.75	2.25
12.22	86.74	2.28
15.06	17.93	2.28
15.55	34.92	2.28
11.65	37.99	2.28
13.09	49.00	2.02
13.54	38.55	2.03
12.00	59.10	1.87
12.65	47.76	1.87

14.26	56.51	1.87
14.79	76.26	2.13
14.39	33.76	2.13
12.40	49.68	2.13
12.67	43.02	2.13
14.77	48.95	2.13
12.51	60.52	2.13
13.82	54.02	2.13
13.72	72.06	2.13
13.61	53.46	2.13
11.03	80.49	2.13
11.97	69.81	1.82
10.69	54.39	1.82
13.95	40.86	2.12
14.78	33.76	2.33
14.94	45.17	2.33
15.44	15.37	2.33
15.21	46.14	2.33
14.48	33.29	2.32
14.99	19.51	2.04
15.72	37.17	2.04
15.20	47.13	2.04
13.46	46.66	2.04

3.9.3.6 Sample 12mfs13

Table 3.21. Thermal history constraints for 12mfs13.

Range for Time (m.y.) general prior	**Range for Temp (°C) general prior**	**Geologic unit and depositional or emplacement age**	**Temp at Deposition (°C)**	**Present Day Surface Temp (°C)**	**Max. ∂T/∂t (°C/m.y.)**	**Pre-dep. History?**
100 ± 100	100 ± 100	Burnt Creek Fm: 82 ± 17 Ma	10 ± 10	10 ± 10	1000	Yes

Table 3.22. Apatite- and zircon-helium inputs to model for 12mfs13.

Raw Age (Ma)	Error (Ma)	eU (ppm)	Grain length (microns)	Grain width (microns)	Grain thickness (microns)
Sample 12mfs13 (apatite)					
1.48	0.07	50.2	95	90	65
7.26	0.32	17.8	115	90	75
2.08	0.09	29.7	120	75	70
2.54	0.13	11.6	110	80	95
Sample 12mfs13 (zircon)					
126.81	3.54	258.7	140	80	70
158.49	3.71	158.3	150	70	70
126.81	3.54	258.7	140	80	70

3.9.3.7 Sample 12mfs25

Table 3.23. Thermal history constraints for 12mfs25.

Range for Time (m.y.) general prior	Range for Temp (°C) general prior	Geologic unit and depositional or emplacement age	Temp at Deposition (°C)	Present Day Surface Temp (°C)	Max. ∂T/∂t (°C/m.y.)	Pre-dep. History?
59.93 ± 59.93*	150 ± 150	Esk Head (Torlesse): 227 ± 21 Ma	10 ± 10	10 ± 10	1000	Yes

*Oldest single-grain age ± itself

Table 3.24. Apatite- and zircon-helium inputs to model for 12mfs25.

Raw Age (Ma)	Error (Ma)	eU (ppm)	Grain length (microns)	Grain width (microns)	Grain thickness (microns)
Sample 12mfs25 (apatite)					
1.17	0.06	26.5	85	105	75
1.03	0.22	12.2	80	85	60
1.15	0.12	12.2	110	95	75
Sample 12mfs25 (zircon)					
23.28	0.56	104.6	135	80	65
59.93	2.70	554.5	135	70	65
25.72	2.08	392.1	135	85	80

3.9.3.8 Sample 15cla04

Table 3.25. Thermal history constraints for model for 15cla04.

Range for Time (m.y.) general prior	Range for Temp (°C) general prior	Geologic unit and depositional or emplacement age	Temp at Deposition (°C)	Present Day Surface Temp (°C)	Max. $\partial T/\partial t$ (°C/m.y.)	Pre-dep. History?
100 ± 100	100 ± 100	Pahau (Torlesse): 120 ± 22 Ma	10 ± 10	10 ± 10	1000	No

Table 3.26. Apatite- and zircon-helium inputs to model for 15cla04.

Raw Age (Ma)	Error (Ma)	eU (ppm)	Grain length (microns)	Grain width (microns)	Grain thickness (microns)
Sample 15cla04 (apatite)					
2.33	0.09	34.8	90	105	105
0.76	0.17	13.9	90	80	70
4.25	0.15	15.5	145	110	85
0.58	0.24	17.5	85	80	65
0.76	0.06	20.4	135	130	90
Sample 15cla04 (zircon)					
150.46	2.58	263.7	270	115	125
90.64	0.87	461.1	280	135	115
71.12	0.93	270.7	175	95	80

3.9.3.9 Sample 15cla06

Table 3.27. Thermal history constraints for model for 15cla06.

Range for Time (m.y.) general prior	Range for Temp (°C) general prior	Geologic unit and depositional or emplacement age	Temp at Deposition (°C)	Present Day Surface Temp (°C)	Max. $\partial T/\partial t$ (°C/m.y.)	Pre-dep. History?
60.18 ± 60.18*	200 ± 200	Pahau (Torlesse): 120 ± 22 Ma	10 ± 10	10 ± 10	1000	No

*Oldest single-grain age ± itself

Table 3.28. Apatite- and zircon-helium inputs to model for 15cla06.

Raw Age (Ma)	Error (Ma)	eU (ppm)	Grain length (microns)	Grain width (microns)	Grain thickness (microns)
Sample 15cla06 (apatite)					
1.06	0.13	21.4	90	85	75
1.02	0.08	29.3	120	90	75
0.98	0.21	8.6	95	90	80
0.83	0.06	38.2	115	90	85

0.94	0.10	9.6	130	110	110
Sample 15cla06 (zircon)					
55.56	1.23	351.3	185	95	80
60.18	0.73	515.0	155	80	75
47.96	0.42	461.7	195	110	110

3.9.3.10 Sample 15mfs04

Table 3.29. Thermal history constraints for model for 15mfs04.

Range for Time (m.y.) general prior	**Range for Temp (°C) general prior**	**Geologic unit and depositional or emplacement age**	**Temp at Deposition (°C)**	**Present Day Surface Temp (°C)**	**Max. ∂T/∂t (°C/m.y.)**	**Pre-dep. History?**
150 ± 150	150 ± 150	Pahau (Torlesse): 120 ± 22 Ma	10 ± 10	10 ± 10	1000	Yes

Table 3.30. Apatite- and zircon-helium inputs to model for 15mfs04.

Raw Age (Ma)	**Error (Ma)**	**eU (ppm)**	**Grain length (microns)**	**Grain width (microns)**	**Grain thickness (microns)**
Sample 15mfs04 (apatite)					
2.84	0.21	15.3	95	75	65
2.23	0.19	12.2	80	80	85
2.73	0.18	31.9	60	75	60
2.50	0.21	13.1	75	95	60
Sample 15mfs04 (zircon)					
84.56	1.18	749.2	115	70	65
35.26	1.17	141.7	125	60	75
85.24	0.97	310.5	140	85	70

3.9.3.11 Sample 15mfs05

Table 3.31. Thermal history constraints for model for 15mfs05.

Range for Time (m.y.) general prior	Range for Temp (°C) general prior	Geologic unit and depositional or emplacement age	Temp at Deposition (°C)	Present Day Surface Temp (°C)	Max. ∂T/∂t (°C/m.y.)	Pre-dep. History?
100 ± 100	250 ± 250	Pahau (Torlesse): 120 ± 22 Ma	10 ± 10	10 ± 10	1000	Yes

Table 3.32. Zircon-helium inputs to model for 15mfs05.

Raw Age (Ma)	Error (Ma)	eU (ppm)	Grain length (microns)	Grain width (microns)	Grain thickness (microns)
Sample 15mfs05 (zircon)					
19.86	0.25	185.0	185	80	80
21.96	0.66	357.9	180	95	95
33.43	0.75	346.3	150	75	65

3.9.3.12 Sample 17mfs20

Table 3.33. Thermal history constraints for model for 17mfs20.

Range for Time (m.y.) general prior	Range for Temp (°C) general prior	Geologic unit and depositional or emplacement age	Temp at Deposition (°C)	Present Day Surface Temp (°C)	Max. ∂T/∂t (°C/m.y.)	Pre-dep. History?
151.83 ± 151.83*	150 ± 150	Pahau (Torlesse): 120 ± 22 Ma	10 ± 10	10 ± 10	1000	No

*Oldest single-grain age ± itself

Table 3.34. Apatite- and zircon-helium inputs to model for 17mfs20.

Raw Age (Ma)	Error (Ma)	eU (ppm)	Grain length (microns)	Grain width (microns)	Grain thickness (microns)
Sample 17mfs20 (apatite)					
6.42	0.31	14.7	100	85	70
4.25	0.10	46.5	95	80	85

4.98	0.18	39.1	95	75	75
4.66	0.21	31.1	70	75	60
7.97	0.22	20.8	130	90	100
Sample 17mfs20 (zircon)					
151.83	2.93	171.6	185	105	90
135.33	2.67	257.9	215	115	115
141.81	1.54	285.0	190	100	115

Table 3.35. Apatite fission track data inputs to model for 17mfs20.

Ns	**Age (Ma)**	**Age‡ Error (Ma)**	**Dpar (microns)**	**Zeta**
Sample 17mfs20 (AFT)				
2	28.11	21.28	2.15	8.2727
6	29	16.22	2.02	8.2727
26	65.2	21.49	1.8	8.2727
2	59	44.69	2	8.2727
1	12.65	10.94	1.84	8.2727
6	15.65	8.75	1.75	8.2727
9	21.76	10.6	1.99	8.2727
1	3.68	3.18	1.93	8.2727
3	4.69	3.21	1.7	8.2727
0	0	51.07	1.62	8.2727
2	5.75	4.36	1.7	8.2727
1	4.01	3.47	1.63	8.2727
72	67.76	14.97	2.84	8.2727
5	9.29	5.51	1.78	8.2727
23	87.13	29.78	2.4	8.2727
0	0	122.63	1.75	8.2727
0	0	30.96	1.96	8.2727
4	7.66	4.85	1.83	8.2727
2	78.36	59.25	2.39	8.2727
1	1.59	1.38	2.12	8.2727
1	11.45	9.9	1.87	8.2727
0	0	52.2	1.76	8.2727
4	12.07	7.65	2.08	8.2727
47	81.9	21.44	2.53	8.2727
110	67.89	12.15	2.73	8.2727
0	0	73.02	1.89	8.2727
8	12.2	6.2	1.65	8.2727
1	0.58	0.5	1.87	8.2727
4	17.07	10.79	1.72	8.2727
5	29.35	17.36	1.66	8.2727

3	5.93	4.06	1.86	8.2727
17	64.67	25.07	1.66	8.2727
8	16.65	8.48	2.06	8.2727
10	68.53	32.35	2.13	8.2727
4	86.74	54.78	1.86	8.2727
7	12.84	6.82	1.86	8.2727
11	39.24	17.81	1.72	8.2727
*50**	*0**	*0**	*1.82**	*8.2727**
1	6.27	5.42	1.93	8.2727
0	0	89.44	2.15	8.2727

***** Italics indicate data not used because age and both positive and negative error = 0

Table 3.36. Apatite fission track length data inputs to model for 17mfs20.

Length (microns)	**C-axis Angle (°)**	**Dpar (microns)**
Sample 17mfs20 (AFT length)		
12.35	76.35	1.82
13.54	37.82	1.82
11.01	57.84	1.84
12.69	34.76	2.25
11.82	48.61	2.25
9.53	65.70	2.22
9.32	55.88	2.22
13.93	50.19	2.02
14.07	58.48	2.02
9.06	38.27	2.02
8.27	56.10	2.21
10.43	55.94	2.21
13.30	19.78	2.21
10.03	37.49	2.25
12.25	71.67	2.25
8.80	75.86	2.27
8.84	79.00	1.84
10.90	37.96	1.84
12.56	49.44	2.03
14.56	54.93	2.03
9.53	60.00	2.03
13.35	41.35	2.07
11.81	73.41	2.07
11.16	60.85	1.95
15.36	24.58	1.95
14.66	54.73	1.95
8.53	48.56	1.95
12.36	47.58	1.95
9.46	61.68	1.95
10.67	75.15	2.51
15.51	20.64	2.51
9.88	82.04	2.51
11.69	40.55	2.51
12.64	48.38	2.09

11.72	51.19	2.09
13.23	62.74	2.47
11.27	79.33	2.47
12.44	82.65	2.47
13.16	36.04	2.47
12.12	43.81	2.47
12.88	59.71	2.17
9.74	45.32	1.92
14.47	48.08	1.92
11.43	13.90	1.92
11.76	71.54	1.92
14.44	38.88	2.44
14.73	72.92	2.44
8.54	47.42	2.44
9.81	85.80	1.92
9.71	62.48	1.92
11.40	44.19	1.92
14.35	48.97	1.92
9.50	81.46	2.00
9.17	50.52	2.00
12.04	54.53	2.42
10.38	65.86	2.42
14.77	51.19	2.03
11.46	58.49	2.53
11.46	75.02	2.53
10.25	33.30	2.19
14.71	31.51	2.19
13.85	84.07	2.19
14.53	56.72	2.58
13.01	76.18	2.58
12.58	51.13	2.58
11.28	50.18	2.58
8.13	32.36	2.58
12.91	36.36	2.58
14.08	56.85	2.26
13.22	66.47	1.90
11.40	56.48	1.90
7.23	46.10	1.82
14.08	52.59	1.82
10.55	28.98	1.84
9.94	36.93	2.00
10.47	73.72	2.00
10.37	51.65	2.00
10.00	46.40	2.00
9.00	61.68	2.00
10.05	63.94	2.00
8.86	50.58	1.95
13.76	49.54	1.95
15.42	39.79	1.99
8.46	60.69	1.97
11.65	39.47	1.97
11.37	80.09	2.26
10.55	55.44	2.26

10.62	74.67	2.26
10.38	55.10	2.13
13.76	24.91	2.13
11.53	51.11	2.57
10.77	52.01	2.57
11.99	52.20	2.85
9.84	41.55	2.85
10.51	51.84	2.85
9.77	37.97	2.09
7.58	62.40	2.09
10.30	66.68	2.09
11.05	31.02	2.09
11.88	57.29	2.09
9.74	71.22	2.09
13.09	47.36	2.09
13.13	72.95	2.15
7.71	68.74	2.15
10.07	33.13	2.10
13.14	41.16	2.12
10.44	53.71	2.12

3.9.3.13 Sample 17mfs21

Table 3.37. Thermal history constraints for model for 17mfs21.

Range for Time (m.y.) general prior	Range for Temp (°C) general prior	Geologic unit and depositional or emplacement age	Temp at Deposition (°C)	Present Day Surface Temp (°C)	Max. ∂T/∂t (°C/m.y.)	Pre-dep. History?
45.70 ± 45.70*	150 ± 150	Pahau (Torlesse): 120 ± 22 Ma	10 ± 10	10 ± 10	1000	No

*Oldest single-grain age ± itself

Table 3.38. Apatite- and zircon-helium inputs to model for 17mfs21.

Raw Age (Ma)	Error (Ma)	eU (ppm)	Grain length (microns)	Grain width (microns)	Grain thickness (microns)
Sample 17mfs21 (apatite)					
2.17	0.17	6.0	90	80	90
2.59	0.26	5.2	115	90	90
2.87	0.15	14.5	80	95	90
3.39	0.27	8.4	120	90	90
2.78	0.13	21.4	115	85	60

Sample 17mfs21 (zircon)					
38.50	0.41	494.3	190	80	90
45.70	0.71	513.3	160	65	75
16.16	0.42	66.6	165	90	75

Table 3.39. Apatite fission track data inputs to model for 17mfs21.

Ns	**Age (Ma)**	**Age‡ Error (Ma)**	**Dpar (microns)**	**Zeta**
Sample 17mfs21 (AFT)				
0	0	74.39	3.08	8.2727
0	0	172.02	1.89	8.2727
1	26.72	23.1	1.81	8.2727
1	15.28	13.21	2.28	8.2727
2	3.54	2.68	1.78	8.2727
2	11.81	8.95	2.22	8.2727
0	0	26.62	2.17	8.2727
*0**	*0**	*0**	*2.22**	*8.2727**
1	15.13	74.39	1.92	8.2727
0	0	172.02	1.77	8.2727
2	4.55	23.1	1.86	8.2727
0	0	13.21	1.92	8.2727
0	0	2.68	2.25	8.2727
1	6.31	8.95	1.85	8.2727
0	0	26.62	2.08	8.2727
1	16.61	74.39	1.85	8.2727
3	74.48	172.02	1.98	8.2727
0	0	23.1	2.27	8.2727
2	35.79	13.21	1.98	8.2727
1	7.67	2.68	2.54	8.2727
2	166.88	8.95	2.44	8.2727
2	48.46	26.62	1.95	8.2727
3	4.61	74.39	2.56	8.2727
1	12.39	172.02	2.16	8.2727
4	3.27	23.1	1.83	8.2727
0	0	13.21	1.66	8.2727
0	0	2.68	2.76	8.2727
6	20.34	8.95	2.62	8.2727
7	12.19	26.62	1.76	8.2727
0	0	74.39	1.8	8.2727
0	0	172.02	2.21	8.2727
1	9.2	23.1	2.48	8.2727
1	52.47	13.21	1.84	8.2727
4	11.1	2.68	2.1	8.2727
1	28.14	8.95	2.25	8.2727

0	0	26.62	1.7	8.2727
1	15.88	74.39	2.16	8.2727
12	5.33	172.02	1.71	8.2727
0	0	23.1	2.25	8.2727
0	0	13.21	3.08	8.2727

***** Italics indicate data not used because age and both positive and negative error = 0

Table 3.40. Apatite fission track length data inputs to model for 17mfs21.

Length (microns)	**C-axis Angle (°)**	**Dpar (microns)**
Sample 17mfs21 (AFT length)		
8.61	50.28	3.18
13.51	32.34	3.13
10.70	76.88	3.21
15.48	38.29	2.92
15.38	2.57	2.64
10.94	51.69	2.64
12.52	67.97	2.47
14.08	53.92	2.49
15.29	43.32	2.47
7.03	55.46	2.59
12.56	77.52	2.51
16.18	17.19	2.51
15.27	49.79	2.51
11.72	67.15	2.51
10.22	78.23	2.83
12.97	3.91	2.90
11.38	40.76	2.90
17.25	30.26	2.45
9.57	46.13	2.99
13.46	33.26	3.11
11.69	67.79	3.22
15.50	41.30	2.89
10.51	70.76	2.43
15.11	51.88	2.44
14.32	38.21	2.45
7.13	49.39	2.54
10.25	72.30	2.79

3.9.3.14 Sample 17mfs22

Table 3.41. Thermal history constraints for model for 17mfs22.

Range for Time (m.y.) general prior	Range for Temp (°C) general prior	Geologic unit and depositional or emplacement age	Temp at Deposition (°C)	Present Day Surface Temp (°C)	Max. ∂T/∂t (°C/m.y.)	Pre-dep. History?
150 ± 150	150 ± 150	Esk Head (Torlesse): 227 ± 21 Ma	10 ± 10	10 ± 10	1000	Yes

Table 3.42. Zircon-helium inputs to model for 17mfs22.

Raw Age (Ma)	Error (Ma)	eU (ppm)	Grain length (microns)	Grain width (microns)	Grain thickness (microns)
Sample 17mfs22 (zircon)					
123.94	1.60	402.5	150	75	75
86.89	2.85	129.1	180	75	70
133.03	3.46	84.6	140	90	80

3.9.3.15 Sample 17mfs23

Table 3.43. Thermal history constraints for model for 17mfs23.

Range for Time (m.y.) general prior	Range for Temp (°C) general prior	Geologic unit and depositional or emplacement age	Temp at Deposition (°C)	Present Day Surface Temp (°C)	Max. ∂T/∂t (°C/m.y.)	Pre-dep. History?
100 ± 100	150 ± 150	Pahau (Torlesse): 120 ± 22 Ma	10 ± 10	10 ± 10	1000	Yes

Table 3.44. Zircon-helium inputs to model for 17mfs23.

Raw Age (Ma)	Error (Ma)	eU (ppm)	Grain length (microns)	Grain width (microns)	Grain thickness (microns)
Sample 17mfs23 (zircon)					
114.03	2.34	200.4	175	75	100
62.35	1.34	120.4	150	80	100
160.66	2.28	386.3	190	80	75

Table 3.45. Apatite fission track data inputs to model for 17mfs23.

Ns	Age (Ma)	Age‡ Error (Ma)	Dpar (microns)	Zeta
Sample 17mfs23 (AFT)				
0	0	39.61	1.93	8.2727
1	18.84	16.87	1.63	8.2727
1	7.75	6.7	1.59	8.2727
28	132.26	62.24	1.94	8.2727
0	0	387.13	1.22	8.2727
1	6.8	5.88	2.04	8.2727
1	7.06	6.11	1.84	8.2727
0	0	8.52	2.18	8.2727
0	0	112.38	2.04	8.2727
30	88.68	27.62	2.41	8.2727
0	0	61.83	1.76	8.2727
1	1.37	1.19	2.16	8.2727
0	0	95.78	2.22	8.2727
0	0	118.33	1.85	8.2727
0	0	24.81	1.98	8.2727
0	0	44.04	1.9	8.2727
0	0	61.88	1.57	8.2727
0	0	76.77	2.36	8.2727
*0**	*0**	*14052.32**	*1.82**	*8.2727**
0	0	54.1	1.8	8.2727
0	0	233.95	1.89	8.2727
0	0	118.39	1.75	8.2727
7	28.57	16.12	1.96	8.2727
0	0	7.9	1.85	8.2727
0	0	663.43	1.97	8.2727
0	0	32.29	1.98	8.2727
0	0	18.22	1.83	8.2727
3	4.96	3.4	1.8	8.2727
2	7.7	5.83	1.77	8.2727

0	0	14.43	2.01	8.2727
0	0	20.36	1.81	8.2727
1	3.16	2.74	2.07	8.2727
0	0	5.54	1.74	8.2727
0	0	110.24	1.58	8.2727
0	0	8.86	1.58	8.2727
1	4.37	3.77	1.91	8.2727
*0**	*0*	*4116.17*	*1.55*	*8.2727*
0	0	3.97	1.92	8.2727
0	0	229.18	1.73	8.2727
1	0.83	0.71	2.2	8.2727

***** Italics indicate data not used because age and negative error = 0 and positive error is extremely large.

Table 3.46. Apatite fission track length data inputs to model for 17mfs23.

Length (microns)	**C-axis Angle (°)**	**Dpar (microns)**
Sample 17mfs23 (AFT length)		
15.70	17.35	1.98
9.99	64.66	2.08
13.29	42.54	2.08
10.82	63.19	2.08
11.84	62.67	2.08
11.28	74.90	2.08
14.78	17.49	2.46
11.59	64.70	2.12
9.43	73.11	2.23
12.91	55.43	2.27
13.83	56.07	2.27
18.16	23.39	2.27
10.27	54.68	2.27
11.49	75.53	2.39
12.83	40.32	2.39
13.16	32.26	1.84
13.68	57.21	2.12

3.9.3.16 Sample 17mfs25

Table 3.47. Thermal history constraints for model for 17mfs25.

Range for Time (m.y.) general prior	Range for Temp (°C) general prior	Geologic unit and depositional or emplacement age	Temp at Deposition (°C)	Present Day Surface Temp (°C)	Max. ∂T/∂t (°C/m.y.)	Pre-dep. History?
150 ± 150	150 ± 150	Esk Head (Torlesse): 227 ± 21 Ma	10 ± 10	10 ± 10	1000	Yes

Table 3.48. Apatite- and zircon-helium inputs to model for 17mfs25.

Raw Age (Ma)	Error (Ma)	eU (ppm)	Grain length (microns)	Grain width (microns)	Grain thickness (microns)
Sample 17mfs25 (apatite)					
7.89	0.37	23.2	75	75	70
3.20	0.13	78.9	85	85	70
4.54	0.26	11.0	90	75	85
2.95	0.08	23.3	95	115	90
Sample 17mfs25 (zircon)					
35.22	0.63	133.6	180	85	105
27.29	0.44	429.9	150	75	90
98.18	1.13	471.0	140	80	75

Table 3.49. Apatite fission track data inputs to model for 17mfs25.

Ns	Age (Ma)	Age‡ Error (Ma)	Dpar (microns)	Zeta
Sample 17mfs25 (AFT)				
0	0	9.58	1.84	8.2727
1	3.39	2.93	2.15	8.2727
1	6.54	5.65	1.87	8.2727
0	0	35.31	2.03	8.2727
0	0	33.5	1.7	8.2727
2	4.62	3.5	2.1	8.2727
0	0	17.33	1.65	8.2727
1	7.17	6.2	1.73	8.2727
0	0	62.92	1.62	8.2727
2	6.93	5.25	2.03	8.2727
1	6.46	5.59	1.93	8.2727

0	0	44.71	1.53	8.2727
0	0	41.56	1.64	8.2727
0	0	8.53	1.91	8.2727
1	39.81	34.42	1.75	8.2727
0	0	27.34	1.99	8.2727
2	9.35	7.08	2.12	8.2727
3	10.37	7.11	2.09	8.2727
2	5.78	4.38	1.8	8.2727
0	0	7.27	1.84	8.2727
0	0	48.98	1.84	8.2727
0	0	26.9	1.68	8.2727
0	0	79.33	1.99	8.2727
0	0	26.89	1.97	8.2727
1	4.05	3.5	1.77	8.2727
0	0	65.85	1.84	8.2727
1	7.9	6.83	2.18	8.2727
1	2.56	2.22	1.73	8.2727
0	0	27.89	1.75	8.2727
0	0	8.96	2.02	8.2727
1	3.96	3.43	2.09	8.2727
0	0	95.9	1.65	8.2727
1	87.16	75.33	1.78	8.2727
3	14.71	10.07	1.89	8.2727
0	0	4.48	1.53	8.2727
1	9.56	8.27	1.99	8.2727
2	42.77	32.36	1.91	8.2727
1	8.81	7.62	1.5	8.2727
14	6.56	2.72	1.99	8.2727
5	14.08	8.33	2.1	8.2727

Table 3.50. Apatite fission track length data inputs to model for 17mfs25.

Length (microns)	**C-axis Angle (°)**	**Dpar (microns)**
Sample 17mfs25 (AFT length)		
14.07	50.26	1.95
14.76	40.51	1.95
12.55	70.96	2.70
16.02	42.00	2.70
12.06	44.19	2.37
13.61	15.33	1.70
12.04	85.48	1.70
14.50	43.12	1.84
12.13	72.00	1.84
11.17	82.22	2.50
15.95	19.24	1.62
16.09	40.68	2.49
16.21	28.92	2.50

14.06	39.59	2.34
16.49	64.63	2.96
9.10	54.42	2.21
11.29	49.53	2.21
12.51	56.34	2.21
14.74	42.60	2.04
11.78	33.27	2.04
12.46	37.87	2.33
14.52	33.78	2.33
13.39	64.84	2.33
9.69	42.63	2.33
12.46	70.06	2.33
12.15	60.82	2.48
12.61	58.47	2.48
16.38	29.51	2.30
15.12	27.22	2.30

3.9.3.17 Sample 17mfs26

Table 3.51. Thermal history constraints for model for 17mfs26.

Range for Time (m.y.) general prior	**Range for Temp (°C) general prior**	**Geologic unit and depositional or emplacement age**	**Temp at Deposition (°C)**	**Present Day Surface Temp (°C)**	**Max. ∂T/∂t (°C/m.y.)**	**Pre-dep. History?**
150 ± 150	200 ± 200	Esk Head (Torlesse): 227 ± 21 Ma	10 ± 10	10 ± 10	1000	Yes

Table 3.52. Zircon-helium inputs to model for 17mfs26.

Raw Age (Ma)	**Error (Ma)**	**eU (ppm)**	**Grain length (microns)**	**Grain width (microns)**	**Grain thickness (microns)**
Sample 17mfs26 (zircon)					
11.96	0.15	335.0	190	95	80
18.00	0.26	360.3	180	100	100
100.85	1.81	257.0	170	80	95

3.9.3.18 Sample 17mfs29

Table 3.53. Thermal history constraints for model for 17mfs29.

Range for Time (m.y.) general prior	Range for Temp (°C) general prior	Geologic unit and depositional or emplacement age	Temp at Deposition (°C)	Present Day Surface Temp (°C)	Max. ∂T/∂t (°C/m.y.)	Pre-dep. History?
100 ± 100	100 ± 100	Pahau (Torlesse): 120 ± 22 Ma	10 ± 10	10 ± 10	1000	Yes

Table 3.54. Apatite- and zircon-helium inputs to model for 17mfs29.

Raw Age (Ma)	Error (Ma)	eU (ppm)	Grain length (microns)	Grain width (microns)	Grain thickness (microns)
Sample 17mfs29 (apatite)					
7.09	0.12	65.5	110	120	90
7.24	0.23	14.6	125	95	75
14.77	0.35	22.2	115	110	85
12.59	0.62	12.6	95	75	65
Sample 17mfs29 (zircon)					
176.87	3.22	570.0	210	110	110
114.45	3.43	261.6	150	80	70
157.12	2.82	199.6	200	85	70

3.9.3.19 Sample 17mfs30

Table 3.55. Thermal history constraints for model for 17mfs30.

Range for Time (m.y.) general prior	Range for Temp (°C) general prior	Geologic unit and depositional or emplacement age	Temp at Deposition (°C)	Present Day Surface Temp (°C)	Max. ∂T/∂t (°C/m.y.)	Pre-dep. History?
100 ± 100	200 ± 200	Pahau (Torlesse): 120 ± 22 Ma	10 ± 10	10 ± 10	1000	Yes

Table 3.56. Zircon-helium inputs to model for 17mfs30.

Raw Age (Ma)	Error (Ma)	eU (ppm)	Grain length (microns)	Grain width (microns)	Grain thickness (microns)
Sample 17mfs30 (zircon)					
17.42	0.68	349.5	140	65	65
15.27	0.32	514.1	160	85	80
39.53	0.62	677.9	200	100	95

3.9.3.20 Sample 17mfs31

Table 3.57. Thermal history constraints for model for 17mfs31.

Range for Time (m.y.) general prior	Range for Temp (°C) general prior	Geologic unit and depositional or emplacement age	Temp at Deposition (°C)	Present Day Surface Temp (°C)	Max. ∂T/∂t (°C/m.y.)	Pre-dep. History?
100 ± 100	150 ± 150	Pahau (Torlesse): 120 ± 22 Ma	10 ± 10	10 ± 10	1000	Yes

Table 3.58. Apatite- and zircon-helium inputs to model for 17mfs31.

Raw Age (Ma)	Error (Ma)	eU (ppm)	Grain length (microns)	Grain width (microns)	Grain thickness (microns)
Sample 17mfs31 (apatite)					
4.76	0.17	16.9	125	150	115
5.37	0.14	47.4	125	100	80
3.22	0.15	12.0	113	90	100
3.54	0.14	41.1	70	90	75
Sample 17mfs31 (zircon)					
103.37	1.58	594.2	180	90	80
184.76	4.07	413.2	210	80	75
77.42	1.65	383.4	145	70	85

3.9.3.21 Sample 17mfs32

Table 3.59. Thermal history constraints for model for 17mfs32.

Range for Time (m.y.) general prior	Range for Temp (°C) general prior	Geologic unit and depositional or emplacement age	Temp at Deposition (°C)	Present Day Surface Temp (°C)	Max. ∂T/∂t (°C/m.y.)	Pre-dep. History?
100 ± 100	150 ± 150	Pahau (Torlesse): 120 ± 22 Ma	10 ± 10	10 ± 10	1000	Yes

Table 3.60. Apatite- and zircon-helium inputs to model for 17mfs32.

Raw Age (Ma)	Error (Ma)	eU (ppm)	Grain length (microns)	Grain width (microns)	Grain thickness (microns)
Sample 17mfs32 (apatite)					
7.57	1.22	5.5	65	75	65
8.36	0.64	21.8	60	80	60
5.37	0.44	27.3	95	70	60
10.12	0.41	14.3	85	75	75
Sample 17mfs32 (zircon)					
81.61	1.64	640.9	110	70	67
142.86	2.35	329.4	120	60	62
82.94	2.65	377.9	130	60	65

3.9.3.22 Sample 17mfs37

Table 3.61. Thermal history constraints for model for 17mfs37.

Range for Time (m.y.) general prior	Range for Temp (°C) general prior	Geologic unit and depositional or emplacement age	Temp at Deposition (°C)	Present Day Surface Temp (°C)	Max. ∂T/∂t (°C/m.y.)	Pre-dep. History?
50 ± 50	200 ± 200	Pahau (Torlesse): 120 ± 22 Ma	10 ± 10	10 ± 10	1000	No

Table 3.62. Apatite- and zircon-helium inputs to model for 17mfs37.

Raw Age (Ma)	Error (Ma)	eU (ppm)	Grain length (microns)	Grain width (microns)	Grain thickness (microns)
Sample 17mfs37 (apatite)					
2.70	0.47	11.0	75	80	60
2.44	0.43	10.9	70	65	60
1.82	0.35	18.6	70	70	65
2.20	0.36	13.3	90	70	60
2.32	0.34	11.6	85	75	60
Sample 17mfs37 (zircon)					
7.18	0.12	101.9	175	110	100
5.67	0.08	130.2	120	60	80
12.49	0.17	160.9	125	75	60

3.9.3.23 Sample 17mfs42

Table 3.63. Thermal history constraints for model for 17mfs42.

Range for Time (m.y.) general prior	Range for Temp (°C) general prior	Geologic unit and depositional or emplacement age	Temp at Deposition (°C)	Present Day Surface Temp (°C)	Max. $\partial T/\partial t$ (°C/m.y.)	Pre-dep. History?
25.2 ± 25.2*	150 ± 150	Pahau (Torlesse): 120 ± 22 Ma	10 ± 10	10 ± 10	1000	No

*Oldest single-grain age ± itself

Table 3.64. Apatite- and zircon-helium inputs to model for 17mfs42.

Raw Age (Ma)	Error (Ma)	eU (ppm)	Grain length (microns)	Grain width (microns)	Grain thickness (microns)
Sample 17mfs42 (apatite)					
2.57	0.15	20.2	85	70	85
3.70	0.15	75.3	80	85	65
1.53	0.10	37.4	90	110	65
3.57	0.27	8.7	120	90	60
2.09	0.20	6.7	85	100	95

Sample 17mfs42 (zircon)					
25.20	0.40	201.6	147	75	70
14.32	0.21	192.6	130	75	65
20.16	0.25	273.2	135	80	65

3.9.4 *Equivalent QTQt Inputs for Unmodelled Samples*

3.9.4.1 Sample 17mfs36

Table 3.65. Zircon-helium data for sample 17mfs36.

Raw Age (Ma)	**Error (Ma)**	**eU (ppm)**	**Grain length (microns)**	**Grain width (microns)**	**Grain thickness (microns)**
Sample 17mfs36 (zircon)					
72.20	0.58	451.7	150	75	95
113.41	1.57	307.4	205	85	70
85.87	1.21	479.7	165	70	80

3.9.4.2 Sample 17mfs38

Table 3.66. Apatite- and zircon-helium data for 17mfs38.

Raw Age (Ma)	**Error (Ma)**	**eU (ppm)**	**Grain length (microns)**	**Grain width (microns)**	**Grain thickness (microns)**
Sample 17mfs38 (apatite)					
1.14	0.07	26.2	110	60	85
3.64	0.15	7.6	130	130	125
0.87	0.08	25.8	110	75	85
Sample 17mfs38 (zircon)					
113.07	1.90	718.0	170	80	90
114.84	1.17	374.7	205	90	120
127.62	2.09	410.3	190	110	105

3.9.5 *Data Used in GLIDE Inversion*

Table 3.67. Thermochronology data used in GLIDE inversion. References for data are listed after table. Note: "Seward, unpublished" data was from Jiao, 2017.

Longitude	Latitude	Elevation	Age, Ma	Age Error, Ma	System	Reference
173.1908	-41.6841	381	77.89	39.46	ZHe	Ch. 2, this dissertation
173.2172	-41.7811	928	173.29	44.75	ZHe	Ch. 2, this dissertation
172.2772	-42.3843	608	2.38	0.22	ZHe	Ch. 2, this dissertation
172.7733	-41.8607	1763	9.14	1.23	ZHe	Ch. 2, this dissertation
172.8096	-41.8323	1387	13.77	4.88	ZHe	Ch. 2, this dissertation
172.8112	-41.8281	1197	13.72	5.3	ZHe	Ch. 2, this dissertation
172.8114	-41.8247	989	8.83	2.23	ZHe	Ch. 2, this dissertation
172.8121	-41.8232	892	30.18	22.12	ZHe	Ch. 2, this dissertation
172.8169	-41.7832	607	51.52	7.15	ZHe	Ch. 2, this dissertation
173.2364	-41.6362	318	37.5	10.28	ZHe	Ch. 2, this dissertation
173.6273	-41.4838	487	24.93	3.84	ZHe	Ch. 2, this dissertation
173.4108	-41.6323	490	110.7	32.47	ZHe	Ch. 2, this dissertation
172.4785	-41.9010	402	110.27	9.12	ZHe	Ch. 2, this dissertation
172.4318	-42.3290	927	3.66	0.51	ZHe	Ch. 2, this dissertation
172.4529	-42.3014	1064	2.65	0.69	ZHe	Ch. 2, this dissertation
173.2172	-41.7811	928	5.41	0.42	AHe	Ch. 2, this dissertation
172.8121	-41.8232	892	9.33	8.1	AHe	Ch. 2, this dissertation
172.5200	-42.0189	420	1.59	0.42	AHe	Ch. 2, this dissertation
172.4785	-41.9010	402	7.03	2.95	AHe	Ch. 2, this dissertation
172.4318	-42.3290	927	1.25	0.22	AHe	Ch. 2, this dissertation
172.4529	-42.3014	1064	1.22	0.06	AHe	Ch. 2, this dissertation
172.8121	-41.8232	892	3.9	0.34	AFT	Ch. 2, this dissertation
172.5200	-42.0189	420	2.01	0.265	AFT	Ch. 2, this dissertation
172.4785	-41.9010	402	68.81	2.47	AFT	Ch. 2, this dissertation
172.4318	-42.3290	927	1.94	0.385	AFT	Ch. 2, this dissertation
172.4529	-42.3014	1064	2.91	0.34	AFT	Ch. 2, this dissertation
173.7433	-41.8494	480	152.13	75.68	ZHe	Ch. 3, this dissertation
173.7604	-41.8842	851	141.85	38.39	ZHe	Ch. 3, this dissertation
172.7729	-42.2923	997	32.16	21.74	ZHe	Ch. 3, this dissertation
173.9145	-41.9528	469	180.35	32.17	ZHe	Ch. 3, this dissertation
172.4497	-42.5884	446	50.07	28.94	ZHe	Ch. 3, this dissertation
173.7925	-42.0101	243	125.58	46.52	ZHe	Ch. 3, this dissertation
173.8741	-42.0056	163	70.06	10.57	ZHe	Ch. 3, this dissertation
173.5209	-41.8204	948	94.41	39.07	ZHe	Ch. 3, this dissertation
173.5907	-41.8772	901	33.09	10.85	ZHe	Ch. 3, this dissertation
173.8220	-41.7325	1104	19.41	9.18	ZHe	Ch. 3, this dissertation
173.7950	-41.7458	1474	25.68	7.03	ZHe	Ch. 3, this dissertation
173.7758	-41.7533	1685	28.87	14.16	ZHe	Ch. 3, this dissertation

172.8184	-42.5797	501	175.73	14.26	ZHe	Ch. 3, this dissertation
172.8696	-42.5100	491	44.22	21	ZHe	Ch. 3, this dissertation
172.7844	-42.3757	1009	151.67	31.3	ZHe	Ch. 3, this dissertation
172.7895	-42.4324	986	145.9	63.73	ZHe	Ch. 3, this dissertation
172.7849	-42.1822	1218	70.93	53.09	ZHe	Ch. 3, this dissertation
172.9094	-42.1032	975	55.69	63.85	ZHe	Ch. 3, this dissertation
173.5808	-41.9101	536	191.09	32.78	ZHe	Ch. 3, this dissertation
173.4051	-41.9843	837	34.53	20.81	ZHe	Ch. 3, this dissertation
173.4087	-42.0126	755	158.82	71.43	ZHe	Ch. 3, this dissertation
173.2328	-42.0966	963	146.61	50.01	ZHe	Ch. 3, this dissertation
173.2196	-42.0496	1784	105.81	40.49	ZHe	Ch. 3, this dissertation
173.2039	-42.0488	1513	90.65	25.02	ZHe	Ch. 3, this dissertation
173.1971	-42.0570	1211	137.33	16.5	ZHe	Ch. 3, this dissertation
172.9924	-42.3343	758	119.09	26.43	ZHe	Ch. 3, this dissertation
172.9189	-42.4333	746	11.58	5.33	ZHe	Ch. 3, this dissertation
172.3974	-42.5196	598	148.6	8.02	ZHe	Ch. 3, this dissertation
172.5783	-42.5917	421	27.25	7.29	ZHe	Ch. 3, this dissertation
173.7433	-41.8494	480	10.18	2.24	AHe	Ch. 3, this dissertation
173.7604	-41.8842	851	5.41	2.32	AHe	Ch. 3, this dissertation
173.9145	-41.9528	469	5.22	4.06	AHe	Ch. 3, this dissertation
172.4497	-42.5884	446	1.84	0.035	AHe	Ch. 3, this dissertation
173.7925	-42.0101	243	1.72	1.19	AHe	Ch. 3, this dissertation
173.8741	-42.0056	163	1.48	0.2	AHe	Ch. 3, this dissertation
173.1934	-42.0698	1016	2.96	0.32	AHe	Ch. 3, this dissertation
173.5209	-41.8204	948	4.46	0.74	AHe	Ch. 3, this dissertation
173.8220	-41.7325	1104	9.16	2.35	AHe	Ch. 3, this dissertation
172.8184	-42.5797	501	9.16	1.93	AHe	Ch. 3, this dissertation
172.8696	-42.5100	491	4.23	0.67	AHe	Ch. 3, this dissertation
172.7849	-42.1822	1218	7.64	4	AHe	Ch. 3, this dissertation
173.5808	-41.9101	536	16.39	6.55	AHe	Ch. 3, this dissertation
173.4087	-42.0126	755	6.41	1.39	AHe	Ch. 3, this dissertation
173.2328	-42.0966	963	14.01	3.22	AHe	Ch. 3, this dissertation
172.9189	-42.4333	746	4.21	0.58	AHe	Ch. 3, this dissertation
172.3974	-42.5196	598	2.68	1.91	AHe	Ch. 3, this dissertation
172.5783	-42.5917	421	4.46	1.78	AHe	Ch. 3, this dissertation
172.7729	-42.2923	997	7.61	0.59	AFT	Ch. 3, this dissertation
172.8184	-42.5797	501	28.53	1.43	AFT	Ch. 3, this dissertation
172.8696	-42.5100	491	7.44	0.845	AFT	Ch. 3, this dissertation
172.7849	-42.1822	1218	4.92	0.625	AFT	Ch. 3, this dissertation
172.7895	-42.4324	986	12.65	0.28	AFT	Ch. 3, this dissertation
173.3600	-42.4200	402	1.9	0.3	AHe	Collett et al., 2019
173.3600	-42.4200	402	318.3	3.05	ZHe	Collett et al., 2019
173.3400	-42.4100	478	2.6	0.45	AHe	Collett et al., 2019
173.3400	-42.4100	478	218.3	11.7	ZHe	Collett et al., 2019
173.3500	-42.4000	759	6.8	2.75	AHe	Collett et al., 2019

173.3500	-42.4000	759	149.5	16.85	ZHe	Collett et al., 2019
173.3400	-42.3900	1118	4.1	0.15	AHe	Collett et al., 2019
173.3400	-42.3900	1118	141.9	38.75	ZHe	Collett et al., 2019
173.6300	-42.3300	457	2.9	0.05	AHe	Collett et al., 2019
173.6300	-42.3300	457	15.4	2.2	ZHe	Collett et al., 2019
173.6100	-42.3100	1596	3.5	0.65	AHe	Collett et al., 2019
173.6100	-42.3100	1596	12.5	2.7	ZHe	Collett et al., 2019
173.7200	-42.3100	65	4.1	0.55	AHe	Collett et al., 2019
173.7200	-42.3100	65	225.2	1.3	ZHe	Collett et al., 2019
173.7700	-42.2600	127	121.91	4.485	AFT	Collett et al., 2019
173.6800	-42.3000	159	177.4	30.65	ZHe	Collett et al., 2019
173.6900	-42.2900	171	4.2	0.6	AHe	Collett et al., 2019
173.6900	-42.2900	171	192.2	4.5	ZHe	Collett et al., 2019
173.6800	-42.2800	219	2.1	0.3	AHe	Collett et al., 2019
173.6800	-42.2800	219	19	1.55	ZHe	Collett et al., 2019
173.6800	-42.2800	219	9.78	0.84	AFT	Collett et al., 2019
173.6700	-42.2500	698	27.5	11.4	AHe	Collett et al., 2019
173.6600	-42.2500	1162	3	1.25	AHe	Collett et al., 2019
173.6600	-42.2400	1562	2.4	0.35	AHe	Collett et al., 2019
173.6500	-42.2300	2120	2.6	0.4	AHe	Collett et al., 2019
173.6200	-42.2200	2494	2	0.25	AHe	Collett et al., 2019
173.6200	-42.2200	2494	114.4	15.5	ZHe	Collett et al., 2019
173.6200	-42.2200	2494	45.78	2.745	AFT	Collett et al., 2019
173.6300	-42.1600	856	1.8	0.55	AHe	Collett et al., 2019
173.6300	-42.1600	856	158.3	30.55	ZHe	Collett et al., 2019
173.1900	-42.3400	913	7.8	1.65	AHe	Collett et al., 2019
173.1900	-42.3400	913	152.2	27.95	ZHe	Collett et al., 2019
173.1900	-42.3300	857	3.8	0.6	AHe	Collett et al., 2019
173.1900	-42.3300	857	25.5	11.6	ZHe	Collett et al., 2019
173.7400	-42.0500	278	1.9	0.35	AHe	Collett et al., 2019
173.7400	-42.0500	278	165.9	35.45	ZHe	Collett et al., 2019
173.7200	-42.0300	447	7.5	0.6	AHe	Collett et al., 2019
173.7200	-42.0300	447	142.5	13.4	ZHe	Collett et al., 2019
173.7000	-42.0200	890	27.5	0.5	AHe	Collett et al., 2019
173.7000	-42.0200	996	6.8	1.85	AHe	Collett et al., 2019
173.7000	-42.0200	996	35.1	5.05	ZHe	Collett et al., 2019
173.7000	-42.0100	1278	3.4	0.05	AHe	Collett et al., 2019
173.6800	-42.0000	2046	71.5	1.7	ZHe	Collett et al., 2019
173.6700	-41.9900	2601	10.1	3.05	AHe	Collett et al., 2019
173.6600	-41.9900	2811	109.2	0.4	ZHe	Collett et al., 2019
173.6400	-41.9700	1350	9.8	0.4	AHe	Collett et al., 2019
173.9755	-41.6079	220	18.5	5	AFT	Kao, 2001
173.9662	-41.6269	300	26.3	3.6	AFT	Kao, 2001
173.6045	-41.7103	300	70.5	9.3	AFT	Kao, 2001
173.5737	-41.7591	500	16.5	2.7	AFT	Kao, 2001

173.4891	-41.7019	320	17.4	3.1	AFT	Kao, 2001
173.4593	-41.7317	400	20	5.8	AFT	Kao, 2001
172.5278	-42.0323	460	2.1	1.5	AFT	Kao, 2001
172.5242	-42.0323	440	5.3	2.2	AFT	Kao, 2001
172.5195	-42.0188	420	3.8	1	AFT	Kao, 2001
172.8653	-41.8045	700	24.7	5.5	AFT	Kao, 2001
172.8902	-41.9747	800	9.7	3	AFT	Kao, 2001
172.9190	-42.0846	940	33.4	4.2	AFT	Kao, 2001
173.7632	-41.8202	400	113.2	13.4	AFT	Kao, 2001
173.7321	-41.8366	400	57.7	9.4	AFT	Kao, 2001
173.6938	-41.8557	400	102.7	10.4	AFT	Kao, 2001
173.6950	-41.8566	400	94.6	9.8	AFT	Kao, 2001
173.6590	-41.8757	400	100.2	6.4	AFT	Kao, 2001
173.5893	-41.8941	510	128.3	12.4	AFT	Kao, 2001
173.4213	-41.9993	1280	107.1	7.2	AFT	Kao, 2001
173.3311	-42.0608	840	95	11.5	AFT	Kao, 2001
173.2695	-42.0771	900	107.3	11.9	AFT	Kao, 2001
173.7317	-42.2336	460	23.2	7	AFT	Kao, 2001
173.9870	-41.9716	70	91.7	9.8	AFT	Kao, 2001
173.9845	-41.9680	120	67.3	8.4	AFT	Kao, 2001
172.7851	-42.3491	900	8.3	1.9	AFT	Kao, 2001
172.7946	-42.4211	840	11.2	2.8	AFT	Kao, 2001
172.9489	-42.4015	780	4.9	1.5	AFT	Kao, 2001
173.1243	-42.6482	110	110.2	9.6	AFT	Kao, 2001
173.2182	-42.6471	140	92.4	6	AFT	Kao, 2001
173.2723	-42.4625	360	113.3	9.4	AFT	Kao, 2001
173.4081	-42.3919	280	14.2	9.9	AFT	Kao, 2001
173.5065	-42.3969	100	45.2	4.7	AFT	Kao, 2001
173.5882	-42.4361	20	64.1	12.1	AFT	Kao, 2001
173.8280	-42.0844	150	98.1	9.5	AFT	Kao, 2001
173.8564	-42.2247	20	108.8	10.7	AFT	Kao, 2001
173.8313	-42.2465	40	19.4	4.5	AFT	Kao, 2001
173.7698	-42.2793	40	63.5	7.9	AFT	Kao, 2001
173.6202	-42.2217	2600	9.1	2.7	AFT	Kao, 2001
173.5899	-42.2227	1780	3.5	1.8	AFT	Kao, 2001
174.0857	-41.8860	60	81.7	7.5	AFT	Kao, 2001
174.0717	-41.8420	160	129	10	AFT	Kao, 2001
174.0402	-41.8297	300	19.5	5.3	AFT	Kao, 2001
174.0561	-41.8449	380	52.5	5.4	AFT	Kao, 2001
174.0681	-41.8439	260	78.1	9.8	AFT	Kao, 2001
173.9755	-41.6079	220	336.2	45.3	ZFT	Kao, 2002
173.9662	-41.6269	300	177	12.4	ZFT	Kao, 2002
173.6545	-41.6605	120	258.3	13.8	ZFT	Kao, 2002
173.6045	-41.7103	300	299	16.2	ZFT	Kao, 2002
173.5737	-41.7591	500	261.5	18.3	ZFT	Kao, 2002

173.6387	-41.6390	220	270.9	16.4	ZFT	Kao, 2002
173.5704	-41.6619	300	281.7	15.9	ZFT	Kao, 2002
173.4891	-41.7019	320	197	24.5	ZFT	Kao, 2002
173.4232	-41.7336	420	179.7	14.7	ZFT	Kao, 2002
173.4593	-41.7317	400	171.7	12.6	ZFT	Kao, 2002
173.2021	-41.7423	480	242.2	12.1	ZFT	Kao, 2002
173.2190	-41.7747	520	215.6	20.9	ZFT	Kao, 2002
173.1887	-41.6982	420	239.3	13.5	ZFT	Kao, 2002
173.1154	-41.7118	380	232.2	18.3	ZFT	Kao, 2002
172.5278	-42.0323	460	10	0.9	ZFT	Kao, 2002
172.5242	-42.0323	440	7.3	0.5	ZFT	Kao, 2002
172.5242	-42.0323	440	6.8	0.5	ZFT	Kao, 2002
172.5146	-42.0223	540	9.5	0.6	ZFT	Kao, 2002
172.8653	-41.8045	700	247.9	17.1	ZFT	Kao, 2002
172.9327	-41.8145	620	176.3	11.4	ZFT	Kao, 2002
172.8902	-41.9747	800	166.7	8.9	ZFT	Kao, 2002
172.9312	-42.0675	980	158.9	9.7	ZFT	Kao, 2002
172.9190	-42.0846	940	222.3	14.9	ZFT	Kao, 2002
172.8403	-42.1448	920	246.6	39.7	ZFT	Kao, 2002
173.9318	-41.5713	60	162.8	14.8	ZFT	Kao, 2002
173.7632	-41.8202	400	162	14.9	ZFT	Kao, 2002
173.6938	-41.8557	400	196.3	24.5	ZFT	Kao, 2002
173.6950	-41.8566	400	136.7	9.9	ZFT	Kao, 2002
173.6590	-41.8757	400	169.4	23.3	ZFT	Kao, 2002
173.5893	-41.8941	510	144.8	9	ZFT	Kao, 2002
173.4213	-41.9993	1280	141.3	11.5	ZFT	Kao, 2002
173.2695	-42.0771	900	132.5	13.1	ZFT	Kao, 2002
173.5917	-41.8941	500	192.6	30.4	ZFT	Kao, 2002
173.7292	-42.2237	620	172.7	13	ZFT	Kao, 2002
173.7305	-42.2282	640	147.5	13.4	ZFT	Kao, 2002
173.7317	-42.2336	460	152.2	9.2	ZFT	Kao, 2002
173.9870	-41.9716	70	143.6	13.2	ZFT	Kao, 2002
173.9845	-41.9680	120	176.3	25.1	ZFT	Kao, 2002
172.7720	-42.2915	1040	221.8	16.5	ZFT	Kao, 2002
172.7851	-42.3491	900	255.7	19.3	ZFT	Kao, 2002
172.7946	-42.4211	840	175.4	16.7	ZFT	Kao, 2002
172.8565	-42.4528	800	137.8	8.4	ZFT	Kao, 2002
172.8783	-42.4996	700	166	15.6	ZFT	Kao, 2002
172.9088	-42.4573	760	157.5	17.9	ZFT	Kao, 2002
172.9489	-42.4015	780	165.5	13.2	ZFT	Kao, 2002
173.1243	-42.6482	110	129	12	ZFT	Kao, 2002
173.2182	-42.6471	140	267.9	28.4	ZFT	Kao, 2002
173.2723	-42.4625	360	181.6	16.1	ZFT	Kao, 2002
172.9161	-42.4402	400	165.5	11.5	ZFT	Kao, 2002
173.4081	-42.3919	280	217	18.5	ZFT	Kao, 2002

173.5065	-42.3969	100	132.6	7.1	ZFT	Kao, 2002
173.5882	-42.4361	20	144.9	11.3	ZFT	Kao, 2002
173.5278	-42.4841	20	143.8	7.7	ZFT	Kao, 2002
173.8280	-42.0844	150	144	9.1	ZFT	Kao, 2002
173.8564	-42.2247	20	150.6	14.7	ZFT	Kao, 2002
173.8313	-42.2465	40	167.2	14.2	ZFT	Kao, 2002
173.7698	-42.2793	40	134.6	8.3	ZFT	Kao, 2002
173.7628	-42.1992	420	135.9	8.2	ZFT	Kao, 2002
173.7099	-42.2266	1200	150.6	15.9	ZFT	Kao, 2002
173.6989	-42.2239	1560	178.3	13.7	ZFT	Kao, 2002
173.6818	-42.2123	2200	158.4	27.4	ZFT	Kao, 2002
173.6601	-42.2170	2300	181.5	13.1	ZFT	Kao, 2002
173.6396	-42.2234	2400	141.9	12.31	ZFT	Kao, 2002
173.6202	-42.2217	2600	124.3	7.6	ZFT	Kao, 2002
173.5899	-42.2227	1780	173.2	11	ZFT	Kao, 2002
174.0857	-41.8860	60	131.7	10.7	ZFT	Kao, 2002
174.0717	-41.8420	160	238.5	15.5	ZFT	Kao, 2002
174.0416	-41.8432	220	159.3	12.9	ZFT	Kao, 2002
174.0402	-41.8297	300	143.8	14.3	ZFT	Kao, 2002
174.0561	-41.8449	380	134.7	13.9	ZFT	Kao, 2002
174.0681	-41.8439	260	165.7	19.2	ZFT	Kao, 2002
173.6387	-41.9675	1350	22	4	AFT	Baker and Seward, 1996
173.6347	-41.9777	1515	22	3	AFT	Baker and Seward, 1996
173.6439	-41.9740	1655	23	4	AFT	Baker and Seward, 1996
173.6435	-41.9744	1690	27	4	AFT	Baker and Seward, 1996
173.6276	-41.9929	1840	23	4	AFT	Baker and Seward, 1996
173.6559	-41.9826	2295	23	3	AFT	Baker and Seward, 1996
173.6585	-41.9835	2420	19	3	AFT	Baker and Seward, 1996
173.6439	-41.9740	1655	94	8	ZFT	Baker and Seward, 1996
173.6618	-41.9853	2705	92	7	ZFT	Baker and Seward, 1996
172.0314	-41.5564	244	6	0.95	AFT	Seward, unpublished
172.0419	-41.4988	470	10.1	0.8	AFT	Seward, unpublished
172.0479	-41.4971	366	5.3	0.75	AFT	Seward, unpublished
172.1559	-41.2098	30	17.1	1.6	AFT	Seward, unpublished
172.2347	-41.5975	213	9	1.5	AFT	Seward, unpublished
172.2634	-41.0881	986	20.1	1.55	AFT	Seward, unpublished

172.2666	-41.5374	305	3.6	0.3	AFT	Seward, unpublished
172.2716	-41.5167	244	7.8	0.5	AFT	Seward, unpublished
172.2874	-41.1729	1125	12.3	1.85	AFT	Seward, unpublished
172.2921	-41.3953	1128	10.3	1.6	AFT	Seward, unpublished
172.3369	-41.3416	1097	8.6	2.5	AFT	Seward, unpublished
172.3375	-41.2903	1280	3.86	0.7	AFT	Seward, unpublished
172.3633	-41.5767	914	6.8	1.03	AFT	Seward, unpublished
172.3638	-41.4066	884	8	1.15	AFT	Seward, unpublished
172.3667	-41.4750	640	8.4	1.69	AFT	Seward, unpublished
172.4989	-41.3021	500	12.2	1.6	AFT	Seward, unpublished
172.5153	-41.2876	100	12.4	1.65	AFT	Seward, unpublished
172.5961	-41.5481	1477	11.2	3.65	AFT	Seward, unpublished
172.4962	-41.7494	774	14.7	3.5	AFT	Gibson, 1993
172.4999	-41.7305	1341	8.9	2.2	AFT	Gibson, 1993
171.3981	-42.3379	288	13	1.4	AFT	Kamp et al., 1989
171.5302	-42.7482	243	0.7	1	AFT	Kamp et al., 1989
171.5919	-42.9811	731	3.9	1.4	AFT	Kamp et al., 1989
171.6140	-42.7802	352	0.8	1.2	AFT	Kamp et al., 1989
171.7299	-43.0105	671	6	3.6	AFT	Kamp et al., 1989
171.7663	-43.1323	702	14.3	21.6	AFT	Kamp et al., 1989
171.0688	-42.9276	159	2	0.3	AFT	Kamp et al., 1992
171.1104	-42.8957	96	0.8	0.6	AFT	Kamp et al., 1992
171.1139	-42.8817	100	4.3	0.5	AFT	Kamp et al., 1992
171.1497	-42.8859	157	1.6	0.9	AFT	Kamp et al., 1992
171.1700	-42.8448	333	3.8	0.5	AFT	Kamp et al., 1992
171.3124	-42.7530	173	4.3	0.6	AFT	Kamp et al., 1992
171.3246	-42.7596	140	7.2	1.6	AFT	Kamp et al., 1992
171.4286	-42.6519	174	10.8	1.1	AFT	Kamp et al., 1992
171.4430	-42.7655	247	3.8	0.6	AFT	Kamp et al., 1992
171.5061	-41.7241	0	23.6	2.8	AFT	Kamp et al., 1996
171.6601	-41.8326	148	17.2	2	AFT	Kamp et al., 1996
171.6630	-41.8358	146	13.2	1.6	AFT	Kamp et al., 1996
171.7127	-41.8467	46	7.4	0.9	AFT	Kamp et al., 1996
171.7565	-41.8575	147	24.5	2.8	AFT	Kamp et al., 1996
171.8030	-41.7842	382	19.7	1.7	AFT	Kamp et al., 1996
171.8089	-41.7578	609	23.6	3.9	AFT	Kamp et al., 1996
171.8224	-41.7128	584	15	2.1	AFT	Kamp et al., 1996
171.8306	-41.7695	861	19.5	5.1	AFT	Kamp et al., 1996
171.8414	-41.7569	677	17.8	5.6	AFT	Kamp et al., 1996
171.8550	-41.7037	983	13	1.4	AFT	Kamp et al., 1996
171.8578	-41.7429	599	8.2	2.8	AFT	Kamp et al., 1996
171.8588	-41.6272	0	19.2	1.6	AFT	Kamp et al., 1996
171.8658	-41.7274	638	12.4	1.9	AFT	Kamp et al., 1996
171.8672	-41.6303	200	18.8	1.2	AFT	Kamp et al., 1996
171.8689	-41.7050	784	12.7	1.2	AFT	Kamp et al., 1996

171.8970	-41.7018	744	7.7	0.7	AFT	Kamp et al., 1996
171.8970	-41.7018	744	10.1	1	AFT	Kamp et al., 1996
171.9188	-41.5517	0	5.4	0.8	AFT	Kamp et al., 1996
171.9343	-41.2703	0	8	0.6	AFT	Kamp et al., 1996
171.9555	-41.7100	355	16.5	1.7	AFT	Kamp et al., 1996
171.9669	-41.5314	14	12.5	6.5	AFT	Kamp et al., 1996
171.9781	-41.6245	262	10.2	0.8	AFT	Kamp et al., 1996
171.9841	-41.6871	362	10.2	0.7	AFT	Kamp et al., 1996
171.9846	-41.5464	17	9.2	1.2	AFT	Kamp et al., 1996
172.0117	-41.6028	362	19.6	3.3	AFT	Kamp et al., 1996
172.3334	-42.1506	1381	12.8	1.4	AFT	Sagar, 2014 (unpublished)
171.6907	-41.7813	200	22.9	2.7	AFT	Schulte et al., 2014
171.7277	-41.8468	128	23.7	3.3	AFT	Schulte et al., 2014
171.9402	-42.2119	330	16.2	4.4	AFT	Seward and Tulloch, 1991
171.9622	-42.2715	423	10.2	2.4	AFT	Seward and Tulloch, 1991
171.9984	-42.2826	596	12	3.7	AFT	Seward and Tulloch, 1991
172.0140	-42.2927	660	22.4	4.7	AFT	Seward and Tulloch, 1991
172.0371	-42.2884	667	11.1	2	AFT	Seward and Tulloch, 1991
172.0371	-42.2884	667	15.7	3.3	AFT	Seward and Tulloch, 1991
172.0419	-42.2947	557	16.9	3.2	AFT	Seward and Tulloch, 1991
172.0819	-42.2923	749	14.4	3.4	AFT	Seward and Tulloch, 1991
172.0886	-42.2501	882	20	3.6	AFT	Seward and Tulloch, 1991
172.0962	-42.2276	1400	23.7	6.1	AFT	Seward and Tulloch, 1991
172.1122	-42.2980	906	18.8	6.8	AFT	Seward and Tulloch, 1991
172.1122	-42.2980	906	20.3	4.2	AFT	Seward and Tulloch, 1991
172.1156	-42.3097	772	10.7	2.2	AFT	Seward and Tulloch, 1991
172.1461	-42.3000	1036	17.8	3.2	AFT	Seward and Tulloch, 1991
172.1503	-42.3460	537	10.9	3	AFT	Seward and Tulloch, 1991

171.5017	-42.1664	1099	20	3.4	AFT	Seward and White, 1992
171.5241	-42.0371	535	20.6	4	AFT	Seward and White, 1992
171.5546	-42.0762	1040	22.9	3.5	AFT	Seward and White, 1992
171.5744	-41.8432	138	16	4	AFT	Seward and White, 1992
171.5779	-41.9531	1184	18.7	1.2	AFT	Seward and White, 1992
171.5833	-41.9280	770	19.4	2.8	AFT	Seward and White, 1992
171.5889	-42.0550	1218	16.1	2.1	AFT	Seward and White, 1992
171.6378	-42.0286	1092	24.5	2.7	AFT	Seward and White, 1992
171.6459	-41.9873	454	15.6	2	AFT	Seward and White, 1992
171.6482	-41.9927	703	23.2	2.9	AFT	Seward and White, 1992
171.6542	-41.9955	1048	11.7	1.7	AFT	Seward and White, 1992
171.5017	-42.1664	1099	17.6	3	AFT	Seward, 1989
171.5546	-42.0762	1040	15.3	2.7	AFT	Seward, 1989
171.6459	-41.9873	454	16.3	2.1	AFT	Seward, 1989
171.7093	-41.8376	108	15.3	3.2	AFT	Seward, 1989
171.7094	-41.8358	139	17.1	2.7	AFT	Seward, 1989
171.7094	-41.8340	174	15.6	3.1	AFT	Seward, 1989
171.7667	-41.7969	214	14	4.1	AFT	Seward, 1989
171.7667	-41.7969	214	16.8	3.6	AFT	Seward, 1989
171.8671	-41.6287	167	22.7	3.6	AFT	Seward, 1989
171.8832	-41.6018	0	22.9	5.3	AFT	Seward, 1989
171.9402	-42.2119	330	19.5	5.4	AFT	Seward, 1989
171.9622	-42.2715	423	15.8	3.8	AFT	Seward, 1989
171.9984	-42.2826	596	13.5	4.1	AFT	Seward, 1989
172.0080	-42.2890	551	11.9	2.2	AFT	Seward, 1989
172.0080	-42.2890	551	15.3	3.2	AFT	Seward, 1989
172.0819	-42.2923	749	16.7	12.1	AFT	Seward, 1989
172.1157	-41.7920	199	11.3	3.1	AFT	Seward, 1989
172.1491	-42.3460	562	16.7	4.6	AFT	Seward, 1989
172.3799	-42.0819	894	17.3	3.9	AFT	Seward, 1989
171.0032	-43.0047	127	0.1	0	AFT	Tippett and Kamp, 1993a
171.0411	-43.0337	354	0.1	0	AFT	Tippett and Kamp, 1993a

171.0578	-43.0593	524	0.1	0	AFT	Tippett and Kamp, 1993a
171.3373	-43.0592	745	0.1	0	AFT	Tippett and Kamp, 1993a
171.3394	-43.0864	711	4.1	0.9	AFT	Tippett and Kamp, 1993a
171.3719	-43.1300	724	8.4	2.2	AFT	Tippett and Kamp, 1993a
171.4777	-42.7457	254	0.1	0	AFT	Tippett and Kamp, 1993a
171.5503	-42.7605	432	0.6	0.4	AFT	Tippett and Kamp, 1993a
171.5916	-42.7654	381	0.1	0	AFT	Tippett and Kamp, 1993a
171.6564	-42.7670	358	0.1	0	AFT	Tippett and Kamp, 1993a
172.0160	-42.4812	432	0.1	0	AFT	Tippett and Kamp, 1993a
172.0472	-42.4917	506	2.6	1.9	AFT	Tippett and Kamp, 1993a
172.0562	-42.5048	494	0.5	0.5	AFT	Tippett and Kamp, 1993a
172.0618	-42.5056	535	0.1	0	AFT	Tippett and Kamp, 1993a
172.0774	-42.5039	584	1	0.6	AFT	Tippett and Kamp, 1993a
172.1972	-42.3732	1068	0.1	0	AFT	Tippett and Kamp, 1993a
172.1994	-42.3748	1046	0.1	0	AFT	Tippett and Kamp, 1993a
172.2435	-42.3482	637	0.1	0	AFT	Tippett and Kamp, 1993a
172.2436	-42.3573	661	0.1	0	AFT	Tippett and Kamp, 1993a
172.2457	-42.3482	673	0.1	0	AFT	Tippett and Kamp, 1993a
172.2525	-42.3630	640	1.4	0.7	AFT	Tippett and Kamp, 1993a
172.2761	-42.3858	837	0.1	0	AFT	Tippett and Kamp, 1993a
172.3028	-42.3848	738	0.4	0.4	AFT	Tippett and Kamp, 1993a
172.3505	-42.5483	610	1.7	1	AFT	Tippett and Kamp, 1993a
172.3704	-42.3761	967	0.1	0	AFT	Tippett and Kamp, 1993a

172.3959	-42.3759	868	0.7	0.7	AFT	Tippett and Kamp, 1993a
172.3985	-42.4006	871	1.2	0.7	AFT	Tippett and Kamp, 1993a
172.4023	-42.4318	818	0.8	0.5	AFT	Tippett and Kamp, 1993a
171.5594	-42.9325	876	3.6	2.4	AFT	Tippett and Kamp, 1993b
171.5717	-42.9597	850	5.5	3.6	AFT	Tippett and Kamp, 1993b
171.5919	-42.9811	731	3.9	2.8	AFT	Tippett and Kamp, 1993b
171.7299	-43.0105	671	6	7.2	AFT	Tippett and Kamp, 1993b
172.4502	-42.5903	507	3	2	AFT	Tippett and Kamp, 1993b
172.5784	-42.5933	460	6.4	5.6	AFT	Tippett and Kamp, 1993b
172.6660	-42.5752	482	11	6	AFT	Tippett and Kamp, 1993b
171.4475	-42.7350	213	4.3	1.8	ZFT	Kamp et al., 1989
171.5302	-42.7482	243	2.7	0.6	ZFT	Kamp et al., 1989
171.0688	-42.9276	159	8.7	0.9	ZFT	Kamp et al., 1992
171.1058	-42.9113	219	1.1	0.2	ZFT	Kamp et al., 1992
171.1081	-42.9138	306	0.7	0.1	ZFT	Kamp et al., 1992
171.1104	-42.8957	96	20.4	7.1	ZFT	Kamp et al., 1992
171.1114	-42.9146	341	0.7	0.2	ZFT	Kamp et al., 1992
171.1250	-42.8990	112	16.3	5.7	ZFT	Kamp et al., 1992
171.1497	-42.8859	157	7.9	0.9	ZFT	Kamp et al., 1992
171.3124	-42.7530	173	20.6	0.9	ZFT	Kamp et al., 1992
171.3246	-42.7596	140	15.6	1.8	ZFT	Kamp et al., 1992
171.4431	-42.7243	140	15.4	0.9	ZFT	Kamp et al., 1992
171.9671	-41.8268	352	19.4	3.5	ZFT	Seward, 1989
171.0032	-43.0047	127	1.3	0.2	ZFT	Tippett and Kamp, 1993a
171.0411	-43.0337	354	1.2	0.3	ZFT	Tippett and Kamp, 1993a
171.0578	-43.0593	524	3.4	0.8	ZFT	Tippett and Kamp, 1993a
171.4777	-42.7457	254	1.7	0.5	ZFT	Tippett and Kamp, 1993a
171.5916	-42.7654	381	14	1	ZFT	Tippett and Kamp, 1993a
171.6564	-42.7670	358	22	4	ZFT	Tippett and Kamp, 1993a

172.0160	-42.4812	432	2.6	1.3	ZFT	Tippett and Kamp, 1993a
172.0562	-42.5048	494	5.7	1.2	ZFT	Tippett and Kamp, 1993a
172.0618	-42.5056	535	7.6	1	ZFT	Tippett and Kamp, 1993a
172.1972	-42.3732	1068	2.1	0.4	ZFT	Tippett and Kamp, 1993a
172.1994	-42.3748	1046	3	0.2	ZFT	Tippett and Kamp, 1993a
172.2435	-42.3482	637	3.7	0.8	ZFT	Tippett and Kamp, 1993a
172.2436	-42.3573	661	3.4	0.2	ZFT	Tippett and Kamp, 1993a
172.2457	-42.3482	673	2.2	0.5	ZFT	Tippett and Kamp, 1993a
171.5503	-42.7605	432	4.6	0.6	ZFT	Tippett and Kamp, 1993b
172.2525	-42.3630	640	5.3	0.8	ZFT	Tippett and Kamp, 1993b
171.0688	-42.9276	159	9.6	1.2	ZFT	White and Green, 1986
171.1058	-42.9113	219	1.3	0.22	ZFT	White and Green, 1986
171.1104	-42.8957	96	20.4	14.2	ZFT	White and Green, 1986
171.1250	-42.8990	112	16.3	11.4	ZFT	White and Green, 1986
171.1497	-42.8859	157	7.3	0.8	ZFT	White and Green, 1986
171.3124	-42.7530	173	20.6	1.8	ZFT	White and Green, 1986
171.3246	-42.7596	140	15.6	3.6	ZFT	White and Green, 1986
171.4431	-42.7366	243	4.3	1.8	ZFT	White and Green, 1986
171.4431	-42.7243	140	15.4	1.8	ZFT	White and Green, 1986

3.9.6 *References for Data Used in GLIDE Inversion*

Baker, J., & Seward, D. (1996). Timing of Cretaceous extension and Miocene compression in northeast South Island, New Zealand: Constraints from Rb-Sr and fission-track dating of an igneous pluton. *Tectonics*, *15*(5), 976-983.

Collett, C. M., Duvall, A. R., Flowers, R. M., Tucker, G. E., & Upton, P. (2019). The Timing and Style of Oblique Deformation Within New Zealand's Kaikōura Ranges and Marlborough Fault System Based on Low-Temperature Thermochronology. *Tectonics*, *38*(4), 1250-1272.

Gibson, H.J. (1993). The Tectonic and thermal evolution of the Murchison Basin, New Zealand: An apatite fission track study. (Doctoral dissertation, University of Melbourne.)

Jiao, R., Herman, F., & Seward, D. (2017). Late Cenozoic exhumation model of New Zealand: Impacts from tectonics and climate. *Earth-science reviews*, *166*, 286-298.

Kamp, P. J., Green, P. F., & White, S. H. (1989). Fission track analysis reveals character of collisional tectonics in New Zealand. *Tectonics*, *8*(2), 169-195.

Kamp, P.J.J., Green, P.F. and Tippett, J.M. (1992). Tectonic architecture of the mountain front-foreland basin transition, South Island, New Zealand, assessed by fission track analysis. *Tectonics, 11*(1): 98-113.

Kamp, P. J., Webster, K. S., & Nathan, S. (1996). Thermal history analysis by integrated modelling of apatite fission track and vitrinite reflectance data: application to an inverted basin (Buller Coalfield, New Zealand). *Basin Research*, *8*(4), 383-402.

Kao, M. H. (2001). Thermo-tectonic history of the Marlborough region, South Island, New Zealand. *Terrestrial, Atmospheric and Oceanic Sciences*, *12*(3), 485-502.

Kao, Ming-Hung. (2002). Thermo-tectonic implications of zircon and apatite FT data of the Marlborough Region, South Island, New Zealand. *Terrestrial, Atmospheric and Oceanic Sciences, 13*(2), 109-124.

Sagar, M. W. (2014). *Geology, petrology and thermochronology of the Glenroy Complex and associated granitoids, southeast Nelson, New Zealand* (Doctoral dissertation, University of Otago).

Schulte, D. O., Ring, U., Thomson, S. N., Glodny, J., & Carrad, H. (2014). Two-stage development of the Paparoa Metamorphic Core Complex, West Coast, South Island, New Zealand: Hot continental extension precedes sea-floor spreading by∼ 25 my. *Lithosphere*, *6*(3), 177-194.

Seward, D. (1989). Cenozoic basin histories determined by fission-track dating of basement granites, South Island, New Zealand. *Chemical Geology: Isotope Geoscience section*, *79*(1), 31-48.

Seward, D., & Tulloch, A. J. (1991). Fission-track analysis of Tertiary uplift history of granitic basement in the Victoria Range, West Coast, New Zealand. *New Zealand journal of geology and geophysics*, *34*(2), 115-120.

Seward, D., & White, P. J. (1992). Evolution and eversion of a tertiary sedimentary basin, Paparoa Range, West Coast, South Island, New Zealand: Evidence from fission-track dating. *New Zealand journal of geology and geophysics*, *35*(3), 265-271.

Tippett, J.M. and Kamp, P.J.J. (1993a). Fission Track Analysis of the Late Cenozoic Vertical Kinematics of Continental Pacific Crust, South Island, New Zealand. *Journal of Geophysical Research, 98*(B9): 16119-16148.

Tippett, J.M. and Kamp, P.J.J. (1993b). The role of faulting in rock uplift in the Southern Alps, New Zealand. *New Zealand Journal of Geology and Geophysics, 36*(4): 497-504.

White, S.H. and Green, P.F. (1986). Tectonic development of the Alpine fault zone, New Zealand: A fission-track study. *Geology, 14*(2): 124-127.

3.9.7 *GLIDE Control Points*

Table 3.68. GLIDE control point locations. Block ID was used in models with fault blocks. In models without blocks, this column was filled in with 1 for every control point. Note: "Control Point ID" column, and column headers, are not used in input file. Coordinates are in WGS84.

Control Point ID	Longitude	Latitude	Block ID (if applicable)
1	173.2121	-41.7586	8
2	173.7983	-41.7476	8
3	173.2086	-42.0582	3
4	172.9137	-42.0862	3
5	172.2280	-42.3664	7
6	171.9667	-41.5752	1
7	173.7089	-41.8529	6
8	173.7331	-42.0344	4
9	173.6633	-42.2305	4
10	173.6158	-42.2217	4
11	173.6929	-42.2985	2
12	173.6682	-41.9900	6
13	172.8901	-42.4727	5
14	172.5177	-42.0236	3
15	172.8116	-41.8283	3
16	172.0607	-42.5042	7
17	171.4952	-42.7597	2
18	171.8148	-41.7549	1
19	172.0617	-42.2916	1
20	171.1075	-42.8779	1

3.10 Supplementary Figures

3.10.1 *GLIDE Results: Map View*

Figure 3.14. GLIDE results: maps of exhumation rate and reduced variance. Exhumation rate (left) and reduction in variance (left) each 2Ma time step in each GLIDE model run.

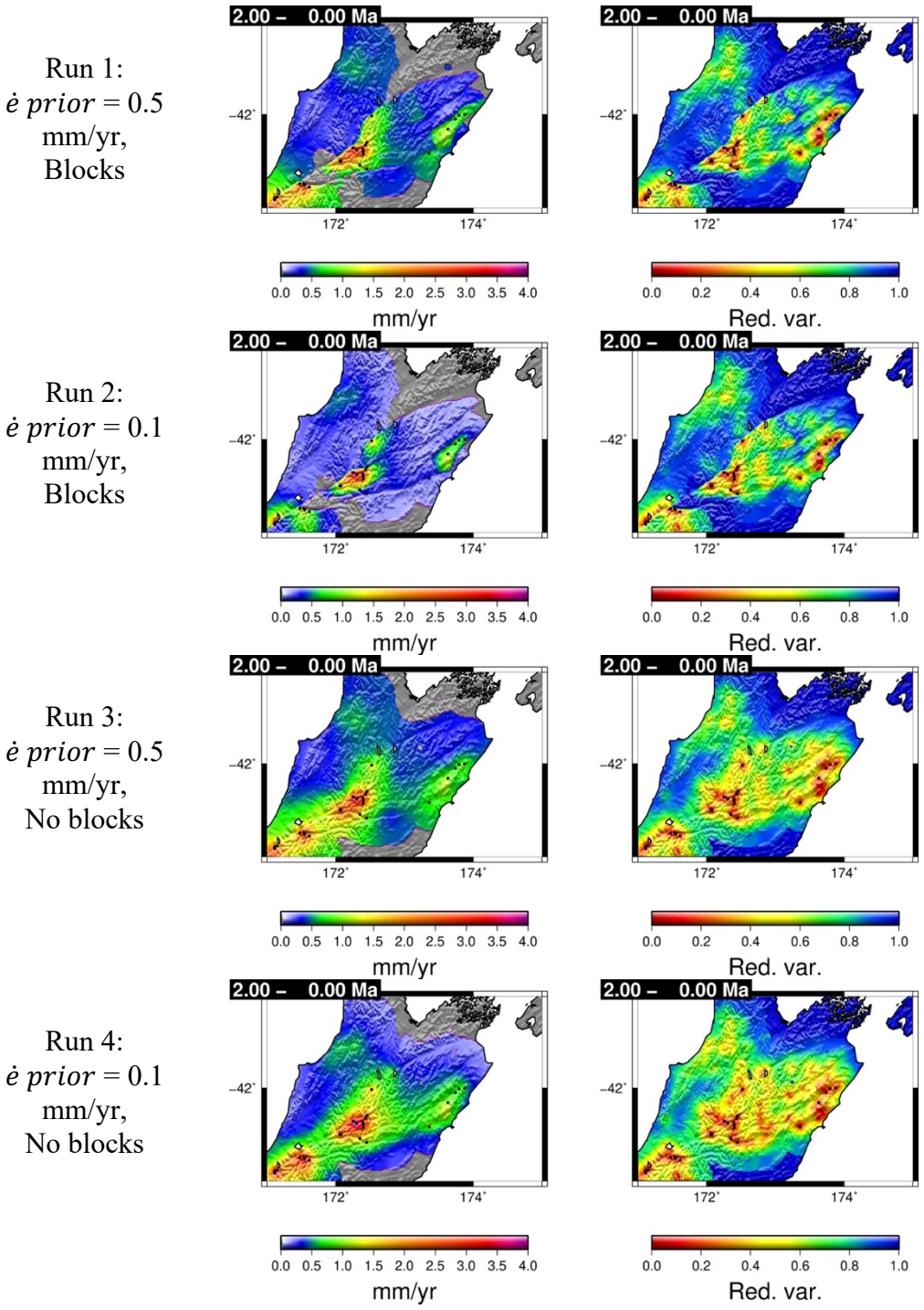

Run 1:
$\dot{e}\ prior$ = 0.5 mm/yr,
Blocks

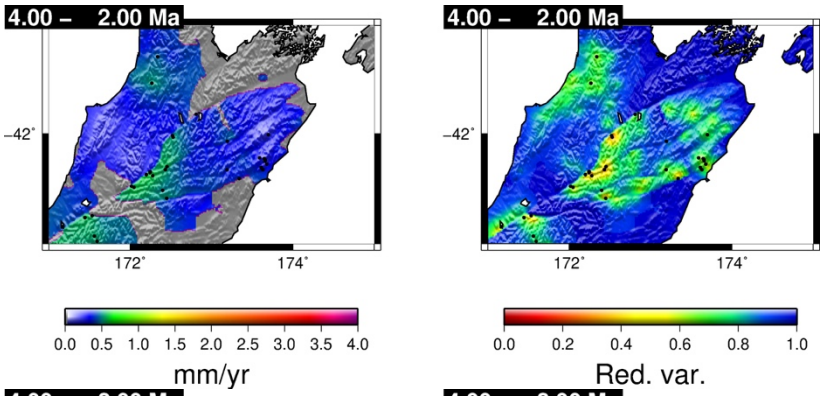

Run 2:
$\dot{e}\ prior$ = 0.1 mm/yr,
Blocks

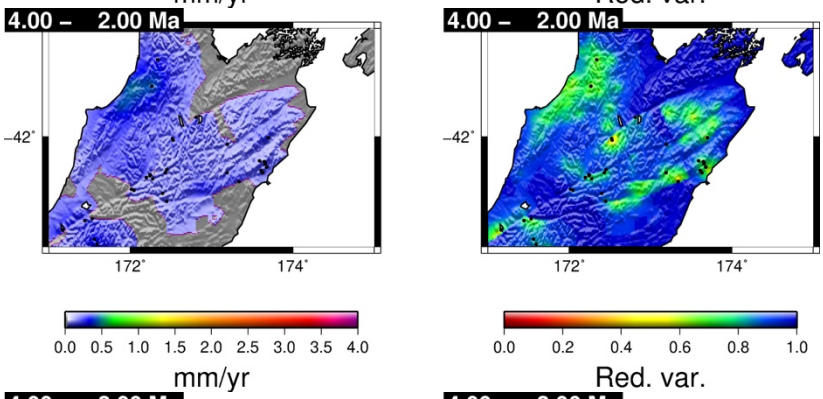

Run 3:
$\dot{e}\ prior$ = 0.5 mm/yr,
No blocks

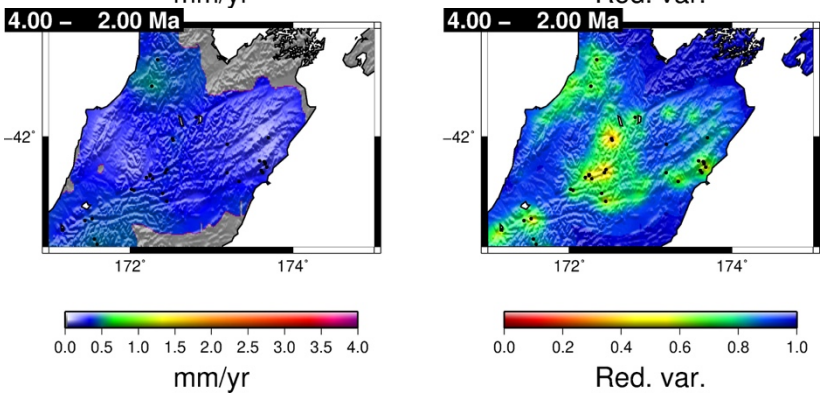

Run 4:
$\dot{e}\ prior$ = 0.1 mm/yr,
No blocks

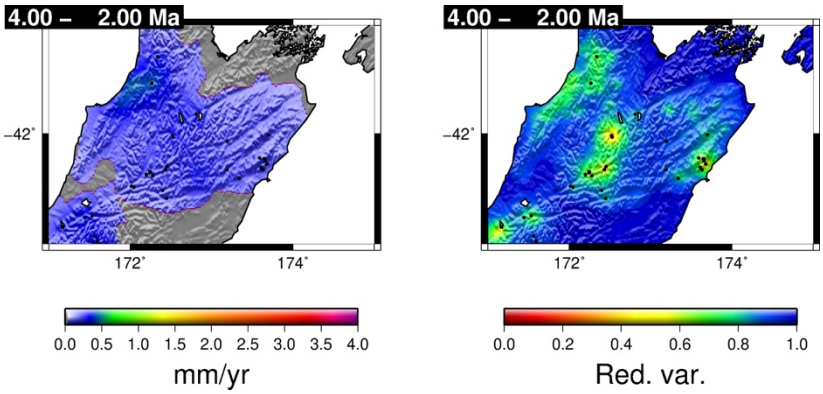

Run 1: $\dot{e}\ prior$ = 0.5 mm/yr, Blocks

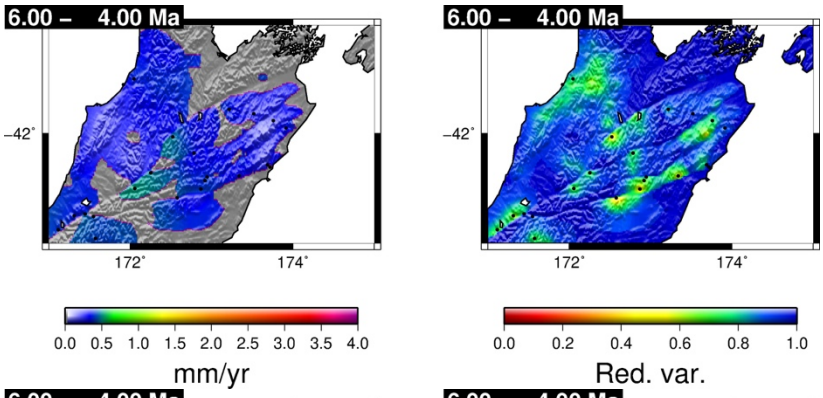

Run 2: $\dot{e}\ prior$ = 0.1 mm/yr, Blocks

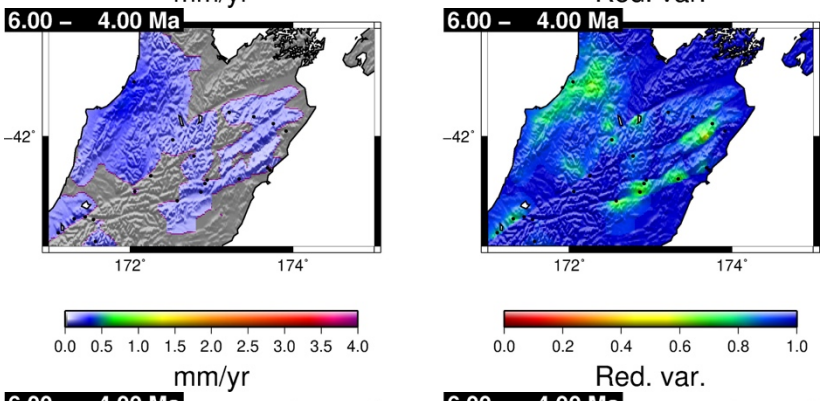

Run 3: $\dot{e}\ prior$ = 0.5 mm/yr, No blocks

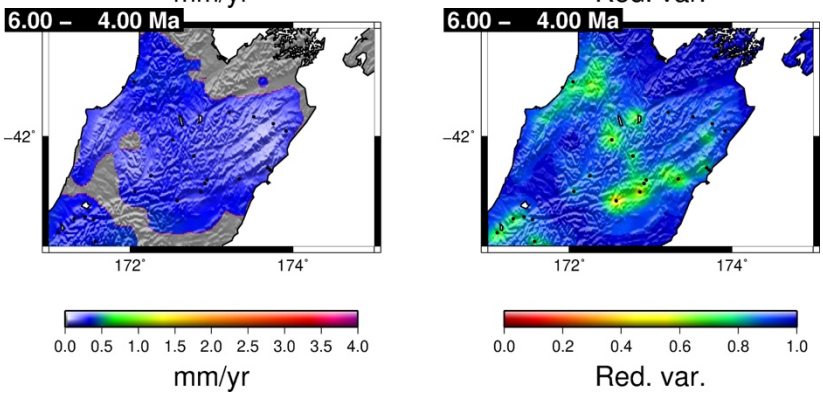

Run 4: $\dot{e}\ prior$ = 0.1 mm/yr, No blocks

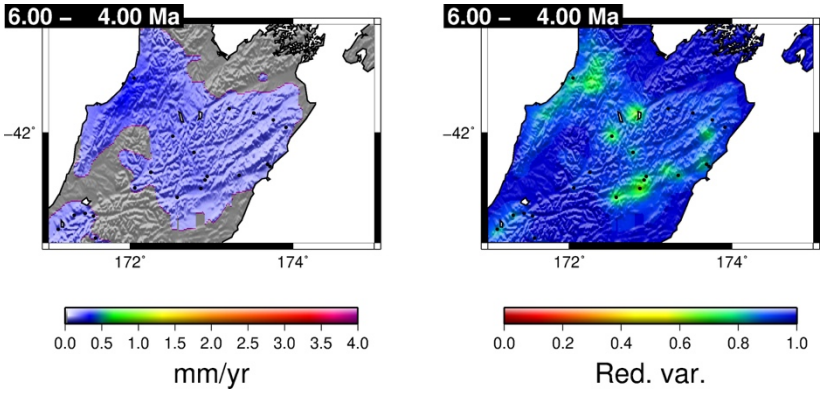

Run 1: $\dot{e}\ prior$ = 0.5 mm/yr, Blocks

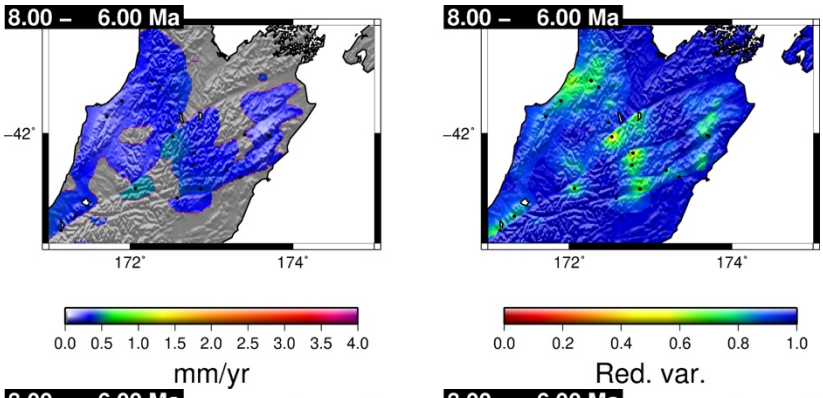

Run 2: $\dot{e}\ prior$ = 0.1 mm/yr, Blocks

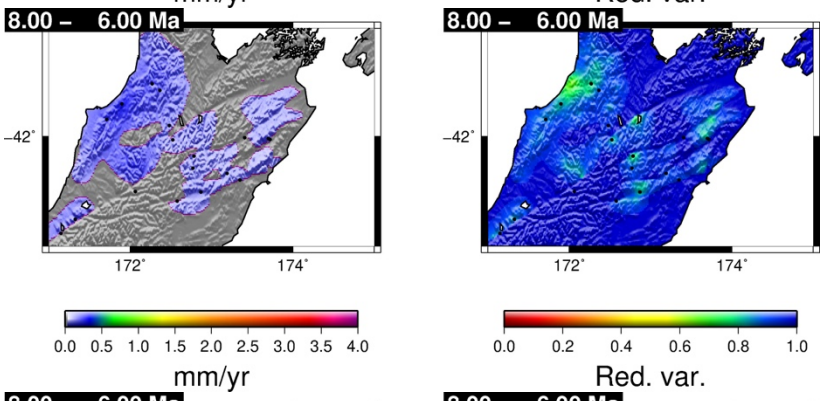

Run 3: $\dot{e}\ prior$ = 0.5 mm/yr, No blocks

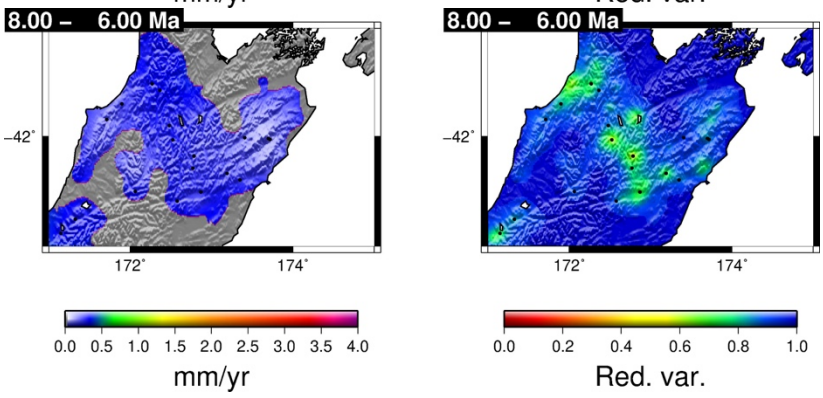

Run 4: $\dot{e}\ prior$ = 0.1 mm/yr, No blocks

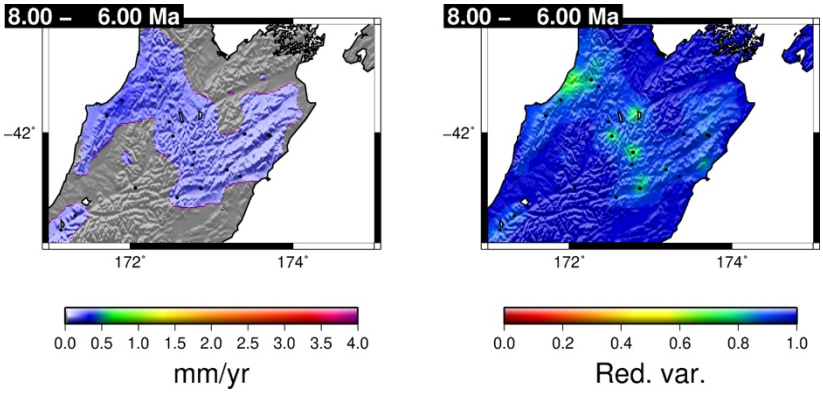

Run 1: $\dot{e}\ prior$ = 0.5 mm/yr, Blocks

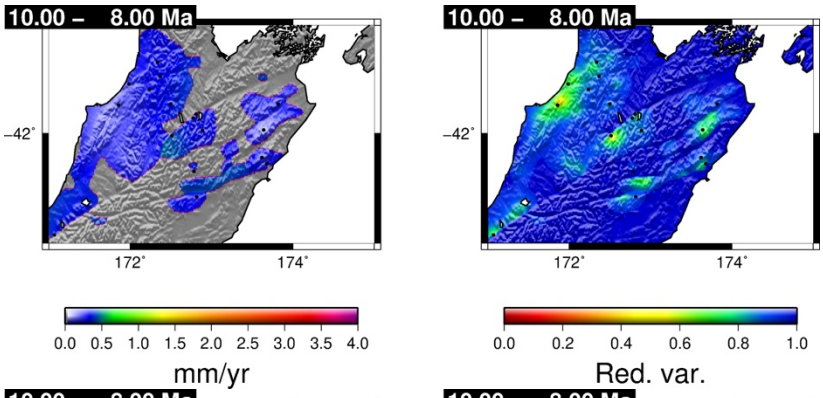

Run 2: $\dot{e}\ prior$ = 0.1 mm/yr, Blocks

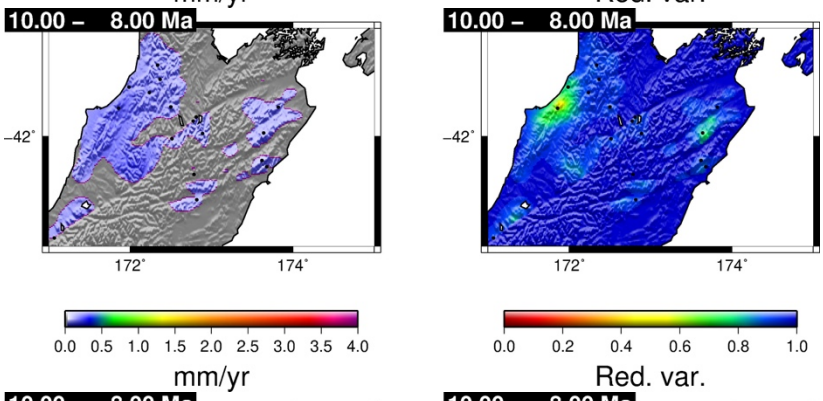

Run 3: $\dot{e}\ prior$ = 0.5 mm/yr, No blocks

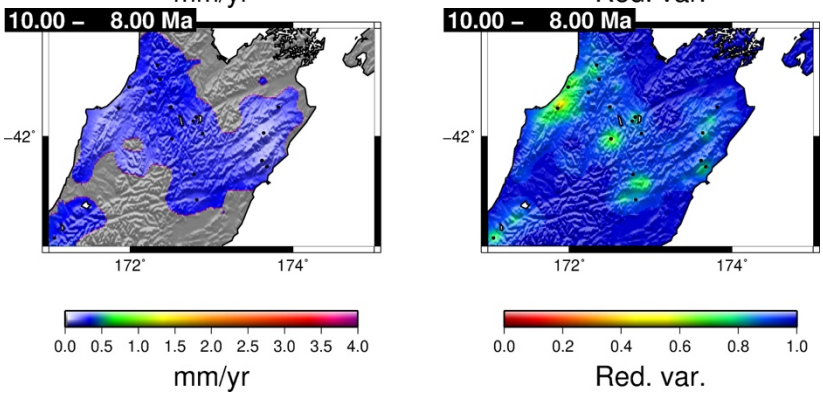

Run 4: $\dot{e}\ prior$ = 0.1 mm/yr, No blocks

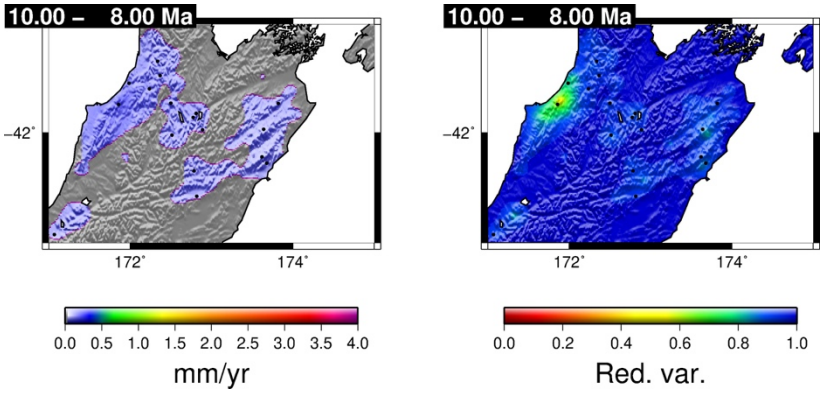

Run 1: $\dot{e}\ prior$ = 0.5 mm/yr, Blocks

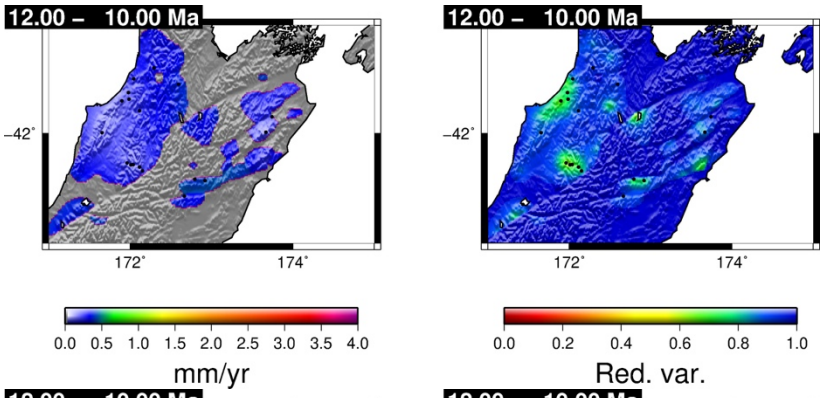

Run 2: $\dot{e}\ prior$ = 0.1 mm/yr, Blocks

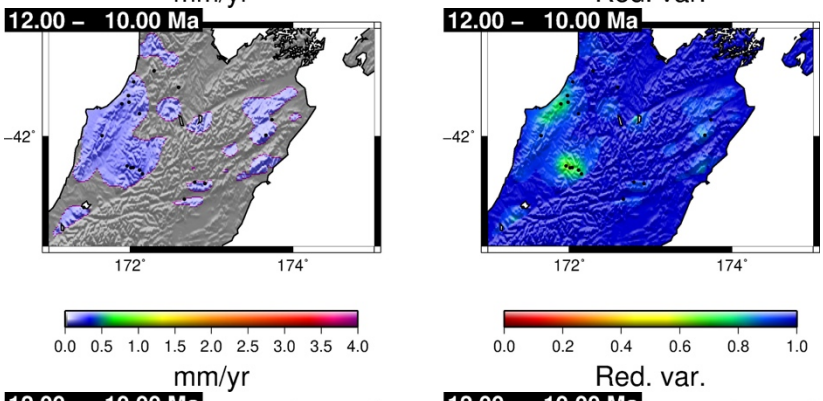

Run 3: $\dot{e}\ prior$ = 0.5 mm/yr, No blocks

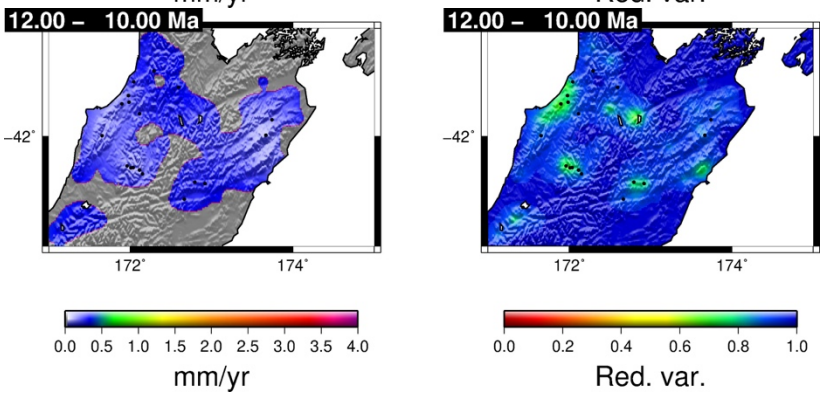

Run 4: $\dot{e}\ prior$ = 0.1 mm/yr, No blocks

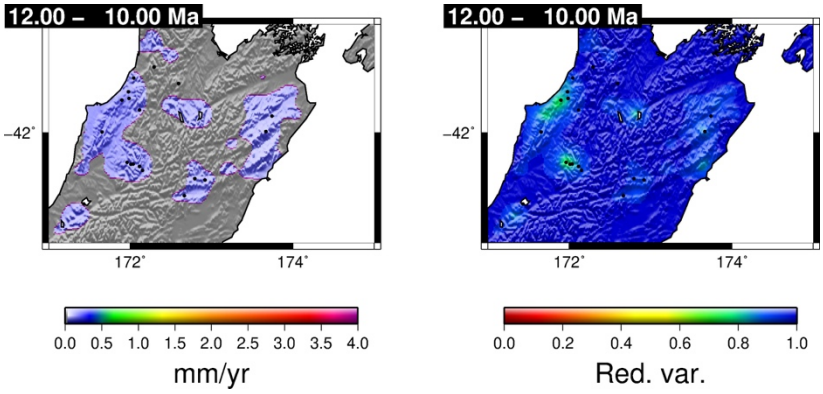

Run 1: $\dot{e}\ prior$ = 0.5 mm/yr, Blocks

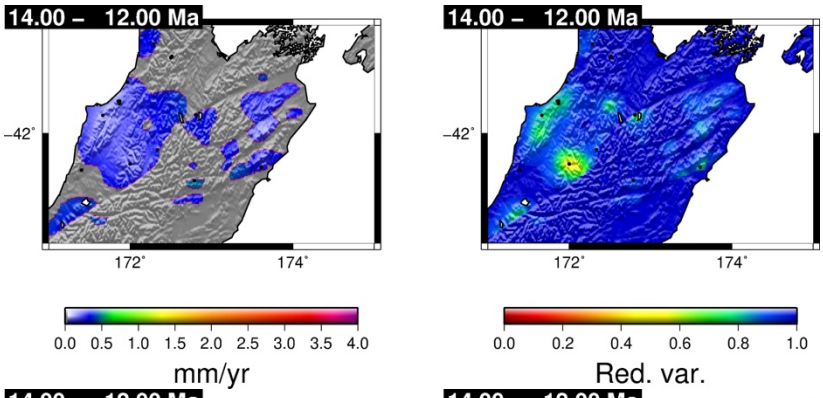

Run 2: $\dot{e}\ prior$ = 0.1 mm/yr, Blocks

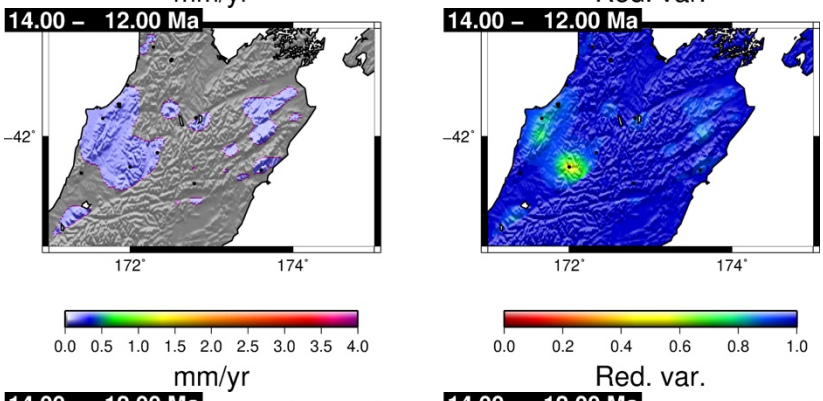

Run 3: $\dot{e}\ prior$ = 0.5 mm/yr, No blocks

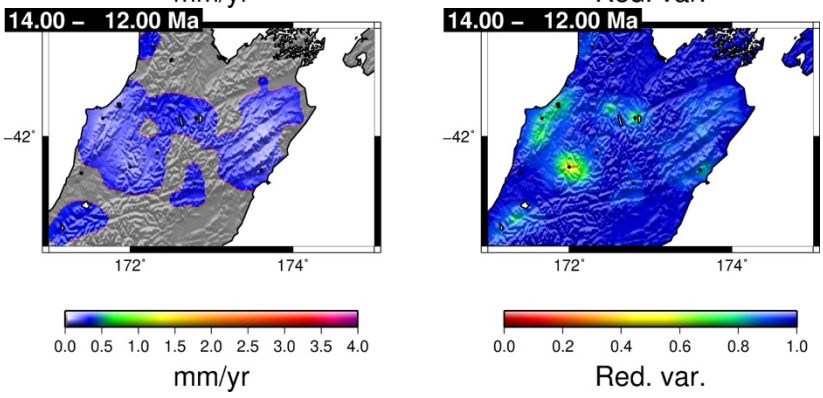

Run 4: $\dot{e}\ prior$ = 0.1 mm/yr, No blocks

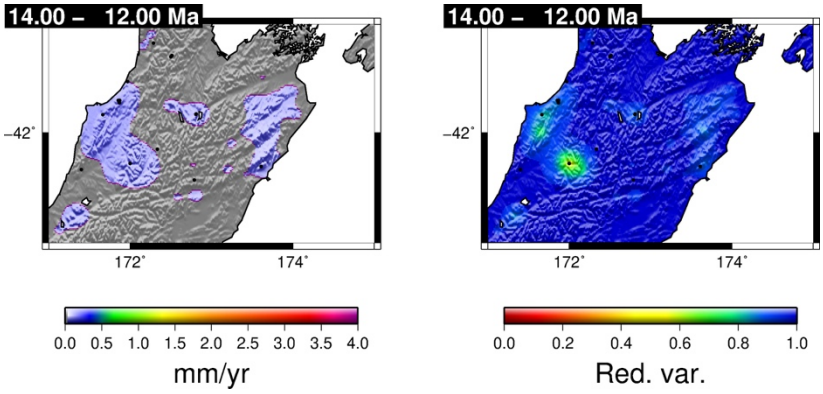

Run 1: $\dot{e}\ prior$ = 0.5 mm/yr, Blocks

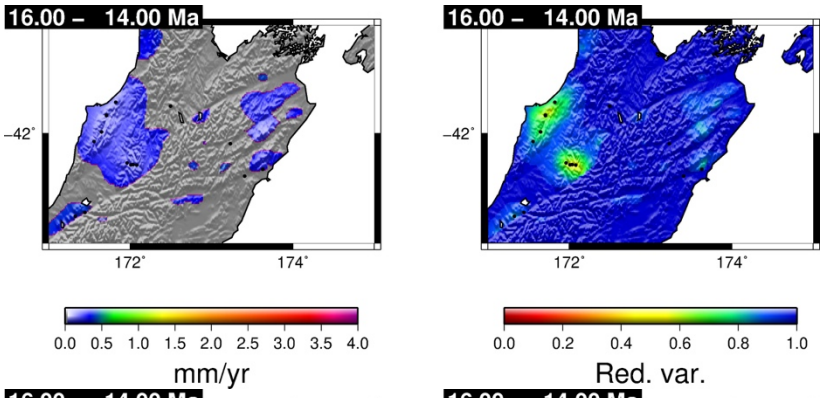

Run 2: $\dot{e}\ prior$ = 0.1 mm/yr, Blocks

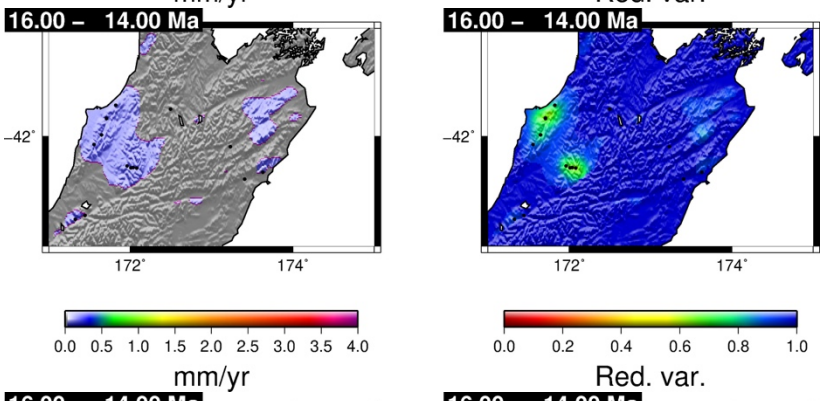

Run 3: $\dot{e}\ prior$ = 0.5 mm/yr, No blocks

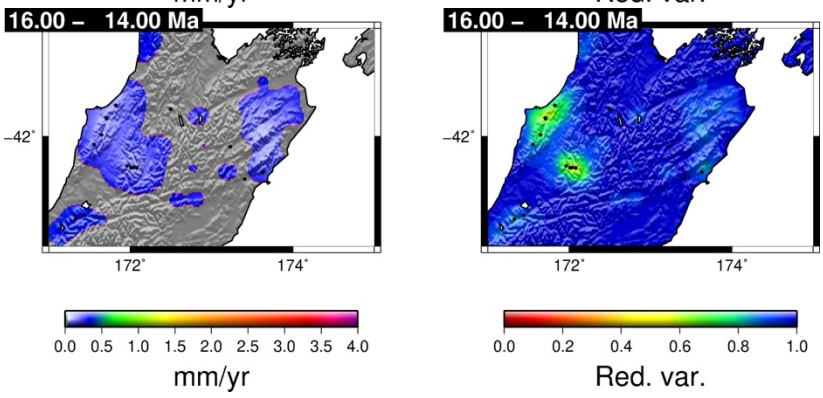

Run 4: $\dot{e}\ prior$ = 0.1 mm/yr, No blocks

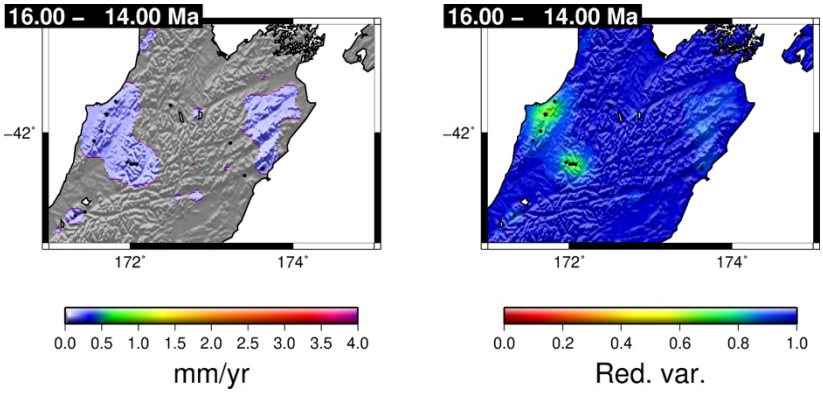

Run 1: $\dot{e}\ prior$ = 0.5 mm/yr, Blocks

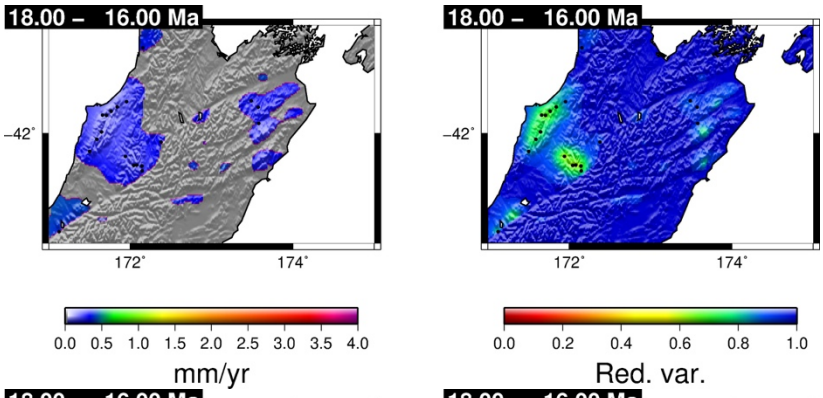

Run 2: $\dot{e}\ prior$ = 0.1 mm/yr, Blocks

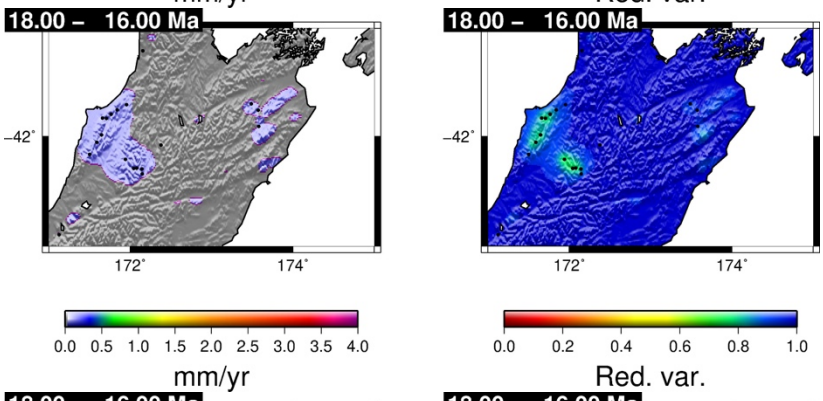

Run 3: $\dot{e}\ prior$ = 0.5 mm/yr, No blocks

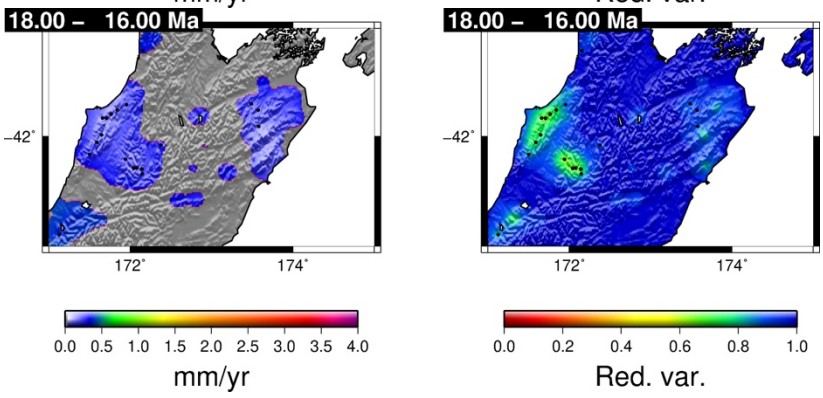

Run 4: $\dot{e}\ prior$ = 0.1 mm/yr, No blocks

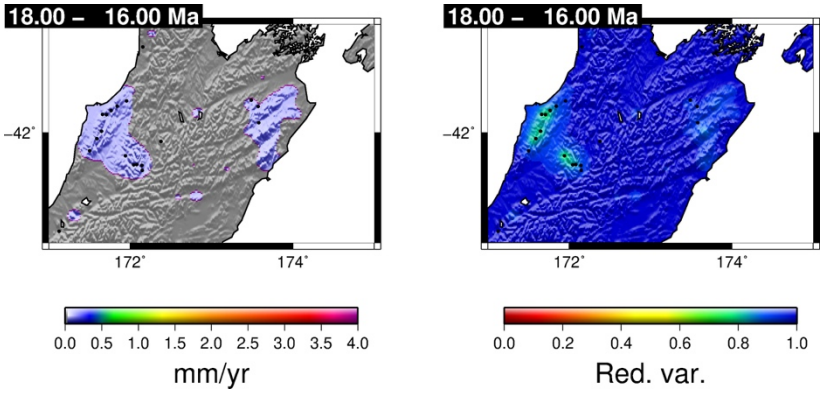

Run 1: $\dot{e}\ prior$ = 0.5 mm/yr, Blocks

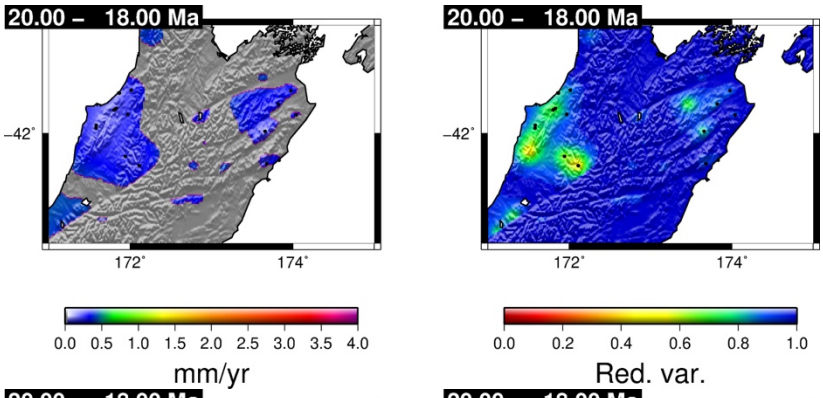

Run 2: $\dot{e}\ prior$ = 0.1 mm/yr, Blocks

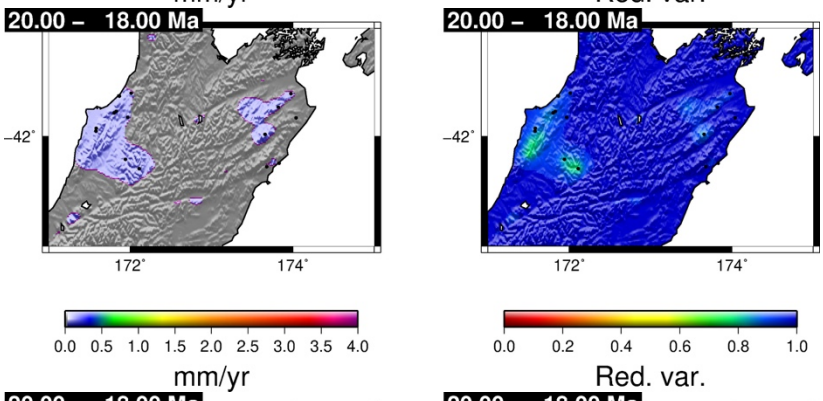

Run 3: $\dot{e}\ prior$ = 0.5 mm/yr, No blocks

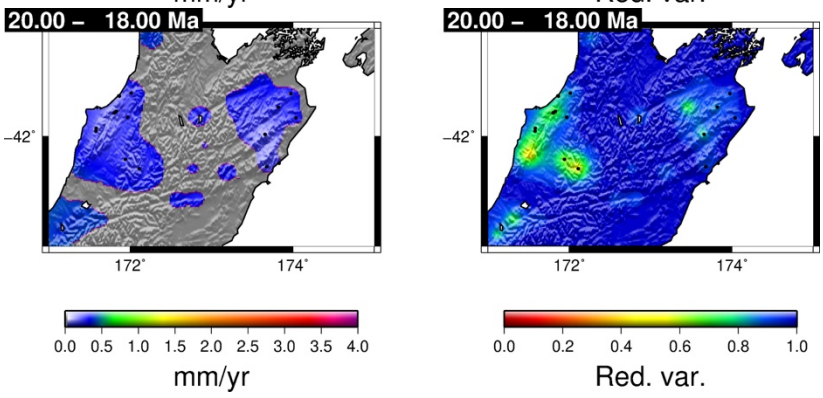

Run 4: $\dot{e}\ prior$ = 0.1 mm/yr, No blocks

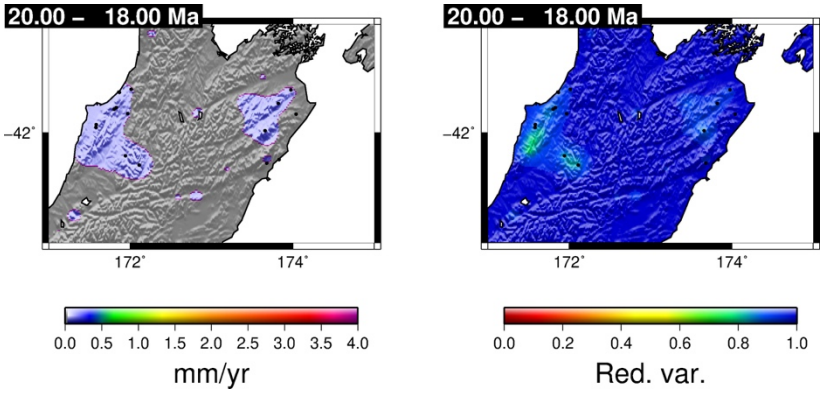

Run 1:
$\dot{e}\ prior$ = 0.5 mm/yr,
Blocks

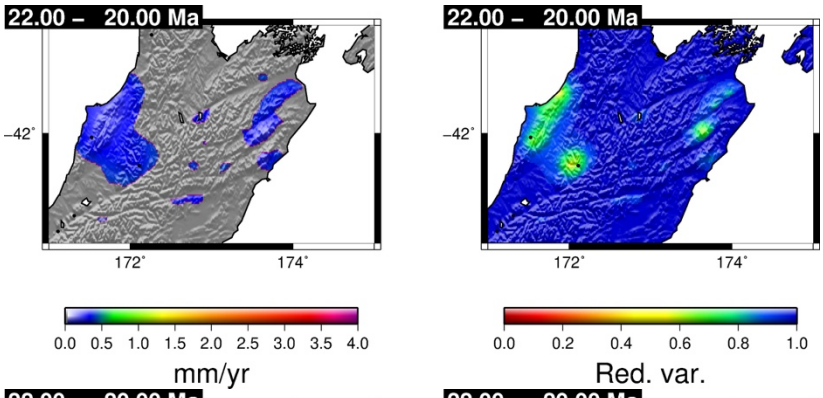

Run 2:
$\dot{e}\ prior$ = 0.1 mm/yr,
Blocks

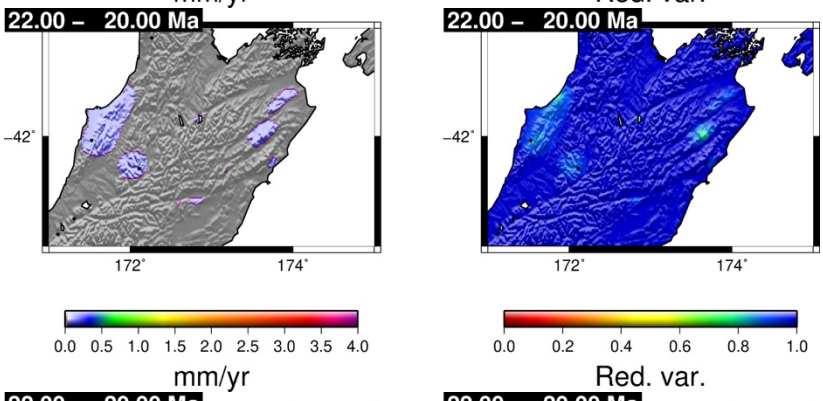

Run 3:
$\dot{e}\ prior$ = 0.5 mm/yr,
No blocks

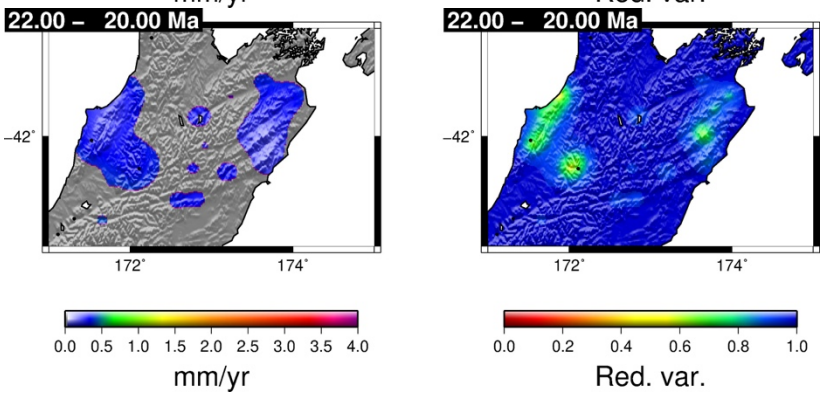

Run 4:
$\dot{e}\ prior$ = 0.1 mm/yr,
No blocks

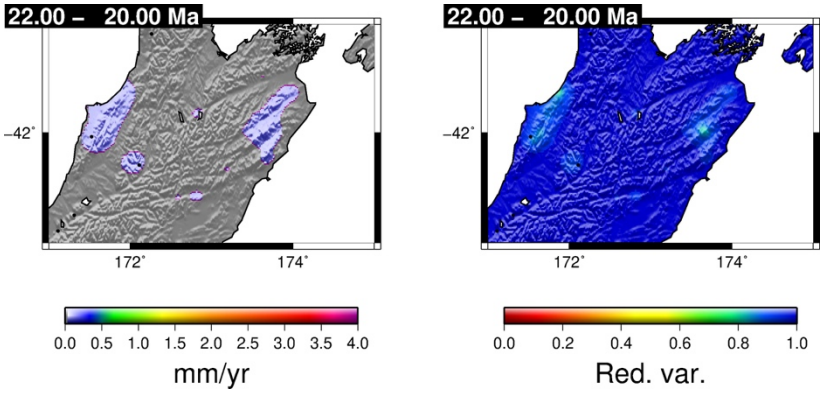

Run 1: $\dot{e}\ prior$ = 0.5 mm/yr, Blocks

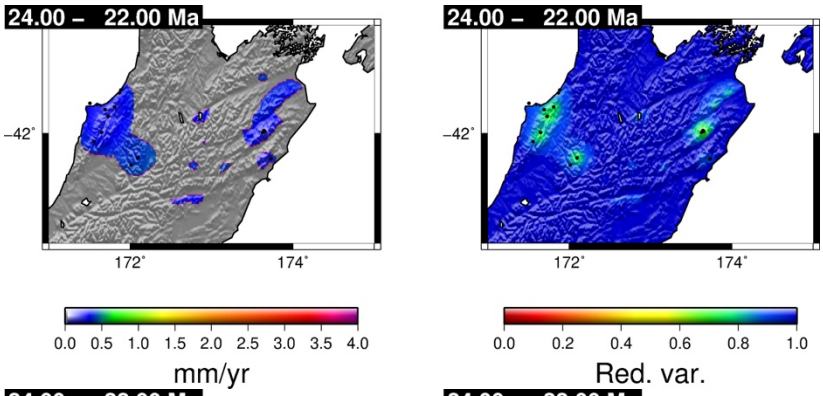

Run 2: $\dot{e}\ prior$ = 0.1 mm/yr, Blocks

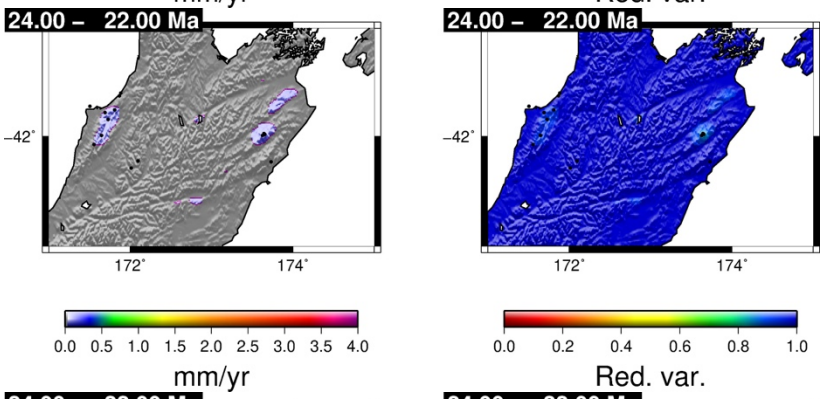

Run 3: $\dot{e}\ prior$ = 0.5 mm/yr, No blocks

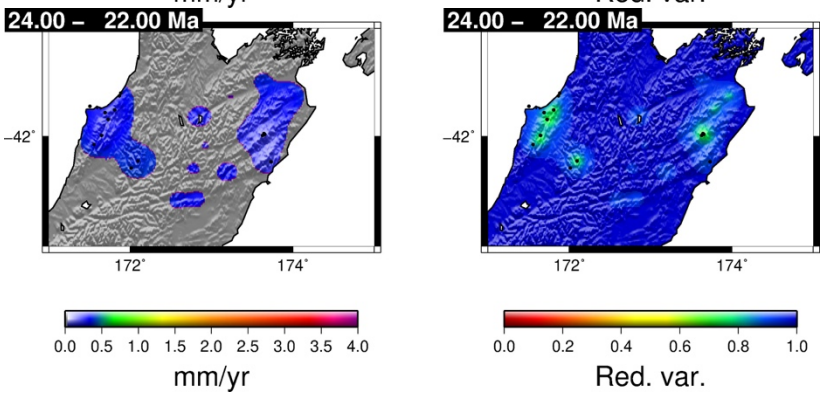

Run 4: $\dot{e}\ prior$ = 0.1 mm/yr, No blocks

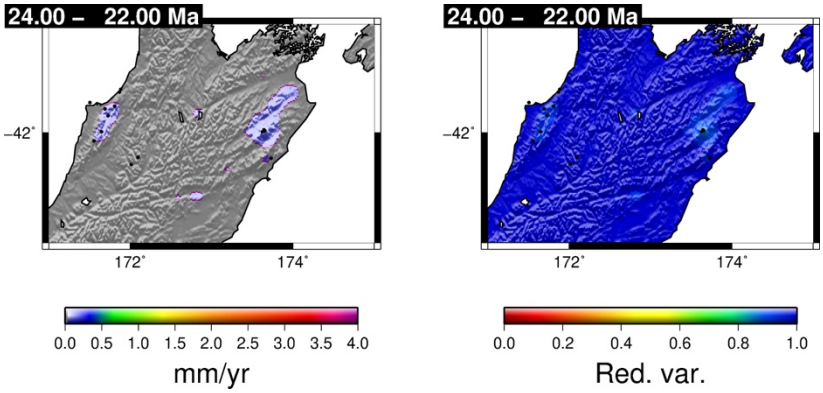

Run 1: $\dot{e}\ prior$ = 0.5 mm/yr, Blocks

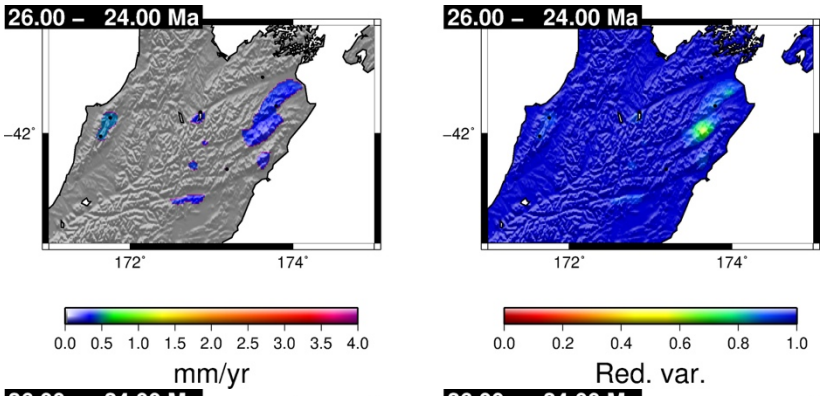

Run 2: $\dot{e}\ prior$ = 0.1 mm/yr, Blocks

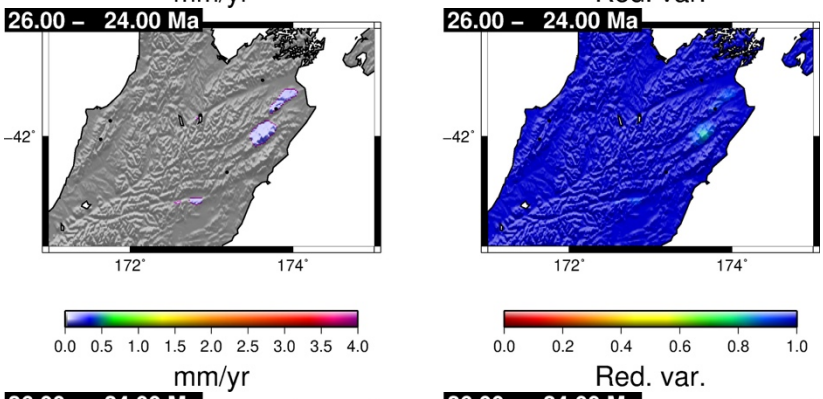

Run 3: $\dot{e}\ prior$ = 0.5 mm/yr, No blocks

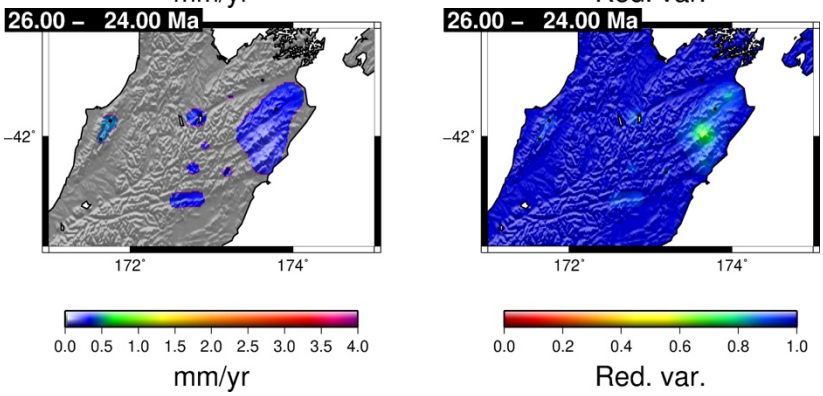

Run 4: $\dot{e}\ prior$ = 0.1 mm/yr, No blocks

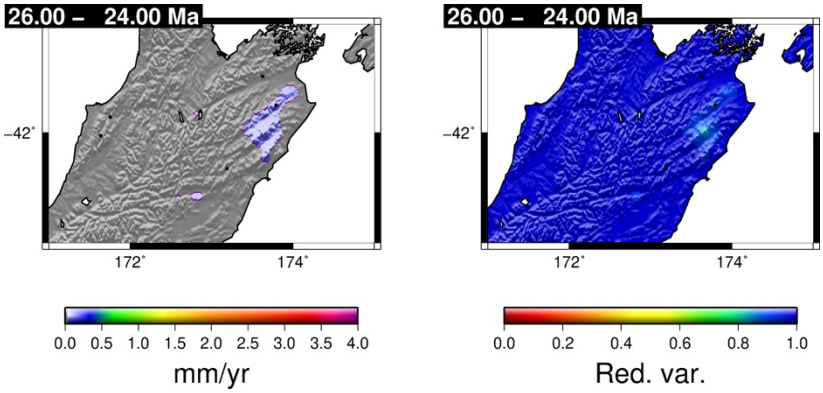

Run 1: $\dot{e}\ prior$ = 0.5 mm/yr, Blocks

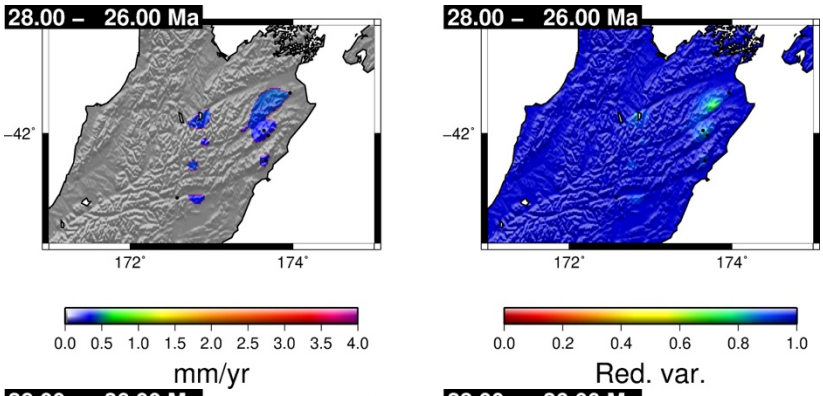

Run 2: $\dot{e}\ prior$ = 0.1 mm/yr, Blocks

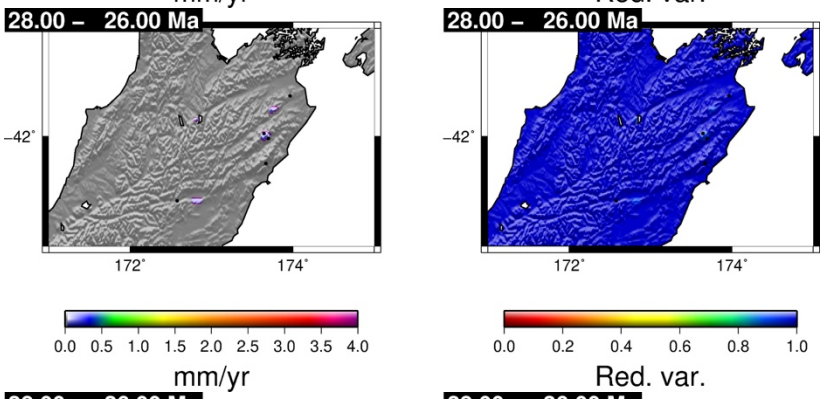

Run 3: $\dot{e}\ prior$ = 0.5 mm/yr, No blocks

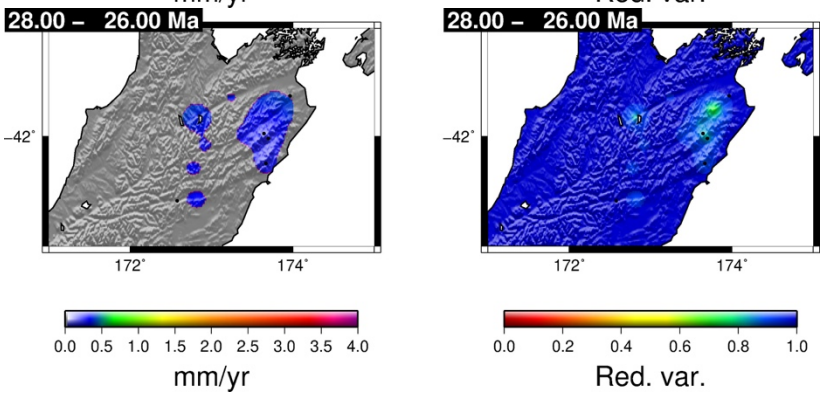

Run 4: $\dot{e}\ prior$ = 0.1 mm/yr, No blocks

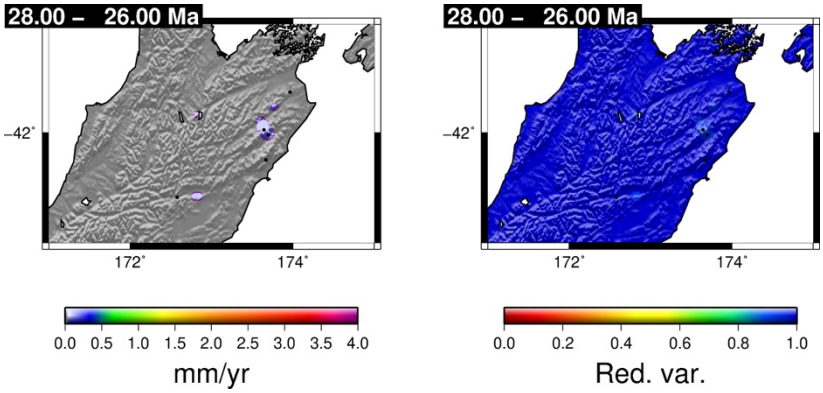

Run 1: $\dot{e}\ prior$ = 0.5 mm/yr, Blocks

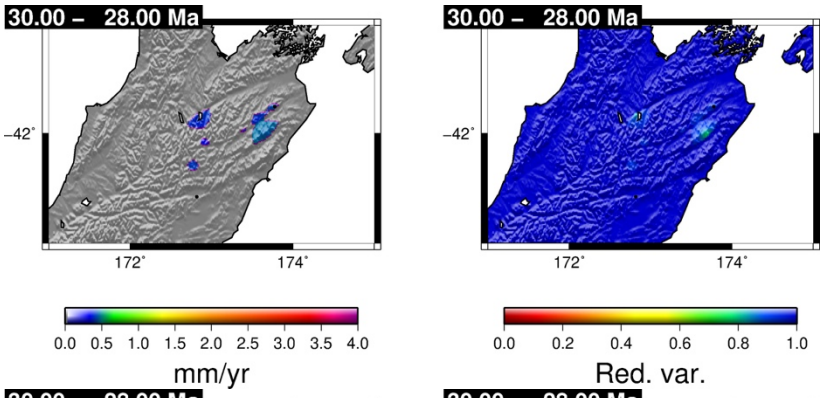

Run 2: $\dot{e}\ prior$ = 0.1 mm/yr, Blocks

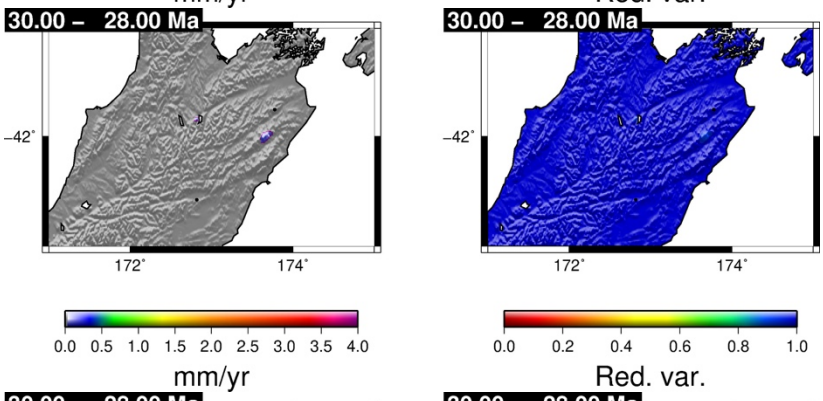

Run 3: $\dot{e}\ prior$ = 0.5 mm/yr, No blocks

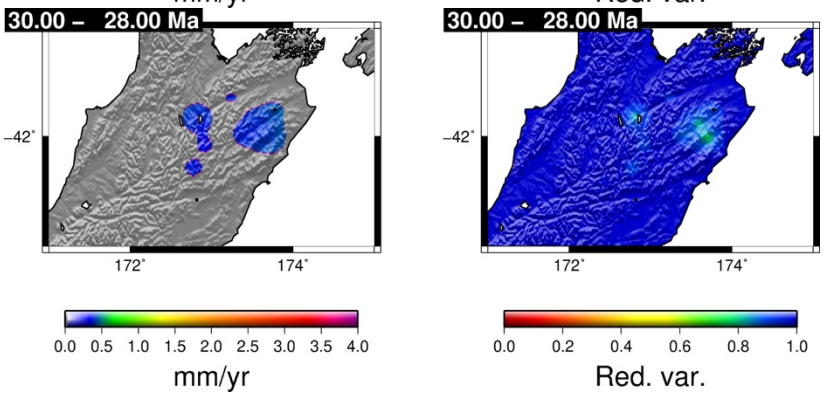

Run 4: $\dot{e}\ prior$ = 0.1 mm/yr, No blocks

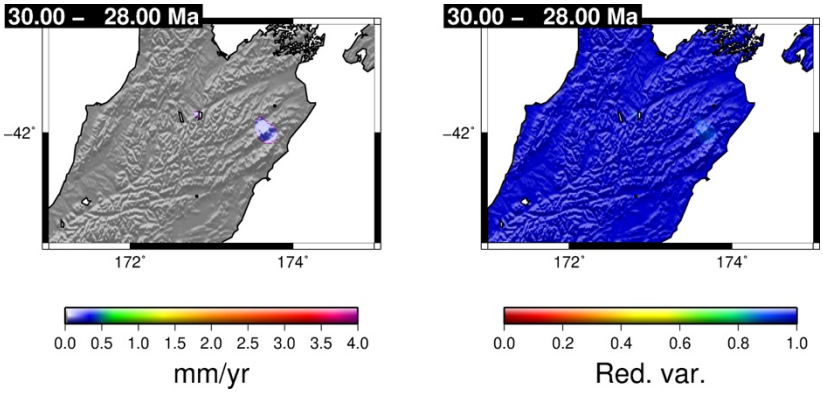

Run 1: $\dot{e}\ prior$ = 0.5 mm/yr, Blocks

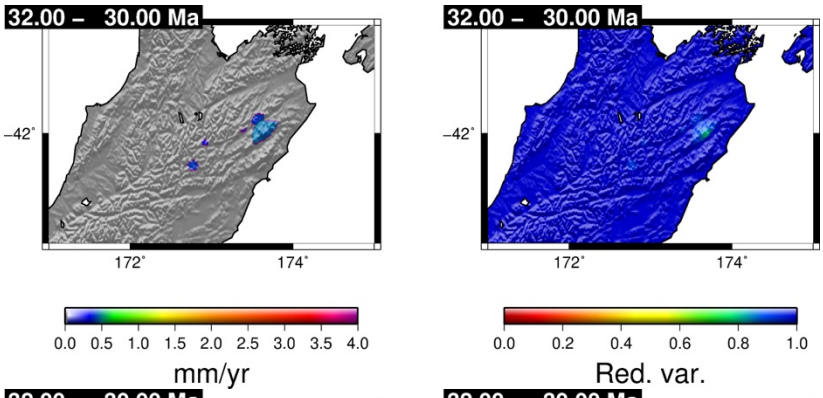

Run 2: $\dot{e}\ prior$ = 0.1 mm/yr, Blocks

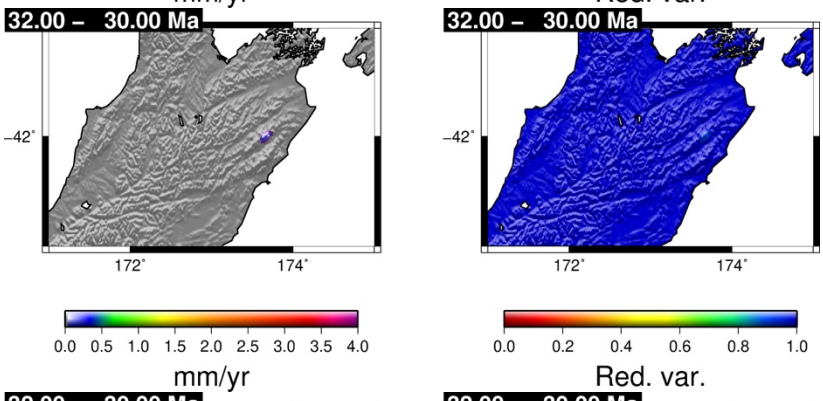

Run 3: $\dot{e}\ prior$ = 0.5 mm/yr, No blocks

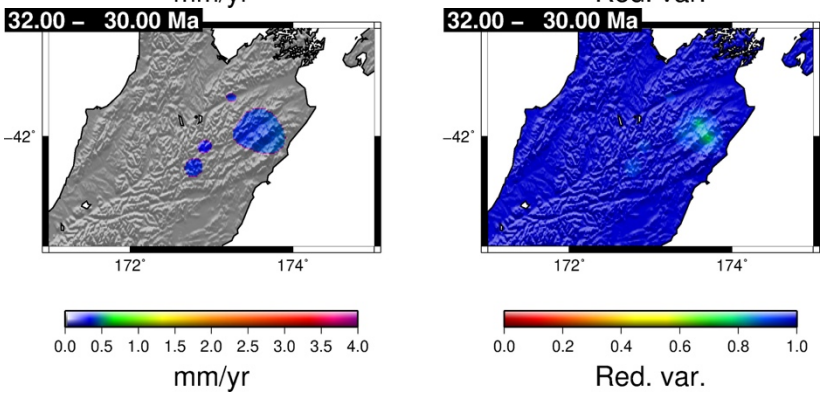

Run 4: $\dot{e}\ prior$ = 0.1 mm/yr, No blocks

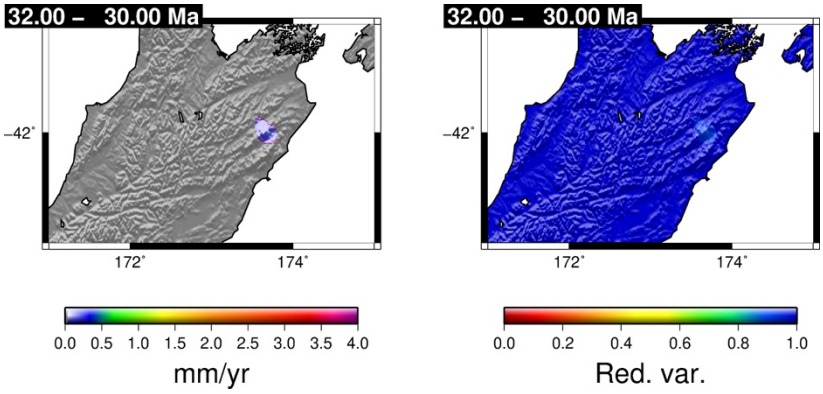

Run 1: $\dot{e}\ prior$ = 0.5 mm/yr, Blocks

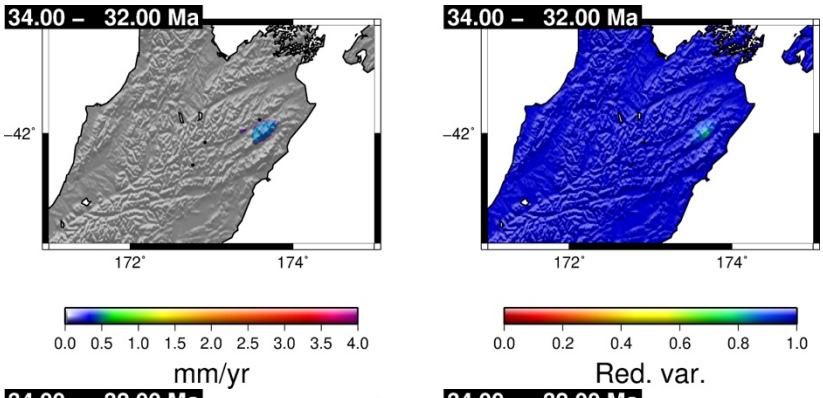

Run 2: $\dot{e}\ prior$ = 0.1 mm/yr, Blocks

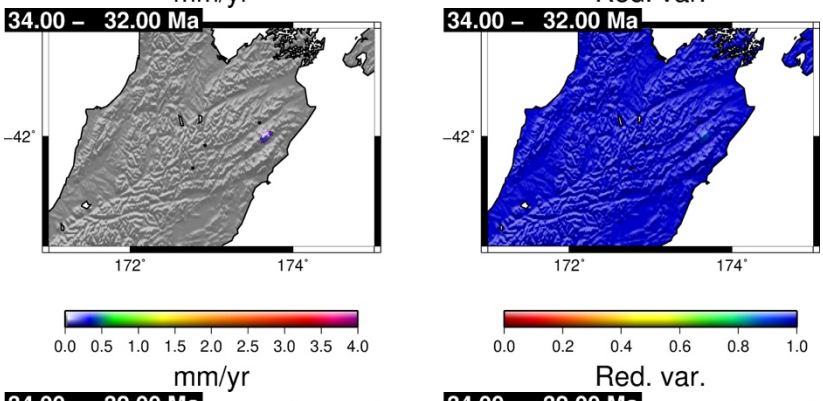

Run 3: $\dot{e}\ prior$ = 0.5 mm/yr, No blocks

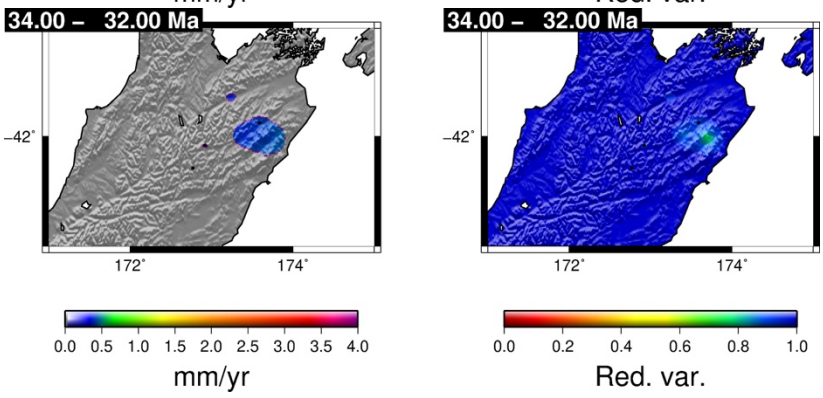

Run 4: $\dot{e}\ prior$ = 0.1 mm/yr, No blocks

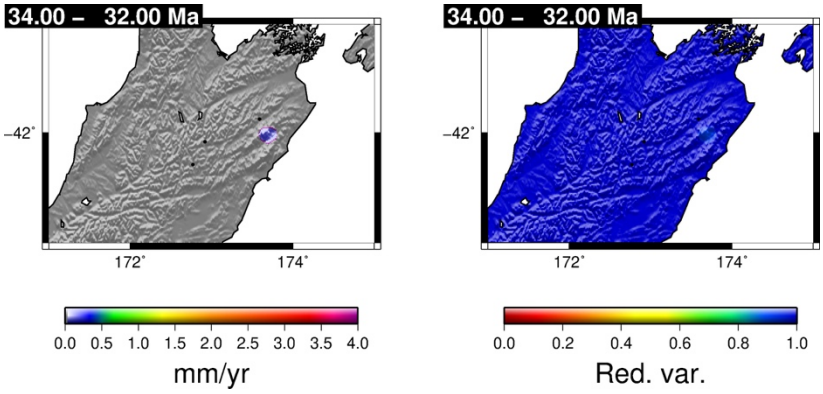

Run 1: $\dot{e}\ prior$ = 0.5 mm/yr, Blocks

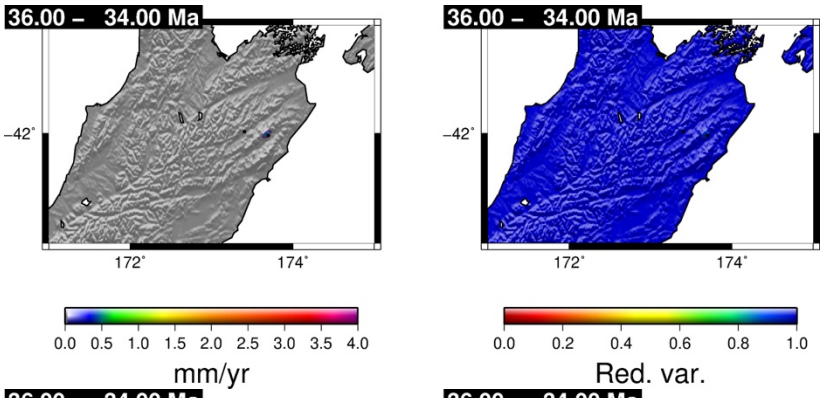

Run 2: $\dot{e}\ prior$ = 0.1 mm/yr, Blocks

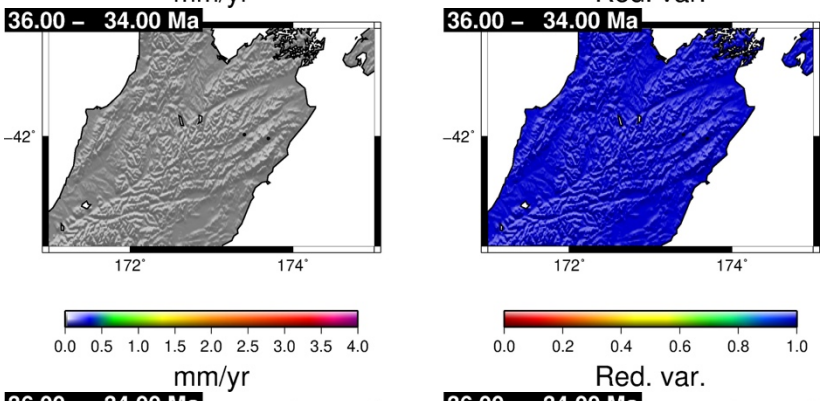

Run 3: $\dot{e}\ prior$ = 0.5 mm/yr, No blocks

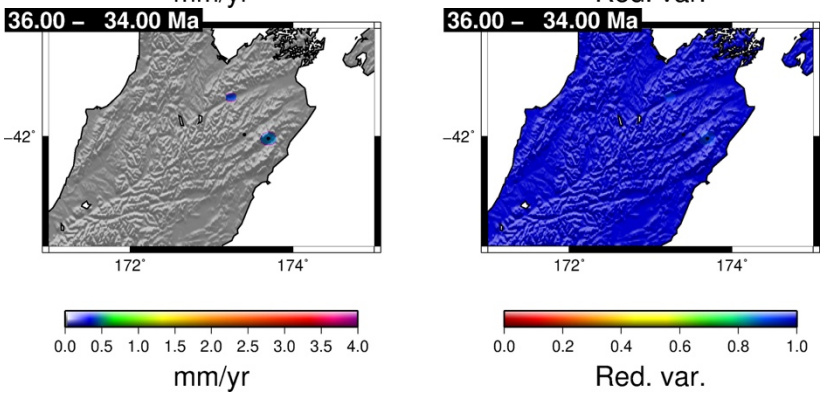

Run 4: $\dot{e}\ prior$ = 0.1 mm/yr, No blocks

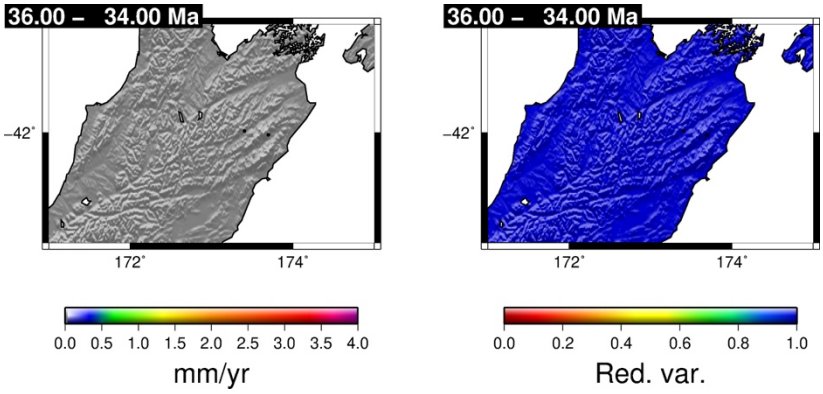

Run 1: $\dot{e}\ prior$ = 0.5 mm/yr, Blocks

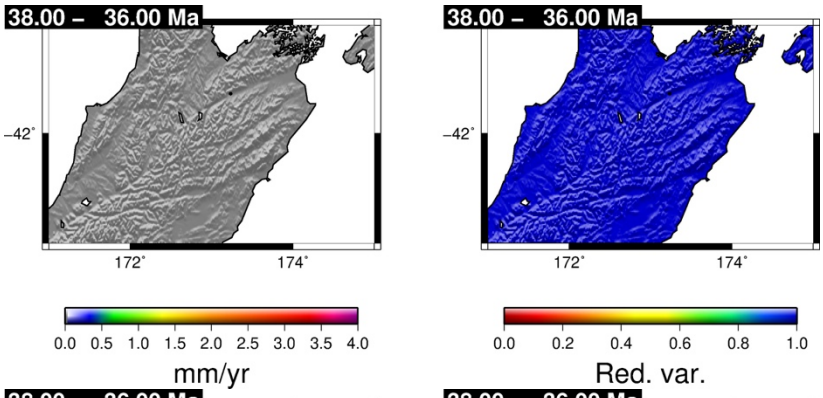

Run 2: $\dot{e}\ prior$ = 0.1 mm/yr, Blocks

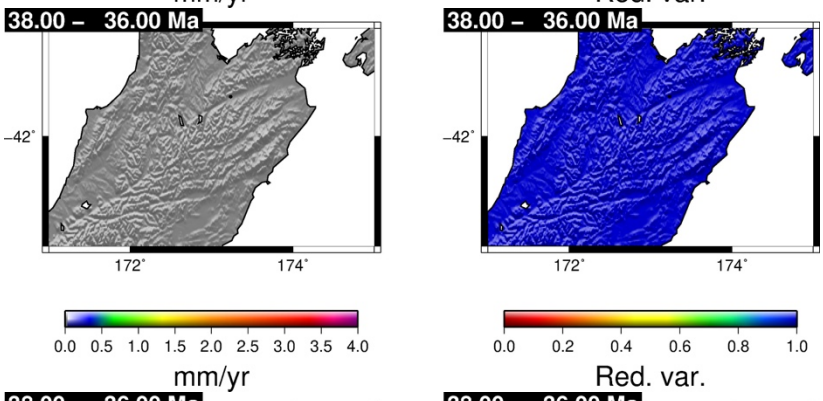

Run 3: $\dot{e}\ prior$ = 0.5 mm/yr, No blocks

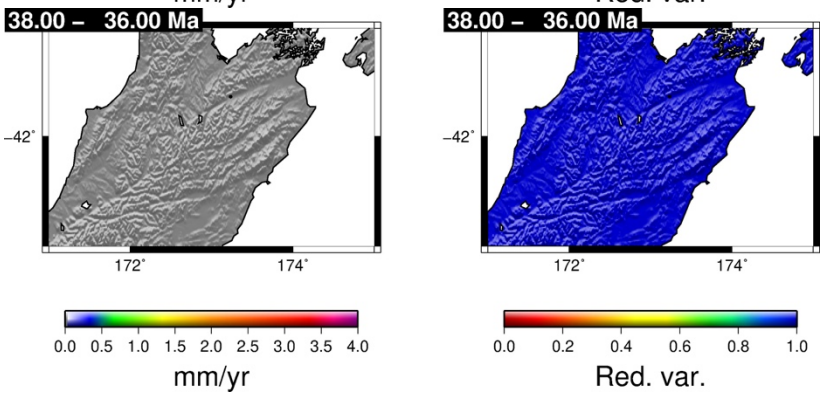

Run 4: $\dot{e}\ prior$ = 0.1 mm/yr, No blocks

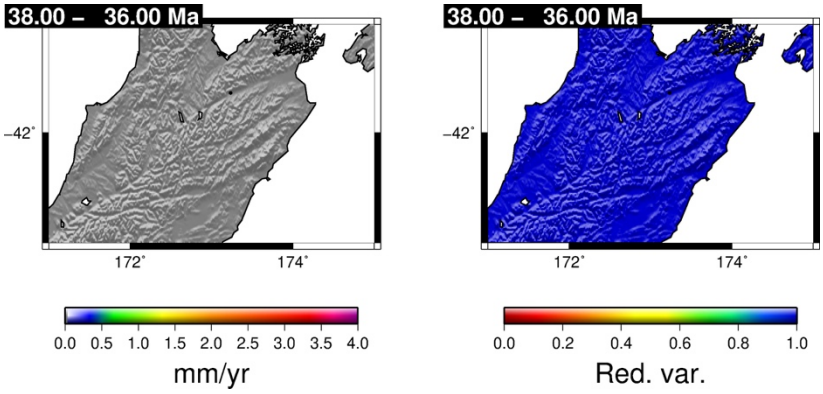

Run 1: $\dot{e}\ prior$ = 0.5 mm/yr, Blocks

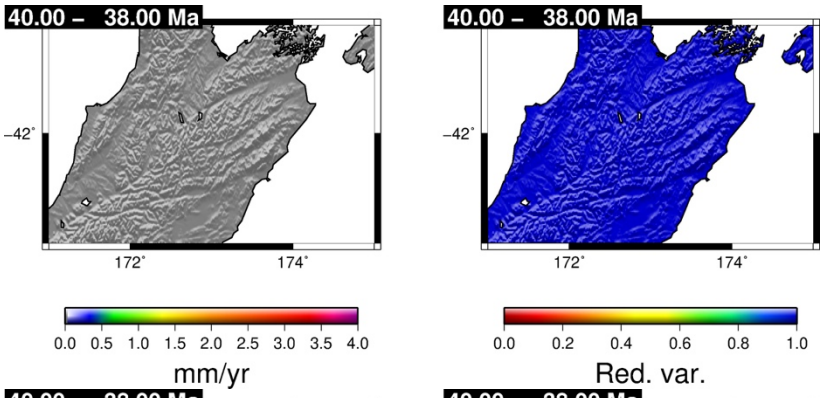

Run 2: $\dot{e}\ prior$ = 0.1 mm/yr, Blocks

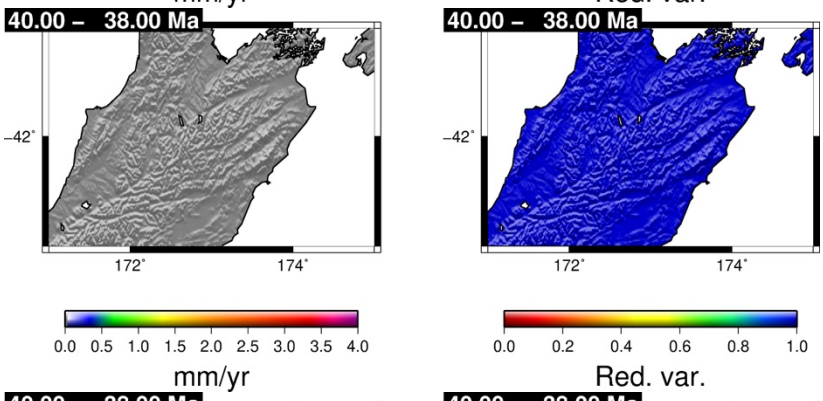

Run 3: $\dot{e}\ prior$ = 0.5 mm/yr, No blocks

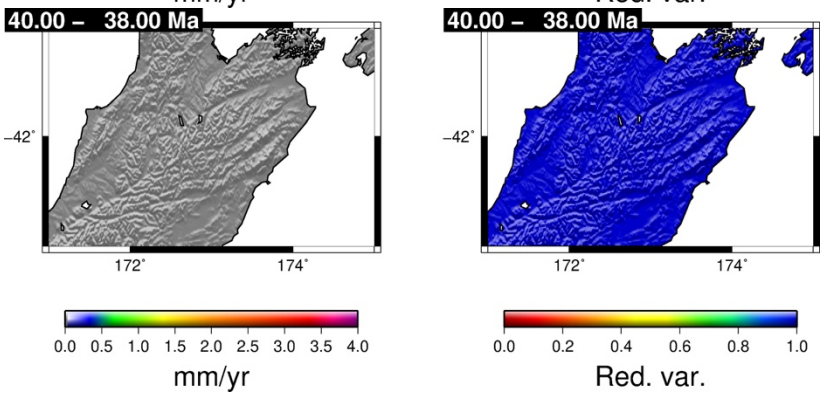

Run 4: $\dot{e}\ prior$ = 0.1 mm/yr, No blocks

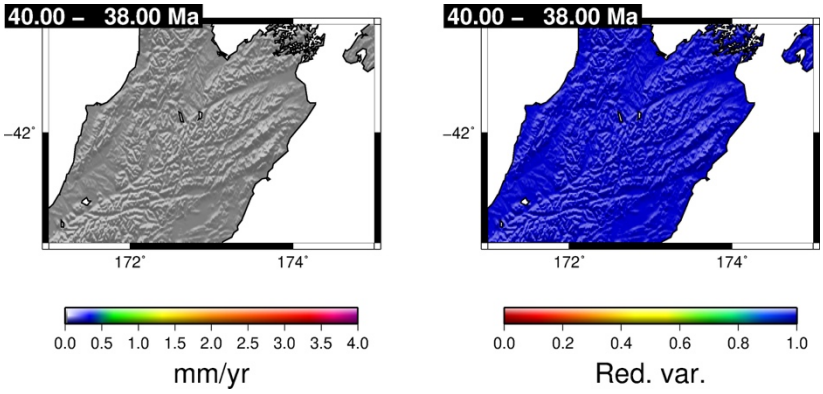

3.10.2 *GLIDE Model Results: Time-Temperature Paths*

Figure 3.15. Modeled time-temperature paths for GLIDE control points.

Control Point #1

	$\dot{e}$ *prior* = 0.5 mm/yr	$\dot{e}$ *prior* = 0.1 mm/yr
Blocks	Run 1 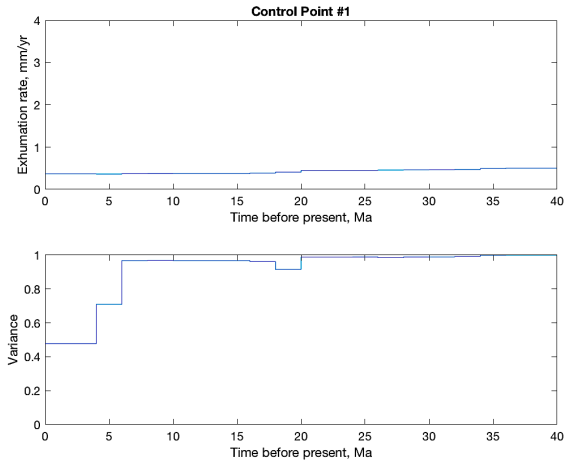	Run 2 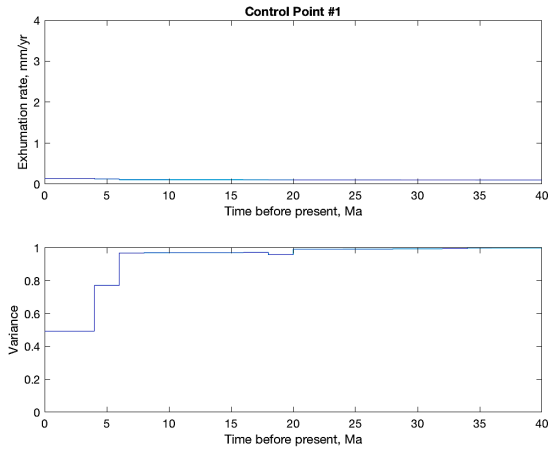
No Blocks	Run 3 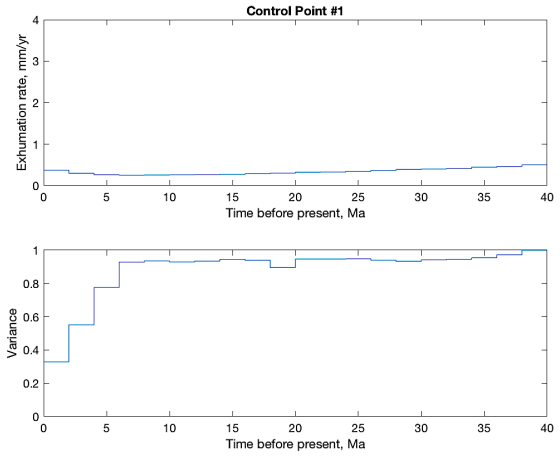	Run 4 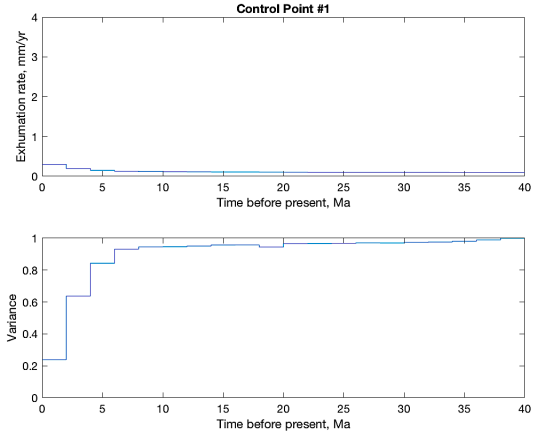

Control Point #2

	$\dot{e}$ *prior* = 0.5 mm/yr	$\dot{e}$ *prior* = 0.1 mm/yr
Blocks	Run 1 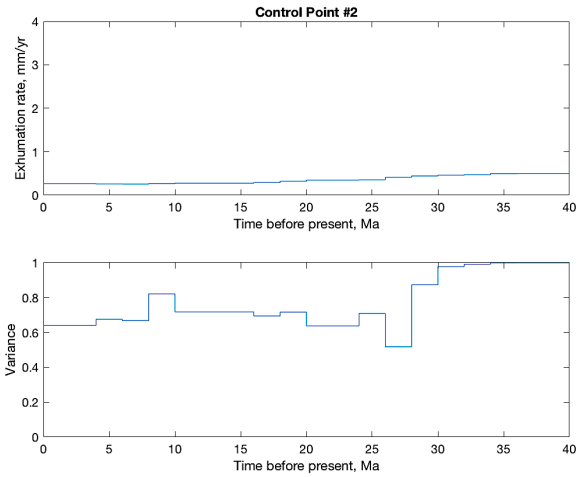	Run 2 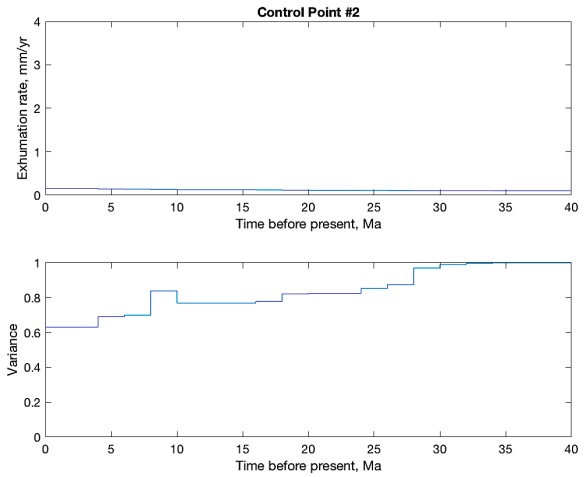
No Blocks	Run 3 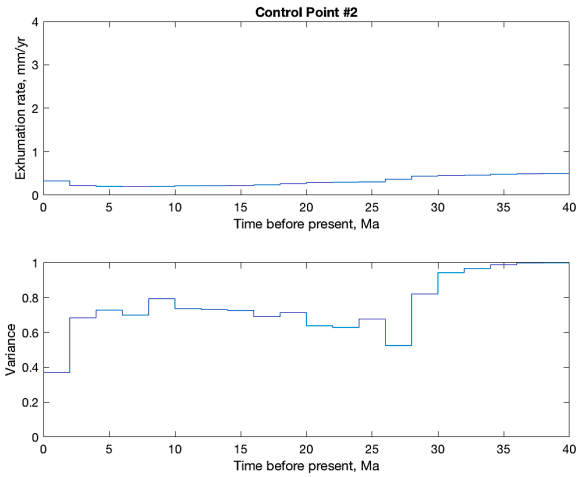	Run 4 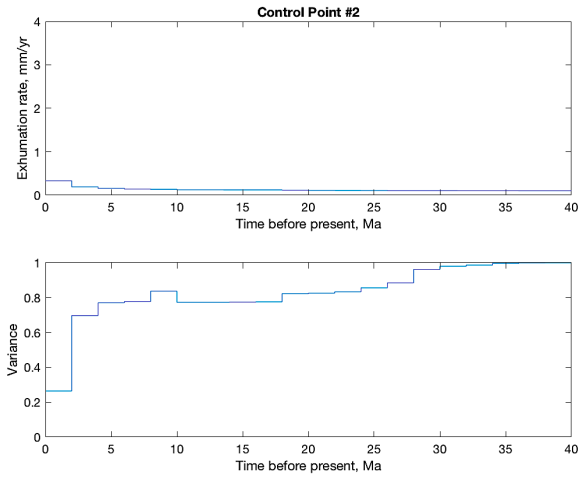

Control Point #3

	$\dot{e}$ *prior* = 0.5 mm/yr	$\dot{e}$ *prior* = 0.1 mm/yr
Blocks	Run 1 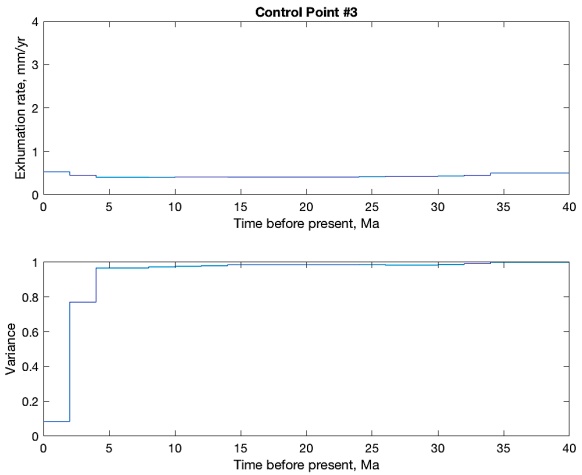	Run 2 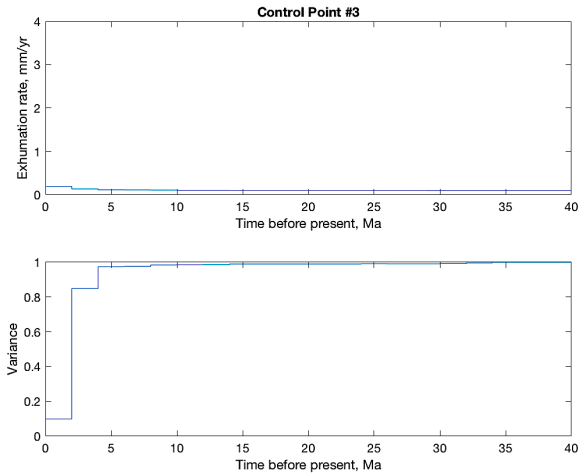
No Blocks	Run 3 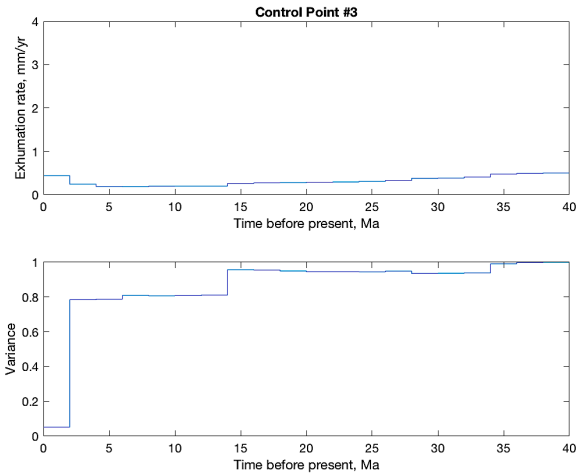	Run 4 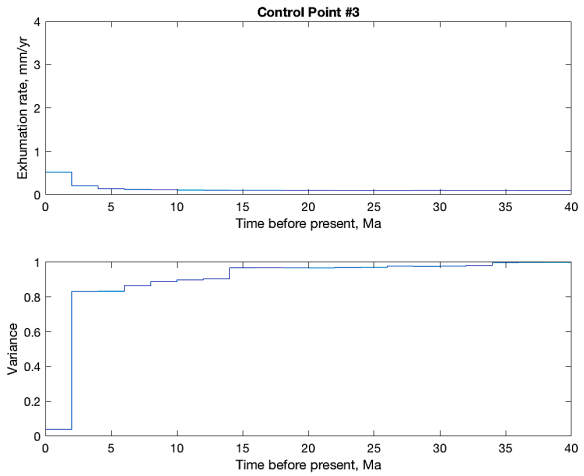

Control Point #4

	$\dot{e}$ *prior* = 0.5 mm/yr	$\dot{e}$ *prior* = 0.1 mm/yr
Blocks	Run 1 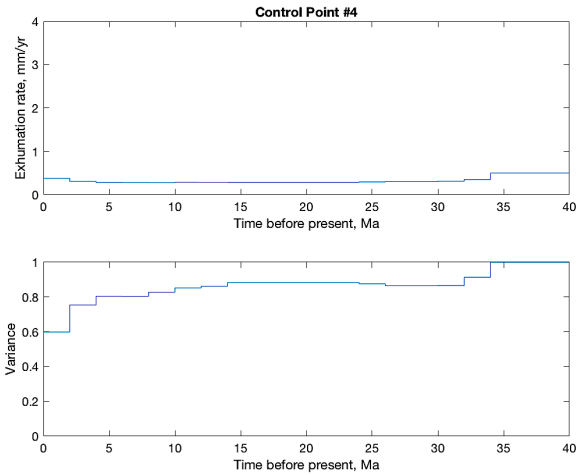	Run 2 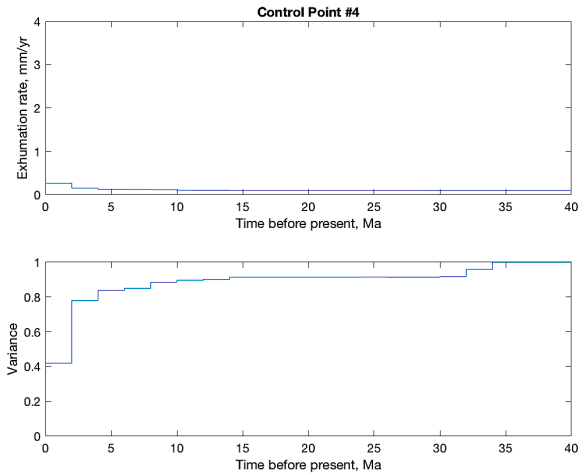
No Blocks	Run 3 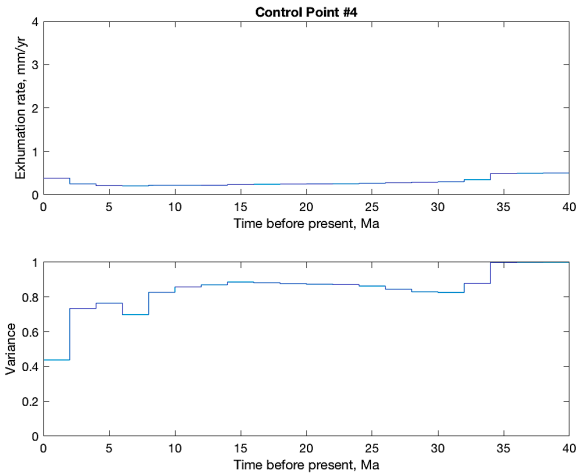	Run 4 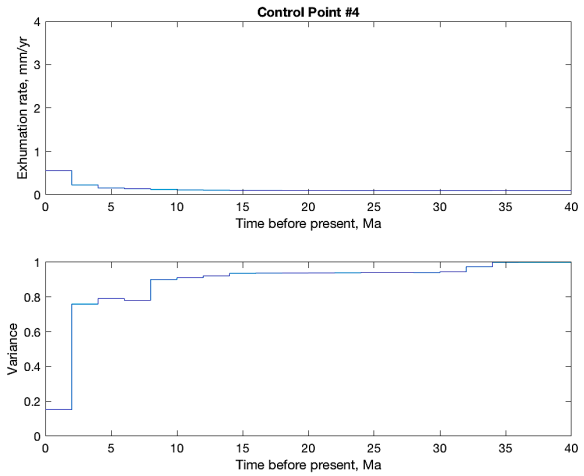

Control Point #5

	$\dot{e}$ *prior* = 0.5 mm/yr	$\dot{e}$ *prior* = 0.1 mm/yr
Blocks	Run 1 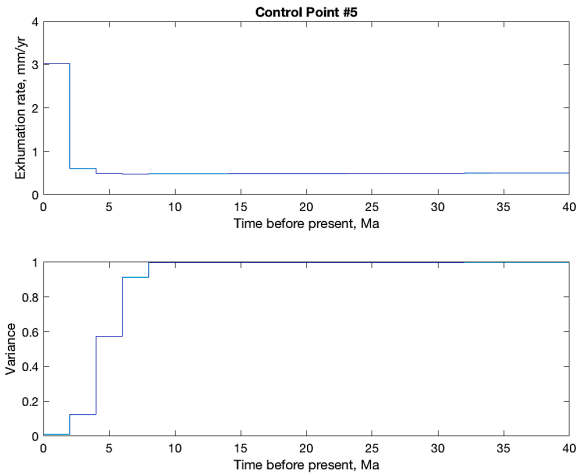	Run 2 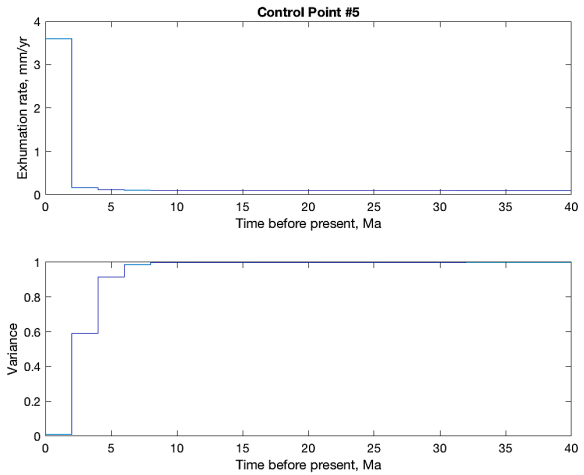
No Blocks	Run 3 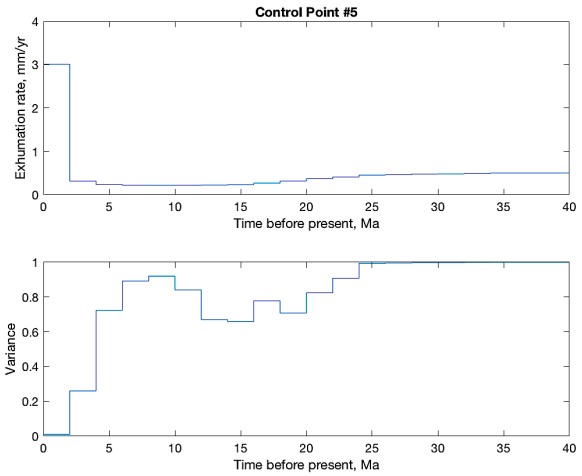	Run 4 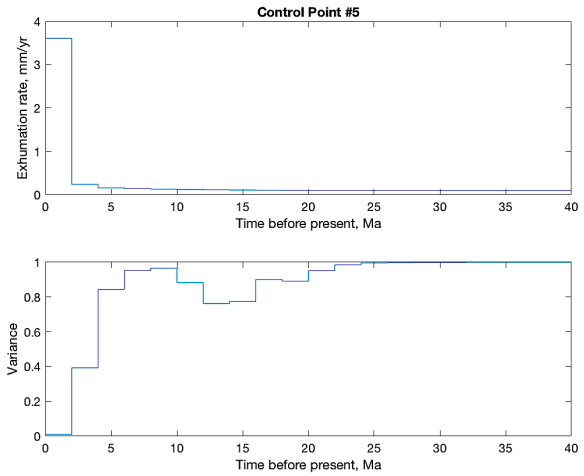

Control Point #6

	$\dot{e}$ *prior* = 0.5 mm/yr	$\dot{e}$ *prior* = 0.1 mm/yr
Blocks	Run 1 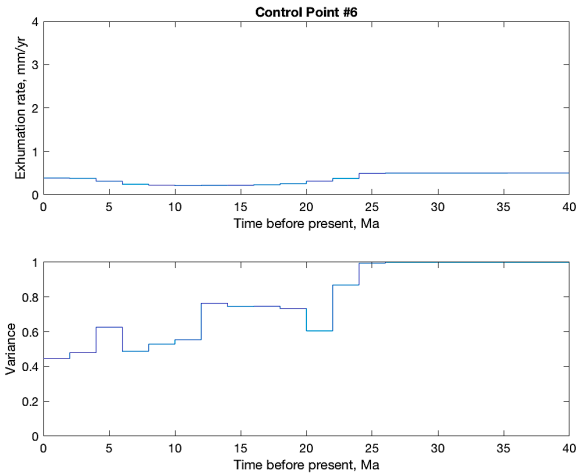	Run 2 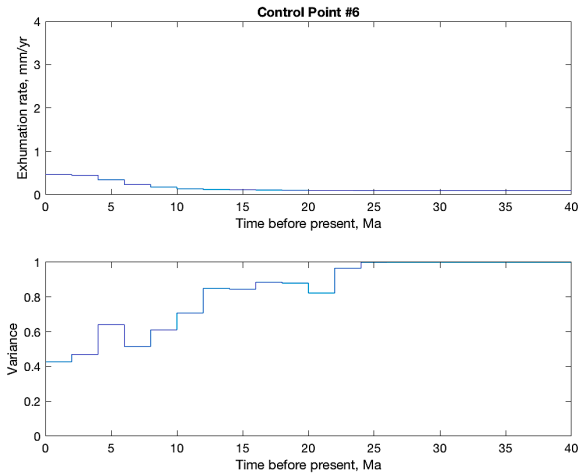
No Blocks	Run 3 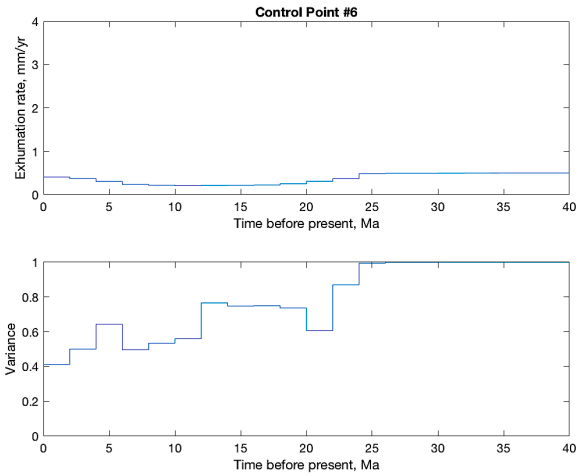	Run 4 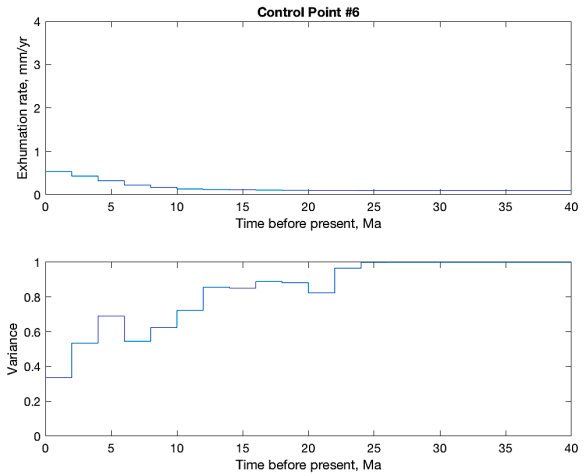

Control Point #7

	$\dot{e}$ *prior* = 0.5 mm/yr	$\dot{e}$ *prior* = 0.1 mm/yr
Blocks	Run 1 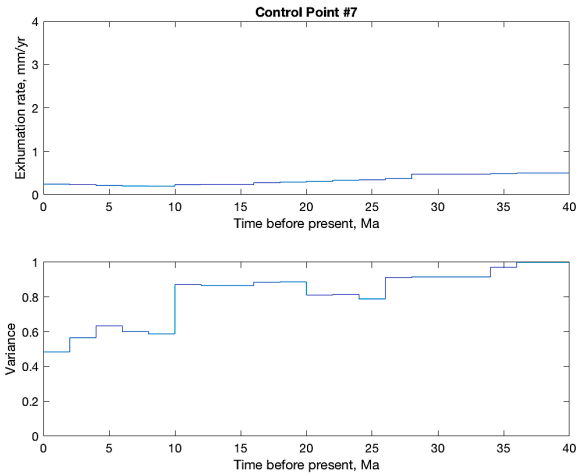	Run 2 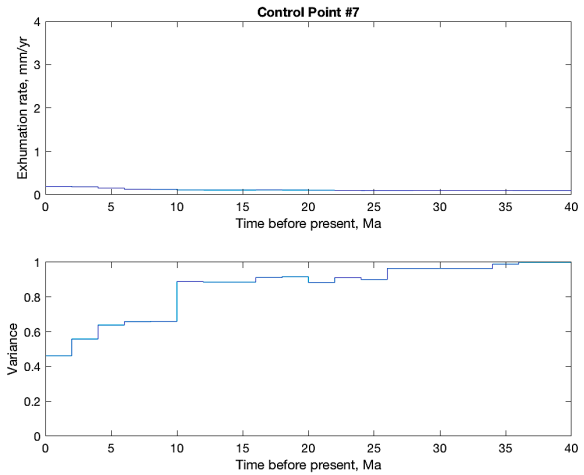
No Blocks	Run 3 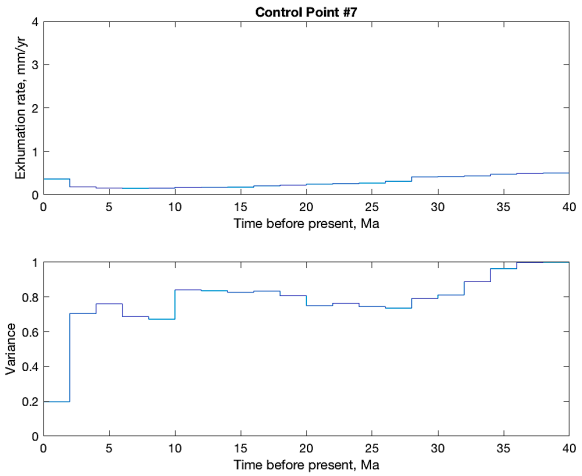	Run 4 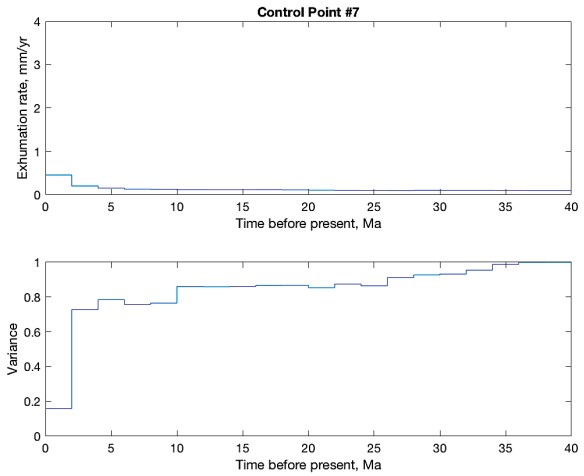

Control Point #8

	$\dot{e}$ *prior* = 0.5 mm/yr	$\dot{e}$ *prior* = 0.1 mm/yr
Blocks	Run 1 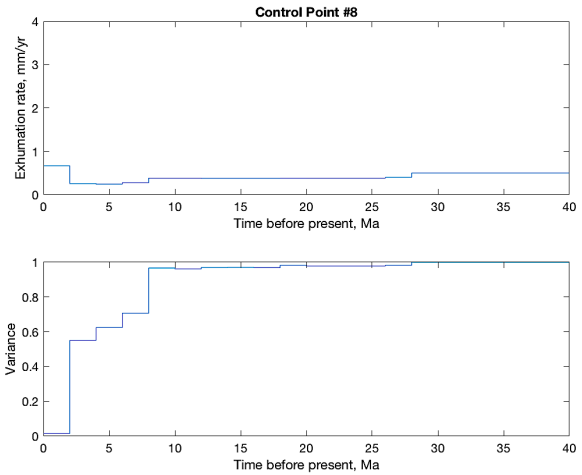	Run 2 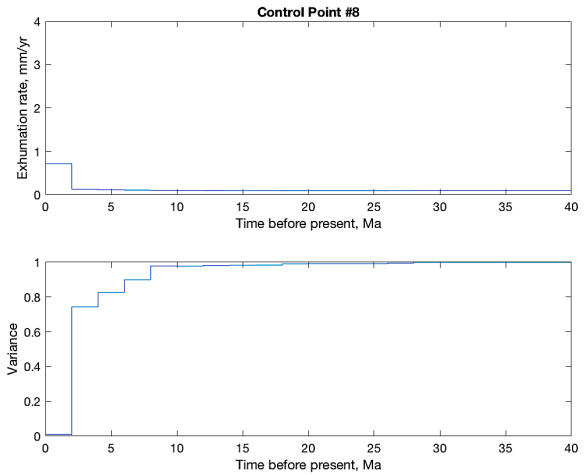
No Blocks	Run 3 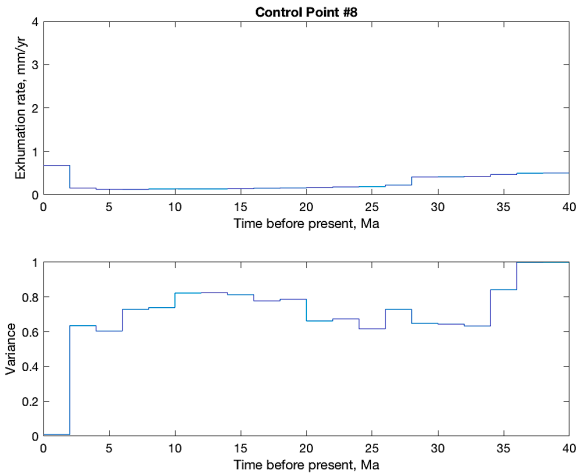	Run 4 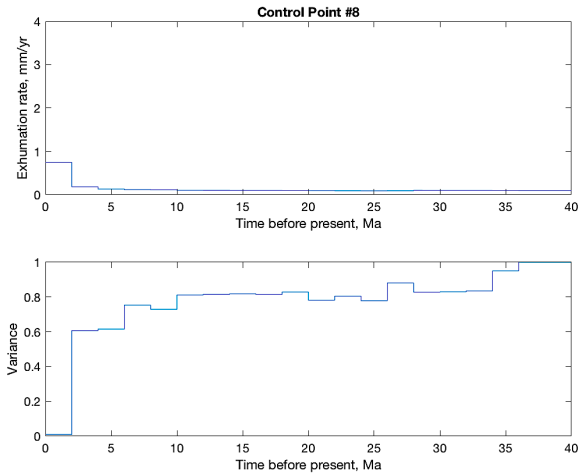

Control Point #9

	$\dot{e}$ *prior* = 0.5 mm/yr	$\dot{e}$ *prior* = 0.1 mm/yr
Blocks	Run 1 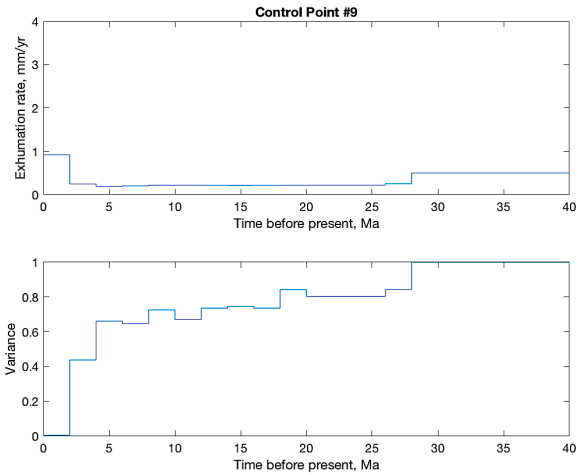	Run 2 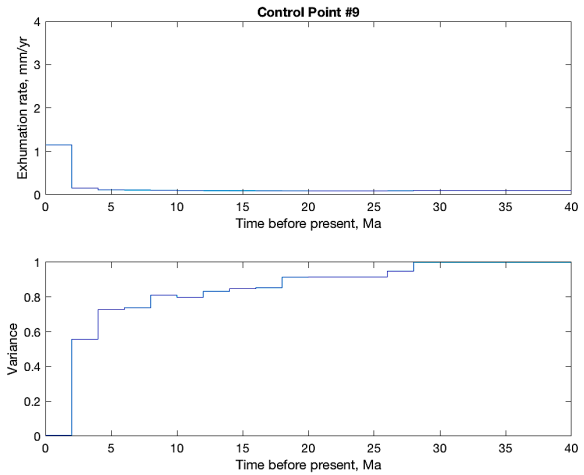
No Blocks	Run 3 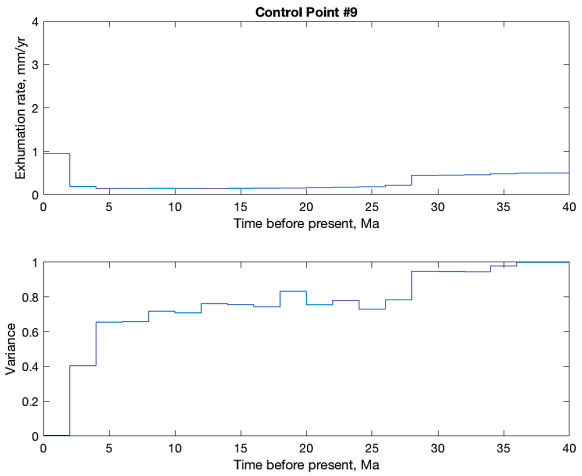	Run 4 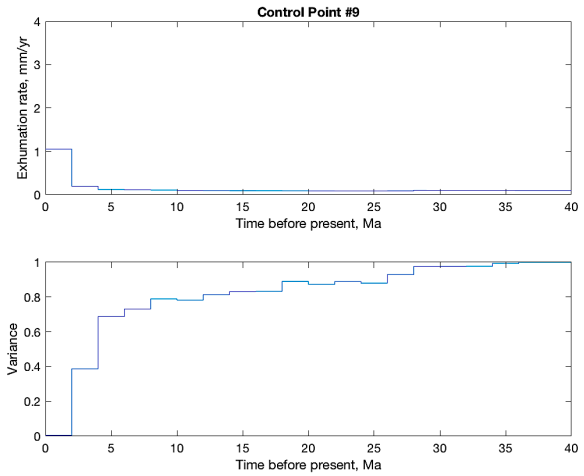

Control Point #10

	$\dot{e}$ *prior* = 0.5 mm/yr	$\dot{e}$ *prior* = 0.1 mm/yr
Blocks	Run 1 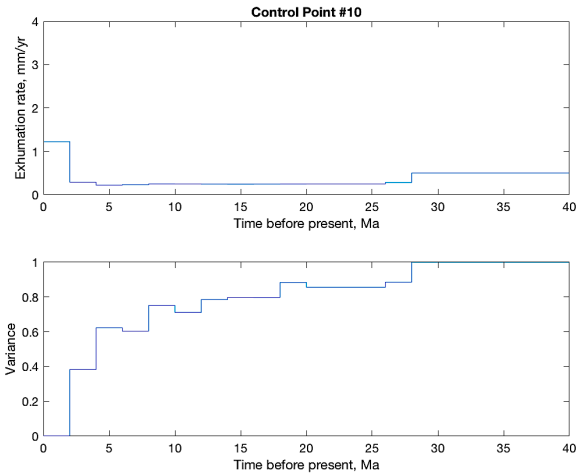	Run 2 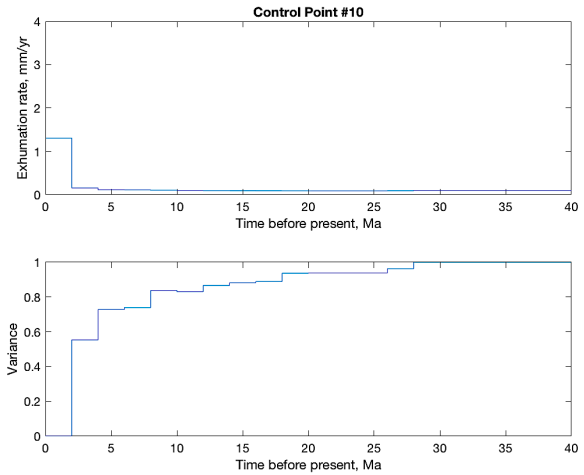
No Blocks	Run 3 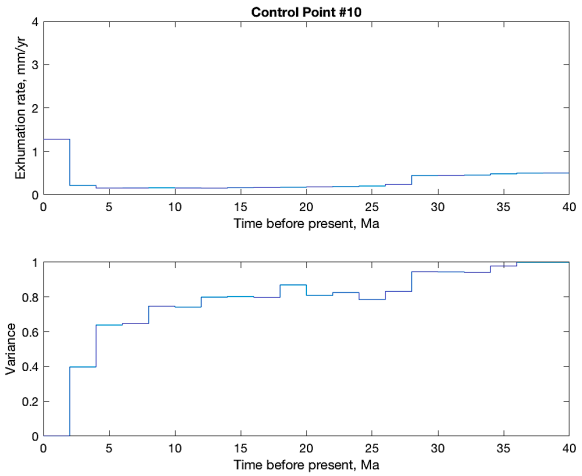	Run 4 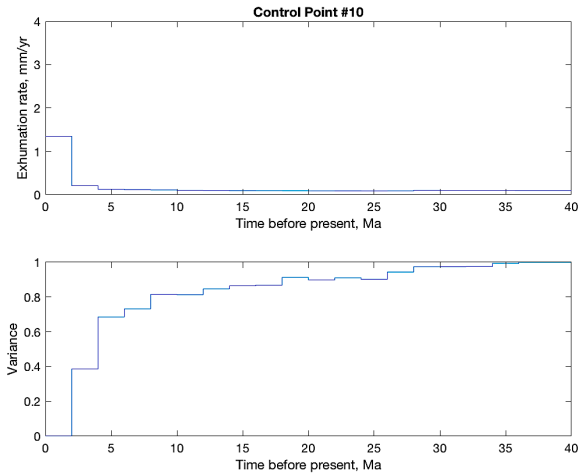

Control Point #11

	$\dot{e}$ *prior* = 0.5 mm/yr	$\dot{e}$ *prior* = 0.1 mm/yr
Blocks	Run 1 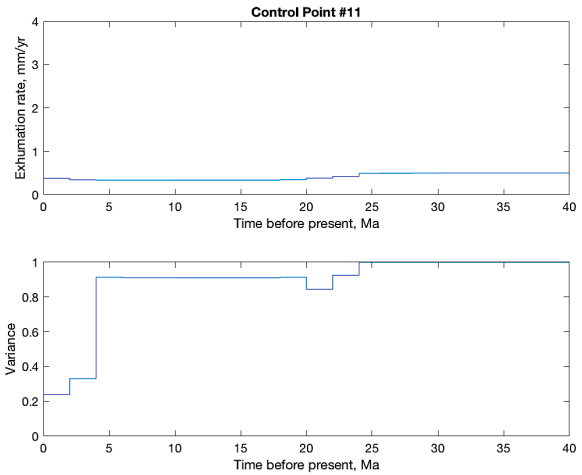	Run 2 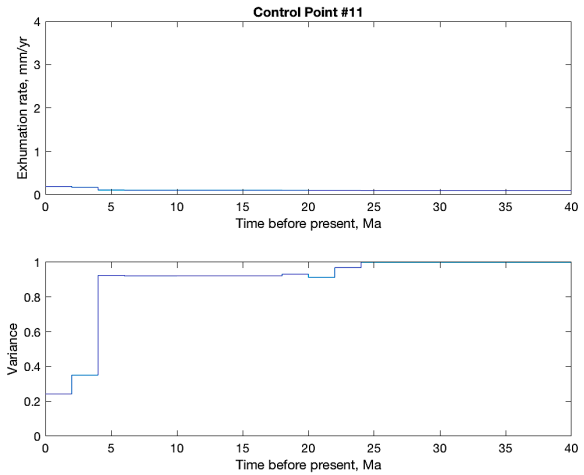
No Blocks	Run 3 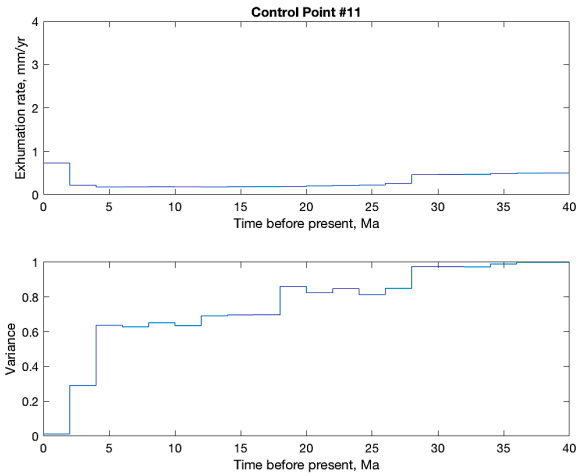	Run 4 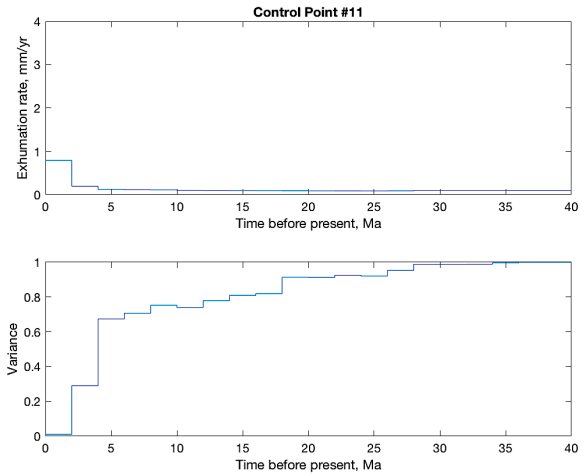

Control Point #12

	$\dot{e}$ *prior* = 0.5 mm/yr	$\dot{e}$ *prior* = 0.1 mm/yr
Blocks	Run 1 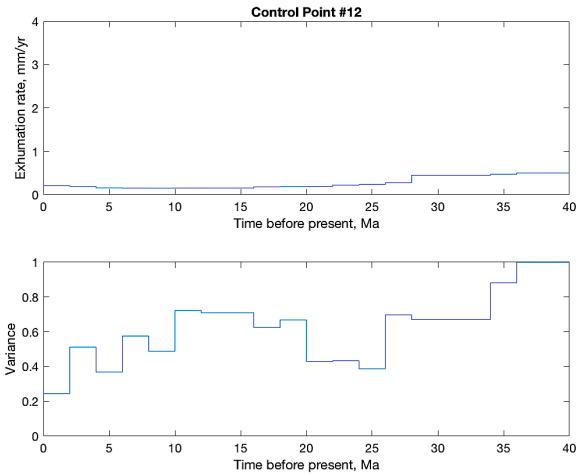	Run 2 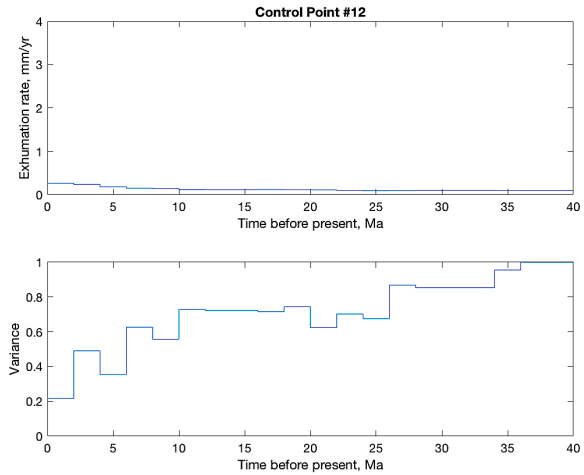
No Blocks	Run 3 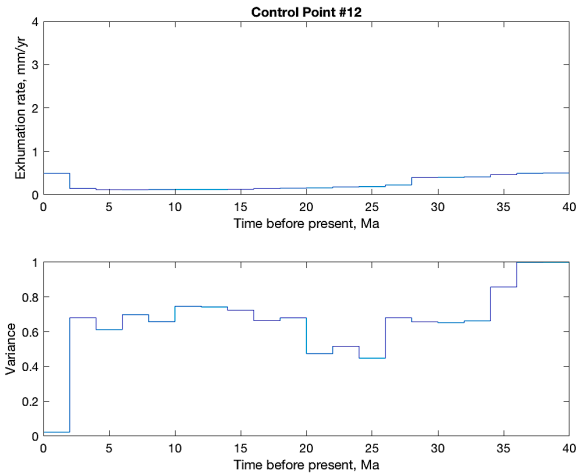	Run 4 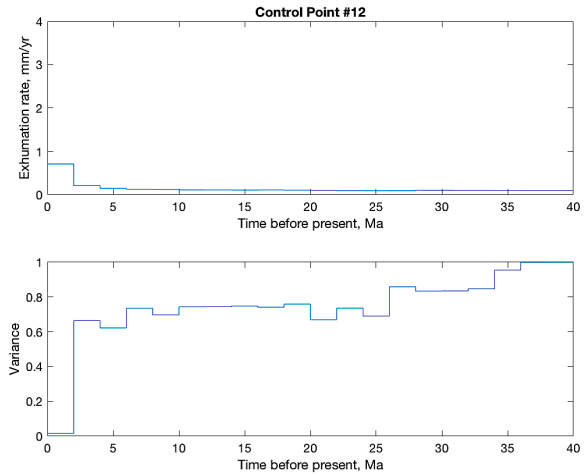

Control Point #13

	$\dot{e}$ *prior* = 0.5 mm/yr	$\dot{e}$ *prior* = 0.1 mm/yr
Blocks	Run 1 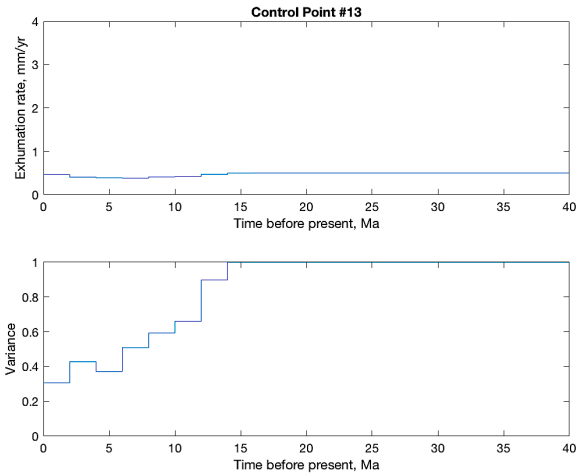	Run 2 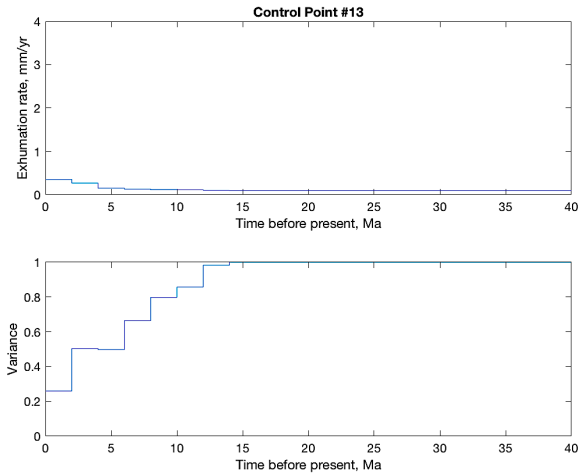
No Blocks	Run 3 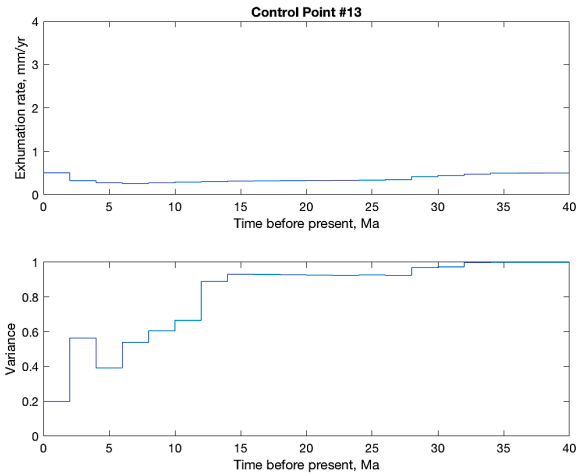	Run 4 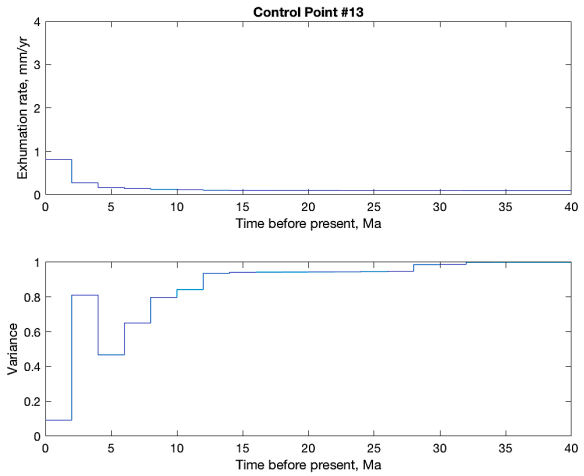

Control Point #14

	$\dot{e}$ *prior* = 0.5 mm/yr	$\dot{e}$ *prior* = 0.1 mm/yr
Blocks	Run 1 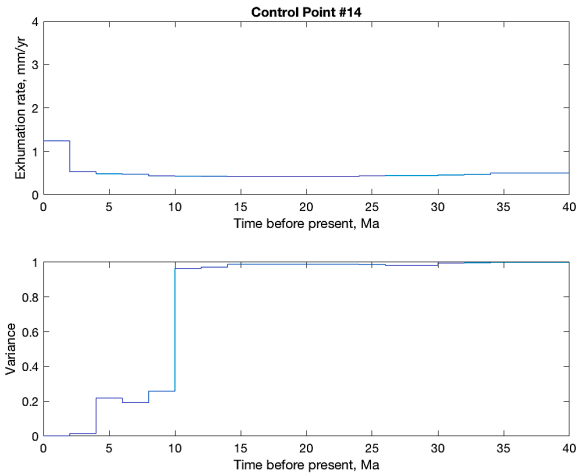	Run 2 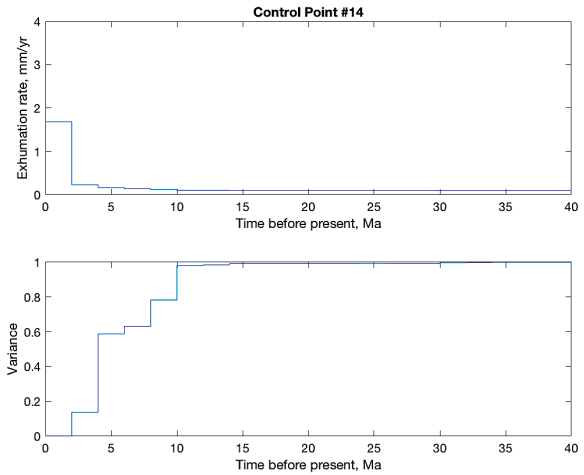
No Blocks	Run 3 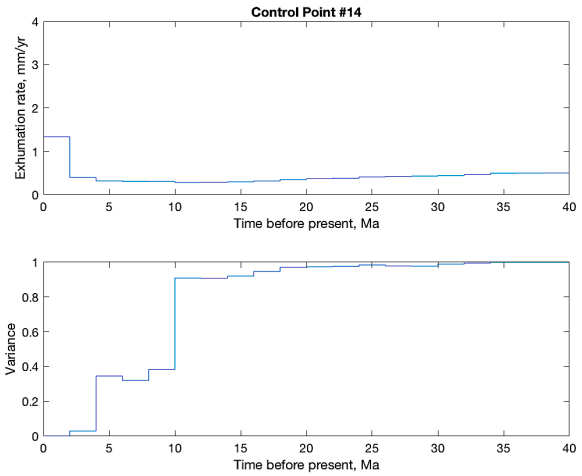	Run 4 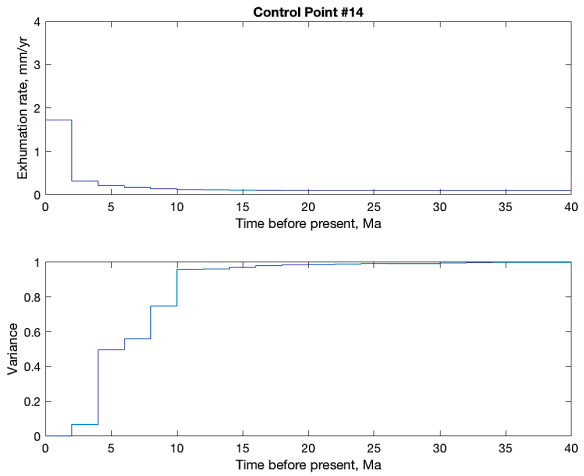

Control Point #15

	$\dot{e}$ *prior* = 0.5 mm/yr	$\dot{e}$ *prior* = 0.1 mm/yr
Blocks	Run 1 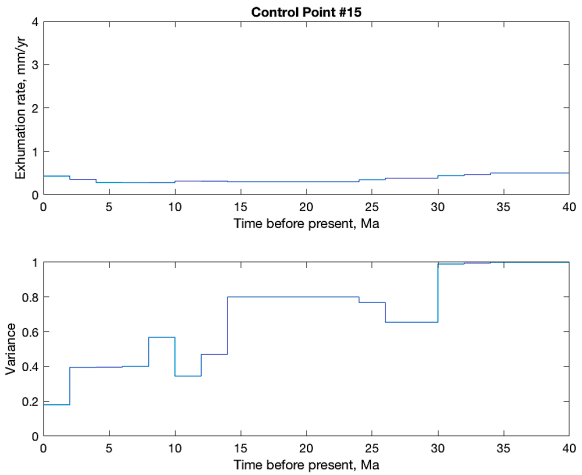	Run 2 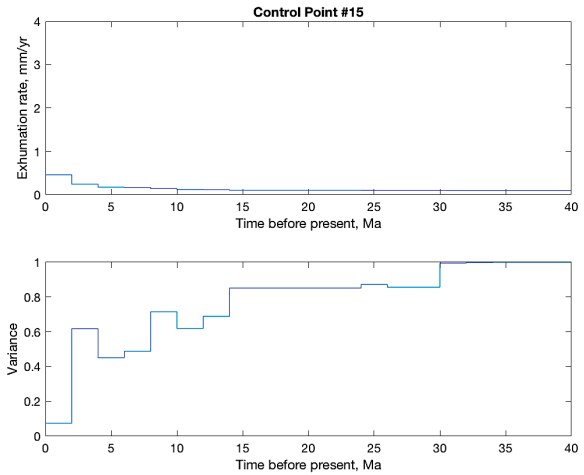
No Blocks	Run 3 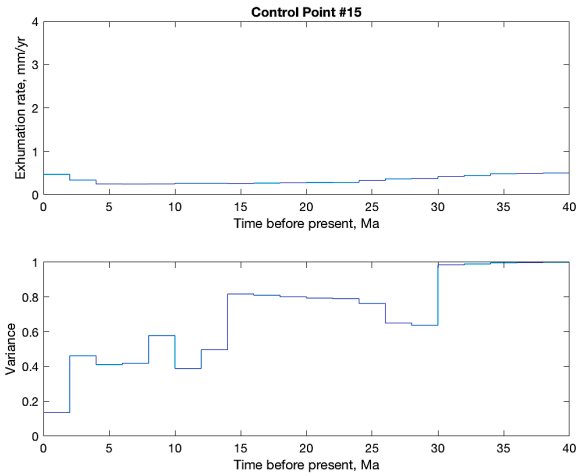	Run 4 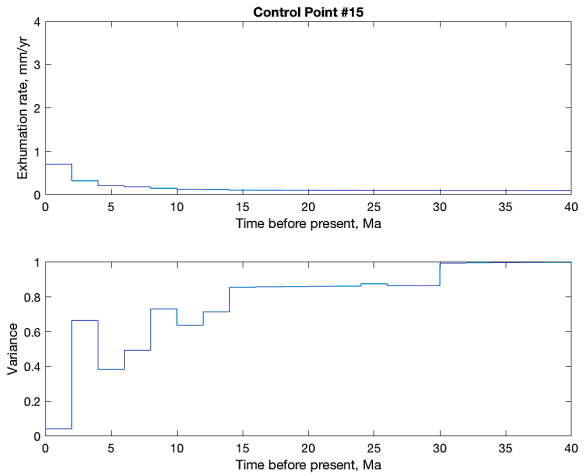

Control Point #16

	$\dot{e}$ *prior* = 0.5 mm/yr	$\dot{e}$ *prior* = 0.1 mm/yr
Blocks	Run 1 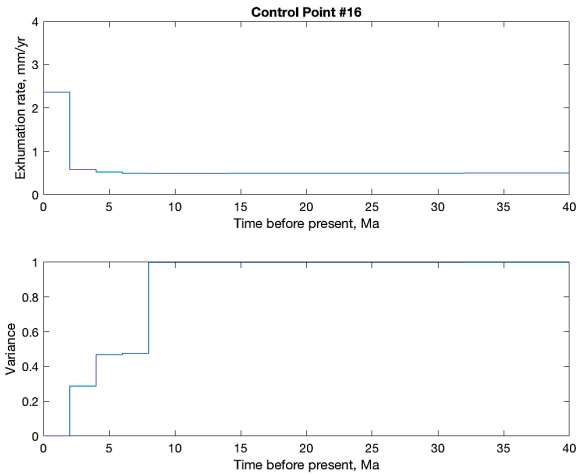	Run 2 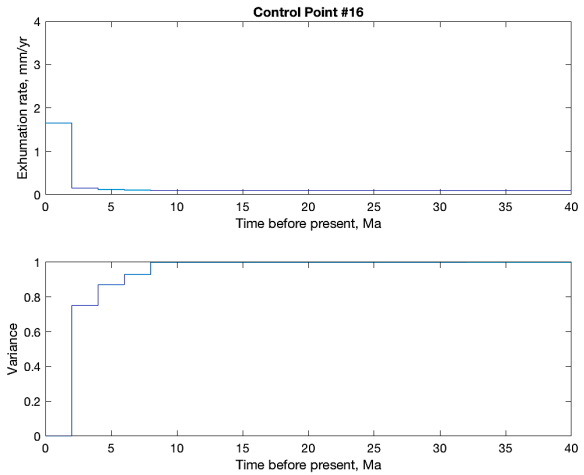
No Blocks	Run 3 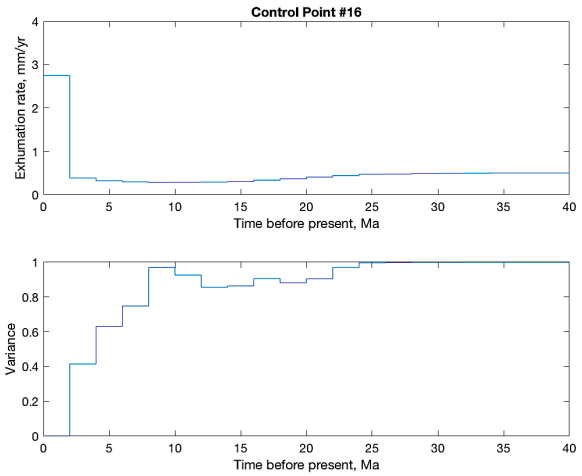	Run 4 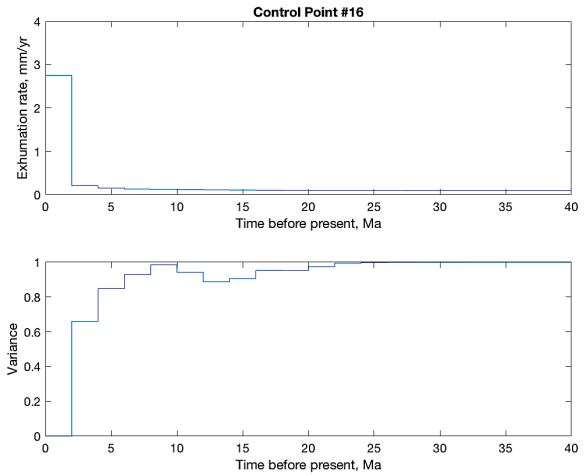

Control Point #17

	$\dot{e}$ *prior* = 0.5 mm/yr	$\dot{e}$ *prior* = 0.1 mm/yr
Blocks	Run 1 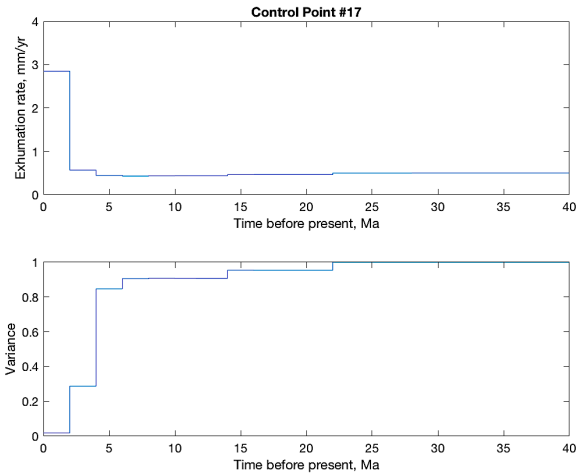	Run 2 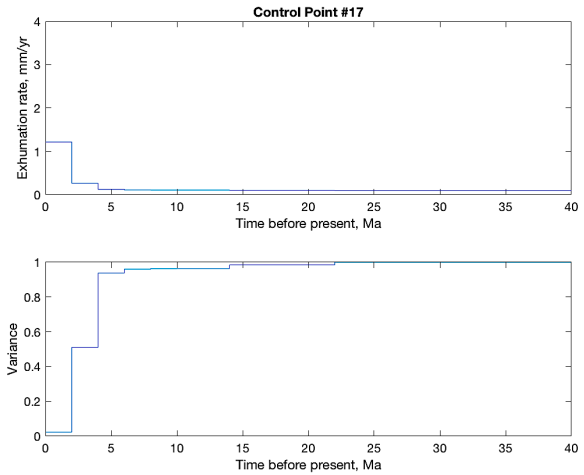
No Blocks	Run 3 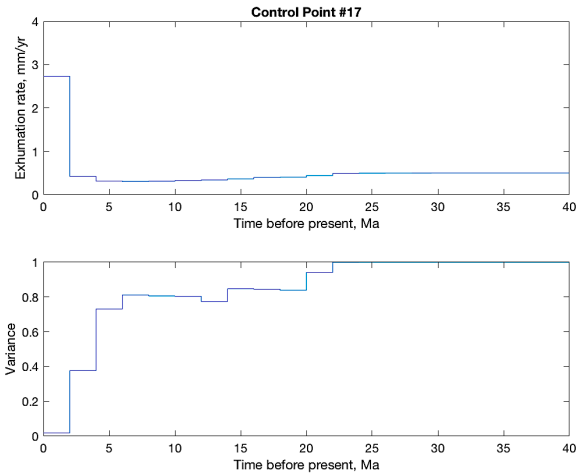	Run 4 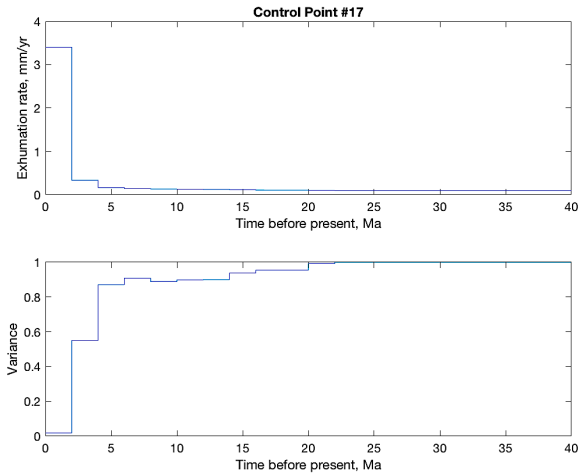

Control Point #18

	$\dot{e}$ *prior* = 0.5 mm/yr	$\dot{e}$ *prior* = 0.1 mm/yr
Blocks	Run 1 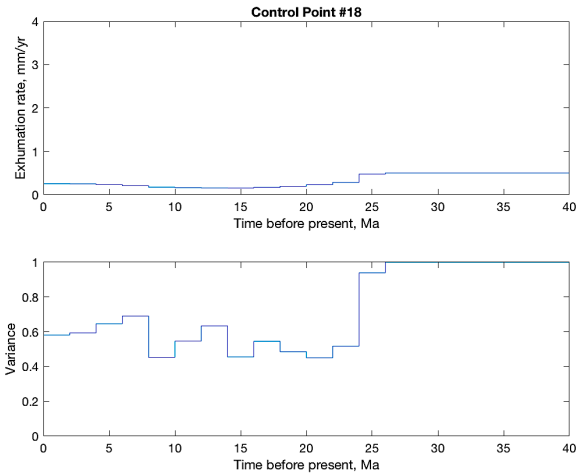	Run 2 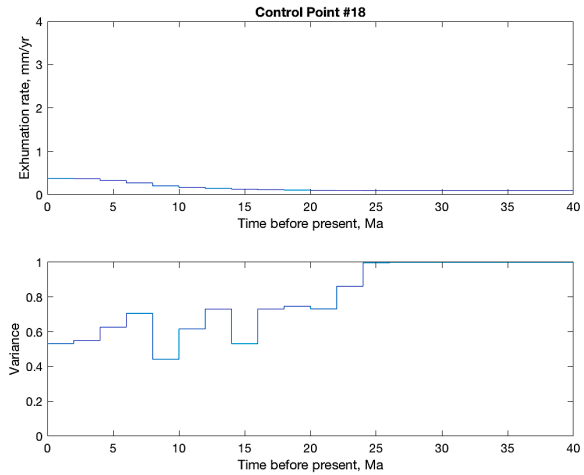
No Blocks	Run 3 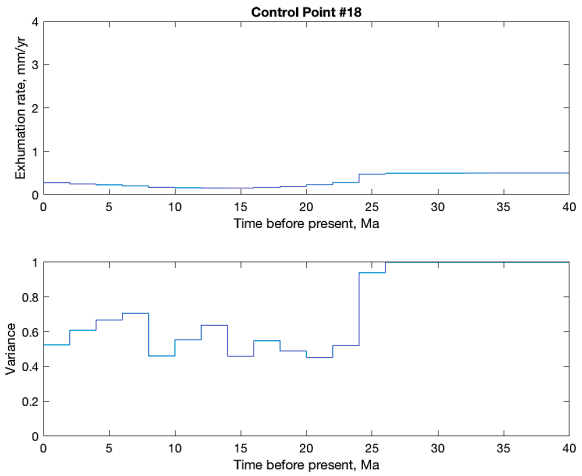	Run 4 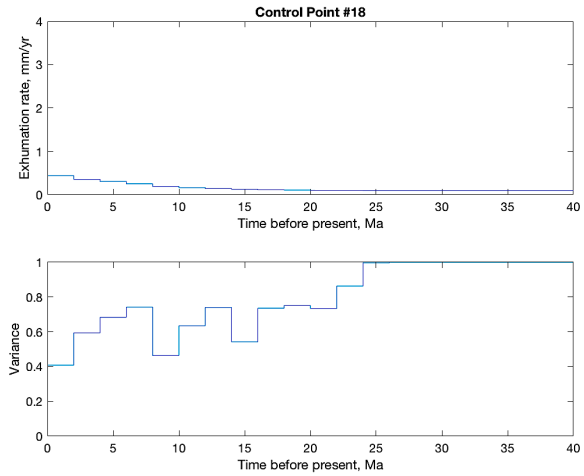

Control Point #19

	$\dot{e}$ *prior* = 0.5 mm/yr	$\dot{e}$ *prior* = 0.1 mm/yr
Blocks	Run 1 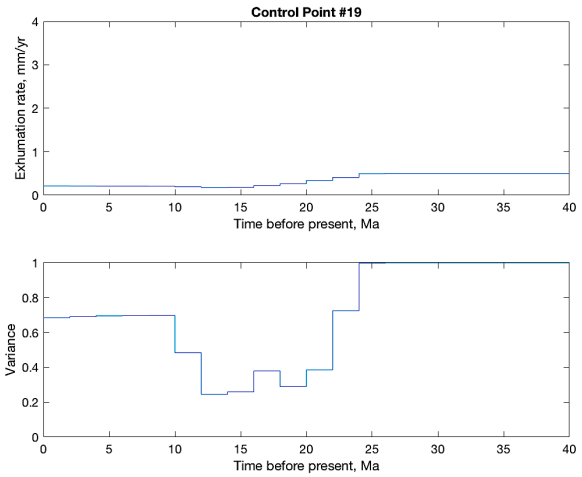	Run 2 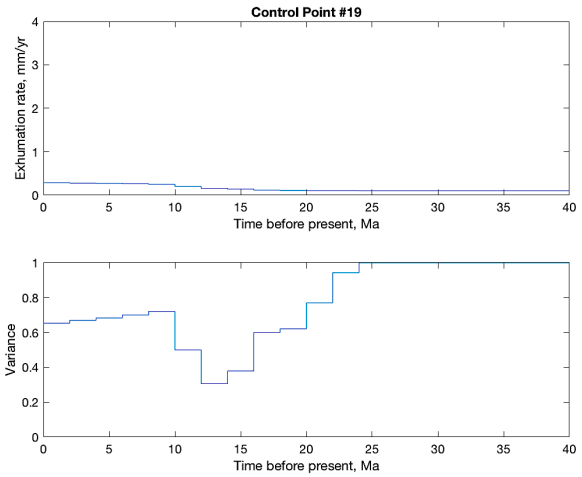
No Blocks	Run 3 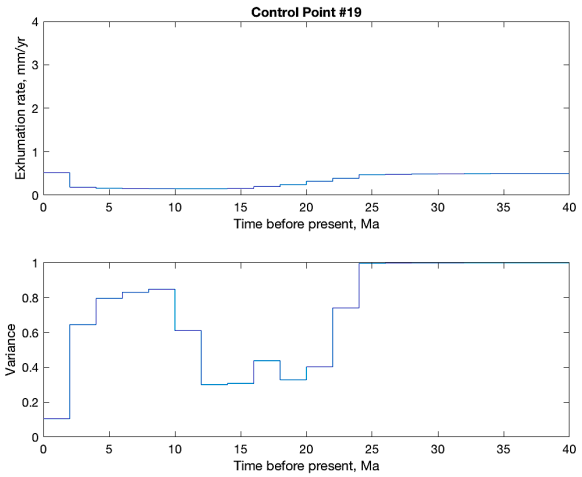	Run 4 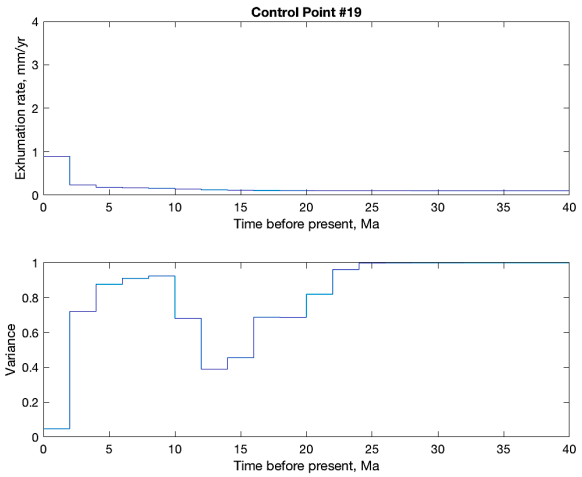

Control Point #20

	$\dot{e}$ *prior* = 0.5 mm/yr	$\dot{e}$ *prior* = 0.1 mm/yr
Blocks	Run 1 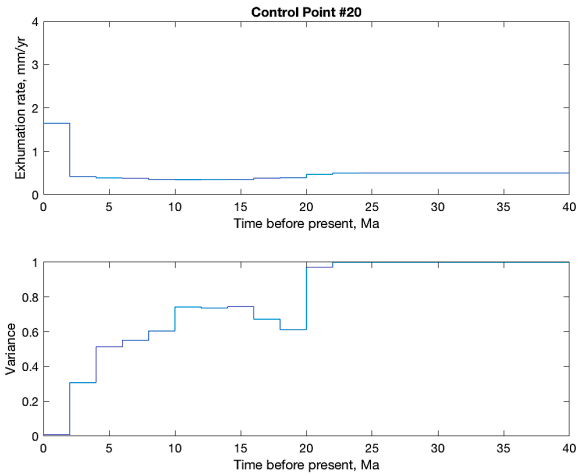	Run 2 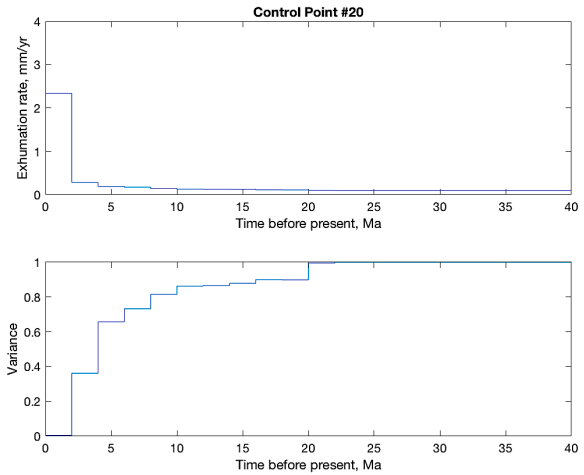
No Blocks	Run 3 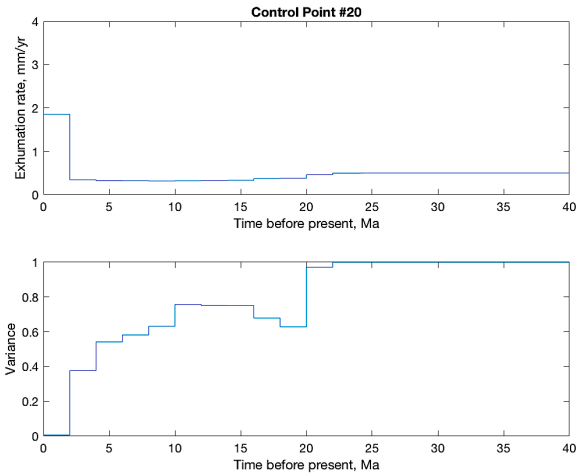	Run 4 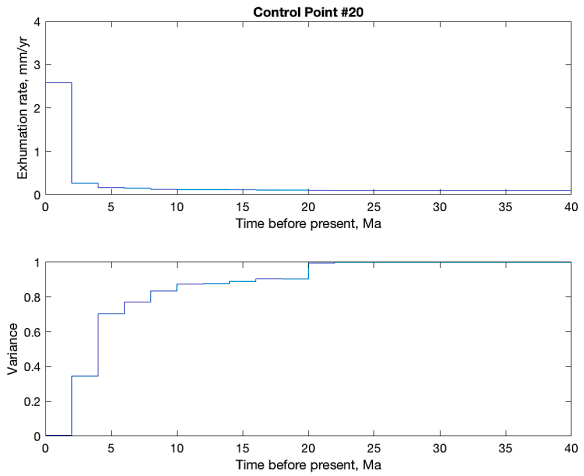

Chapter 4. THE ROLE OF NEAR-FAULT RELIEF ELEMENTS IN CREATING AND MAINTAINING A STRIKE-SLIP LANDSCAPE[3]

Strike-slip landscapes are often associated with a suite of characteristic geomorphic features that provide primary evidence for interpreting fault slip histories. Here we explore the role of shutter ridges, areas of relief advected laterally along faults, in generating two classic strike-slip processes: progressive lateral offset of channels, and stream capture. Landscape models and comparative analysis of the Marlborough Fault System, NZ, show that the length of channel offsets observable in a landscape is primarily controlled by the length of shutter ridges. In our simple landscape model, this scale is controlled by the drainage spacing, and therefore by the geometry of the mountain range. In a more complex landscape, this scale may be controlled by lithologic or structural contrasts. We also find that shutter ridge relief inhibits stream capture, especially at slow fault slip rates relative to hillslope erosion rates. In this case, lateral drainage advection enables streams to "outrun" capture.

4.1 Introduction and Background

Geomorphic features characteristic of strike-slip settings, such as linear, fault-parallel valleys, sag ponds, shutter ridges, elongated, offset, and warped stream channels, and laterally offset

[3] This chapter has been published in *Geophysical Research Letters.* The citation is as follows:
Harbert, S. A., Duvall, A. R., & Tucker, G. E. (2018). The role of near-fault relief elements in creating and maintaining a strike-slip landscape. *Geophysical Research Letters*, *45*(21), 11-683. **https://doi.org/10.1029/2018GL080045**.
Author contributions were as follows: Duvall, Tucker, and Harbert conceived of the general study. Harbert designed the specific experiment and performed the modeling and data analysis. Harbert, Duvall and Tucker all contributed to interpreting the results. Harbert wrote the manuscript and all authors reviewed it.

glacial moraines and river terraces, have long aided in the identification and study of strike-slip fault systems (e.g., Wallace, 1949, 1968; Walker and Jackson, 2002; Arrowsmith and Zielke, 2009; Walker and Allen, 2012; Jiang et al., 2017), including estimation of fault slip rates and off-fault deformation rates (Sieh and Jahns, 1984; Replumaz et al., 2001; Fu et al., 2005; Pucci et al., 2008; Goren et al., 2015; Gray et al, 2017). Despite this widely recognized suite of "classic" strike-slip landscape features, one key observable yet to be addressed carefully in the literature is that not all strike-slip faults, even the longest and fastest slipping among them, demonstrate consistently similar geomorphology. For example, Gaudemer et al. (1989) found that only 30% of channels crossing segments of the San Andreas fault were offset in the "correct" direction, while Walker and Allen (2012) found a proportion of about 80% along the Kuh Banan fault in Iran. Fu et al. (2005) observed that channel offset lengths across the Kunlun fault in Tibet cluster around a few particular values. In order to successfully interpret landscapes for tectonic information, it is important to know what controls the topographic expression of a fault. Are tectonic variables such as slip rate, slip sense, and maturity most important? Or do characteristics of the surrounding landscape, such as topographic relief and relief structure, drainage density/spacing, slope angles, and bedrock erodibility dictate the near-fault landscape patterns?

Previous studies of streams that cross strike-slip faults demonstrate an ongoing cycle of fault-parallel channel lengthening by offset, followed by shortening of fault-parallel river segments by stream capture, as in Figure 4.1a (Wallace, 1968; Gaudemer et al, 1989; Huang, 1993; Repulmaz et al., 2001; Hubert-Ferrari et al., 2002; Ouchi, 2004, 2005; Goren et al., 2014; Duvall and Tucker, 2015). These two processes have opposing effects on horizontal channel offset lengths—a measure of the "strength" of the landscape signature of strike-slip faulting—that can be observed at any snapshot in time. With each stream capture, apparent offset on a

stream channel will be reduced or erased even as total offset on the fault continues to accumulate (Wallace, 1968; Keller et al., 1982; Replumaz et al., 2001; Walker and Jackson, 2002; Walker and Allen, 2012). Because geomorphology often provides the first line of evidence as to a fault's activity, slip rate, slip sense, or even existence, we must thoroughly understand the landscape characteristics that influence the expression of distinctive strike-slip features. At present, we lack studies that specifically address why classic strike-slip features, such as long stream offsets or occurrences of stream capture, exist in some places but not in others.

Here we examine modeled landscapes and the dextral Marlborough Fault System of New Zealand (Figure 4.1b) to study the effects of shutter ridges, and their specific dimensions, on the length of channel offsets and on the frequency of stream capture in mountainous terrain, and compare these effects at a variety of fault slip rates. We define shutter ridges as relief elements of any shape that are advected along one side of a strike-slip fault. Shutter ridges by definition block and divert channels (Wallace, 1968), and thus could prove critical elements in setting the landscape response to strike-slip faulting. When formed from advected interfluves, they reflect the local drainage spacing, which in turn is set by the geometry of the range (Hovius, 1996). Their length could also be set by more resistant lithologies or structural elements such as pressure ridges. We find that this length scale, in turn, sets the length scale of along-fault stream channel offsets, regardless of total fault offset. This close correspondence is imposed by a regular cycle of stream capture; however, the presence of high-relief shutter ridges or the lateral migration of hillslopes near the fault can reduce or eliminate the likelihood of stream capture.

4.2 METHODS

4.2.1 *Landscape Model Setup*

We use the Channel-Hillslope Integrated Landscape Development model (CHILD), a landscape evolution model that simulates the development of 3D topography given tectonic, climatic, and material properties (Tucker et al., 2001; Tucker, 2012). In this configuration of the CHILD model, hillslope erosion is modeled by nonlinear hillslope diffusion, and fluvial incision rate is proportional to unit stream power (Roering et al, 1999; Whipple and Tucker, 1999).

Our model setup broadly follows the methods of Duvall and Tucker (2015; details in Section 4.7). In order to create conditions that allow stream capture, as in Figure 4.1a, we modeled an uplifting, one-sided mountain ridge cut by a strike-slip fault. We ran 21 simulations, varying the relative rock uplift rate on the downhill side of the fault ("below") between 0.2 and 1 mm/yr, and the lateral fault slip rate between 1 and 10 mm/yr to test a range of shutter ridge morphologies and fault slip scenarios (Table 4.1). Relative rock uplift rate on the uphill side of the fault ("above") stayed fixed at 1 mm/yr. We model a creeping fault, rather than one subject to earthquakes of a characteristic offset length and recurrence interval, in order to focus on the effects of long-term deformation and offset.

In our simple landscape model, shutter ridges originate naturally as interfluves advect horizontally along the fault. Varying the rock uplift rate on the downhill side of the fault creates shutter ridges with different amounts of relief. The length scale of shutter ridges is set by the drainage spacing of the landscape, which arises from the dimensions of the model domain, natural variability within the model, and the uplift rate below the fault.

We tracked three evenly spaced individual shutter ridges per model run over a time interval equivalent to 750 meters of cumulative slip (75,000-750,000 years, depending on slip

rate), recording the number of times that stream capture breached each ridge. Measurements were made after an initial 250 meters of right-lateral slip in order to exclude transience from the initiation of strike-slip motion. We tracked shutter ridges rather than individual streams because shutter ridges maintained a consistent size and morphology throughout each model run. Upper watersheds of streams in some model runs changed in size and shape as models progressed. The total number of stream captures that breached a ridge was converted to stream captures per meter of lateral fault slip for comparison of stream capture frequency among faults with different slip rates.

To examine controls on offset channel length, we measured the along-fault length of the channel offset by the fault, shutter ridge height and length, and relief of the divide between adjacent streams (Figure 4.1d) for the three shutter ridges, and for five additional streams spaced at a regular along-strike interval, at the beginning of and halfway through the period of record. We focus on determining which size dimensions of shutter ridges (length, height, interfluve divide relief) play the strongest role in determining channel offset length. Height and divide relief account for how great an obstacle a shutter ridge presents to stream capture. Measuring both metrics allows assessment of the relative importance of absolute shutter height versus relief across the drainage divide in the river capture process. Fault-parallel channel offset length was measured between the stream's position at consistent distances from the open boundary (Figure 4.1d) that were chosen because they captured the extent of fault-related offset for most streams, in order to apply a consistent standard to all modeled streams. We made measurements at regular time steps, rather than immediately before capture events, in order to replicate the real-world experience of viewing a landscape at only one random point in time.

4.2.2 *Field Comparison: The Marlborough Fault System (MFS), New Zealand*

The model results were compared to analogous sites in the Marlborough Fault System. The MFS comprises four major right-lateral strike-slip faults, with various slip rates and ages, at the obliquely convergent boundary between the Australian and Pacific Plates on the South Island of New Zealand (Figure 4.1b; e.g., Yeats and Berryman, 1987; Wallace et al., 2007). The bedrock in the MFS is mostly sandstone and mudstone of the Permian-Cretaceous Torlesse Supergroup (Rattenbury et al., 2006), but other, more resistant units are found in some parts of the field area (see supporting information for more field site details).

We analyzed 77 tributaries flowing across the Awatere, Clarence, and Kekerengu faults (Figure 4.1b,c). These faults bound the southeast flanks of mountain ranges of significant relief, making them near-ideal sites to compare to our model experiments. Shutter ridges of different sizes formed from advected interfluves, like those in our model, exist throughout the MFS. Some shutter ridges form in less erodible lithologies and appear much longer than the surrounding drainage spacing (e.g., Figure 4.5.) Evidence also exists in the field area for previous stream captures, mostly in the form of beheaded channels, though we cannot comprehensively quantify stream captures through time as we do with the numerical model. We measure channel offset lengths throughout the field area using DigitalGlobe satellite imagery viewed through Google Earth, a 15m DEM (NZDEM SoS v1.0), and where available, 0.5m LiDAR, to document channel offset length, shutter ridge length, shutter ridge height, and relief of divides between adjacent streams (Columbus et al., 2011; University of Otago – National School of Surveying, 2011; NSF OpenTopography Facility, 2016;). Channel offsets in our field area are more variable in shape than those in our model. Many channels are offset diagonally, like those measured by Huang (1993) on the Yishi fault, rather than exactly along the fault trace. We determine offset

length by projecting the inflection point of the channel on each side of the offset to the fault, and measuring the along-fault distance between these points. While some authors (Huang, 1993; Fu et al., 2005) project the course of the stream on either side back to the fault, then measure the fault-parallel distance between these points, irregularity in the courses of MFS streams would cause such projections to introduce additional uncertainty.

4.2.3 *Statistical Regressions*

We performed simple and multiple linear regressions to assess which variables best predict channel offset length in the model and field data, and stream capture frequency in the model data. To calculate the contribution of each predictor variable to total model fit and assess statistical significance, we used the Relative Importance package in the R programming language for statistical computing (version 3.3.3; Grömping et al., 2006; R Core Team, 2017). Specifically, we used the LMG method, which averages over all possible orderings of the predictor variables to assign relative importance (Lindeman et al., 1980). Channel offset length and stream capture frequency were considered separately.

4.3 Results and Analysis

4.3.1 *Model Results*

In general, the models demonstrate the expected cycle of steady channel lengthening with lateral fault offset, punctuated by abrupt shortening caused by stream capture (Figure 4.1d, Videos 2 and 3). In some model experiments in which the lateral slip rate is slow relative to the erosive response of the landscape, we observe lateral ridge migration as described by Duvall and Tucker (2015; Video 3). Duvall and Tucker (2015) observed that, when hillslope erosion is fast relative to lateral fault slip, ridges migrate, allowing shutter ridges to maintain connectivity with

interfluves on the opposite side of the fault. This connectivity is briefly broken when stream capture breaches the divide between adjacent streams, but reestablishes as fault motion continues, allowing ridges to realign across the fault. In extreme cases, streams may evade capture temporarily or indefinitely as interfluves migrate in advance of captor streams (Videos 4 and 5). When the lateral slip rate is fast relative to hillslope erosion, topography on either side of the fault is relatively stable, and shutter ridges do not stay connected to topography across the fault (Video 2).

4.3.1.1 Channel Offset Length

Statistical regressions demonstrate the influence of shutter ridge length on channel offset length. Multiple linear regression models show that shutter ridge length dominates as the most important predictor of channel offset length, accounting for 70-90% of the model fit (adjusted $r^2 = 0.70 – 0.80$; r^2 throughout this paper refers to adjusted r^2) (Figure 4.2a,b, Table 4.2. Simple linear regressions support this result, showing a strong correlation between the two lengths (Figure **4.**2c**,** Table 4.3). Two measures of shutter ridge stature—height and divide relief—have a smaller and less robust correlation with channel offset length (Figure 4.2a,b, Figure 4.6, Table 4.3). Divide relief is a significant predictor of channel offset length and accounts for 8% of the model fit, whereas shutter ridge height is not a significant predictor. Shutter ridge height does account for 27% of the fit of the statistical model in which it was included (Figure 4.2a), but this correlation likely reflects a correlation between shutter ridge length and height, rather than an independent influence on channel offset length by shutter ridge height. Removing shutter ridge height from the regression does not substantially change the fit ($r^2 = 0.66$). Lateral fault slip rate is not a significant predictor of channel offset length, accounting for 1% or less of the fit in

multiple regression models (Figure 4.2a,b, Table 4.2) and showing no meaningful correlation in simple regression plots (Figure 4.6, Table 4.3).

4.3.1.2 Stream Capture Rate

Statistical regressions demonstrate that shutter ridge dimensions and fault slip rate factor into the stream capture process. Multiple linear regression models show that all of the predictor variables play a roughly equal role in determining the rate of stream capture (Figure 4.3a,b, Table 4.2). Both multiple linear regression models fit the data fairly well, explaining about 60% of the variance ($r^2 = 0.59$). In these models, all variables were significant predictors of stream capture rate, and each accounted for 25-41% of the model fit. These results are supported by simple linear regression plots. Shutter ridge length and both measures of shutter ridge stature negatively correlate with stream capture frequency, with longer or taller ridges leading to less frequent stream captures (Figure 4.3c-f, Table 4.3). Lateral fault slip rate has a modest positive correlation with stream capture rate, which is driven by the low stream capture rates in the slowest-slip models (Figure 4.3f).

4.3.2 *Field Results*

4.3.2.1 Channel Offset Length

Multiple linear regression models of the MFS field data are consistent with model results: shutter ridge length is by far the most important predictor of channel offset length, contributing 72-90% of the model fit. The only other significant predictor in these models is divide relief, which contributes only 3% of the fit in the linear model that includes it as a predictor variable (Figure 4.2a,b, Table 4.4). Simple linear regressions of the MFS data show a positive correlation between channel offset length and shutter ridge length, shutter ridge height, and divide relief, with the strongest correlation being with shutter ridge length (Figure 4.2c, Figure 4.7, Table 4.5).

The large Clarence River appears as an outlier in these results. With an offset of nearly 20 kilometers, it likely records the entire offset of the Kekerengu fault, thought to initiate only ~1 Ma (Wallace et al., 2007).

4.4 Discussion and Conclusions

Our work demonstrates the fundamental role that the presence (or absence) of shutter ridges plays in strike-slip fault landscapes. We found that the length of shutter ridges sets the scale of horizontally offset channels observed in a landscape, regardless of cumulative fault offset or fault slip rates (Figure 4.2). On the other hand, the topographic prominence of a shutter ridge, its lateral extent, and fault slip rate all impact rates of stream capture in a strike-slip landscape (Figure 4.3). These results confirm intuition that longer shutter ridges divert channels over greater distances, and that taller/higher-relief shutter ridges act as greater barriers to stream capture. Less intuitively, shutter ridge length also affects the stream capture process because longer topographic obstacles juxtapose streams closely enough for capture less often.

Both shutter ridge height and divide relief reasonably predict stream capture occurrence, with a similar inverse linear relationship and moderate relative importance (Figure 4.3 c,d). Shutter ridge height, which stays fairly consistent over time in our models, may serve as a better time-averaged representation of the height of obstruction. Divide relief changes over time as shutter ridges vary in degree of attachment to ridges above the fault, but likely serves as the best predictor of capture vulnerability at snapshots in time when adjacent streams have become closely juxtaposed. Stream capture acts to reduce the length of horizontally offset river channels, though temporarily. Therefore, the subtle correlations among shutter ridge height, divide relief, and channel offset length may be secondary effects of the stream capture process.

The models predict a weak positive relationship between fault slip rate and stream capture rate (Figure 4.3f). The models with conditions encouraging hillslope mobility—higher relative rock uplift and erosion rates, and smaller lateral slip rates (as expressed by advection-erosion number (N_{ae}) of Duvall and Tucker (2015))—tend toward lower rates of stream capture. Streams in these cases can lose drainage area through vigorous ridge migration rather than through stream capture, as entire watersheds translate laterally and "outrun" capture (Figure 4.4, Videos 4 and 5). Thus, in certain circumstances, channel offsets shorter than the total fault offset can be maintained without stream capture.

Results from this study underscore the impact of the stream capture cycle, modulated by the presence and size of shutter ridges, in dictating whether strike-slip fault motion shows a clear geomorphic signature. In our simple landscape models, shutter ridges are advected interfluves with lengths set by drainage spacing, which in turn is set by the geometry of the mountain range (Hovius, 1996). As a result of the regular and effective process of stream capture in the models, as well as ridge migration in some cases, we also observe a close match between maximum magnitudes of channel offset length and shutter ridge length. As discussed above, shutter ridge height somewhat reduces stream capture, but in general, once a stream becomes offset far enough to reach its neighbor, capture eventually occurs and prevents lengthening of the offset channel beyond the drainage spacing. We conclude that the surrounding landscape – the relief structure and drainage spacing that set up its shutter ridges – is primarily responsible for creating and maintaining the geomorphic signature of a strike-slip fault, whereas the fault properties are of lesser importance. In complex landscapes, erodibility contrasts or preexisting structural elements also create shutter ridges and set their length scales, and stream captures are not guaranteed even when two streams are juxtaposed in close proximity. Questions surrounding

how high and fast-moving advected topography must be relative to the efficiency of fluvial processes in order to become a true shutter ridge await future detailed studies.

Our work confirms that if fault-crossing rivers are positioned such that stream capture can occur, long channel offsets are better interpreted as transient features than as indicators of total fault offset (Walker and Allen, 2012). Evidence of a series of captures of a single stream, for example, a series of knickpoints (e.g., Prince et al., 2011; Yanites, 2013), could provide a longer record of slip on the fault than channel offset could. In cases of slow fault slip or highly erosive landscapes, hillslope migration could laterally advect entire streams without creating long offsets or easily allowing stream capture to occur, further dampening the landscape signature of the fault. In these cases, the profile relief ratio, suggested by Duvall and Tucker (2015) to assess ridge migration by determining the degree of ridge connectivity across the fault, may provide a good indicator of slip rate.

In all cases, a thorough understanding of the physical processes that control the occurrence of strike-slip features is essential to our predictive capability and our ability to read a particular landscape. Many geoscientists look for horizontal stream deflection as a litmus test for identifying the presence and sense of slip of a strike-slip fault. We suggest caution with this approach, as results from this study reveal the dependence of offset length on the preexisting scale of the landscape, and on the degree of hillslope mobility. Without topographic elements to impede the courses of streams, even a very long-lived and fast-slipping strike-slip fault may not develop and sustain long channel offsets.

4.5 Acknowledgements, Samples, and Data

We thank the National Science Foundation (EAR-1321859 and 1321735) and the University of Washington for support of this research. The CHILD model is distributed through the

Community Surface Dynamics Modeling System (CSDMS) Model Repository, which is supported by NSF (EAR-1226297). Model input files are available in the supporting information. Feedback from Lindsay Schoenbohm and an anonymous reviewer improved this manuscript.

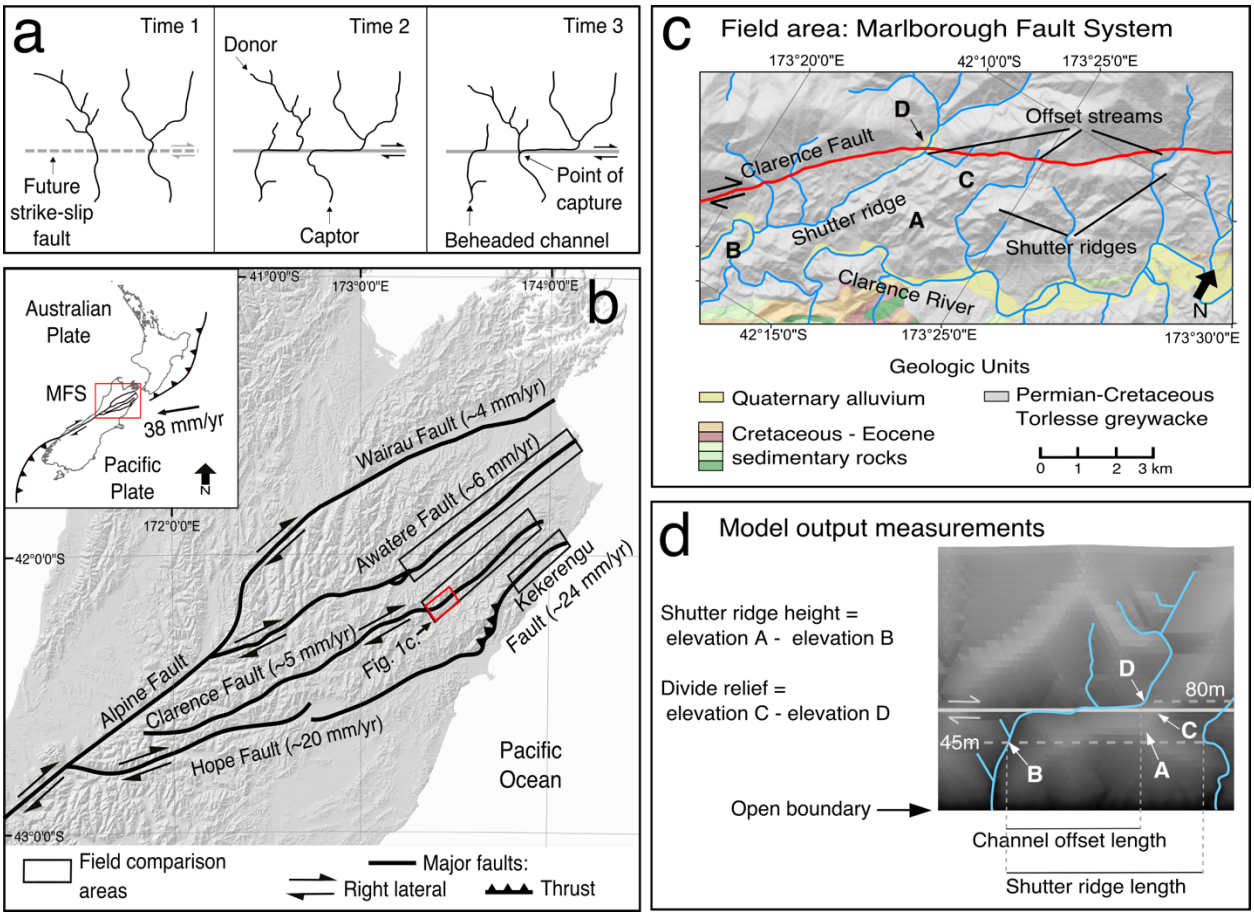

Figure 4.1. Field area and model measurements. **a.** The stream capture cycle. Time 1: Pre-strike-slip fault; streams flow straight across the future fault. Time 2: Right-lateral slip offsets streams and juxtaposes lower reaches of captor streams with upper reaches of eventual donors. Time 3: Stream capture. The cycle of offset and capture continues with fault activity. **b.** Map of Marlborough Fault System (MFS), New Zealand. Inset map shows plate tectonic setting. Black boxes in main map show analyzed sections of strike-slip faults. Fault slip rates from: Wairau: Zachariasen et al., 2006, Awatere: Little et al., 1998, Clarence: Knuepfer, 1992, Hope: Van Dissen and Yeats, 1991, Kekerengu: Little et al, 2018. **c.** Example of offset streams along the Clarence fault. Geology simplified from Rattenbury et al. (2006). A, B, C, D correspond to A, B, C, D in panel d. **d.** Model output measurements. Shutter ridge length: horizontal distance between adjacent streams at 45m above the open boundary. Channel offset length: horizontal distance between a stream's position at 80m (4m above the fault) and its position at 45m. Shutter ridge height: difference between the highest elevation on a shutter ridge, anywhere between the open boundary and 70m from it, and elevation of the stream at 45m. Divide relief: elevation difference between the stream at its point of inflection, where it turns from flowing toward the fault to flowing parallel to the fault, and the point where the smallest amount of relief separates it from the captor stream.

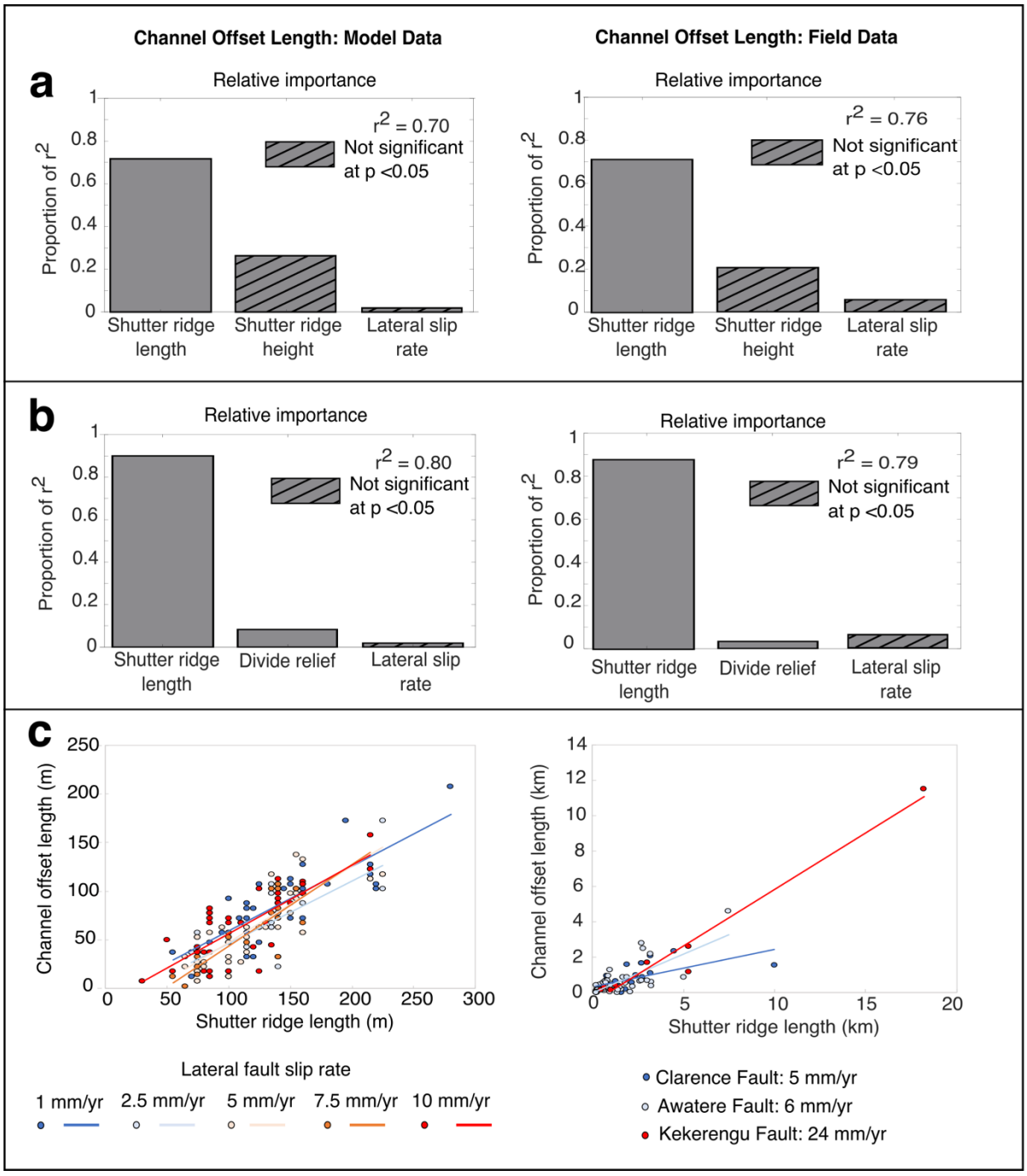

Figure 4.2. Channel offset length results. Model (left) and field (right) results for channel offset length. **a,b.** Multiple linear regression models predicting channel offset length. Adjusted r^2 values shown for each regression. **c.** Plot and simple linear correlations of channel offset length and shutter ridge length. r^2 for trend lines are in Tables 4.3 and 4.5. Uncertainty on field measurements made from the NZDEM is approximately 15m, and in those measurements made from the LiDAR, about 0.5m, based on the resolution of the data. Additional, unquantified uncertainty likely arises from human measurement errors.

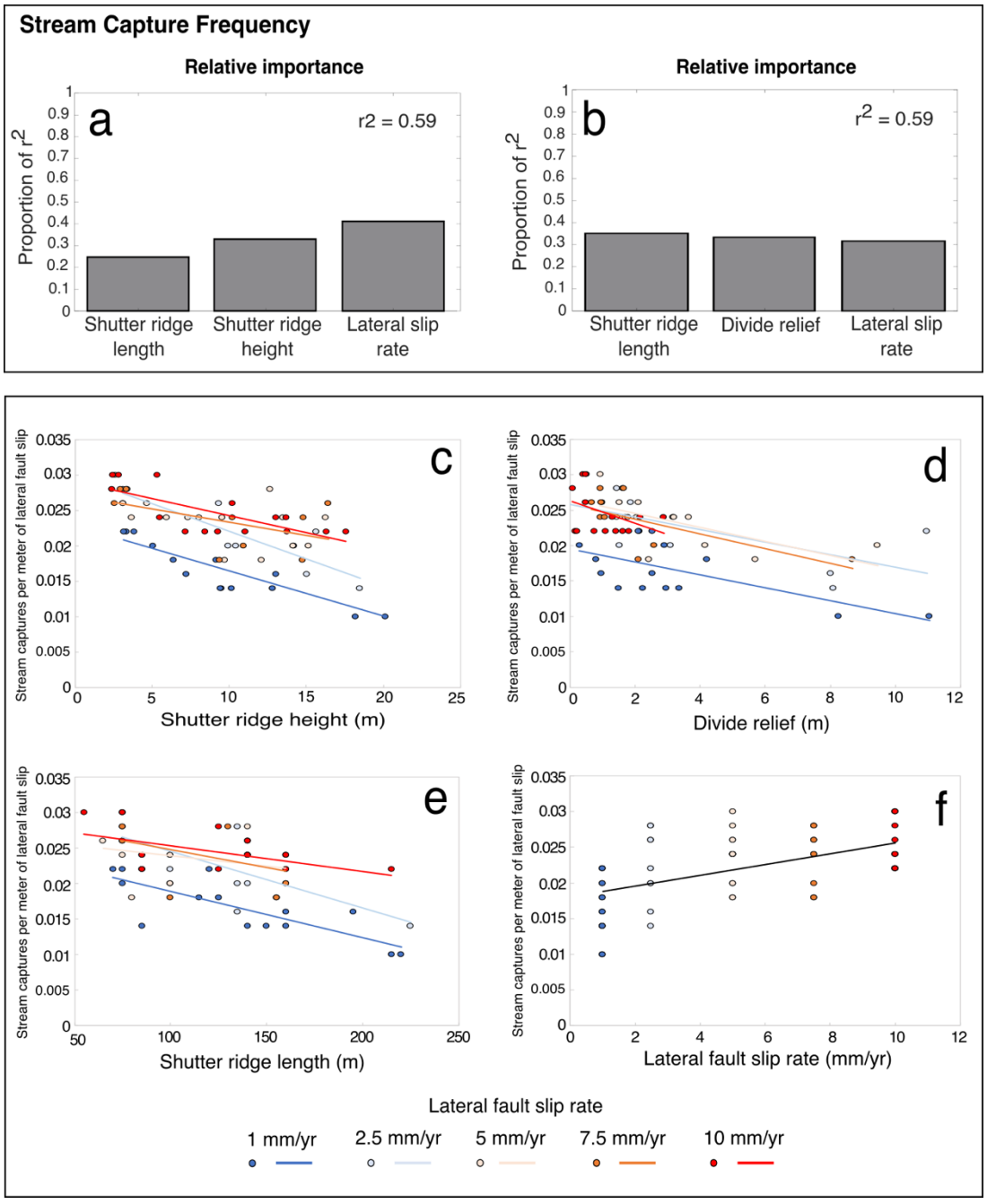

Figure 4.3. Modeled stream capture frequency results. Model output results. **a,b.** Multiple linear regression models predicting stream capture frequency. Adjusted r^2 values shown for each regression model. Plots and simple linear correlations of stream capture frequency and **c**. shutter ridge height, **d.** divide relief, **e.** shutter ridge length, and **f.** lateral slip rate. r^2 for trend lines are in Table 4.3.

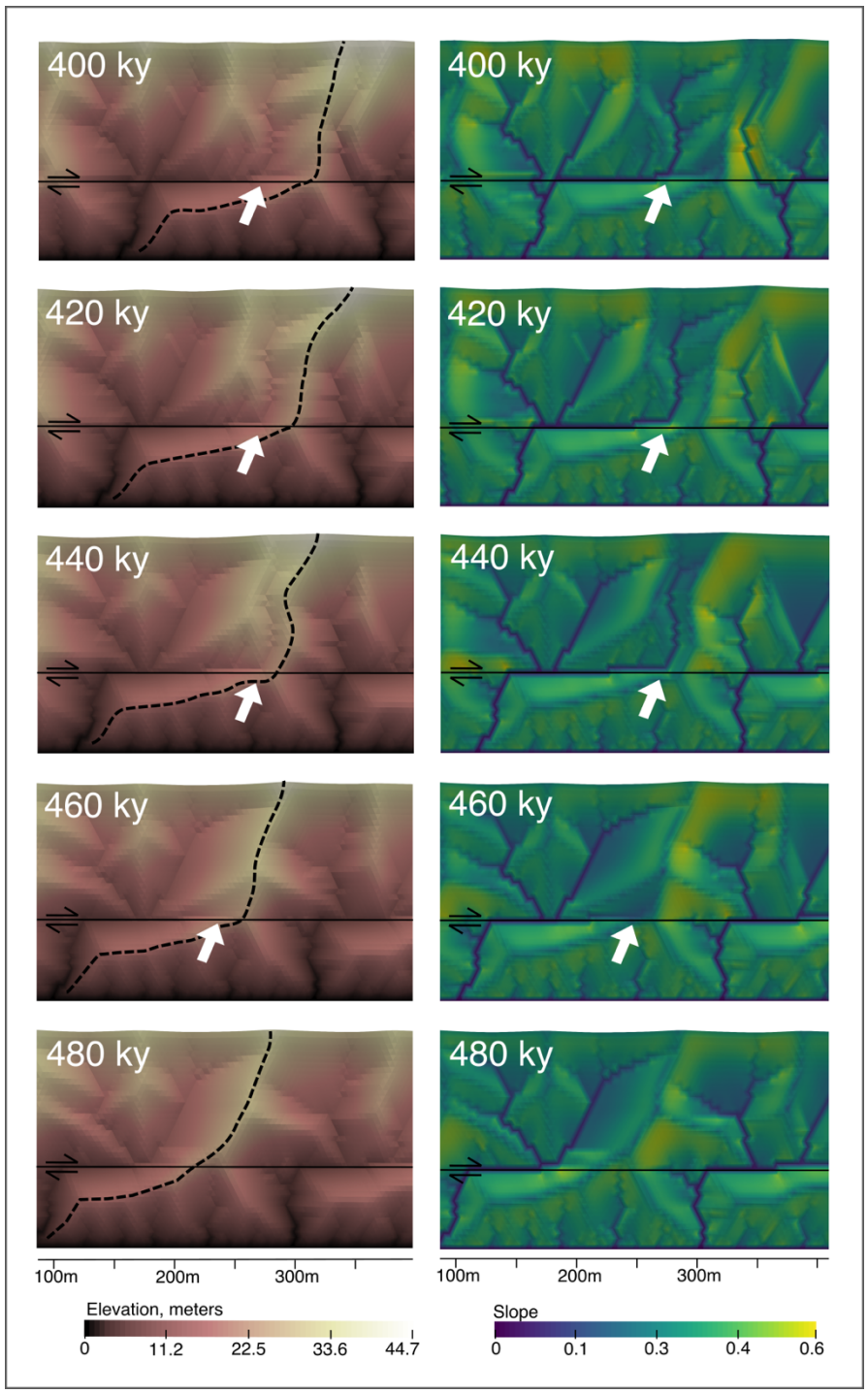

Figure 4.4. Example of stream evading capture. CHILD model output showing a catchment "outrunning" capture through ridge migration. Dashed line shows drainage divide between left and right catchments. White arrows show tributary that is reduced in drainage area and ultimately defeated before it can be captured by the stream to the right.

4.6 CHAPTER 4 REFERENCES

Adams, C. J., Mortimer, N., Campbell, H. J., & Griffin, W. L. (2009). Age and isotopic characterisation of metasedimentary rocks from the Torlesse Supergroup and Waipapa Group in the central North Island, New Zealand. *New Zealand Journal of Geology and Geophysics, 52*(2), 149-170. https://doi.org/10.1080/00288300909509883

Arrowsmith, J. R., & Zielke, O. (2009). Tectonic geomorphology of the San Andreas fault zone from high resolution topography: An example from the Cholame segment. *Geomorphology*, *113*(1-2), 70-81. https://doi.org/10.1016/j.geomorph.2009.01.002

Baker, I. A., Gamble, J. A., & Graham, I. J. (1994). The age, geology, and geochemistry of the Tapuaenuku igneous complex, Marlborough, New Zealand. *New Zealand Journal of Geology and Geophysics, 37*(3), 249-268. https://doi.org/10.1080/00288306.1994.9514620

Chappell, P. R. (2016). The climate and weather of Marlborough. NIWA Science and Technology Series 69.

Columbus, J., Sirguey, P., & Tenzer, R. (2011). A free, fully assessed 15-m DEM for New Zealand. *Survey Quarterly 66*, 16-19.

Dolan, J. F. (2014). Data collection and processing report: LiDAR survey of five fault segments (Eastern Clarence, Western Clarence, Central Eastern Awatere, West Wairau and East Hope-Conway) of the Marlborough Fault System on the northwestern portion of New Zealand's South Island. National Center for Airborne Laser Mapping.

Duvall, A. R., & Tucker, G. E. (2015). Dynamic Ridges and Valleys in a Strike-Slip Environment. *Journal of Geophysical Research: Earth Surface*, *120*(10), 2016-2026. https://doi.org/10.1002/2015JF003618

Fu, B., Awata, Y., Du, J., & He, W. (2005). Late Quaternary systematic stream offsets caused by repeated large seismic events along the Kunlun fault, northern Tibet. *Geomorphology, 71*(3), 278-292. https://doi.org/10.1016/j.geomorph.2005.03.001

Gaudemer, Y., Tapponnier, P., & Turcotte, D. L. (1989). River offsets across active strike-slip faults. *Annales Tectonicoe*, *3*, 55-76.

Goren, L., Willett, S. D., Herman, F., & Braun, J. (2014). Coupled numerical–analytical approach to landscape evolution modeling. *Earth Surface Processes and Landforms, 39*(4), 522-545. https://doi.org/10.1002/esp.3514

Goren, L., Castelltort, S., & Klinger, Y. (2015). Modes and rates of horizontal deformation from rotated river basins: Application to the Dead Sea fault system in Lebanon. *Geology, 43*(9), 843-846. https://doi.org/10.1130/G36841.1

Gray, H. J., Shobe, C. M., Hobley, D. E., Tucker, G. E., Duvall, A. R., Harbert, S. A., & Owen, L. A. (2017). Off-fault deformation rate along the southern San Andreas fault at Mecca Hills, southern California, inferred from landscape modeling of curved drainages. *Geology*, *46*(1), 59-62. https://doi.org/10.1130/G39820.1

Grömping, U. (2006). Relative Importance for Linear Regression in R: The Package relaimpo. *Journal of Statistical Software, 17*(1*),* 1-27. http://hdl.handle.net/10.18637/jss.v017.i01

Hovius, N. (1996). Regular spacing of drainage outlets from linear mountain belts. *Basin Research, 8*(1), 29-44. https://doi.org/10.1111/j.1365-2117.1996.tb00113.x

Huang, W. (1993). Morphologic patterns of stream channels on the active Yishi Fault, southern Shandong Province, Eastern China: implications for repeated great earthquakes in the Holocene. *Tectonophysics*, *219*(4), 283-304. https://doi.org/10.1016/0040-1951(93)90179-N

Hubert-Ferrari, A., Armijo, R., King, G., Meyer, B., & Barka, A. (2002). Morphology, displacement, and slip rates along the North Anatolian Fault, Turkey. *Journal of Geophysical Research: Solid Earth, 107*(B10). https://doi.org/10.1029/2001JB000393

Jiang, W., Han, Z., Guo, P., Zhang, J., Jiao, Q., Kang, S., & Tian, Y. (2017). Slip rate and recurrence intervals of the east Lenglongling fault constrained by morphotectonics: Tectonic implications for the northeastern Tibetan Plateau. *Lithosphere, 9*(3), 417-430. https://doi.org/10.1130/L597.1

Kamp, P. J., Vincent, K. A., & Tayler, M. J. (2015). Cenozoic sedimentary and volcanic rocks of New Zealand: A reference volume of lithology, age and paleoenvironments with maps (PMAPs) and database.

Keller, E. A., Bonkowski, M. S., Korsch, R. J., & Shlemon, R. J. (1982). Tectonic geomorphology of the San Andreas fault zone in the southern Indio Hills, Coachella Valley, California. *Geological Society of America Bulletin, 93*(1), 46-56. https://doi.org/10.1130/0016-7606(1982)93<46:TGOTSA>2.0.CO;2

Knuepfer, P. L. (1992). Temporal variations in latest Quaternary slip across the Australian-Pacific plate boundary, northeastern South Island, New Zealand. *Tectonics, 11*(3), 449-464. https://doi.org/10.1029/91TC02890

Lindeman, R. H., Merenda, P. F., & Gold, R. Z. (1980). Introduction to Bivariate and Multivariate Analysis. Scott, Foresman, Glenview, IL.

Little, T. A. (1995). Brittle deformation adjacent to the Awatere strike-slip fault in New Zealand: Faulting patterns, scaling relationships, and displacement partitioning. *Geological Society of America Bulletin, 107*(11), 1255-1271. https://doi.org/10.1130/0016-7606(1995)107<1255:BDATTA>2.3.CO;2

Little, T. A., Grapes, R., & Berger, G. W. (1998). Late Quaternary strike slip on the eastern part of the Awatere fault, South Island, New Zealand. *Geological Society of America Bulletin, 110*(2), 127-148. https://doi.org/10.1130/0016-7606(1998)110<0127:LQSSOT>2.3.CO;2

Little, T. A., Van Dissen, R., Kearse, J., Norton, K., Benson, A., & Wang, N. (2018). Kekerengu fault, New Zealand: Timing and size of Late Holocene surface ruptures. *Bulletin of the Seismological Society of America. 108*(3B), 1556-1572. https://doi.org/10.1785/0120170152

Macara, G. R. (2016). The climate and weather of Canterbury (2nd ed.). NIWA Science and Technology Series 68.

Mason, D. P., Little, T. A., & Van Dissen, R. J. (2006). Rates of active faulting during late Quaternary fluvial terrace formation at Saxton River, Awatere fault, New Zealand. Geological Society of America Bulletin, *118*(11-12), 1431-1446. https://doi.org/10.1130/B25961.1

NSF OpenTopography Facility. (2016). Marlborough Fault System, South Island, New Zealand. https://doi.org/10.5069/g9g44n75

Ouchi, S. (2004). Flume experiments on the horizontal stream offset by strike-slip faults. *Earth Surface Processes and Landforms*, *29*(2), 161-173.

Ouchi, S. (2005). Development of offset channels across the San Andreas fault. *Geomorphology*, *70*(1-2), 112-128. https://doi.org/10.1002/esp.1017

Prince, P. S., Spotila, J. A., & Henika, W. S. (2011). Stream capture as driver of transient landscape evolution in a tectonically quiescent setting. *Geology*, *39*(9), 823-826. https://doi.org/10.1130/G32008.1

Pucci, S., De Martini, P. M., & Pantosti, D. (2008). Preliminary slip rate estimates for the Düzce segment of the North Anatolian Fault Zone from offset geomorphic markers. *Geomorphology*, *97*(3), 538-554. https://doi.org/10.1016/j.geomorph.2007.09.002

Rattenbury, M.S.; Cooper, R.A.; Johnston, M.R. (compilers) (1998). Geology of the Nelson area: scale 1:250,000. Lower Hutt: Institute of Geological & Nuclear Sciences Limited. Institute of Geological & Nuclear Sciences 1:250,000 geological map 9. 67 p. + 1 sheet.

Rattenbury, M. S., Townsend, D. B., and Johnston, M. R. (compilers), (2006). Geology of the Kaikoura area. Lower Hutt: Institute of Geological and Nuclear Sciences Limited. 1:250000 geological map 13. 70 p. + 1 sheet.

R Core Team. (2017). R: A language and environment for statistical computing. R Foundation for Statistical Computing, Vienna, Austria. https://www.R-project.org/.

Replumaz, A., Lacassin, R., Tapponnier, P., & Leloup, P. H. (2001). Large river offsets and Plio-Quaternary dextral slip rate on the Red River fault (Yunnan, China). *Journal of Geophysical Research: Solid Earth*, *106*(B1), 819-836. https://doi.org/10.1029/2000JB900135

Roering, J. J., Kirchner, J. W., & Dietrich, W. E. (1999). Evidence for nonlinear, diffusive sediment transport on hillslopes and implications for landscape morphology. *Water Resources Research, 35*(3), 853-870. https://doi.org/10.1029/1998WR900090

Sieh, K. E., & Jahns, R. H. (1984). Holocene activity of the San Andreas fault at Wallace Creek, California. *Geological Society of America Bulletin*, *95*(8), 883-896. https://doi.org/10.1130/0016-7606(1984)95<883:HAOTSA>2.0.CO;2

Tucker, G., Lancaster, S., Gasparini, N., & Bras, R. (2001). The channel-hillslope integrated landscape development model (CHILD). In *Landscape erosion and evolution modeling* (pp. 349-388).. https://doi.org/10.1007/978-1-4615-0575-4_12

Tucker, G.E. (2012). CHILD. Interdisciplinary Earth Data Alliance (IEDA). doi:10.1594/IEDA/100102

University of Otago – National School of Surveying. (2011). NZ_SoS_DEM v1.0. University of Otago – National School of Surveying.

Van Dissen, R., & Yeats, R. S. (1991). Hope fault, Jordan thrust, and uplift of the seaward Kaikoura Range, New Zealand. *Geology*, *19*(4), 393-396. https://doi.org/10.1130/0091-7613(1991)019<0393:HFJTAU>2.3.CO;2

Walker, F., & Allen, M. B. (2012). Offset rivers, drainage spacing and the record of strike-slip faulting: The Kuh Banan Fault, Iran. *Tectonophysics*, *530*, 251-263. https://doi.org/10.1016/j.tecto.2012.01.001

Walker, R., & Jackson, J. (2002). Offset and evolution of the Gowk fault, SE Iran: a major intra-continental strike-slip system. *Journal of structural Geology*, *24*(11), 1677-1698. https://doi.org/10.1016/S0191-8141(01)00170-5

Wallace, R. E. (1949). Structure of a portion of the San Andreas rift in southern California. *Geological Society of America Bulletin*, *60*(4), 781-806. https://doi.org/10.1130/0016-7606(1949)60[781:SOAPOT]2.0.CO;2

Wallace, R. E. (1968). Notes on stream channels offset by the San Andreas fault, southern Coast Ranges, California. In *Conference on Geologic Problems of the San Andreas Fault System. Stanford University Publication in Geological Sciences* (Vol. 11, pp. 6-21).

Wallace, L. M., Beavan, J., McCaffrey, R., Berryman, K., & Denys, P. (2007). Balancing the plate motion budget in the South Island, New Zealand using GPS, geological and seismological data. *Geophysical Journal International*, *168*(1), 332-352. https://doi.org/10.1111/j.1365-246X.2006.03183.x

Wandres, A. M., & Bradshaw, J. D. (2005). New Zealand tectonostratigraphy and implications from conglomeratic rocks for the configuration of the SW Pacific margin of

Gondwana. *Geological Society, London, Special Publications*, *246*(1), 179-216. https://doi.org/10.1144/GSL.SP.2005.246.01.06

Whipple, K. X., & Tucker, G. E. (1999). Dynamics of the stream-power river incision model: Implications for height limits of mountain ranges, landscape response timescales, and research needs. *Journal of Geophysical Research: Solid Earth*, *104*(B8), 17661-17674. https://doi.org/10.1029/1999JB900120

Yanites, B. J., Ehlers, T. A., Becker, J. K., Schnellmann, M., & Heuberger, S. (2013). High magnitude and rapid incision from river capture: Rhine River, Switzerland. *Journal of Geophysical Research: Earth Surface*, *118*(2), 1060-1084. https://doi.org/10.1002/jgrf.20056

Yeats, R. S., & Berryman, K. R. (1987). South Island, New Zealand, and transverse ranges, California: a seismotectonic comparison. *Tectonics, 6*(3), 363-376. https://doi.org/10.1029/TC006i003p00363

Zachariasen, J., Berryman, K., Langridge, R., Prentice, C., Rymer, M., Stirling, M., & Villamor, P. (2006). Timing of late Holocene surface rupture of the Wairau fault, Marlborough, New Zealand. *New Zealand Journal of Geology and Geophysics*, *49*(1), 159-174. https://doi.org/10.1080/00288306.2006.9515156

Zinke, R., Dolan, J. F., Van Dissen, R., Grenader, J. R., Rhodes, E. J., McGuire, C. P., ... & Hatem, A. E. (2015). Evolution and progressive geomorphic manifestation of surface faulting: A comparison of the Wairau and Awatere faults, South Island, New Zealand. *Geology*, *43*(11), 1019-1022. https://doi.org/10.1130/G37065.1

4.7 APPENDIX

4.7.1 *Landscape Evolution Model Setup*

The CHILD model is a landscape evolution model implemented in C++, with output interpreted using MATLAB and Paraview (Tucker et al., 2001; Tucker, 2012). The equation governing the evolution of the land surface in the CHILD model is:

$$\frac{\partial h}{\partial t} = U - V\frac{\partial h}{\partial x} - E_f - E_h$$

Where U is rock uplift rate (or base level lowering rate), V is lateral fault slip rate, E_f is fluvial erosion rate, and E_h is hillslope erosion rate caused by soil creep.

In detachment-limited mode, in which streams are assumed to be able to easily transport any material they can detach from their beds, E_f is proportional to unit stream power, modulated by a coefficient of bedrock erodibility, K:

$$E_f = \Omega = KA^m S^n$$

where Ω is unit stream power, Q is water discharge, W is channel width, S is channel slope, m = 1/2, and n = 1 are constants.

E_h, the hillslope erosion rate, is

$$E_h = \nabla q_s$$

where the expression for mass flux by nonlinear soil creep is

$$q_s = \frac{-D\nabla h}{\left(1 - \left[\frac{\nabla h}{S_c}\right]^2\right)}$$

where h is elevation, D is hillslope diffusivity, and S_c is a critical slope. CHILD solves these equations using a finite difference method over an irregular mesh (Delauney triangulation).

Some authors have pointed out that landscape models are unable to accurately represent the dynamics of divide migration when grid spacing is large (e.g., Goren et al., 2014). In our model setup, the grid spacing of five meters is much smaller than the length of a typical hillslope, allowing our experiments to fully and accurately resolve the hillslopes and drainage divides.

4.7.2 *Elaboration on Methods*

Our model setup broadly follows the methods of Duvall and Tucker (2015). We model a 2000 m by 200 m grid with five-meter grid spacing and one open boundary, in order to construct a one-sided mountain ridge hosting a suite of subparallel streams. First, we impose uplift on this grid while allowing it to erode, in order to create the mountain ridge (see Video S1). Uplift is continued until the ridge reaches steady state, i.e. until the average elevation and the volume of material above base level do not change over time. Once steady state has been achieved, strike-slip motion is initiated along a fault 76 m from the lower boundary of the grid. The nodes below this boundary are advected to the left relative to those above the boundary. Uplift continues while the strike-slip fault is active in order to maintain topography. The fault continues to slip until 750 m of right-lateral offset has been achieved.

We ran 21 simulations in order to generate shutter ridges of different sizes and shapes along the fault. (see Table 4.1 for the model inputs that were varied.) Shutter ridges with different amounts of relief were generated by varying the amount of uplift in the region between the fault and the open boundary ("below" the fault) in different runs, while the uplift rate "above" the fault was always 1 mm/yr. In all cases, the uplifting model domain reaches steady state with regard to average elevation and volume above base level, but in runs with more gradual uplift below the fault, the relief in this region is lower, thus creating lower-relief shutter ridges. Shutter ridges of different lengths result from the natural variability within each modeled landscape, as well as the distance from the ridge crest to the open boundary of the model. This configuration is comparable to real-world settings, as the model boundary represents a relatively fixed base level such as the ocean or a large, fault-parallel river. We combined all uplift rate combinations with right-lateral fault slip rates ranging between 1 and 10 mm/yr. In all model runs, erodibility of the substrate (K and D) and all climatic inputs were held constant.

We tracked three evenly spaced individual shutter ridges per model run, recording the number of times that a stream capture breached each ridge through the time it took the fault in each model to slip 750 meters. Measurements were made after the initial 250 meters of right-lateral slip in order to exclude any transience from the initiation of strike-slip motion. We avoided rare shutter ridges that changed length during the model run due a stream being beheaded and failing to regain drainage area. We chose to track shutter ridges rather than individual streams traced from the divide at the top of the model domain because shutter ridges maintained a consistent size and morphology throughout each model run, while the upper watersheds of streams changed in size and shape as models progressed, sometimes dramatically. The total number of stream captures that breached a ridge was converted to stream captures per

meter of lateral fault slip for comparison of stream capture frequency among faults that slip at different rates.

To examine controls on offset channel length, we measured the along-fault length of the channel offset by the fault, shutter ridge height and length, and divide relief between adjacent streams that would later be breached by capture (Figure 4.1d) for the three shutter ridges, and for five additional streams spaced at a regular along-strike interval, at the beginning of the period of record and at a time step halfway through the period of record. We made measurements at regular time steps, rather than at time steps selected to be immediately before capture events, in order to most closely replicate the real-world experience of viewing a landscape at only one random point in time. Rarely, a sampled stream would cross the fault from left to right, instead of the right-to-left configuration that fault-related offset should cause, due to a recent stream capture. These streams were excluded from our analysis because, even if ridges separated adjacent streams in these cases, the amount of time before such streams once again become "set up" for capture through right-lateral offset would be so great that it was not realistic to anticipate a site of eventual stream capture. As in the model, streams offset in the "wrong" direction in the MFS site were excluded from the analysis.

4.7.3 *The Marlborough Fault System*

The Marlborough Fault System (MFS) is a system of dextral faults at the boundary between the Australian and Pacific Plates on the South Island of New Zealand (Figure 4.1b). The MFS connects the oblique-slip Alpine fault to the south with the Hikurangi Subduction Zone to the north. The faults of the MFS generally increase in slip rate from north to south: the Wairau fault slips at about 4 mm/yr (Zachariasen et al., 2006), the Awatere fault at 6 mm/yr (Little et al., 1998), the Clarence fault at 5 mm/yr (Knuepfer, 1992), the Hope fault at about 20 mm/yr, though

with variation in slip rate along its length (Van Dissen and Yeats, 1991), and the Kekerengu fault at about 24 mm/yr (Little et al., 2018). Several of the faults in the MFS bound mountain ranges, from which many subparallel tributaries drain to fault-parallel rivers. This topography makes the MFS an excellent analogue to our model. The Kekerengu fault is adjacent to the northeastern Seaward Kaikōura mountains, which in this area have relief of up to 1000 meters. The highest point in the Inland Kaikōura mountains, Tapuae-o-Uenuku, is about 2600 meters above the adjacent Clarence River and Clarence fault. The relief of the mountains bounded by the Awatere fault is more modest, but still reaches about 1200 meters. Many of the streams draining these mountain ranges have been offset by slip on the Marlborough faults. As in Figures 4.1c and 4.5, these streams often cross the fault at a diagonal, or have fault-parallel offsets that are not located exactly on the fault trace. This pattern has been observed in other strike-slip fault systems (e.g., Huang, 1993). This diagonal channel pattern can occur when a channel migrates laterally in order to steepen its offset reach, the grade of which had been reduced by lengthening with fault slip (Ouchi, 2004). This pattern could also result from offset across a fault that has multiple strands or off-fault deformation (e.g., Ouchi, 2005; Gray et al., 2017), which could be the case in some or all parts of our field area (e.g., Little, 1995; Zinke et al., 2015). Ridge migration, which allows interfluves to stay connected across the fault, could also contribute to channel offsets that are not exactly aligned with the fault trace. Furthermore, while we used standardized distances from the fault to measure horizontal offset in our model results, the several scales of channels in our field area meant that absolute distances from channel inflection points to faults vary.

Precipitation-bearing weather systems come primarily from the west, resulting in rain shadow effects to the east of each mountain range. Mean annual rainfall ranges from more than

2000 mm/yr in the mountain ranges to about 550 mm/yr in the Awatere Valley and areas along the coast in the rain shadows of these mountains (Chappell, 2016; Macara, 2016).

Underlying bedrock in the MFS is mostly the Permian-Cretaceous Torlesse Supergroup, which is primarily composed of alternating sandstone and mudstone deposited in an accretionary wedge setting on the margin of Gondwana (Wandres and Bradshaw, 2005; Rattenbury et al., 2006; Adams et al., 2009). As New Zealand began to rift away from Gondwana during the Cretaceous Period, intrusive and extrusive igneous rocks were formed, including the Lookout Volcanics in the Awatere Valley (Figure 4.5; Baker et al., 1994). Later, marine sedimentary formations were deposited, including the Paleocene-Eocene Amuri Limestone and numerous sandstone units (Kamp et al., 2005; Rattenbury et al., 2006). The strata overlying the Torlesse Supergroup are concentrated in basins along the Pacific coast but also exist sporadically in the Clarence and Awatere Valleys (Rattenbury et al., 2006).

Our model experiments simulate detachment-limited rivers; they do not include any measure of sediment transport or deposition. However, almost all rivers in the real world contain some amount of sediment, and those in the MFS are no exception. Most streams we have observed in the MFS have a blanket of alluvium on their beds but also exhibit areas of exposed bedrock. A stream with a high sediment load could be subject to aggradation, particularly along the part of the channel lengthened by slip on the fault. In such a scenario, the possibility of avulsion, in addition to capture by a neighboring stream, should be considered. The effects of sediment deposition on stream capture in a strike-slip setting are beyond the scope of this work but will be addressed in a forthcoming study.

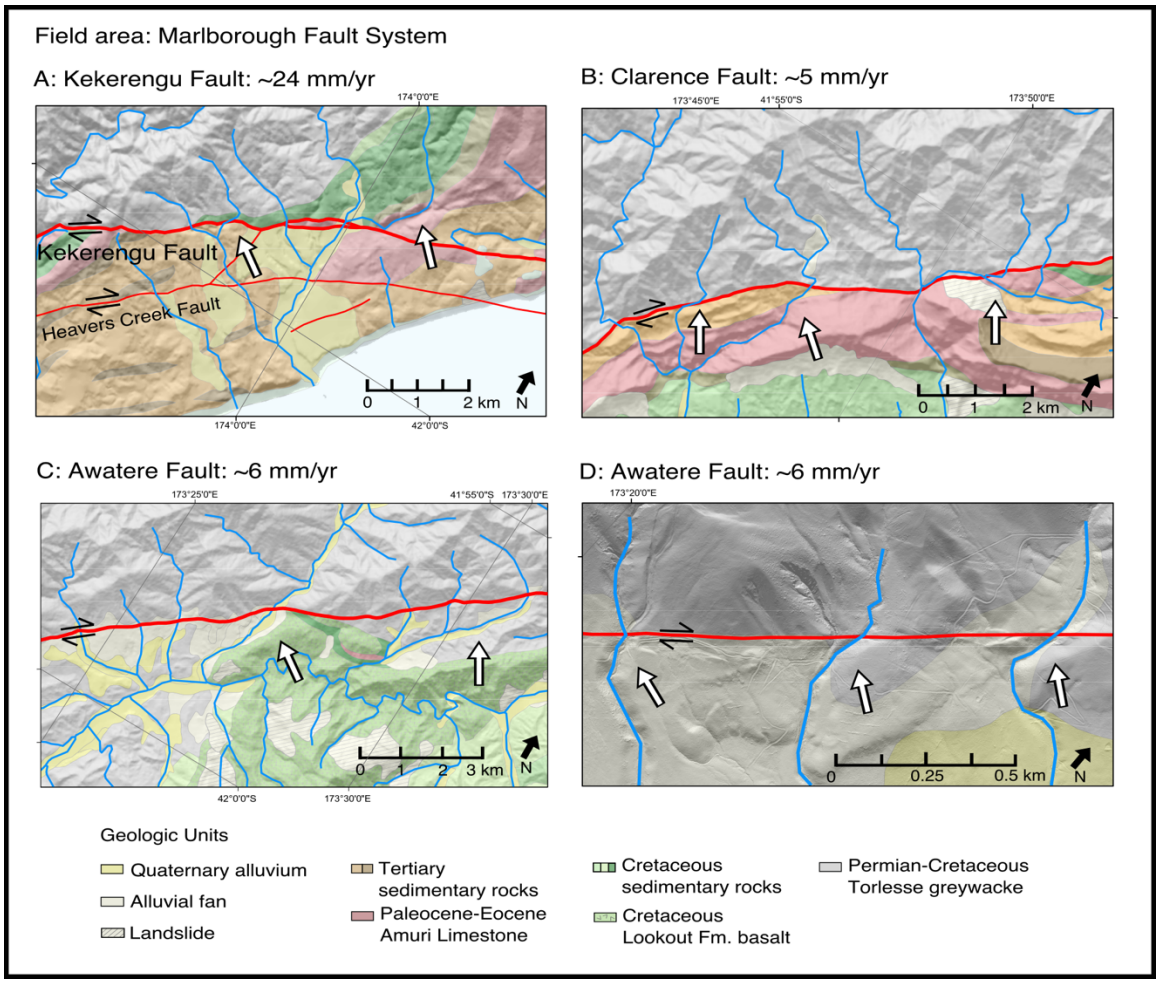

Figure 4.5. Examples of streams in the Marlborough Fault System. White arrows point to examples of dextrally offset streams. Note long shutter ridges formed from resistant units, such as the Lookout basalt and Amuri limestone. Note: in panel D, while the interfluves below the fault look quite flat, there is ~20m of relief between these alluvial fan surfaces and their adjacent channels. Geology simplified from Rattenbury et al., 2006. Slip rates from: Kekerengu fault: Little et al., 2018, Clarence fault: Knuepfer et al., 1992, Awatere fault: Little et al., 1998.

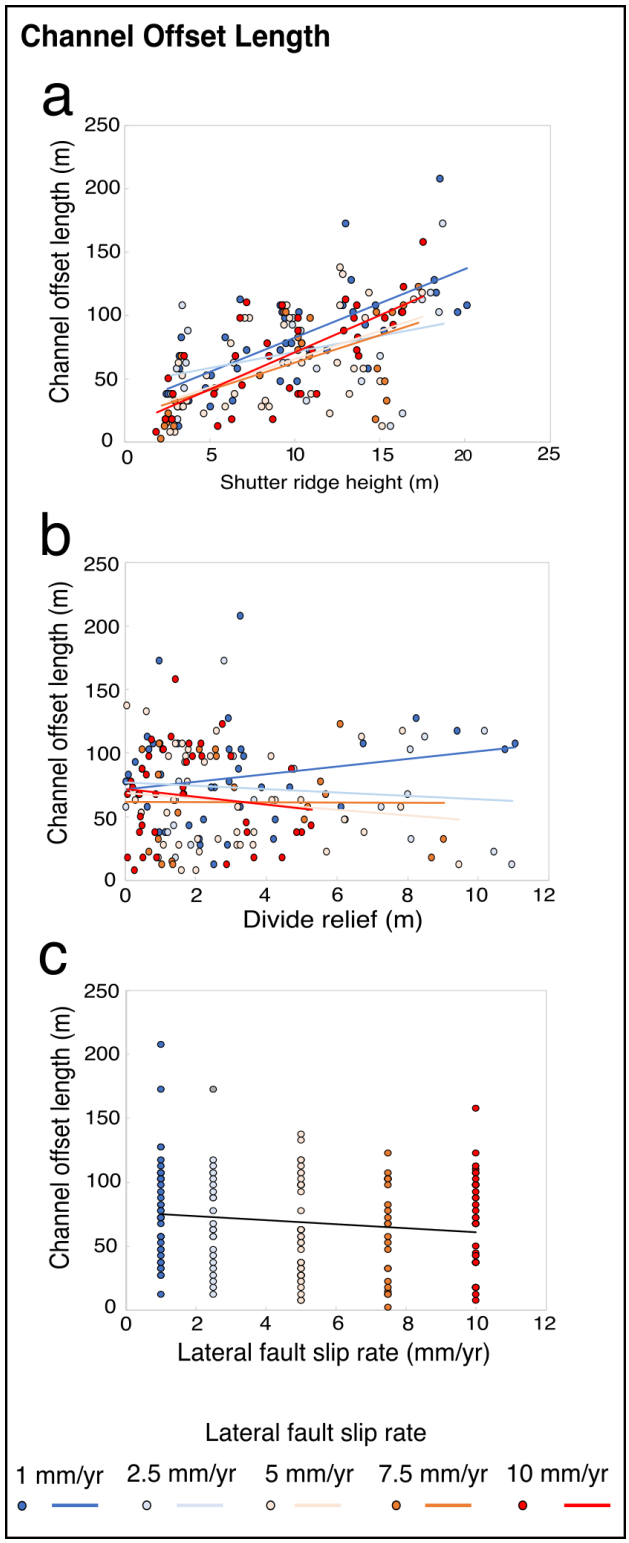

Figure 4.6. Model results: channel offset length. Plot and simple linear correlations of channel offset length with a. shutter ridge height, b. divide relief, and c. lateral fault slip rate. r^2 for trend lines are in Table 4.3.

.

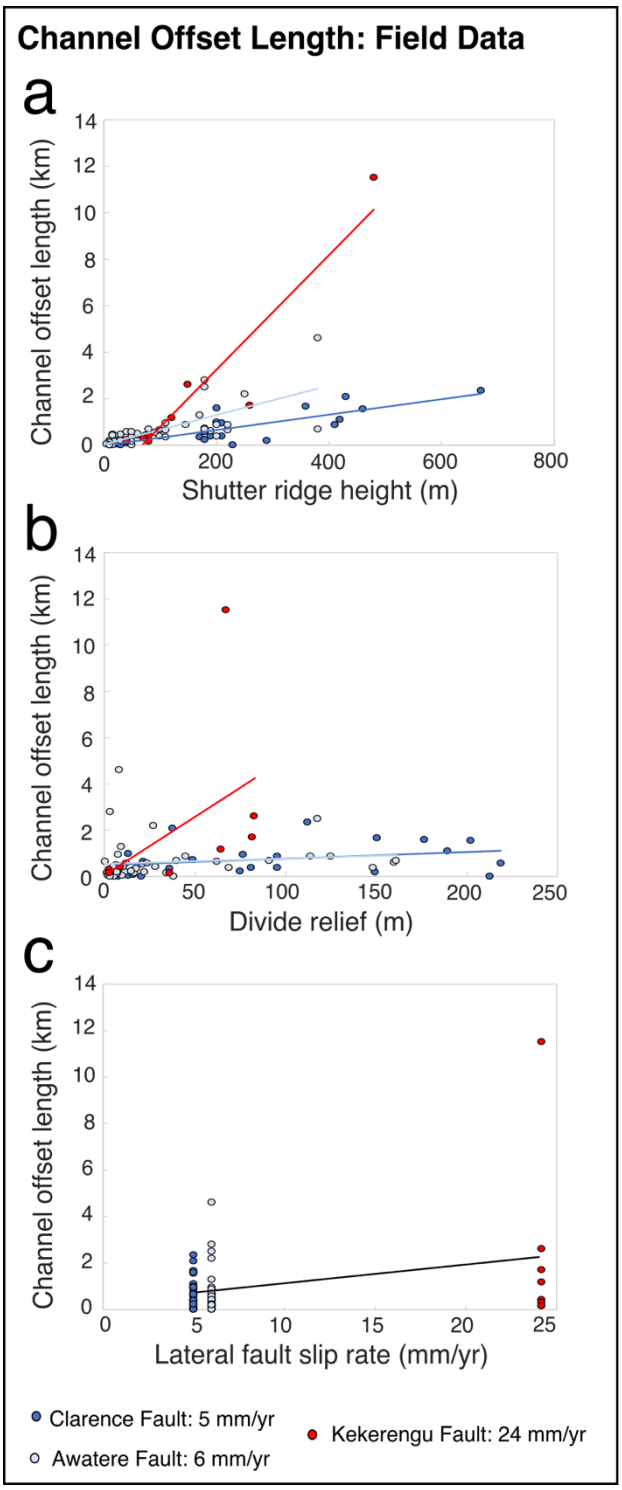

Figure 4.7. Marlborough Fault System results: channel offset length. Plot and simple linear correlations of channel offset length with a. shutter ridge height, b. divide relief, and c. lateral fault slip rate. r^2 for trend lines are in Table 4.5. Data-related uncertainties on channel offset length measurements are about 15m for measurements taken from the NZDEM, and about 0.5m for those taken from the LiDAR. Data-related uncertainties in shutter ridge height and divide relief are less than 0.12 m for measurements made from LiDAR, based on maximum estimated mismatches between adjacent LiDAR flight paths (Dolan, 2014). For the NZDEM, vertical mean absolute error is reported as 5.1m (RMSE 7.1m), but relative uncertainty when comparing elevations of proximal points is likely much smaller and mostly related to human measurement error (Columbus et al., 2011). Slip rates from: Clarence fault: Knuepfer, 1992, Awatere fault: Little et al., 1998, Kekerengu fault: Little et al., 2018.

Table 4.1. CHILD model tectonic inputs. Lateral fault slip rates and rock uplift rates for CHILD model runs.

Model Run	**Lateral slip rate, mm/yr**	**Uplift rate above fault, mm/yr**	**Uplift rate below fault, mm/yr**
1	1	1	1
2	1	1	0.8
3	1	1	0.6
4	1	1	0.4
5	1	1	0.2
6	2.5	1	0.2
7	2.5	1	0.6
8	2.5	1	1
9	5	1	0.2
10	5	1	0.4
11	5	1	0.6
12	5	1	0.8
13	5	1	1
14	7.5	1	0.2
15	7.5	1	0.6
16	7.5	1	1
17	10	1	0.2
18	10	1	0.4
19	10	1	0.6
20	10	1	0.8
21	10	1	1

Table 4.2. Results of multiple linear regressions using model data. Results of multiple linear regressions using CHILD model data to predict channel offset length and stream capture rate.

Multiple linear regressions with channel offset length: model data					
Model	**Variable**	**Adjusted r^2**	**Variance explained**	**p-value**	**Relative importance**
Shutter ridge length, shutter ridge height, lateral slip rate		0.70	67.5%	<2e-16	
	Shutter ridge length			<2e-16	0.72
	Shutter ridge height			0.09	0.27
	Lateral slip rate			0.91	0.01
Shutter ridge length, divide relief, lateral slip rate		0.80	80.2%	<2e-16	
	Shutter ridge length			<2e-16	0.90
	Divide relief			<2e-16	0.08
	Lateral slip rate			0.11	0.01
Multiple linear regressions with stream capture rate: model data					
Model	**Variable**	**Adjusted r^2**	**Variance explained**	**p-value**	**Relative importance**
Shutter ridge length, shutter ridge height, lateral slip rate		0.59	61.3%	3.44e-12	
	Shutter ridge length			0.034	0.25
	Shutter ridge height			0.00019	0.33
	Lateral slip rate			1.33e-7	0.41
Shutter ridge length, divide relief, lateral slip rate		0.59	60.5%	6.11e-12	
	Shutter ridge length			1.07e-5	0.35
	Divide relief			0.00035	0.33
	Lateral slip rate			0.00010	0.32

Table 4.3. Results of simple linear regressions using model data. Results of linear regressions using subsets of CHILD model data to predict channel offset length and stream capture frequency.

Linear regressions with channel offset length: model data			
Lateral slip rate	**Variable**	**Adjusted r^2**	**p-value**
All	Shutter ridge length	0.67	<2e-16
All	Shutter ridge height	0.35	<2e-16
All	Divide relief	-0.0061	0.96
All	Lateral slip rate	0.013	0.078
Linear regressions with channel offset length: subsets of model data			
Lateral slip rate	**Variable**	**Adjusted r^2**	**p-value**
1 mm/yr	Shutter ridge length	0.70	1e-11
1 mm/yr	Shutter ridge height	0.49	3.39e-7
1 mm/yr	Divide relief	0.018	0.20
2.5 mm/yr	Shutter ridge length	0.58	9.69e-6
2.5 mm/yr	Shutter ridge height	0.11	0.067
2.5 mm/yr	Divide relief	0.55	-0.028
5 mm/yr	Shutter ridge length	0.68	3.23e-11
5 mm/yr	Shutter ridge height	0.27	0.00035
5 mm/yr	Divide relief	-0.0070	0.40
7.5 mm/yr	Shutter ridge length	0.74	8.09e-08
7.5 mm/yr	Shutter ridge height	0.35	0.0017
7.5 mm/yr	Divide relief	-0.048	0.97
10 mm/yr	Shutter ridge length	0.66	2.05e-10
10 mm/yr	Shutter ridge height	0.50	3.4e-7
10 mm/yr	Divide relief	-0.0063	0.39
Linear regressions with stream capture rate: model data			
Lateral slip rate	**Variable**	**Adjusted r^2**	**p-value**
All	Shutter ridge length	0.28	5.65e-6
All	Shutter ridge height	0.31	1.46e-6
All	Divide relief	0.31	1.25e-6
All	Lateral slip rate	0.27	6.95e-6
Linear regressions with stream capture rate: subsets of model data			
Lateral slip rate	**Variable**	**Adjusted r^2**	**p-value**
1 mm/yr	Shutter ridge length	0.61	0.00037
1 mm/yr	Shutter ridge height	0.64	0.00020

1 mm/yr	Divide relief	0.37	0.010
2.5 mm/yr	Shutter ridge length	0.42	0.036
2.5 mm/yr	Shutter ridge height	0.74	0.0018
2.5 mm/yr	Divide relief	0.38	0.044
5 mm/yr	Shutter ridge length	0.020	0.28
5 mm/yr	Shutter ridge height	0.20	0.054
5 mm/yr	Divide relief	0.36	0.011
7.5 mm/yr	Shutter ridge length	0.050	0.27
7.5 mm/yr	Shutter ridge height	0.15	0.164
7.5 mm/yr	Divide relief	0.35	0.054
10 mm/yr	Shutter ridge length	0.18	0.063
10 mm/yr	Shutter ridge height	0.50	0.0020
10 mm/yr	Divide relief	0.090	0.15

Table 4.4. Results of multiple linear regressions using field data. Results of multiple linear regressions using field data to predict channel offset length.

Multiple linear regressions with channel offset length: field data					
Model	**Variable**	**Adjusted r^2**	**Variance explained**	**p-value**	**Relative importance**
Shutter ridge length, shutter ridge height, lateral slip rate		0.76	76.9%	< 2e-16	
	Shutter ridge length			4.04e-16	0.72
	Shutter ridge height			0.93	0.21
	Lateral slip rate			0.47	0.069
Shutter ridge length, divide relief, lateral slip rate		0.79	79.6%	< 2e-16	
	Shutter ridge length			< 2e-16	0.90
	Divide relief			0.027	0.033
	Lateral slip rate			0.94	0.069

Table 4.5. Results of simple linear regressions using field data. Results of linear regressions with channel offset length using field data.

Linear regressions with channel offset length: field data			
Fault	**Variable**	**Adjusted r^2**	**p-value**
All	Shutter ridge length	0.76	< 2e-16
All	Shutter ridge height	0.31	7.2e-8
All	Divide relief	0.0084	0.20
All	Lateral slip rate	0.095	0.0038
Clarence	Shutter ridge length	0.39	0.00090
Clarence	Shutter ridge height	0.63	4.1e-6
Clarence	Divide relief	0.045	0.17
Awatere	Shutter ridge length	0.53	7.3e-9
Awatere	Shutter ridge height	0.49	4.1e-8
Awatere	Divide relief	-0.0067	0.41
Kekerengu	Shutter ridge length	0.96	1.1e-5
Kekerengu	Shutter ridge height	0.86	0.00055
Kekerengu	Divide relief	0.078	0.25

4.7.4 *Descriptions of Supplementary Materials*

4.7.4.1 Data Set

CHILD input files. This zipped folder contains the CHILD model input files that we used in this paper. Files contain the tectonic scenarios outlined in Table 4.1, as well as all other variables related to model options, material properties, and climate that were held constant throughout our experiments. Each model experiment is accomplished by using CHILD to run an input file beginning with “Up_” to generate the initial modeled topography, then running a corresponding input file beginning with “SS_” to initiate a strike-slip fault through that topography. The file naming convention is described in detail in the readme in this folder.

4.7.4.2 Movies

1. Movie S1. Example of block uplift of CHILD model domain before strike-slip fault is initiated. Open boundary is at lower edge of model domain. This example has a uniform uplift rate of 1 mm/yr. Axes are in meters.
2. Movie S2. Example of a CHILD model run that does not exhibit ridge migration. This example has a lateral slip rate of 5 mm/yr and uplift rates of 1 and 0.4 mm/yr above and below the fault, respectively. Axes are in meters.
3. Movie S3. Example of ridge migration in a CHILD model output. This example has a lateral slip rate of 1 mm/yr and uplift rates of 1 and 0.8 mm/yr above and below the fault, respectively. Axes are in meters.
4. Movie S4. Example of ridge migration causing a catchment to evade drainage capture. This CHILD model run has a lateral fault slip rate of 1 mm/yr and uplift of 1 mm/yr above and below the fault. Axes are in meters.
5. Movie S5. View of Movie S4 displaying a slope map. Note asymmetry of slopes on either side of migrating interfluves. This CHILD model run has a lateral fault slip rate of 1 mm/yr and uplift of 1 mm/yr above and below the fault. Axes are in meters.

Chapter 5. CONCLUSION

Chapters 2 and 3 contribute to a large and vibrant body of work on the Cenozoic tectonic evolution of New Zealand. In these chapters I derive tectonic histories from low-temperature thermochronology, by interpreting timing and relative rates of exhumation across the landscape of the Marlborough Fault System. Chapter 2 reveals the 10-13 Ma development of the Wairau fault, the resultant formation of a restraining bend at the Alpine-Wairau fault junction, and the onset of exhumation in a broad region caused by this restraining bend. This sequence of events was a consequence of changing plate motion and is a tectonic history related to, yet distinct from, the subsequent formation of the Southern Alps in response to the same plate motion change.

Chapter 3 applies the same method to the rest of the Marlborough Fault System. This work greatly extends the work of Baker and Seward (1996) and Collett et al. (2019). I identify the earliest manifestation of the Early Kaikōura Orogeny, with exhumation focused on the (present-day) north side of the Awatere fault beginning in the early Eocene. In the western MFS, thermochronology results show a different tectonic history, in which the modern MFS faults do not exert a strong control on exhumation. By conducting an inversion of my new thermochronology data from Chapters 2 and 3, as well as other published data, I construct a model of recent exhumation rates across the MFS. This work reveals exhumation rates of ~3-3.6 mm/yr adjacent to the Alpine fault, as well as ~0.9-1.4 mm/yr in the Seaward Kaikōura range.

Chapter 4 has a more theoretical approach and a more local-scale focus. In this chapter I use the CHILD landscape evolution model to examine the effects of preexisting topography on the landscape expression of a strike-slip fault. This study showed that, in simple modeled landscapes, channels crossing a strike-slip fault were subject to a regular and effective cycle of channel offset by fault slip and shortening by stream capture. Channel offset length observable at

any point in time was strongly limited by the length of shutter ridges, which in this model was in turn controlled by the drainage spacing of the landscape. Relief of shutter ridges was shown to make stream capture more difficult, especially when the fault slip rate is slow relative to channel and hillslope erosion. Field comparison to the MFS shows that real-world complexities – in this case, lithological differences between shutter ridges and the surrounding landscape – can disrupt these expected patterns, allowing long, fault-parallel channel offsets to form.

The conclusions of this dissertation shed light on the tectonic and geomorphic evolution of the New Zealand plate boundary, as well as having implications for other strike-slip and oblique systems. The MFS has undergone multiple phases of fault initiation, fault reactivation, distributed deformation, and regional uplift in response to changing plate motion boundary conditions. Its landscape reflects this ongoing history, from its broad-scale topography to individual drainage patterns.